University of Naples Federico II

Polytechnic and Basic Sciences School

Department of Earth, Environmental and Resources Science, Italy

Doctorate Program in
Earth, Environmental and Resources Sciences
XXXII Cycle

Ph.D. Thesis

Degassing of alkaline magmas in volcanic conduit during explosive eruptions

by

Gianmarco Buono

Tutors:
Prof. Paola Petrosino
Dr. Lucia Pappalardo

Ph.D. Coordinator:
Prof. Maurizio Fedi

Naples, 2019

Abstract

Degassing of magma strongly controls its transfer into the Earth's crust from reservoirs towards the surface and, in case of eruption, the eruptive style, which in turn drives tephra transport and emplacement as well as atmospheric impact. Understanding how degassing works is particularly challenging in the case of poorly explored alkaline magmas. In fact, they frequently fed powerful eruptions, although their low viscosity is generally more typical of magmas related to less explosive or effusive eruptions.

In this work, degassing mechanisms and timescales of alkaline melts have been investigated combining petrological characterization of natural volcanic rocks emitted during eruptions with different volcanic explosivity index (VEI) from the Neapolitan alkaline volcanism (including Campi Flegrei caldera and Somma-Vesuvius), HT-HP (high temperature and pressure) decompression experiments, numerical modeling of magma vesiculation and reviewed literature data. In particular, 3D microtextural explorations on natural and experimental samples have been performed using X-ray computed microtomography, an imaging technique only recently introduced in Earth science applications.

The obtained results have allowed (i) the definition of a new protocol of 3D imaging textural characterization based on automatic algorithms aimed at correctly examining rocks with highly interconnected pore networks, which are difficult to quantitatively investigate using the procedures employed so far in volcanology; (ii) furnishing of conceptual models and constraints useful to better improve knowledge on degassing of alkaline magmas during different eruptive scenarios and ascent conditions as well as interpret surface-monitored signals associated with explosive eruptions; (iii) the exploration of the influence of external environmental factors (e.g. interactions between magma and wall-rocks or external water) on magma degassing, particularly focusing on the effects of the rapid release of external carbon dioxide on the increment of eruption explosivity in volcanic systems located in carbonate bedrocks.

Contents

1. General introduction

Explosive volcanic eruptions are one of the most dangerous causes of natural hazard and can have severe effects on human life. In fact, they can occur with a wide spectrum of eruptive styles, which affect tephra transport and emplacement as well as atmospheric impacts. For example, although the relatively weak explosivity, 2010 eruptions of Eyjafjallajökull caused the biggest shutdown of airspace in Europe since World War II, affecting at least 10 million passengers worldwide (BBC online, 24 May 2010), whereas paroxysmal explosions of the Stromboli volcano, interrupting the normal (Strombolian) activity twice in the summer of 2019, provoked the death of a person (ANSA online, 3 July 2019). On the other hand, during Campanian Ignimbrite eruption (~40 ka) of Campi Flegrei caldera, one of the most explosive eruptions in Europe of the past 200 ka, ~388–588 km^3 of tephra volume were emitted, covering an area of over ~3 million km^2 (tephra thickness ≥ 0.5 cm), and ~50–250 Tg of SO_2 were delivered to the stratosphere with a consequent temperature decrease of ~2-4 °C in Western Europe, likely impacting on the final decline of Neanderthals (Black et al., 2015; Marti et al., 2016).
However, although in the last decades advanced monitoring networks have been extended to the main active volcanoes and provided warnings for variations in volcano dynamics, one of the main challenges in volcanology remains the correct interpretation of surface-monitored signals in terms of magma transfer from reservoirs towards the surface and its influence on the eruptive style. The main purpose of this thesis is to try to contribute on this open issue investigating on degassing mechanisms and timescales during ascent of alkaline magmas in explosive eruptions. In order to better clarify motivations and objectives of the present work it can be useful to introduce two questions about why to focus on magma degassing and melts with alkaline compositions.

Why magma degassing?
Magmatic melts with specific physico-chemical properties rising in the Earth's crust undergo decompression, leading to degassing (i.e. exolution of volatiles dissolved in the melt: H_2O > CO_2 > S, Cl, F) through formation of bubbles, which in turn allow for magma (i.e. melts + bubbles ± crystals) compressibility and buoyancy, promoting its ascent. Volatiles exolution can also affect magma rheology directly, reducing H_2O in the melt and then increasing degree of polymerization, as well as indirectly, promoting formation of tiny (≤ 100s μm) crystals (i.e. microlites) if there is enough time (Gonnermann and Manga, 2012). Therefore, degassing controls magma vesiculation (nucleation, growth - by volatile diffusion and gas expansion – and thus interactions of bubbles) and rheological changes in the volcanic conduit, which strongly influence magma ascent as well as fragmentation and thus eruptive style and scenarios. Ultimately these last processes are driven by: (i) initial magmatic variables (e.g. temperature, pressure, melt and volatile composition) and their evolution (e.g. Blundy and Cashman, 2008), (ii) degassing (and outgassing, i.e. gases loss from magma; e.g. Gonnermann and Manga, 2012), (iii) external environmental factors (e.g. conduit geometry, interactions with wall-rock and external water; e.g. Houghton et al., 2010). In fact, more schematically, magma ascent in a cylindrical volcanic conduit during explosive eruptions, assuming isothermal and steady-state conditions and mechanical equilibrium between melt and bubbles, is governed in one dimension by:

$$\frac{d(\rho v)}{dz} = 0 \qquad \text{(mass conservation)}$$

$$\rho v \frac{dv}{dz} = -\frac{dP}{dz} - \left(\frac{dP}{dz}\right)_{\rho} - \left(\frac{dP}{dz}\right)_{\mu} = -\frac{dP}{dz} - \rho g - \frac{4f}{D}\rho\frac{v^2}{2} \qquad \text{(momentum conservation)}$$

where v is the vertical (z direction) magma velocity, P is the pressure, ρ and μ are magma density and viscosity (which are strongly influenced by degassing-induced vesiculation and rheological changes), f is the wall friction coefficient and D is the conduit diameter (Macedonio et al., 2005; Gonnermann and Manga, 2012).
Finally, different magma degassing behaviours lead to different eruptive styles and thus to volcanic rocks with different textural (e.g. number density and size distribution of vesicles – i.e. "frozen" bubbles within tephra – or microlites) and chemical (e.g. glass volatile content) features, from which is possible to decode information (Cashman and Mangan, 1994; Sparks et al., 1994).
Consequently degassing can be explored by (i) petrological (textural and chemical) characterization of natural volcanic rocks (e.g. Cashman and Mangan, 1994; Baker et al., 2012), (ii) high temperature and pressure (HT-HP) decompression experiments (e.g. Shea et al., 2017) and (iii) numerical modeling of magma vesiculation (e.g. Toramaru, 1989; Huber et al., 2014). In this framework, new potentialities have been demonstrated by recent investigations through X-ray computed microtomography (X-μCT), a technique only recently applied to Earth science, which allows three-dimensional and direct (i.e. without mathematical corrections to convert 2D data in 3D) quantitative analyses of the internal structure of rocks, with a very high resolution (down to submicron) and in a non-destructive way (Baker et al., 2012). In this work the mentioned approaches have been coupled to improve our knowledge on degassing of alkaline magmas for different eruptive scenarios.

Why alkaline magmas?
The main conceptual and theoretical models of magma degassing are mainly focused on rhyolitic or basaltic volcanism (e.g. see Cashman and Sparks, 2013 and references therein), thus partially neglecting the wide variability in composition, and then in physico-chemical properties, of magmas. In particular, the high alkalis (especially K_2O and Na_2O) concentration in the alkaline magmas determines more depolymerized, and consequently low viscous, melts even for the more differentiated terms (Lesher and Spera, 2015). However, alkaline melts are frequently able to feed highly explosive eruptions, albeit their low viscosity, which instead usually promotes efficient outgassing (mainly driven by bubble buoyancy) and short structural relaxation time, hindering development of high gas overpressure inside bubbles, brittle magma fragmentation and highly explosive behaviour (Gonnermann and Manga, 2012; Cashman and Scheu, 2015). This is demonstrated, for example, by the Neapolitan alkaline volcanism in southern Italy which includes, in a densely populated area, two of the most dangerous volcanoes in Europe: Campi Flegrei caldera (CFc) and Somma-Vesuvius (S-V) volcanic complex. This active volcanic area has been selected as a case study for this work. The alert state of the first volcano was raised from the green (quiet) to yellow (scientific attention) level at the end of 2012 by Civil Protection Department whereas the latter is at green level. The main volcanological investigations on these volcanoes have been so far focused on superficial (e.g. transport and emplacement in pyroclastic plume and flows) and magma chamber processes (e.g. CFc: Forni et al., 2018; S-V: Baxter et al., 2008 and references in these studies). Therefore to improve knowledge on magma ascent dynamics in the volcanic conduit could be a further crucial step to better understand how this volcanism works.

Thesis organization and objectives
Starting from these premises, the present thesis is organized in the three following chapters:

- In the chapter 2 a new protocol of 3D textural characterization for volcanological application has been defined, effective for volcanic rocks with highly interconnected pore network scanned with X-ray computed microtomography;
- In the chapter 3 the protocol has been applied to alkaline products of eruptions with different volcanic explosivity index (VEI) from Neapolitan alkaline volcanism. These investigations have been combined with further examinations (chemical analyses as well as

thermodynamics and fluid-dynamics simulations) and integrated in a review study trying to reconstruct a general model of degassing for this volcanism;

- In the chapter 4 the achieved data have been used to plan and perform experimental and numerical simulations through HP-HT decompression experiments and numerical modeling of magma vesiculation aimed at examining degassing behaviour of evolved alkaline melts under controlled conditions.

References

Baker, D. R., Mancini, L., Polacci, M., Higgins, M. D., Gualda, G. A. R., Hill, R. J., Rivers M.L. (2012). An introduction to the application of X-ray microtomography to the three-dimensional study of igneous rocks. Lithos 148, 262-276. https://doi.org/10.1016/j.lithos.2012.06.008.

Baxter, P. J., Neri, A., Blong, R. (2008). Evaluating explosive eruption risk at European volcanoes. J. Volcanol. Geotherm. Res. 178, v-ix. https://doi.org/10.1016/j.jvolgeores.2008.11.012.

Black, B., Neely, R., Manga, M. (2015). Campanian Ignimbrite volcanism, climate, and the final decline of the Neanderthals. Geology 43, 1–4. https://doi.org/10.1130/G36514.1.

Blundy, J., Cashman, K.V. (2008). Petrologic reconstruction of magmatic system variables and processes. Rev. Mineral. Geochem. 69, 179–239. https://doi.org/10.2138/rmg.2008.69.6.

Cashman, K. V., Mangan, M. T. (1994). Physical aspects of magmatic degassing: II. Constraints on vesiculation processes from textural studies of eruptive products. Rev. Mineral. Geochem. 30, 447–478.

Cashman, K. V., Scheu, B. (2015). Magma Fragmentation. In H. Sigurdsson, B. Houghton, S. R. McNutt, H. Rymer, J. Stix (Eds.), The Encyclopedia of Volcanoes (Second Edition) (pp. 459-471). Academic Press, London. https://doi.org/10.1016/B978-0-12-385938-9.00025-0.

Cashman, K. V., Sparks, R. S. J. (2013). How volcanoes work: a 25 year perspective. Geol. Soc. Am. Bull. 125, 664–690. https://doi.org/10.1130/B30720.1.

Forni, F., Degruyter, W., Bachmann, O., De Astis, G., Mollo, S. (2018). Long-term magmatic evolution reveals the beginning of a new caldera cycle at Campi Flegrei. Sci. Adv. 4, eaat9401. https://doi.org/10.1126/sciadv.aat9401.

Gonnermann, H.M., Manga, M. (2012). Dynamics of magma ascent in the volcanic conduit. In S.A. Fagents, T.K.P. Gregg, R.M.C. Lopes (Eds.), Modeling Volcanic Processes, the Physics and Mathematics of Volcanism (pp. 55–84). Cambridge University Press, Cambridge. https://doi.org/10.1017/CBO9781139021562.004.

Houghton, B.F., Carey, R.J., Cashman, K.V., Wilson, C.J.N., Hobden, B.J., Hammer, J.E. (2010). Diverse patterns of ascent, degassing, and eruption of rhyolite magma during the 1.8 ka Taupo eruption, New Zealand: evidence from clast vesicularity. J. Volcanol. Geoth. Res. 195, 31–47. https://doi.org/10.1016/j.jvolgeores.2010.06.002.

Huber, C., Su, Y., Nguyen, C., Parmigiani, A., Gonnermann, H.M., Dufek, J. (2014). A new bubble dynamics model to study bubble growth, deformation, and coalescence. J.Geophys. Res. Solid Earth 119, 216–239. https://doi.org/10.1002/2013JB010419.

Lesher, C. E., Spera, F. J. (2015). Thermodynamic and Transport Properties of Silicate Melts and Magma. In H. Sigurdsson, B. Houghton, S. R. McNutt, H. Rymer, J. Stix (Eds.), The Encyclopedia of Volcanoes (Second Edition) (pp. 113-141). Academic Press, London. https://doi.org/10.1016/B978-0-12-385938-9.00005-5.

Macedonio, G., Neri, A., Martí, J., Folch, A. (2005). Temporal evolution of flow conditions in sustained magmatic explosive eruptions. J. Volcanol. Geotherm. Res. 143, 153–172. https://doi.org/10.1016/j.jvolgeores.2004.09.015.

Marti, A., Folch, A., Costa, A., Engwell, S. (2016). Reconstructing the plinian and co-ignimbrite sources of large volcanic eruptions: A novel approach for the Campanian Ignimbrite. Sci. Rep. 6, 21220. https://doi.org/10.1038/srep21220.

Shea, T. (2017). Bubble nucleation in magmas: a dominantly heterogeneous process? J. Volcanol. Geotherm. Res. 343, 155–170. https://doi.org/10.1016/j.jvolgeores.2017.06.025.

Sparks, R.S.J., Barclay, J., Jaupart, C., Mader, H.M., Phillips, J.C. (1994). Physical aspects of magmatic degassing. I. Experimental and theoretical constraints on vesiculation. Rev. Mineral. Geochem. 30, 413–445.

Toramaru, A. (1989). Vesiculation process and bubble size distributions in ascending magmas with constant velocities. J. Geophys. Res. 94, 17523–17542. https://doi.org/10.1029/JB094iB12p17523.

2. 3D textural characterization of highly interconnected pore networks: volcanological applications

X-ray computed microtomography (X-µCT): benefits and limitations

In this thesis X-ray computed microtomography has been applied to natural volcanic rocks erupted during explosive eruptions and experimental samples obtained from HT-HP decompression experiments in order to examine magma degassing and vesiculation.

This technique has been only recently introduced in Earth science and applied in several fields (e.g. hydrogeological, geotechnical, structural geology, petroleum, planetary applications; e.g. Cnudde and Boone, 2013 and references therein). In volcanology, it showed an enormous potential, however only few systematic studies have been so far performed (Baker et al., 2012; Gurioli et al., 2015 and references therein).

X-µCT allows quantitative investigation of the internal texture of materials with a very high resolution (down to submicron), three-dimensionally and directly (i.e. without mathematical corrections to convert 2D data in 3D), impossible to obtain with more conventional 2D techniques. In fact, in two-dimensional methods, data are acquired form 2D sections (often thin sections) that lack of 3D information (e.g. connectivity, permeability) and need to be converted in 3D using stereological methods, which are complicated by two main effects: the cut-section and intersection-probability effects. The former takes into account that, even in a monodisperse population of particles of interest (with one true size), intersection plane (i.e. the obtained 2D section) rarely cuts through the center of each particle (Fig. 1a); the latter effect takes into account that, in a polydisperse population, smaller particles are less likely to be intersected by a plane (Fig 1b; Higgins et al., 2000; 2006). In this framework the particle shape assumed for the conversion plays a fundamental role, however particles (especially vesicles) in volcanic rocks can form networks with complex morphologies (Fig. 4a).

On the contrary, the main limitation of 3D methods, in addition to the higher costs, is the low manual control on the 3D images, which requires the correct application of automatic algorithms (see below).

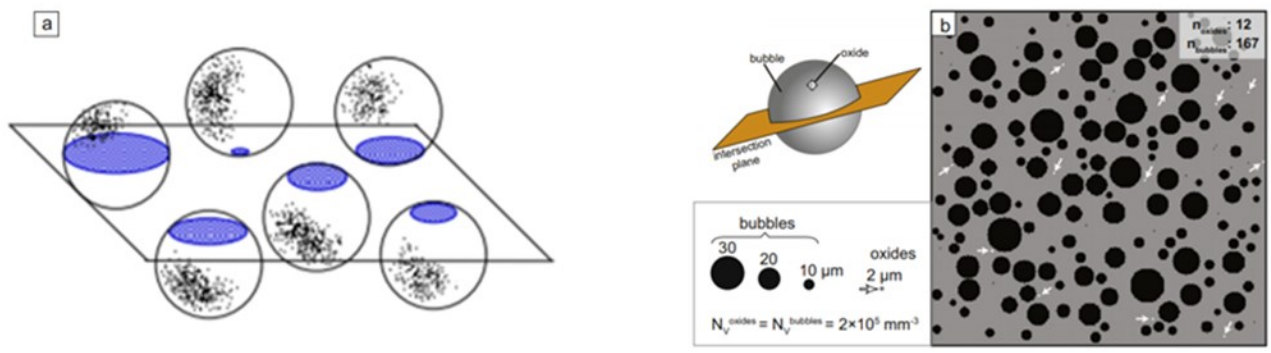

Fig.1. Examples of cut-section (a; after Armienti, 2008) and intersection-probability (b; after Shea, 2017) effects. In (b) starting from a 3D virtual pyroclast containing bubbles of 10-30 µm and oxides of 2 µm with the same number density (2 x 10^5 mm^{-3}), randomly taken 2D images can display oxides ~10–15 times fewer than bubbles.

A new protocol of 3D textural characterization for volcanological applications

This work is one of the first studies performed at the X-ray computed microtomography laboratory of the National Institute of Geophysics and Volcanology – Vesuvius Observatory (INGV – Naples), recently equipped with a ZEISS Xradia 410 Versa. Therefore it contributed to define 3D image acquisition and processing procedures concerning the stages summarized in Fig. 2.

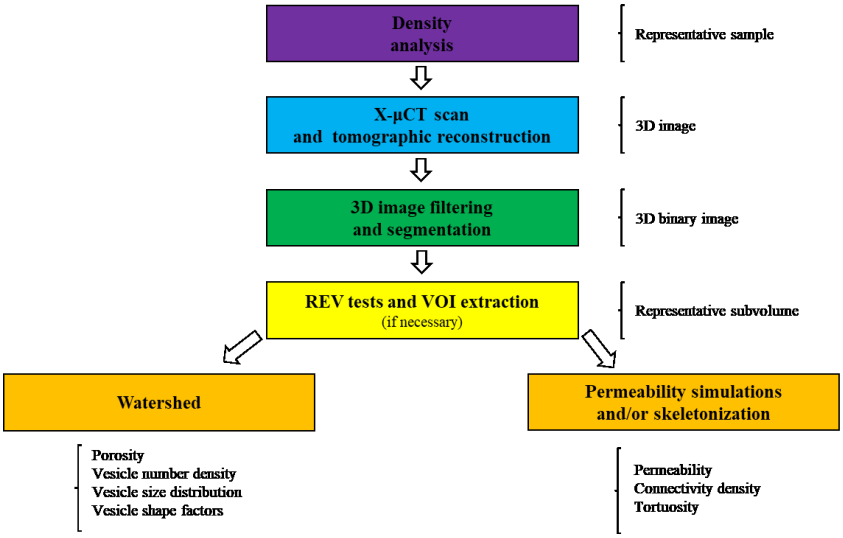

Fig. 2. Schematic representation of the 3D image acquisition and processing pipeline.

As shown in Fig. 2, density analyses were realized to select representative samples with modal densities, from which were acquired 3D images using X-µCT, then filtered and segmented in order to isolate particles of interest in 3D binary images and quantify their properties.

The main phases that constitute a volcanic rock are: glass (i.e. the correspondent of melt in magma), vesicles (or pores; i.e. bubbles) and crystals (both phenocrysts and microlites). In detail, investigations on magma degassing need to decrypt textural information mainly contained in populations of vesicles. However this operation is complicated by the presence of networks of highly interconnected vesicles in 3D images acquired from rocks erupted during intense explosive volcanism. The high interconnection can easily exceed even the 90% of total porosity in this rocks and can result from: (i) the rupture of glass walls separating vesicles once a critical porosity is reached during the latter stages in the volcanic conduit (e.g. Rust and Cashman, 2011 and references therein), (ii) the presence of very thin (less than few µm) glass walls not properly detected during image acquisition or lost during image processing. Consequently, the reconstruction of glass walls in these 3D stacks (of about 1000 2D slices; see chapter 2) - necessary to correctly examine the vesiculation evolution during magma ascent (e.g. Shea et al., 2010) - is much more complex than by 2D methods, in which there is a greater manual control on only few 2D images taken from one (or few) 2D section (e.g. thin section). However the main procedures (e.g. erosion-dilation operations, skeletonization plus maximal inscribed sphere method) adopted so far in 3D volcanological analyses for this purpose were found to be inadequate for these highly interconnected pore networks.

Therefore, starting from the 3D binary images, becomes challenging to define a new protocol based on automatic algorithms able to (i) correctly separate vesicles from the network and (ii) examine the degree of interconnection of the network:

- for the point (i), marker-based watershed algorithm proved to be very effective to preserve the original volume and shape of the isolated vesicles as well as to need short computational time, allowing analysis of large volumes, which reduces the uncertainties in the measurements (Figs. 3

and 4a-e). It works similarly to watershed lines (applying watershed transformations) dividing catchment basins filled from the flooding on a topographic map (applying and inverting Chamfer Distance Maps; a priority map where each voxel within a vesicle assumes a "height" related to its distance from the vesicle-glass interface) starting from specific seed points or markers (applying H-Maxima transformations; regions with local maximum values of the map, i.e. the innermost part of the vesicles);

- for the point (ii), permeability simulations (solving Stokes equations with finite volume method and applying Darcy's law) and skeletonization (creating a medial axis of the binarized network with thinning and boundary propagation or general-field functions) based algorithms have been adopted (Fig. 4f).

More information on these methods are furnished for example in Harlow and Welch (1965), Soille et al. (2003) and Cornea et al. (2007).

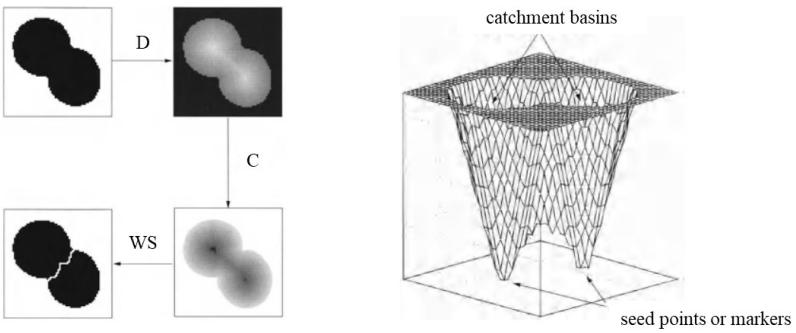

Fig. 3. Principles of marker-based watershed using distance maps. Left: D = distance map, C = complemented (or inverted) distance map, WS = watershed. Right: Perspective view of complemented distance map. After Soille (2003).

These procedures have been mainly performed using Avizo, ImageJ, Pore3D and Dragonfly. The quantified parameters are briefly summarized in Fig. 2. In the case of long computational times, Volumes of Interest (VOI) larger than Representative Elementary Volumes (REV; obtained with the box counting method, i.e. evaluating when parameters like porosity reach constant values progressively increasing the analyzed volume) have been extracted and processed.

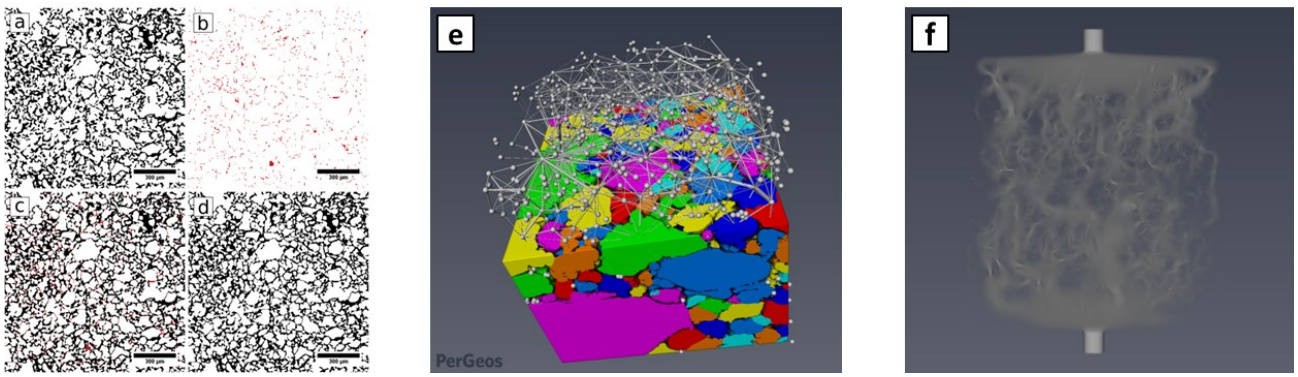

Fig. 4. Examples of: (a-d) 2D slices (640 x 640 pixels, 2 μm/pixel) obtained applying marker-based watershed on a 3D binary image; (e) volume rendering of labeled separated vesicles and connecting lines between them, internal portion (cube side: 300 pixels, 1 μm/pixel); (f) velocity field in the permeability simulations (cylinder diameter and height: ~1000 pixels, 2 μm/pixel).

References

Armienti, P. (2008). Decryption of igneous rock textures: crystal size distribution tools. Rev. Mineral. Geochem. 69, 623-649. https://doi.org/10.2138/rmg.2008.69.16.

Baker, D. R., Mancini, L., Polacci, M., Higgins, M. D., Gualda, G. A. R., Hill, R. J., Rivers M.L. (2012). An introduction to the application of X-ray microtomography to the three-dimensional study of igneous rocks. Lithos 148, 262-276. https://doi.org/10.1016/j.lithos.2012.06.008.

Cornea, N.D., Min, P., Silver, D. (2007). Curve-skeleton properties, applications, and algorithms. IEEE Trans. Vis. Comput. Graph. 13, 3, 530–548. https://doi.org/10.1109/TVCG.2007.1002.

Cnudde, V., Boone, M.N. (2013). High-resolution X-ray computed tomography in geosciences: a review of the current technology and applications. Earth Sci. Rev. 123, 1–17. http://dx.doi.org/10.1016/j.earscirev.2013.04.003.

Gurioli, L., Andronico, D., Bachelery, P., Balcone-Boissard, H., Battaglia, J., Boudon, G., Burgisser, A., Burton, M. R., Cashman, K., Cichy, S., Cioni, R., Di Muro, A., Dominguez, L., D'Oriano, C., Druitt, T., Harris, A. J. L., Hort, M., Kelfoun, K., Komorowski, J. C., Kueppers, U., Le Pennec, J. L., Menand, T., Paris, R., Pioli, L., Pistolesi, M., Polacci, M., Pompilio, M., Ripepe, M., Roche, O., Rose-Koga, E., Rust, A., Schiavi, F., Scharff, L., Sulpizio, R., Taddeucci, J., Thordarson, T. (2015). MeMoVolc consensual document: a review of cross-disciplinary approaches to characterizing small explosive magmatic eruptions. Bull. Volcanol. 77, 49. http://dx.doi.org/10.1007/s00445-015-0935-x.

Higgins, M. D. (2000). Measurement of Crystal Size Distributions. Am. Mineral. 85, 1105-1116. https://doi.org/10.2138/am-2000-8-901.

Higgins, M. D. (2006). Quantitative textural measurements in igneous and metamorphic petrology. Cambridge University Press, Cambridge. https://doi.org/10.1017/CBO9780511535574.

Harlow, F. H., Welch, J. E., (1965). Numerical calculation of time-dependent viscous incompressible flow of fluid with free surface, Phys. Fluids 8, 2182. https://doi.org/10.1063/1.1761178.

Rust, A.C., Cashman, K.V. (2011). Permeability controls on expansion and size distributions of pyroclasts. J. Geophys. Res. 116, B11202. https://doi.org/10.1029/2011JB008494.

Shea, T. (2017). Bubble nucleation in magmas: a dominantly heterogeneous process? J. Volcanol. Geotherm. Res. 343, 155–170. https://doi.org/10.1016/j.jvolgeores.2017.06.025.

Shea, T., Houghton, B.F., Gurioli, L., Cashman, K.V., Hammer, J.E., Hobden, B.J. (2010). Textural studies of vesicles in volcanic rocks: an integrated methodology. J. Volcanol. Geotherm. Res. 190, 271–289. https://doi.org/10.1016/j.jvolgeores.2009.12.003.

Soille, P. (2003). Morphological Image Analysis (Second edition). Springer, . Heidelberg. https://doi.org/10.1007/978-3-662-05088-0.

3. Degassing of alkaline melts during different eruptive scenarios: case study of the Neapolitan alkaline volcanism

In this chapter, eruptions with different explosivity from the Neapolitan alkaline volcanism have been selected as case studies with the aim of exploring degassing of alkaline magmas in function of eruptive styles and scenarios. Volcanic events representative of highly and weakly explosive volcanism have been chosen, favouring those affected by variations in eruptive dynamics or in physico-chemical properties of magma in order to better identify the main factors which drive changes in degassing behaviour.

The first section (3.1) is focused on degassing during highly explosive volcanism, selecting as case study the Pomici di Base Plinian eruption (22 ka, VEI~6), the largest (volume > 4.4 km^3) volcanic event of the Somma-Vesuvius. Interestingly, it was fed in the first part by a magma with an evolved trachytic composition, whereas in the second and larger part by a more mafic latitic-shoshonitic compositions (which constitutes the 75% of total erupted magma), despite these last less differentiated melts are not usually associated with high explosive events in Neapolitan alkaline volcanism. Degassing during this eruption has been investigated starting from a 3D textural exploration of representative products (applying the protocol previously described in the Chapter 2) summarized in Pappalardo et al. (2018; section 3.1.1). This study allowed also the evaluation of the probability that rapid release of external CO_2 happened during highly energetic, caldera-forming eruptions and the effects that it can have on degassing and ascent dynamics. Therefore, this aspect has been deepened through a detailed chemical investigation (major/minor elements and stable/radiogenic isotopes) constrained with thermodynamic and kinetic calculations, presented in Buono et al. (submitted; section 3.1.2). Preliminary data used or improved in these studies have been also reported and discussed in Buono et al. (2019; Appendix 1).

The second section (3.2) is focused on degassing during weakly explosive volcanism, selecting as case study the Monte Nuovo eruption (1538 AD, VEI~2), the latest volcanic event of the Campi Flegrei caldera, fed by a trachy-phonolitic magma. Volcanic activity in the first few days of the eruption produced a 132 m high, 800 m wide monogenetic tuff cone, then proceeded to a stasis, to resume with two discrete explosions of less intensity and magnitude. Here, degassing during this eruption has been examined by processing (applying and improving the protocol of the Chapter 2) 3D images acquired from representative products at the SYRMEP beamline of the Elettra Sincrotrone Trieste facility, where X-µCT approaches for volcanological applications are being improved since several years ago. This work is summarized in Liedl et al. (2019; section 3.2.1). Subsequently the obtained data have been better constrained performing one-dimensional conduit flow simulations, presented in Buono et al. (2018; section 3.2.2).

Finally, in the third section (3.3) information obtained from these investigations have been integrated with chemical and textural data available from literature in a review study summarized in Pappalardo and Buono (2019; section 3.3.1) aimed at proposing a general model of magma storage and degassing for the Neapolitan alkaline volcanism based on the knowledge acquired so far.

3.1. Highly explosive volcanism: the case study of the largest Somma-Vesuvius eruption

3.1.1. Combining textural and geochemical investigations to explore the dynamics of magma ascent during Plinian eruptions: a Somma-Vesuvius volcano (Italy) case study

This work is published on Contributions to Mineralogy and Petrology (vol.: 173, 61; doi: https://doi.org/10.1007/s00410-018-1486-x; year: 2018) under the same title with authors:

Pappalardo L.[a], Buono G.[a,b], Fanara S.[c], Petrosino P.[b]

a - Istituto Nazionale di Geofisica e Vulcanologia, Osservatorio Vesuviano, Italy
b - University of Naples Federico II, Department of Earth, Environmental and Resources Science, Italy
c - Georg-August University of Göttingen, Department of Experimental and Applied Mineralogy, Germany

I contributed to all phases (field activities, rock characterization, data interpretation, writing) and investigations of this work except the measurement of glass volatile (H_2O and CO_2) content, performed at the Department of Experimental and Applied Mineralogy of the Georg-August University of Göttingen.

Abstract

Trigger mechanisms and syn-eruptive processes of Plinian eruptions are poorly understood especially in the case of mafic powerful events. In the last decades, the combined geochemical and textural studies on volcanic rocks have proven to be fundamental tools for exploring the dynamics of magma ascent in volcanic conduits and for improving our ability to interpret volcano-monitoring signals and assess hazard.
In this case study, we quantitatively investigate 2D and 3D micro-textural, geochemical and isotopic features of pyroclastic rocks erupted during the Pomici di Base Plinian eruption (22 ka), the generally acknowledged first and most powerful event of the Somma-Vesuvius volcano. A peculiar aspect of this eruption is its high intensity that remained stable during the entire Plinian phase despite the strong magma compositional variation towards mafic terms. We infer that the transfer of magma towards the surface was intensified by the occurrence of rapid vesiculation pulses driven by limestone assimilation (skarn recycling) during magma ascent through the carbonatic bedrock. We conclude that limestone assimilation can hence be a syn-eruptive process, able to trigger further gas nucleation with deep impact on the eruption intensity, particularly crucial in the case of mafic/intermediate magma compositions.

1. Introduction

In the twentieth century, at least a dozen of worldwide strato-volcanoes generated high-magnitude eruptions that killed thousands of people and caused extensive damage with severe social and economic impacts. Some of these events interrupted long lasting periods of quiescence (e.g. Pinatubo, Philippines, 1991) while others followed a short volcanic rest (e.g. Colima, Mexico, 1913) or occurred with only little warning (e.g. Chaiten, Chile, 2008). Hence, understanding the trigger mechanisms as well as the syn-eruptive dynamics of these eruptions is crucial for their forecasting. Combined quantitative textural and geochemical studies on volcanic rocks have proven to be a valuable approach in exploring the conditions related to magma ascent in volcanic conduits (e.g. Klug et al., 2002; Adams et al., 2006; Mastrolorenzo and Pappalardo, 2006; Gurioli et al., 2008; Polacci et al., 2009; 2014; Shea et al., 2010a; 2010b; Rust and Cashman, 2011; Gonnermann and Houghton, 2012; Pappalardo et al., 2014; Rotella et al.; 2014), improving our ability to interpret volcano-monitoring signals and perform hazard evaluations. Particularly, 3D textural data has played a key role in assessing nucleation, growth and coalescence of gas bubbles and magma fragmentation that in turn influence the style and intensity of explosive eruptions. In fact 3D data allows the direct observation and quantification of the dimension, shape and orientation of the vesicles, as well as of their degree of interconnectedness and related permeability, difficult to determine using the more conventional 2D techniques (e.g. Song et al., 2001; Okumura et al., 2008, 2012; Polacci et al., 2009; 2012; 2014; Degruyter et al., 2010; Giachetti et al., 2011; Baker et al., 2012). X-ray computed microtomography (micro-CT) is a powerful, non-destructive method to carry out 3D textural studies of igneous rocks (e.g Jerram and Higgins, 2007; Baker et al., 2012; Cnudde and Boone, 2013). Nevertheless, only a few studies of volcanic pyroclasts using this tool are available especially on alkaline rocks (e.g. Polacci et al., 2009; Hughes et al., 2017).

The Somma-Vesuvius alkaline volcanic complex, located east of the metropolitan area of Naples, is one of the most dangerous volcanoes in the world (e.g. Mastrolorenzo et al., 2008; Lirer et al., 2010; Mastrolorenzo and Pappalardo, 2010 and the references therein), Fig. 1. The volcanic activity has been characterized by at least four Plinian eruptions, interposed to minor events covering a large range of magnitude and intensity (Cioni et al., 2008; Santacroce et al., 2008; De Vivo et al., 2010), the latest occurred on March 1944 (e.g. Cole and Scarpati, 2010; Pappalardo et al., 2014; Cubellis et al., 2016). The Pomici di Base eruption (Andronico et al., 1995; Delibrias et al., 1979; Bertagnini et al., 1998; Landi et al., 1999; Siani et al., 2004; Santacroce et al., 2008; Klebesz et al., 2012; 2015; Scarpati et al., 2016), occurred about 22 ka, is generally acknowledged as the first and most intense Vesuvian Plinian event. It marks the passage, after a period of prevalent effusive activity, to the explosive character of the volcano as well as the beginning of the caldera collapse events. The eruption was characterized by the emission, during a sustained-column Plinian phase, of at least 4.4 km^3 (bulk volume) pyroclastic products dispersed towards the E-NE, followed by a phreatomagmatic phase during which fallout activity has alternated with minor pyroclastic density currents confined to the volcano slopes. The Plinian fallout deposit is characterized by a strong compositional variation from white trachytic pumices (0.34 km^3 DRE**;** Landi et al., 1999) to black latitic-shoshonitic scoriae (0.96 km^3 DRE); during this phase the mass discharge rate remained stable in the range of 2–2.5 x 10^7 kg/s corresponding to a column height of 16–17 km (Bertagnini et al., 1998), despite the change towards mafic composition.

In this case study the microtextural features of clasts from the whole Pomici di Base Plinian fallout succession have been quantitatively investigated by generating high-resolution three-dimensional digital maps via X-ray computed microtomography. The obtained textural information (i.e. density measurements, bubble and throat number density and size distributions, bubble interconnectivity, etc.), combined with geochemical and Sr- and Nd- isotopic data on both separated groundmass and phenocrysts, has contributed to reconstruct the trigger mechanisms and conduit dynamics that controlled this Plinian eruption fed by a less evolved magma.

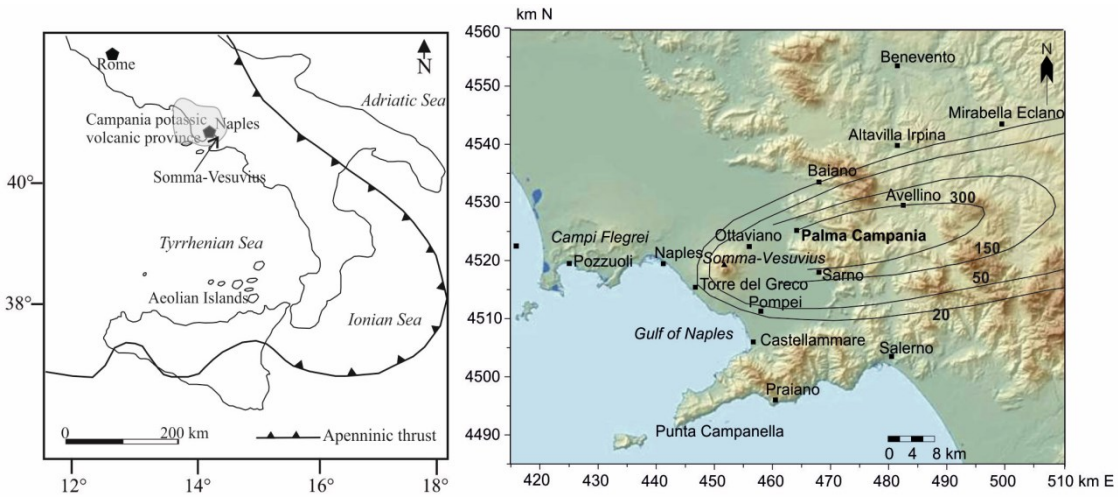

Fig. 1. On the left: Location Map for Somma-Vesuvius volcano (Italy), situated within Campanian Potassic Volcanic Province (grey field). On the right: Distribution of Pomici di Base fallout unit (Bertagnini et al., 1998).

2. Sampling and Methods

Representative juvenile pumice and scoria clasts of the entire Plinian fallout succession of the Pomici di Base eruption were collected from two key stratigraphic sections located at about 15 km NE of the Somma-Vesuvius (Palma Campania, near Naples), Fig. 1. The Plinian deposit is composed of a basal white pumiceous layer, overlain by a transitional gray pumice layer and an upper black scoria bed (Fig. 2). The three beds have an approximately constant relative thickness of 2:1:5 (Bertagnini et al., 1998). The sampling interval was dictated by changes in type, grain size and color of the pyroclastic products, according to the different stratigraphic units recognized by Bertagnini et al. (1998), Fig. 2. Samples location within eruptive units is reported in Fig. 2.

2.1. Bulk density

In order to account for possible density variations with size, we used juvenile clasts within a -5 to -2 phi size range ($\varphi = -log_2 D/D_0$ where D is the diameter of the clasts in mm and D_0 is a reference diameter, equal to 1 mm) for density measurements. Sets of 100 clasts for each granulometric class (where present) were weighted and coated with a thin film of paraffin wax, and their density was determined using a pycnometer. We calculated bulk vesicularity for each clast following the procedure described in Houghton and Wilson (1989), using a dense-rock equivalent (DRE) density of 2700 (latite-shoshonite) and 2400 (trachyte) kg/m^3, obtained by pycnometry measurements on fine-grained whole-rock powder as described in ASTM (2007).

No differences in clast-density distributions have been observed between the analyzed granulometric classes. Moreover, juvenile clasts with different sizes and same density, accurately observed under optical microscope, show comparable textural features. However to avoid any possible influence of post-fragmentation expansion, we have selected clasts within 4 ad 8 mm size range, as larger clasts do not necessarily preserve the vesicularity of the magma immediately prior to fragmentation (e.g. Thomas et al., 1994; Gardner et al., 1996; Kaminski and Jaupart, 1997).

Modal density clasts were selected from the base to the top of the deposits to investigate micro-textural variations with stratigraphic height (see also Gurioli et al., 2005; Balcone-Boissard et al., 2008; 2012; Houghton et al., 2010).

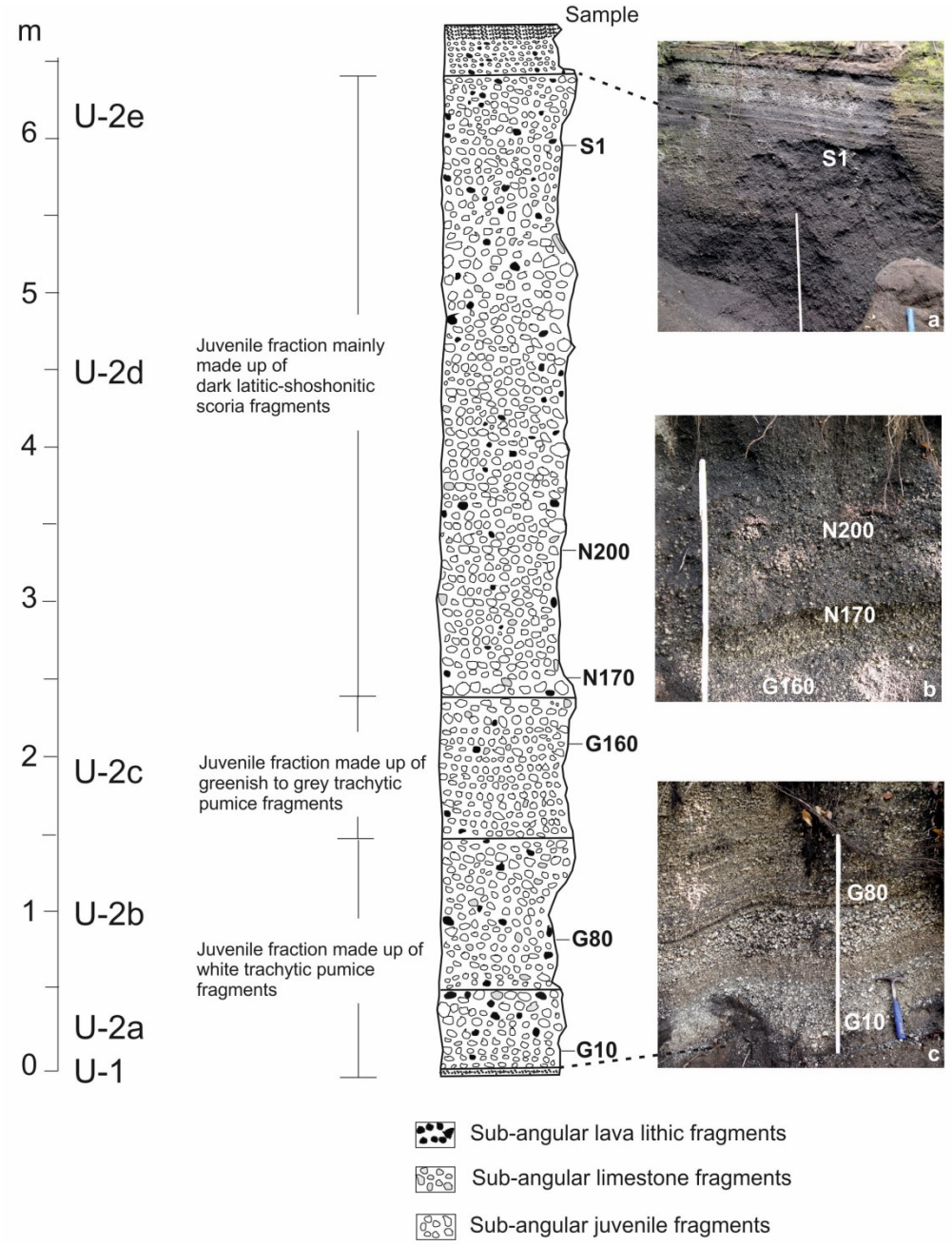

Fig. 2. Representative photos and schematic stratigraphic column for the Pomici di Base Plinian deposits and sample-number for clasts collected for this study. Samples were collected from two stratigraphic sections (a and b-c respectively; on the right). Sampling interval was dictated by changes in type, grain size and color of the pyroclastic products, according to the different stratigraphic units recognized by Bertagnini et al., 1998 (on the left): U-1 - ash and pumice fall deposits; U-2 – Plinian fallout deposit composed by a basal white pumiceous layer (U-2a and U-2b), a transitional layer (U-2c), an upper thick black scoria bed (U-2d and U-2e); U-3 – U-6 lithic-rich fallout and PDCs (pyroclastic surge and flow) deposits.

2.2. Microtomographic investigation

The microstructure of the samples was investigated by X-ray computed microtomography (micro-CT) using a Carl Zeiss Xradia Versa-410 3D X-ray microscope at the Istituto Nazionale di Geofisica e Vulcanologia—Sezione di Napoli ‘‘Osservatorio Vesuviano’’ (INGV-OV, Naples).

X-ray computed microtomography is a non-destructive analysis technique that offers the opportunity to visualize and quantify the internal structure of rock samples by generating three-

dimensional digital maps with a very high resolution (down to submicron). Particularly, the result of microtomographic investigation is a three-dimensional gray-level image proportional to the X-ray attenuation coefficient of the sample (that for the same energy is a function of the density and atomic number of the interested material), which allows the observation and measurement of the properties of objects (e.g. shape, size, distribution and orientation of fractures, pores, crystals, etc.) entirely avoiding the stereological corrections needed for measurements carried out in two dimensions.

Particularly, Xradia Versa architecture uses a two-stage magnification technique. First a geometric magnification, as with conventional micro-CT, is obtained. In the second stage, a scintillator converts X-rays to visible light, which is then optically magnified. Reducing dependence upon geometric magnification enables Xradia Versa instruments to maintain submicron resolution at large working distances.

In this study, cylinders of maximum diameter 0.5 cm were cut from the samples and the scan was performed over a 360° rotation using 4001 projections, 80 KV voltage, 10 W power. The resulting nominal voxel (volumetric pixel) size ranges from 0.9 to 2 μm depending on the optical magnification used (10X and 20X, see Table 1). However, imaging using any method (optical, SEM, XMT, etc.) where the smallest feature (vesicle or vesicle wall) is less than three pixels/voxels in diameter is subject to significant uncertainty (Hughes et al., 2017). So we consider that the minimum measurable voxel size ranges from ≈ 3 to 6 μm (corresponding to 3 voxel size) as also confirmed by accurate visual inspection of slices.

Reconstruction of the attenuation data was performed through the filtered back-projection algorithm using XRMReconstructor Xradia proprietary software producing a stack of 967 cross-sectional, grey-scale digital images, Fig. 3.

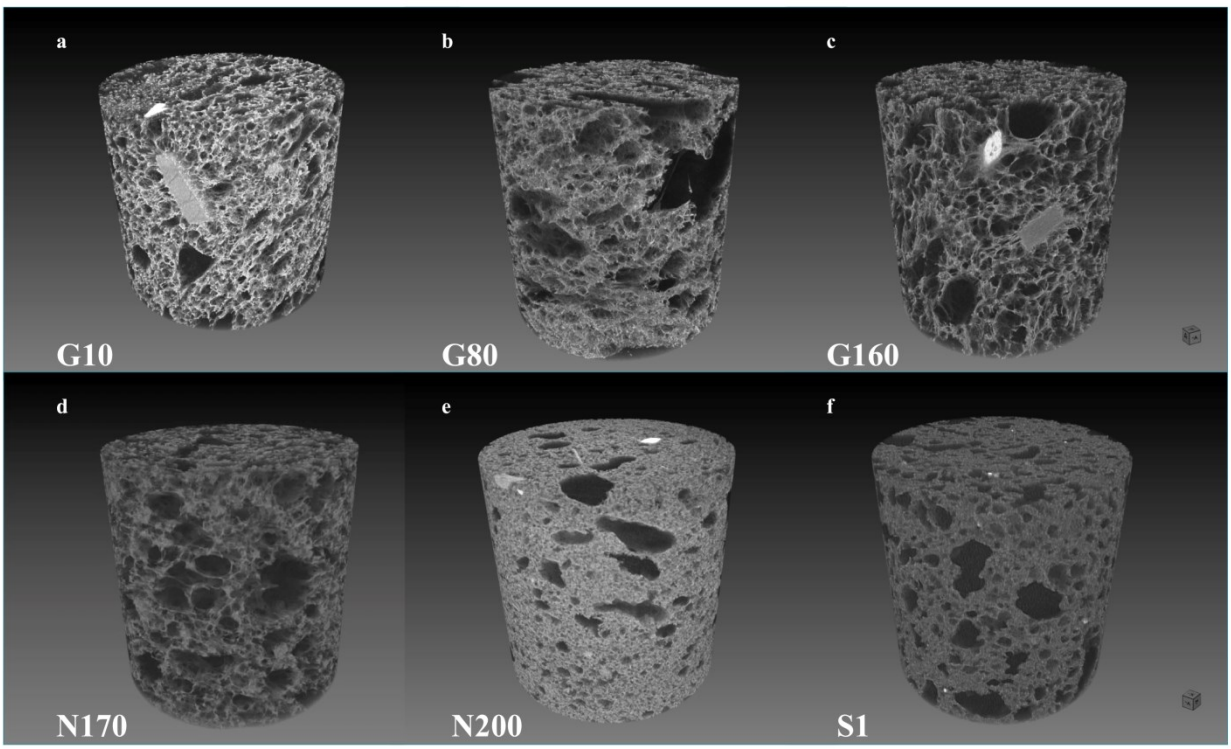

Fig. 3. Examples of volume rendering showing 3D microstructure of Pomici di Base trachytic (a-d) and latitic-shoshonitic (e-f) rocks. Cylinders diameter: 1000 μm. Vesicles are black, melt/feldspars/pyroxenes are grey and oxides are white.

2.3. 3D and 2D textural measurements

Vesicle and throat size distributions and number densities were obtained by processing the 3D tomographic images. First, the obtained 3D micro-CT images were filtered using grayscale-to-grayscale filters available in Blob3D software (Ketcham et al., 2005) in order to improve the brightness and contrast and to obtain an edge enhancement of the vesicles. Then the 3D images were segmented in order to isolate vesicles from matrix-glass and crystals on the basis of their gray level values (thresholding), which are related to the X-ray attenuation coefficient. In particular the automatic Otsu algorithm (Otsu, 1979) was adopted, manually adjusting the threshold when necessary by using ImageJ (Schneider et al., 2012) software (e.g. Okumura et al., 2008; Caricchi et al., 2011; Zandomeneghi et al. 2010; Voltolini et al., 2011; Berg et al., 2016). A further step involved the extraction of a volume of interest (VOI) with dimensions suitable for the available computing resources but preserving sample representativeness in order to separate the connected pores and restore the pre-fragmentation conditions. The VOI has to be larger than the Representative Elementary Volume (REV; Bear, 1972), which corresponds to the smallest portion of the sample that statistically represents all features of the entire sample (e.g. Degruyter et al., 2010; Zandomeneghi et al. 2010; Berg et al., 2016; Kennedy et al., 2016). The determination of REV is estimated by an iterative process based on the calculation of porosity on increasing 3D image volumes until reaching a plateau value. Potential cutting effects from sample preparation and artifacts of the cone-beam reconstruction were avoided by selecting VOIs in the central parts of the imaged volumes.

Connected vesicles have been separated reconstructing the thin glass films lost during image acquisition and processing or partially retracted in a late-stage of coalescence (Shea et al., 2010a; Giachetti et al., 2011; Rust and Cashman, 2011; Hughes et al., 2017). Separations of connected vesicles were obtained by using the Separate Objects tool available in Avizo FEI software based on a combination of watershed, distance map and H-maxima. In order to quantitatively and graphically characterize pore interconnection we adopted Pore Network Statistics Extension in Avizo FEI software. The obtained Pore Network Model (PNM, Fig. 4d) is composed of branching or endpoints of the network called pores (or vesicles for volcanic rock) and lines connecting pores called throats. The results of the different analyzed components (vesicles and throats) and their distributions are reported in Table 1. Volume rendering was obtained using Dragonfly ORS software.

Moreover, permeability measurement were carried out by using Avizo FEI software (Petrophysics Extension), which contains the Absolute Permeability Experiment Simulation tool. Permeability has been calculated along the three orthogonal directions assuming a gas viscosity of 10^{-5} Pa s (Rust and Cashman, 2011; Okumura et al., 2012).

Small density contrast between microlites (clinopyroxene and feldspar) and matrix glass has prevented a 3D quantitative investigation of microlites, for which conventional 2D analytical methods have been adopted.

Microlite crystallinity and size distributions were obtained by 2D Back Scattered Electron images. For each sample, at least 4-5 BSE images (270 x 200 μm) were acquired by a Field Emission Scanning Electron Microscope (FE-SEM) JEOL JSM-6500F (Istituto Nazionale di Geofisica e Vulcanologia, Rome, Italy) and a Scanning Electron Microscope (SEM) Jeol JSM 5310 (DiSTAR, Università di Napoli Federico II) equipped with energy dispersive system and operating at 15kV. BSE images were processed and analyzed using ImageJ software. They were first reduced to binary images and then manipulated to reduce noise and separate individual microlites. Microlite size distributions were obtained by using CSD Corrections 1.5 program (Higgins, 2000, 2002, 2006; Higgins and Chandrasekharam, 2007) that includes corrections for both the intersection probability and the cut section effects.

Sample	modal density (g/cm^3)	modal porosity (%)	objective	voxel size (µm)	FieldOfView (mm^3)	vesicularity (%)	Vg/Vl	Y
G10	0.59	75	10x	2.01	5.28	73	3.22	0.999
G10	-	-	20x	1.07	0.83	81	5.37	0.999
G80	0.58	76	10x	2.01	5.37	74	3.23	0.999
G80	-	-	20x	1.07	0.83	87	8.99	0.999
G160	0.57	76	10x	2.00	5.28	75	3.46	0.999
G160	-	-	20x	1.07	0.83	81	5.27	0.999
N170	0.61	75	10x	1.41	1.83	69	2.46	0.999
N170	-	-	20x	1.09	0.89	74	3.16	0.999
N200	1.10	59	10x	1.87	4.26	55	0.73	0.992
N200	-	-	20x	1.09	0.89	59	1.54	0.996
S1	1.40	48	10x	2.02	5.36	53	1.18	0.996
S1	-	-	20x	0.94	0.56	58	1.46	0.990

Sample	objective	VOI (mm^3)	isolated/ connected	n bubbles total	VND (m^{-3}) meltcorr	Power-law exp	R^2	VND* (m^{-3}) meltcorr
G10	10x	2.77	0.05	23571	3.74×10^{13}	4.07	0.99	-
G10	20x	0.36	0.04	14308	2.62×10^{14}	-	-	3.63×10^{14}
G80	10x	3.14	0.02	24178	3.36×10^{13}	5.05	0.97	-
G80	20x	0.46	0.08	10047	2.27×10^{14}	-	-	3.5×10^{14}
G160	10x	3.09	0.02	27496	4.08×10^{13}	4.34	0.99	-
G160	20x	0.46	0.09	10436	1.47×10^{14}	-	-	3.21×10^{14}
N170	10x	1.07	0.03	20660	6.88×10^{13}	4.98	0.98	-
N170	20x	0.49	0.13	15322	1.34×10^{14}	-	-	3.11×10^{14}
N200	10x	2.49	0.22	61815	4.42×10^{13}	4.52	0.99	-
N200	20x	0.37	0.43	24342	1.70×10^{14}	-	-	1.07×10^{15}
S1	10x	3.14	0.28	31642	2.23×10^{13}	3.99	0.99	-
S1	20x	0.31	2.21	39246	3.16×10^{14}	-	-	2.88×10^{15}

Sample	objective	VOI (mm^3)	n throats	#th/#por (#th/#con)	TND (m^{-3}) meltcorr	Power-law exp	R^2	k (m^2)
G10	10X	4.74	135130	2.08 (3.43)	8.59×10^{13}	3.42	0.98	2.70×10^{-12}
G80	10X	5.37	228113	3.45 (4.67)	1.16×10^{14}	5.27	0.97	1.42×10^{-12}
G160	10X	5.28	211709	3.59 (4.22)	1.18×10^{14}	4.72	0.98	2.58×10^{-12}
N170	10X	1.83	151654	2.74 (5.17)	3.90×10^{14}	5.02	0.98	4.09×10^{-12}
N200	10X	4.26	276023	1.84 (4.55)	1.21×10^{14}	4.37	0.99	4.50×10^{-13}
S1	10X	5.36	101343	1.62 (3.04)	4.44×10^{14}	3.27	0.95	8.90×10^{-13}

Table 1. Textural parameters for Pomici di Base rocks.
Vesicles (VND) and Throats (TND) number density has been corrected for clast vesicularity and phenocrysts content. * Following Adams et al., 2006, VND values have been extended to 1 µm vesicle diameter size by extrapolating the exponential curve described by the small bubbles (Fig. 4).

2.4. Electron microprobe analyses (EMPA)

Analyses of major and volatile elements in groundmass glasses were performed with a JEOL-JXA-8200 electron microprobe (WD/ED combined micro analyzer) at the laboratories of the Istituto Nazionale di Geofisica e Vulcanologia (Rome). Element concentrations were measured with a 10 µm beam at 15 keV, a beam current of 10 nA and a counting time of 10 s. For each analysis a defocused beam was used to minimize losses of alkalis and volatiles, which were counted first to avoid diffusion effects. The following standards have been adopted for the various chemical elements: jadeite (Si and Na), corundum (Al), forsterite (Mg), andradite (Fe), rutile (Ti), orthoclase (K), barite (Ba), celestine (S), fluorite (F), apatite (P and Cl) and spessartine (Mn). Data reduction was carried out using ZAF4/FLS software by Link Analytical. The analytical uncertainty was about 1 wt.% for most elements. In a first attempt, the water content of all analyzed glass was estimated by using the ''volatile by difference'' method based on EMPA analyses (Devine et al., 1995; King et al., 2002). EMPA data are reported in Table 2.

Samples	***G10***	***G80***	***G160***	***N170***	***N200***	***S1***
number of analyzed points	8	8	9	8	10	6
SiO_2	61.68 (0.25)	61.59 (0.92)	60.01 (0.85)	60.25 (0.78)	57.24 (0.84)	55.44 (1.47)
TiO_2	0.32 (0.04)	0.29 (0.06)	0.35 (0.05)	0.39 (0.06)	0.53 (0.09)	0.71 (0.16)
Al_2O_3	17.66 (0.14)	17.41 (0.20)	17.60 (0.27)	17.72 (0.15)	18.28 (0.23)	17.34 (0.76)
FeO	2.56 (0.13)	2.59 (0.11)	3.23 (0.14)	3.21 (0.14)	4.71 (0.29)	7.00 (0.87)
MnO	0.17 (0.04)	0.15 (0.06)	0.15 (0.04)	0.12 (0.05)	0.15 (0.04)	0.16 (0.05)
MgO	0.24 (0.02)	0.25 (0.03)	0.46 (0.04)	0.47 (0.05)	0.96 (0.24)	1.34 (0.46)
CaO	2.49 (0.06)	2.67 (0.09)	3.27 (0.14)	3.21 (0.16)	4.77 (0.20)	4.85 (1.00)
Na_2O	4.36 (0.08)	3.83 (0.52)	3.89 (0.22)	4.00 (0.23)	3.32 (0.15)	3.31 (0.28)
K_2O	8.21 (0.20)	8.15 (0.18)	8.41 (0.37)	8.54 (0.23)	7.69 (0.15)	7.72 (0.41)
P_2O_5	0.07 (0.04)	0.06 (0.05)	0.12 (0.06)	0.09 (0.03)	0.31 (0.05)	0.62 (0.17)
Cl	0.71 (0.02)	0.68 (0.02)	0.55 (0.03)	0.57 (0.05)	0.54 (0.06)	0.64 (0.05)
F	0.24 (0.04)	0.21 (0.06)	0.20 (0.04)	0.18 (0.08)	0.19 (0.08)	0.22 (0.07)
SO_3	0.02 (0.01)	0.02 (0.02)	0.03 (0.01)	0.02 (0.01)	0.04 (0.02)	0.04 (0.02)
Total	98.72 (0.41)	97.88 (1.19)	98.27 (1.15)	98.75 (0.94)	98.73 (0.91)	99.38 (1.09)
H_2O by diff.	1.28 (0.41)	2.12 (1.19)	1.73 (1.15)	1.25 (0.94)	1.27 (0.91)	0.62 (1.09)
H_2O (TGA, wt.%)	1.26 ± 10	2.57 ± 17	1.86 ± 9	1.31 ± 6	1.33 ± 14	0.68 ± 9
CO_2 (CSA, ppm)	1054 ± 170	788 ± 95	356 ± 35	1143 ± 100	268 ± 58	317 ± 135

Table 2. EMPA analyses of selected Pomici di Base volcanic rocks.
Values in wt.%.

2.5. H_2O and CO_2 determination

Carefully selected natural pumice and scoria fragments were stored overnight in an H_2O_2 (20% in acqueous solution) bath to remove organic materials. Successively, the samples were left to dry in air for 24 h and lately stored overnight in a drying oven at 110 °C to release water possibly adsorbed on the glass surface.

After this treatment, the H_2O-CO_2 contents in the scorias and in the pumices were analysed with different methods at the Institute of Mineralogy at the University of Göttingen.

Water contents on bulk samples were measured by thermogravimetric analyses (TGA) using a SetaramTM TGA92. During a typical analyses, 10-20 mg of coarsely powdered material is loaded into a Pt crucible (4mm diameter, 10 mm height) and covered with a Pt lid. The sample is heated

from ambient temperature to 1200 °C with a ramp rate of 10 °C/min. After 30 min dwell time, the sample is cooled to room temperature again with a cooling rate of 30 °C/min. In the case of iron poor samples, the measurements are performed in air, while iron rich samples (FeO > 5 wt.%) are measured in helium to avoid the oxidation of Fe^{2+} to Fe^{3+} by reaction with the dissolved water. During the analyses, the weight loss of the material is constantly recorded. Once a day, a final heating and cooling cycle is performed after a simple run to account for buoyancy changes dependent on the temperature of the sample and therefore to correct the measured sample weight loss (Schmidt and Behrens, 2008).
For each sample, three to six thermogravimetric analyses were performed.
The determination of the CO_2 content on bulk samples was performed with an ElementarTM Inductar CS Cube Carbon-Sulfur Analyser (CSA). About 100-150 mg of coarsely crushed sample mixed with 0.5 g of Fe and 2 g of W chips are filled in a corundum crucible. After inductive firing, the mixture is burned in an oxygen stream releasing the CO_2 which is then measured with an IR cell. According to the manufacturer, a temperature of approx. 2000 °C is reached within 1 min.
Several steel samples with known carbon contents are used as standard calibration (Behrens et al., 2009).

$^{87}Sr/^{86}Sr$	**Glass**		**Minerals**			
samples		2sigma	***Sanidine***	2sigma	***Pyroxene***	2sigma
G10	0.707527	±6	0.707499	±6	0.707500	±6
G80	0.707530	±7	-		-	
G160	0.707539	±6	0.707550	±6	0.707477	±6
N170	0.707556	±8	0.707506	±6	0.707470	±6
N200	0.707602	±6	-		-	
S1	0.707605	±7	0.707534	±6	-	±6
$^{143}Nd/^{144}Nd$	**Glass**		**Minerals**			
samples		2sigma	***Sanidine***	2 sigma	***Pyroxene***	2sigma
G10	0.512439	±7	-		0.512437	±7
G80	0.512447	±7	-		-	
G160	0.512432	±6	0.512440	±6	0.512444	±6
N170	0.512435	±6	0.512429	±7	0.512452	±6
N200	0.512436	±6	-		-	
S1	0.512431	±6	-		0.512452	±7

Table 3. Isotopic ratios of separated glass and minerals of Pomici di Base rocks.

2.6. Radiogenic isotopes

Isotopic analyses for Sr and Nd via thermal ionization mass spectrometry (TIMS) were carried out at the Istituto Nazionale di Geofisica e Vulcanologia—Sezione di Napoli ‘‘Osservatorio Vesuviano’’ (INGV-OV, Naples), using a ThermoFinnigan Triton TI multi-collector mass spectrometer. Samples were processed through conventional HF–HNO_3–HCl dissolution before Sr and middle REE (MREE) were separated by standard cation exchange column chemistry, and Nd was further purified on an anion column. Sr and Nd were then loaded onto Ta and Re filaments, respectively. Sr and Nd blanks were negligible for the analyzed samples during the periods of measurements. Measured $^{87}Sr/^{86}Sr$ ratios were normalized for within-run isotopic fractionation to

$^{87}Sr/^{86}Sr$ = 0.1194, and $^{143}Nd/^{144}Nd$ ratios to $^{143}Nd/^{144}Nd$ = 0.7219. The mean measured value of $^{87}Sr/^{86}Sr$ for NIST–SRM 987 was 0.710215 ± 0.000008 (2 sigma, n = 36) and of $^{143}Nd/^{144}Nd$ for LaJolla was 0.511843 ± 0.000006 (2 sigma, n = 11). The quoted error is the standard deviation of the mean (2 sigma) for n = 180. Sr and Nd isotope ratios have been normalized to the recommended values of NIST SRM 987 ($^{87}Sr/^{86}Sr$ = 0.71025) and La Jolla ($^{143}Nd/^{144}Nd$ = 0.51185) standards, respectively. Results are reported in Table 3.

3. Results

3.1. Clast density, vesicularity and crystallinity

All samples show less than 5 wt.% content of phenocrysts that are present both as isolated crystals and in aggregate and are made up of sanidine > plagioclase > clinopyroxene > biotite in order of decreasing abundance, together with minor amount of amphibole, magnetite and garnet.

Clast densities as well as the degree of vesicularity and microlite crystallinity vary progressively upward in the stratigraphic sequence, Table 1, similarly to what previously observed by Bertagnini et al. (1998). In particular, the basal and intermediate (white to gray) trachytic pumices show low-density modal values (0.57-0.61 g/cm^3), high vesicularity (69-87%) and absence of microlites, while the upper (black) latitic-shoshonitic scoriae are characterized by higher density values (1.1-1.5 g/cm^3) and poorly vesiculated (45-59%) microlite-rich groundmass. Bulk-vesicularities calculated by pycnometry are generally consistent with those obtained by the 3D images at lower 10X magnification (see Table 1), while the values slightly increase in high-resolution three-dimensional images (however the dissimilarity is always less than 15% as also observed by Giacchetti et al. (2011) by using a similar procedure for Vulcanian pyroclasts erupted from Montserrat.

Two vesicle populations characterize highly-vesiculated trachytic pumices: small (diameter < 25 μm) spherical bubbles and irregular-shaped large bubbles (> 25 μm) showing many stages of coalescence (Fig. 3a-d and supplementary movie 1). Particularly, large bubbles have smooth pore apertures or interstitial filaments between coalesced cavities. In these cases melt films between bubbles can be very thin, reaching a 1 μm minimum thickness. This corresponds to the inferred critical thickness of liquid film rupture (Cashman and Mangan, 1994) that, in the case of equally-sized bubbles, is suggested to be caused by approximately equal pressure acting on the film from inside each bubble (Klug et al., 2002). Concurrently, small bubbles present wrinkled melt retraction films, possible in response to release of gas overpressure (Adam et al., 2006). Poorly-vesiculated latitic-shoshonitic scoriae have different textures that are predominantly characterized by small bubble population (< 40 μm) and subordinately by large polylobate, amoeboid bubbles separated by thick (> 10 μm) microlite-bearing glass (Fig. 3e-f, and supplementary movie 2).

Microlite types are small (<5-150 μm) blocky clinopyroxene in the lower part of scoriaceous level (15 vol.%, N200 sample) joined to elongated plagioclase in the upper scoria samples (30 vol.%, S1 sample).

3.2. Vesicle Number density and size distributions

Textures of pyroclasts, specifically the Vesicle Number Density (VND) and Size Distribution (VSD), can be quantified from image analyses (see Methods) and used to constrain processes and conditions of magma decompression during the course of the eruption (e.g. Cashman and Mangan, 1994; Mangan and Cashman, 1996; Hammer, et al., 1999). Particularly, VND (number of vesicles per volume unit) is potentially a powerful tool to explore rates of magma ascent because of the relationship between number density and decompression rate observed in laboratory experiments as well as numerical models, while VSDs are largely used to constrain the processes of bubbles nucleation, growth and coalescence and then to investigate the relationships between magma

degassing and eruptive behavior (e.g. Gaonac'h et al., 1996; Blower et al., 2002; Toramaru, 2006; Proussevitch et al., 2007a; 2007b).
Table 1 includes VND values calculated by using all the micro-CT images acquired at different resolutions; however, as suggested by other authors (Shea et al., 2010a and b; Rotella et al., 2014), we consider the VND data measured from the higher resolution micro-CT images more representative as small bubbles dominate the bubble density in silicic pyroclasts. Moreover, following the method proposed by Adams et al. (2006) for the 1912 eruption of Novarupta, VND values have been extended to 1 μm vesicle diameter size by extrapolating the exponential curve described by the small bubbles. Particularly, following the last authors we fitted the trend of smaller bubbles with an exponential curve and extended it to 1 μm vesicle diameter size. As in the case of 1912 eruption of Novarupta, for our trachytic pumice samples the exponential size distribution corresponds with vesicles ≤ 30-25 μm, while for our scoria samples the exponential trend fits vesicles smaller than 10-15 μm.
VNDs are quite similar for all trachytic pumice clasts collected at different stratigraphic levels ranging from 3.1 to 3.6 x 10^{14} m^{-3}, while increase in latitic-shoshonitic scoria samples at the top of the deposit that show VND values up to 2.8 x 10^{15} m^{-3}, Table 1. The obtained VND values are consistent with those produced by heterogeneous nucleation during decompression experiments on Neapolitan trachytes (4.8 x 10^{13} - 2.9 x 10^{14} m^{-3}; Mastrolorenzo and Pappalardo, 2006) and phonolites (4.3 x 10^{13} - 3.8 x 10^{14} m^{-3}; Larsen, 2008; 8 x 10^{13} - 9 x 10^{15} m^{-3}; Shea et al., 2010b), as well as those produced by homogeneous nucleation on phonolites (5.7 x 10^{14} - 7.7 x 10^{14} m^{-3}; Iacono-Marziano et al., 2007).
Cumulative Vesicle Size Distributions (CVSDs) of trachytic pumices show a continuous trend characterized by an exponential distribution for small bubbles (less than 25 μm) and a power law distribution for large bubbles (Fig. 4a). Similar trends have been observed in other Plinian events and widely interpreted as due to expansion and coalescence of earlier formed vesicles (large bubbles pattern) during a continuous nucleation process (Gaonac'h et al., 1996; Blower et al., 2002), while the small bubbles reflect the last nucleation event in the shallow conduit (e.g. Baker et al., 2012; Gonnermann and Houghton, 2012; Rotella et al., 2014).
On the contrary CVSDs of scoria samples show irregular trends formed by multiple curved segments suggesting discrete vesiculation events (Fig. 4b). These sort of distributions are generally not typical of Plinian clasts, however they have been previously recognized in experimental samples that suffered carbonate interaction and explained as due to vesiculation pulses triggered by fast release of CO_2-rich fluids (Blythe et al., 2015). Interestingly it is the first time that these trends have been observed in natural Somma-Vesuvius rocks, possibly thanks to the high-resolution of the applied 3D microtomographic technique (examples of 3D micro-CT data for trachytic and latitic-shoshonitic rocks are in supplementary movie 1 and 2, respectively).

3.3. Number density and size distribution of throats, connectivity and permeability

Total Throats Number Densities (TNDs) range from 8.6 x 10^{13} to 4.4 x 10^{14} m^{-3}, not showing substantial differences between latitic-shoshonitic scoriae and trachytic pumices, Table 1. The ratio between numbers of throats/total pores (#th/#por in Table 1) and throats/connected pores (#th/#con) ranges respectively from 2.1-3.6 and 3.4-5.2 in trachyte and 1.6-1.8 and 3-4.5 in latite-shoshonite. Their cumulative distributions (CTSDs, Cumulative Throats Size Distributions) follow broadly power-law trends for large sizes, while seem to follow exponential trends for the small sizes, similar to those observed in the vesicle size distributions of trachytic pumice, Fig. 4c. These observations are consistent with the fact that bubble growth in pumices is better developed than in scoriae, resulting in thinner melt films, which facilitate the occurrence of coalescence between neighboring vesicles (e.g. higher #th/#por in trachyte respect to latite). Moreover they reflect the high number of small isolated vesicles contained in scoriae, characterized by different CVSDs trends. The degree of bubble interconnection has been evaluated based on bubble connectivity by the procedures described in Okumura et al. (2012). Connectivity is defined as Ψ = Nmax/Ntotal (where Nmax and

Ntotal represent the voxel numbers belonging to the largest bubble and to all of the bubbles, respectively) and reaches the very high value of about 0.99 in all samples. Permeability values (see Methods) range from 1.42 to 4.09 x 10^{-12} m^2 for trachytic pumices and from 0.45 to 0.89 x 10^{-12} m^2 for latitic-shoshonitic scoriae, without showing significant variations among the three orthogonal directions (Table 1).

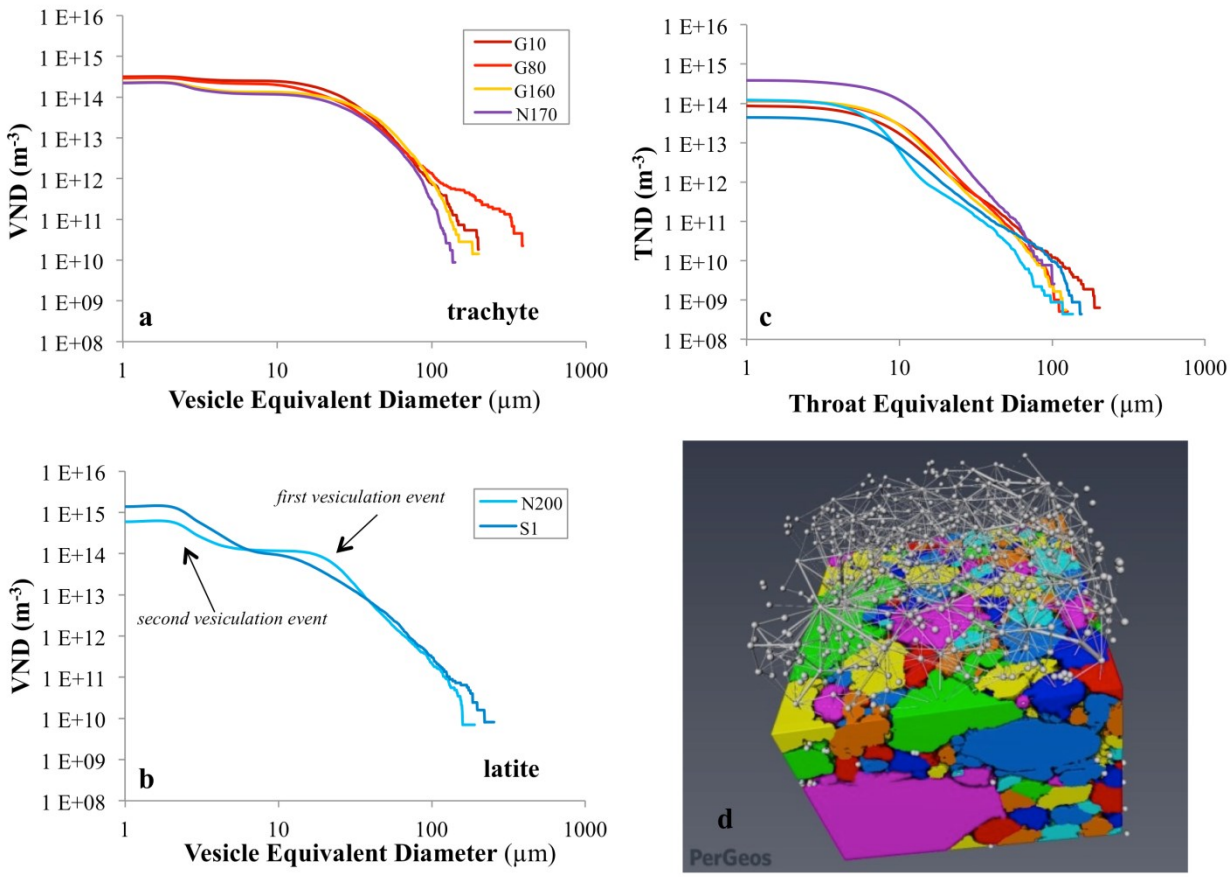

Fig. 4. Cumulative Vesicles size distributions (CVSDs) for trachytic (a) and latitic-shoshonitic (b) Pomici di Base rocks and Cumulative Throats size distributions (c). CVSDs of trachytic pumices show a curved continuous trend characterized by exponential distribution for the small bubbles and power law distribution for the large bubbles, indicating a continuous nucleation process (see text). The presence of pre-existing bubbles in the upper gas-rich level of the chamber could justify the large bubble population observed in G80 sample. On the contrary CVSDs of scoria latitic-shoshonitic samples show irregular trends formed by multiple curved segments suggesting discrete vesiculation events, attributed to nucleation pulses driven by fast CO_2 release during the ongoing decarbonation process (see text for further explanation). Example of Image of Pore Network Model (sample G10) obtained by Avizo FEI software (d). A PNM is composed of labeled branching or endpoints of the network called pores (or vesicles for volcanic rocks) and lines connecting pores called throats. Pores are displayed using spheres, and throats are displayed using cylinders. Cube side: 300 µm (pixel size = 1 µm).

3.4. Microlite Size Distributions

Following the pioneering work of Marsh (1988) and Cashman and Marsh (1988) the size of microlites and their abundance can be represented as Crystal Size Distributions (CSDs), generally shown as a semi-logarithmic plot of population density (number of crystals per unit volume) versus

crystal size (maximum length) with the slope equal to 1/(growth rate x residence time). Thus, if the growth rate is known, the crystallization time can be computed.
CSDs for clinopyroxene present in the glassy groundmass of our latitic-shoshonitic samples were obtained by textural analyses of 2D backscattered electron images, however it was not possible to analyze plagioclase crystals as their average atomic mass is close to that of the surrounding matrix-glass thus they cannot be quantitatively resolved in the BSE images.
These distributions show intercept and slope values of 17.69 and 19.31 mm^{-4} and -63 and -93.2 mm^{-1} (for N200 and S1 samples respectively, Fig. 5a). Because decompression experiments indicate that the growth rate of microlites can be highly dependent on the decompression rate, in our timescale calculations we used the entire range of growth rates (from 1 x 10^{-6} to 1 x 10^{-8} mm/s, Brugger and Hammer, 2010) available for microlites. By applying this range of growth rates, we calculated a crystallization time ranging from hours to days, in agreement with clinopyroxene texture displaying elongate, tabular and swallowtail morphologies that indicate rapid crystallization close to the surface (Fig. 5).

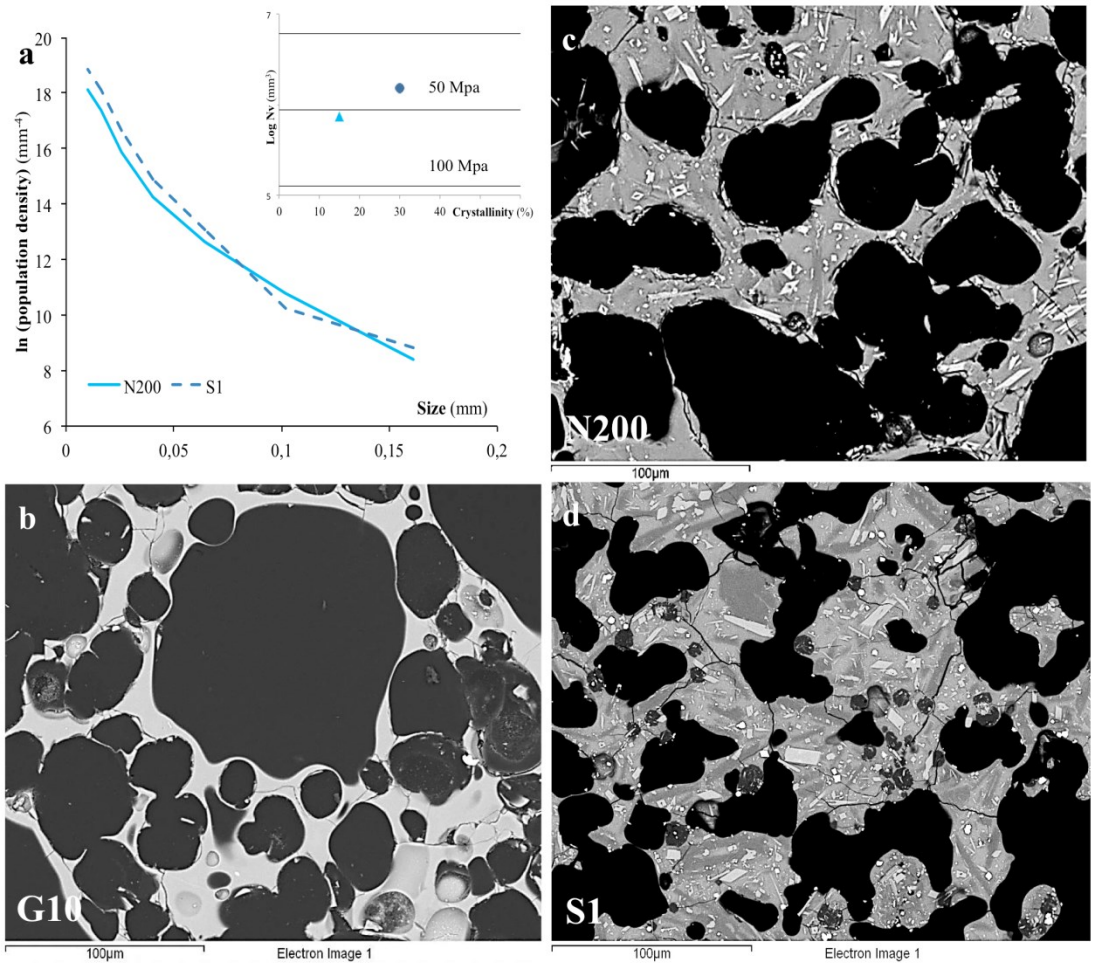

Fig. 5. a) Crystal size distributions for clinopyroxene microlites (white microcrystals in BSE images). Insert: Microlite number volume (Nv) against crystallinity showing microlite formation depths. These must be considered gross estimates as the equilibrium lines are calibrated on the basis of experimental rhyolitic samples (Blundy and Cashman, 2008).
Back-scattered electron (BSE) images of groundmass textural features in Pomici di Base trachytic (b) latitic-shoshonitic (c and d) samples.

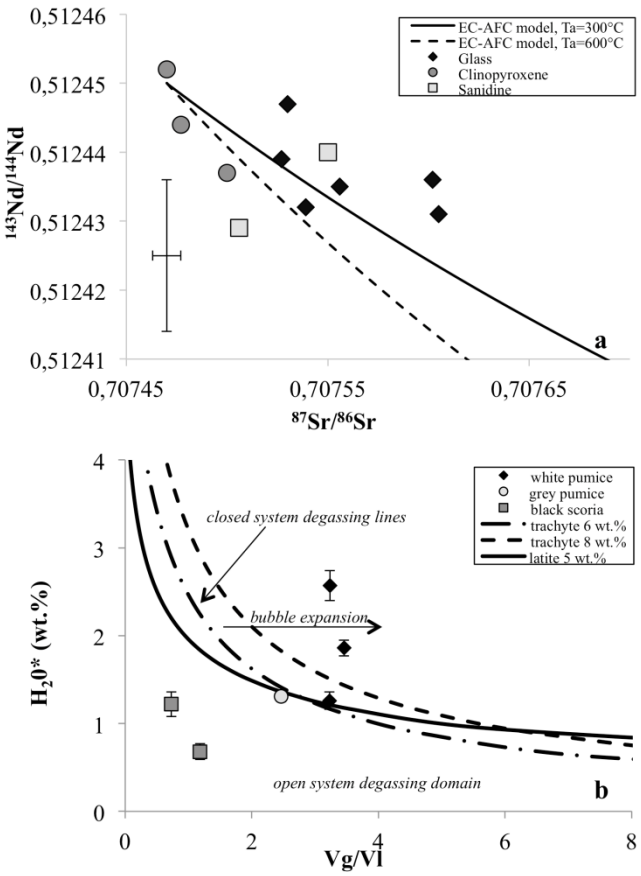

Fig. 6. a) $^{87}Sr/^{86}Sr$ versus $^{143}Nd/^{144}Nd$ compositions for separated matrices and minerals. Lines represent the results of Energy-Constrained Assimilation and Fractional Crystallization (EC–AFC; Spera and Bohrson, 2001) simulations (see text for further explanations). Ta = initial T assimilant.
b) H_2O^* (water in residual melts) vs Vg/Vl (ratio of the volume of gas (Vg) to the volume of melts (Vl), after Balcone-Boissard et al., 2008). Lines correspond to theoretical closed-system degassing evolution for initial water content of 5 wt.% (latite-shoshonite), 6 and 8 wt.% (trachyte), representative of saturation conditions (Di Matteo et al., 2004; 2006).

3.5. Radiogenic isotope

To explore the potential influence of limestone assimilation in the evolution of the Pomici di Base magmas we performed Sr-Nd isotopic analyses on separated phenocrysts (feldspar and clinopyroxene) and groundmass in all studied samples. Radiogenic systems are in fact a powerful tool to spot magma contamination, due to the different Sr and Nd isotopic signature of primary magmas with respect crustal rocks.

The obtained results show a marked increment in $^{87}Sr/^{86}Sr$ ratios from trachytic (0.70753-56) to latitic-shoshonitic melts (0.70760) (Fig. 6a, Table 3), thus suggesting a prominent involvement of crustal contamination in the petrogenesis of the hotter mafic melts (Tliquidus = 1200 °C, calculated by using MELTS program; Ghiorso and Sack, 1995; Asimov and Ghiorso, 1998), as also supported by the abundance of carbonate-metamorphic clasts present as lithic fraction in the Pomici di Base fallout deposits and included as fragments inside juvenile products (Bertagnini et al, 1998; Landi et al., 1999). Particularly the highest $^{87}Sr/^{86}Sr$ ratios have been measured in separated latitic-shoshonitic glassy groundmass (0.70760) with respect to sanidine (0.70750-55) and clinopyroxene (0.70747-50) phenocrysts implying that contamination was a later process occurred possibly at shallow level after precipitation of phenocrysts, Fig. 6a.

In other volcanic contexts partial/selective assimilation has been advocated to explain isotopic disequilibrium between groundmass and feldspars (e.g. Duffield and Ruiz, 1998); however in the

case of Pomici di Base rocks this feature is restricted to mafic melts while it is not significant in evolved trachyte, thus excluding that fractionation was coupled to a continuous selective assimilation process.
Nd isotopic compositions are much less variable and cluster around 0.51243-45 both in matrix glasses and phenocrysts (Fig. 6a), this in agreement with the low Nd content of sedimentary carbonates that leave a very slight fingerprint in the contaminated magmas.
The effects of assimilation on isotope variations have been modeled by using the Energy-Constrained Assimilation and Fractional Crystallization (EC-AFC) model of Spera and Bohrson (2001), Table 4. We consider an early intrusion of a primitive shoshonitc magma at a liquidus temperature of 1200 °C into the upper crust at 350-600 °C ambient temperature (De Lorenzo et al., 2006) and 6-8 km depth supposed to be the top of the magma reservoir (Scaillet et al., 2008; Pappalardo and Mastrolorenzo, 2010, 2012; Balcone-Boissard et al., 2016), possibly developed inside carbonatic sequences as suggested by borehole (Brocchini et al., 2001) and geophysical investigations (e.g. Berrino et al., 1998; Improta and Corciulo, 2006). The model shows that the observed Sr and Nd isotopic variation is justified by 2-4% of carbonate rocks contaminating a magma already crystallized for about 55% of its initial mass, Fig. 6a.

Thermal parameters		***Compositional parameters***		
Liquidus T magma	1200 °C	*Elements*	Sr	Nd
Initial T magma	1200 °C	*Magma (ppm)*	1039	45.5
Liquidus T assimilant	1000 °C	*bulk D_m*	1.6	0.1
Initial T assimilant	300 - 600 °C	*Assimilant (ppm)*	500	10
Solidus	780 °C	*bulk D_a*	0.7	0.15
Equilibrium temperature	900 °C			
Specific heat of magma	1484 J/kg per K			
Specific heat of assimilant	1370 J/kg per K	*Isotopic ratios*	$^{87}Sr/^{86}Sr$	$^{143}Nd/^{144}Nd$
Crystallization enthalpy	396000 J/kg	*Magma*	0.70747	0.51245
Fusion enthalpy	270000 J/kg	*Assimilant*	0.709	0.512

Table 4. EC-AFC parameters used for modeling isotopic trend.
In the model melts temperature was calculated using Melts program. An ambient temperature of 350 and 600 °C was assigned to crustal rocks consistent with mid-crustal magma storage. The liquidus (Tla = 1000 °C) and solidus (Tsa = 780 °C) temperature for limestone are from Mollo et al., 2010. Bulk distributions coefficient for Sr and Nd are from Villemant et al., 1988; Pappalardo et al., 2008, Gebauer et al., 2014.

4. Discussion

4.1. Dynamics of magma ascent in the volcanic conduit

The Plinian fallout phase of the Pomici di Base eruption was fed in its early beginning by sialic (0.34 km^3 DRE trachytic) melts followed by a larger volume of mafic (0.96 km^3 DRE latitic-shoshonitic) magmas for the entire course of the sustained-column phase. This chemical variation towards mafic composition was not associated to any changes in eruption style, as flow rate as well as column height remained firmly high (Bertagnini et al., 1998) for tens of hours during the whole Plinian phase.
However our 2D and 3D quantitative textural data and isotopic ratios show a significant difference between sialic and mafic rocks suggesting contrasting degassing as well as crystallization regime during magma ascent and fragmentation in the volcanic conduit.

Bubble nucleation and growth recorded in microlite-free trachytic pumice

Trachytic pumices have high degree of vesiculation (69-87%) and are characterized by large coalescent bubbles separated by thin glass walls whose thickness approaches the critical rupture threshold. These features, commonly observed in pumice samples of Plinian eruptions from worldwide volcanoes (e.g. Rotella et al., 2014 and references therein), allow us to hypothesize that during decompression, bubble growth occurred for exsolution up to the achievement of a vesicularity threshold that for silicic melts generally ranges from 70 to 80% in function of magma characteristics (expansion rate, melt viscosity, shear stresses, presence of different phases). Above this value experimental data (Namiki and Manga, 2008; Takeuchi et al., 2009; Rust and Cashman, 2011) indicate the existence of an abrupt increase in permeability due to bubbles coalescence. High throat number densities, power law exponents > 3 in CVSDs as well as high bubble connectivity and permeability values of trachytic pumice also support extended bubble coalescence during magma ascent.

On the basis of the numerical model developed by Toramaru (2006), we estimated the decompression rate during this eruptive stage by using the VND values calculated for pumice samples, surface tension of 0.1 N/m (Iacono Marziano et al., 2007; Mangan e Sisson, 2000; Moutada Bonnefoi and Laporte, 2004), 6 wt.% pre-eruptive H_2O content at saturation pressure of 150-200 MPa (Di Matteo et al., 2004) and water diffusivity of 2.41 x 10^{-12} m^2/s. This last value has been calculated using the empirical equation proposed by Fanara et al. (2013) at 1100 °C (minimum experimental temperature adopted by the authors) and a correction factor of 100 to take into account the influence of the temperature (scaling from 1100 to 900 °C; following Watson, 1994; Larsen, 2008; Shea et al., 2010b). The resulting decompression rate is in the order of 5.5-6.1 MPa/s, however these values must be considered maximum values as the used formulation does not take into account the role of pre-eruptive magmatic CO_2 in the melt that may influence water solubility at saturation.

The obtained high decompression rate implies that during the climax of this early phase of the eruption, magma degassing occurred rapidly under closed-system regime (see also Fig. 6b) from a storage depth of 150-200 MPa (Pappalardo et al., 2004; Scaillet et al., 2008; Pappalardo and Mastrolorenzo, 2010, 2012; Balcone-Boissard et al., 2016) up to the fragmentation surface localized at ≤ 40 MPa, as inferred on the basis of residual water content of glass (Fig. 6b). At this point the viscosity of trachytic magmas shifted from $10^{2.9}$ to $10^{4.91}$ Pa s (average values assuming saturation conditions for pre-eruptive stage and T = 900 °C, calculated by using the model of Giordano et al., 2010).

Moreover some pumice clasts show evidence of expansion without further water exsolution (Fig. 6b), a degassing regime that may correspond to the expansion of preexisting bubbles in the chamber, despite we cannot completely exclude post fragmentation vesiculation. We consider however the first hypothesis more plausible because this feature is limited to the very first erupted trachytic products that represent the upper gas–rich level in the chamber possibly at critical conditions of volatile oversaturation; the occurrence of hydrous minerals (such as biotite) in the phenocryst assemblage supports crystallization under hydrous melt conditions; in fact crystallization experiments on alkaline trachytic melts (e.g. Fabbrizio and Carroll, 2008) indicate that biotite instead of amphibole is stable as hydrous phase in alkaline trachytic compositions due to the high K_2O/Na_2O ratios of these melts. We speculate that the presence of melts in near-saturation conditions at the top of the chamber could act as an eruption trigger generating an excess pressure (5–25 MPa, following Blake, 1984) sufficient to cause the wall-rock rupture.

Bubble and microlite nucleation and growth recorded in microlite-rich latitic- shoshonitic scoriae

Latitic-shoshonitic scoriae erupted in the late Plinian fallout stage, on the counterpart, are characterized by poorly-vesicular texture (45-59%) as well as thick microlite-rich (crystallinity between 15-30 vol.%) interstitial-glass.

These features imply low magma ascent rate favoring open-system degassing regime (outgassing) and in turn bubble collapse as well as degassing-induced microlite crystallization (see also Fig. 5 and 6b). On the other hand a peculiar aspect of these rocks is their high vesicle number density and multiple CVSDs patterns, in contrast with their low-porosity and high-crystallinity nature. Similar behavior (high VND values and CVSDs distributions) has been previously observed in experimental mafic samples from Somma-Vesuvius and Merapi volcanoes exposed to limestone contamination (Blythe et al., 2015) and presumed due to fast (hours to days, Sottili et al., 2009; 2010; Deegan et al. 2010, 2011; Freda et al., 2011; Troll et al., 2012; Jolis et al., 2013) CO_2 nucleation pulses. This last process can be possibly driven by magma digestion of skarn blocks detached by contact aureole formed during an early magma-limestone metamorphic stage (skarn recycling, Jolis et al., 2015). Although, we did not observe clear evidence of metasomatic nodules in our juvenile fragments, possibly due to their rare occurrence, Landi et al. (1999) reported the presence, within juvenile clasts, of metasomatic carbonates/skarn nodules (< 0.2 wt.% of the total rock) commonly associated with interstitial trachytic glass interpreted as portions of the metasomatized carbonate walls of the upper part of the Pomici di Base magma chamber. In any case we cannot exclude that magma/wall-rock interaction would involve also CO_2-rich pristine limestone Hence, we suggest that a mechanism of carbonate/skarn dissolution can reconcile all the 2D and 3D textural as well as isotopic parameters documented in Pomici di Base mafic rocks. We propose that the evacuation of the more evolved trachytic liquids from the cap of the reservoir has caused the inception of caldera collapse with the consequent digestion/assimilation of carbonate/skarn blocks into the remnant latitic-shoshonitic liquids, Fig. 7.

Specifically, we suggest that the widening of the lower part of the plumbing system causes a reduced magma ascent rate giving more time both to gas to escape (outgassing) and to microlite to grow, with a consequent increment of melt viscosity ($10^{4.43-7.48}$ Pa s, average values calculated on the basis of the model proposed by Vona et al. (2011), assuming an equilibrium temperature of 1000 °C). In fact decompression experiments (e.g. Rutherford and Gardner, 2000; Hammer and Rutherford, 2002; Couch et al., 2003; Martel and Schmidt, 2003) demonstrated that number density and modal content of microlites change accordingly to decompression rate and that microlite crystallization requires timescales of days to weeks, while it can be absent in the case of fast magma ascent.

This stage of conduit collapse as well as the associated phase of slow magma ascent through the conduit, possibly lasted from hours to days as indicated by our CSDs data on clinopyroxene microlite. During this time the consequent digestion/assimilation of carbonate/skarn blocks triggered CO_2 bubble formation and growth, forcing rising and fragmentation of the more viscous magma. Dallai et al. (2001) reported that the occurrence of CO_2 degassing due to the interaction of hot magma with carbonate has the potential to change the overall volatile solubility of magmas, thus justifying their ability to rapidly rise and explosively erupt to the surface. Recently Carr et al. (2018) by applying a numerical model of magma ascent to 2006 Merapi eruption, found that the addition of 1000 ppm of CO_2 can reduce water solubility in the melt, forcing vesiculation and generating overpressure at the top of the storage region in a short time (1-2 days).

Our EC-AFC simulations indicate the ingestion of 2-4 wt.% of limestone by 0.96 km^3 (Landi et al., 1999) of latitic-shoshonitic melts that corresponds to the release of a maximum of 0.04 Gt of CO_2 during the eruption (considering that for 1 kg of limestone, 439 g of CO_2 are liberated for complete decarbonation, Deer et al., 1992). Similar values of CO_2 liberation are reported during the AD 79 Pompeii (0.31 - 0.56 Gt) and the AD 472 Pollena (0.04 - 0.07 Gt) eruptions at Somma-Vesuvius (Jolis et al., 2015).

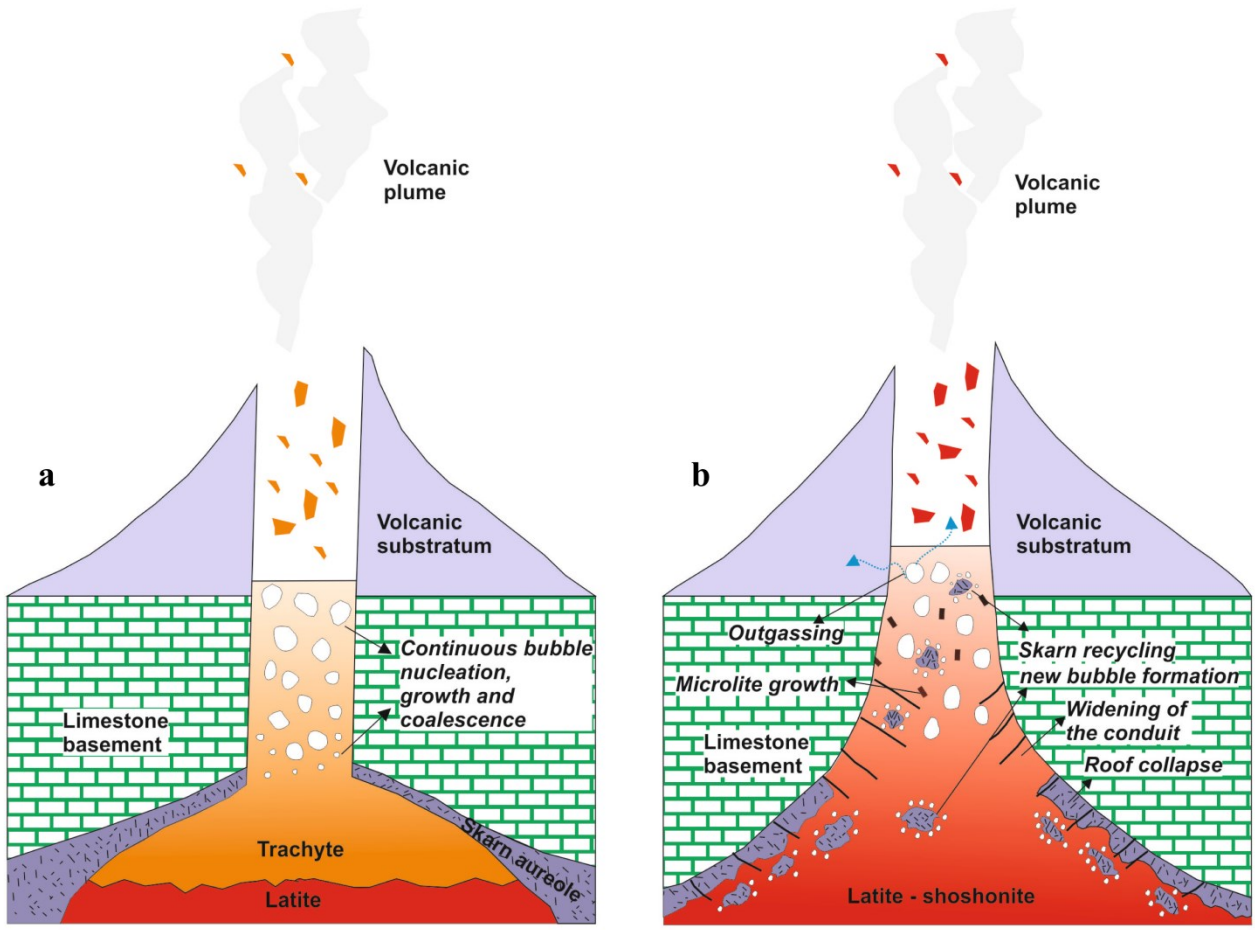

Fig. 7. Schematic model for conduit processes during the Plinian phase of Pomici di Base eruption. The fast evacuation of the more evolved trachytic liquids from the cap of the reservoir, caused the inception of the collapse of the deeper part of the plumbing system and the digestion/assimilation of skarn blocks into the remnant hotter latitic-shoshonitic liquids.

4.2. The fragmentation mechanisms

Trachytic magma

In high-viscous magma, fragmentation occurs when 1) a critical viscosity-dependent strain rate is exceeded (strain-rate criterion; Papale, 1999), 2) gas overpressure overcomes the tensile strength of the melt (stress-criterion; Alidibirov, 1994; Zhang, 1999), or 3) expanding magma exceeds a critical vesicularity (critical volume fraction criterion; Sparks, 1978).

The *strain-rate criterion* is based on the view that rapid acceleration may cause the melt to cross the glass transition and therefore fail brittlely. Papale (1999) indicates that magmas fragment in a brittle fashion when a critical, viscosity-dependent strain-rate is exceeded. The minimum bulk viscosity (μ) required for strain-induced fragmentation is defined as $\mu \geq (CG_{\infty}\pi r^3 / Q)^{(1/0.9)}$, where r is the conduit radius (m), Q is the volume flux (m^3/s), G_{∞} is the elastic modulus at infinite frequency (10 GPa) and C is a fitting parameter ($0.01\ (Pa\ s)^{-0.1}$) (Gonnermann and Manga, 2003). Thus to verify this criterion for the studied trachyte, we used in the above formulation the known mass flux for Pomici di Base eruption of $Q = 2.5 \times 10^7$ kg/s (Bertagnini et al., 1998) (equivalent to a volume flux of $Q = 10^4\ m^3/s$) and the calculated average viscosity for trachytic melt ($10^{4.91}$ Pa s); however the obtained conduit radius results around 1 m and thus geologically unrealistic.

The *stress criterion* establishes that fragmentation takes place when volatile overpressure, ΔP_{fr}, exceeds the tensile strength of the melt and ruptures bubble walls (Alidibirov, 1994; Zhang, 1999).

Spieler et al. (2004) provide a formulation with good fit to a broad range of experimental data: $\Delta P_{fr} = \sigma_m/\varphi$, where σ_m is the effective tensile strength of the melt (0.995 MPa) and φ is the porosity. This formulation has been modified by Mueller et al. (2008) to account for permeability (k) as follows: $\Delta P_{fr} = (a\ k^{1/2} + \sigma_m)/\varphi$, with a = 8.21 x 10^5 MPa/m and σ_m = 1.54 MPa, respectively. Thus applying in the above formulations the measured porosity and permeability for trachyte melt (0.75 and 2.7 x 10^{-12} m^2), a bubble overpressure ranging from 1.33 to 3.85 MPa is required to cause fragmentation. As the calculated melt viscosity gives relaxation times (τ_s) of 8.13 x 10^{-6} s using the expression $\tau_s = \mu_s/G_\infty$ (Dingwell and Webb, 1989), then the onset of non-Newtonian, un-relaxed, viscoelastic behavior can be fixed at 8.13 x 10^{-4} s (2 orders of magnitude below, Webb, 1997). The above calculated ΔP_{fr} (1.33-3.85 MPa) and timescale (8.13 x 10^{-4} s) implies unrealistic huge decompression rates (comprised between 1.63 and 4.74 x 10^3 MPa/s) needed to initiate fragmentation.

The *critical volume fraction criterion* is thought to arise from some form of instability within the thin bubble walls, once porosity ≈ 75% is reached (Verhoogen, 1951; Sparks, 1978). At high bubble-interconnectivity condition, the fragmentation efficiency strongly depends on the balance between rate of magma decompression and rate at which gases escape from the rising magma (outgassing). Okumura et al. (2012) have estimated the rate of outgassing from magmas ascending in volcanic conduits on the basis of Darcy's law and by using the calculated gas permeability for silicic melts. This author reports that when the pressure gradient driving the permeable gas flow is assumed to be lithostatic (0.03 MPa/m), as can be postulated on the basis of the results of numerical models for silicic magma ascent during plinian eruptions (Papale and Dobran, 1993), the gas velocity is estimated to be less than 10 x 10^{-5} m/s at vesicularities up to 70 vol%. As this velocity is much smaller than the decompression rate (5.5-6.1 MPa/s) calculated by VND values in the previous section 4.1, the degree of outgassing can be considered inefficient on the timescale of the eruption, thus allowing the reaching of the 75% porosity threshold necessary for fragmentation also in presence of high bubbles connectivity.

We can hence suppose that fragmentation of trachytic magma can occur after bubble expansion when a fixed gas volume threshold is reached (bubble packing state) as also suggested by Mastrolorenzo and Pappalardo (2006) on the basis of a compositional and textural study on both experimental and natural trachytes from Campania volcanoes.

Latitic-shoshonitic magma

In low-viscous liquids fragmentation can be controlled by inertia due to inertial stretching and hydrodynamic breakup during rapid bubble growth.

Actually the examined scoria clasts lack the textural features typical of low-viscous inertia-driven fragmentation products (fluidal shapes, very low VND values etc), possibly due to the large increment in melt viscosity caused by outgassing and microlite precipitation processes that affected mafic melts during magma rise in the conduit. On the other hand, the calculated high viscosity values suggest that brittle fragmentation can be a possible mechanism for latitic-shoshonitic melts.

To verify this hypothesis we applied the mass flux measured for Pomici di Base eruption and the calculated viscosity values for latitic-shoshonitic compositions ($10^{4.43-7.48}$ Pa s) in the expression of Gonnerman and Manga (2003) for strain-induced brittle fragmentation (strain-rate criterion); a wide range of conduit radius values from 0.31 to 171.73 m results from calculation in function of viscosity variation depending on microlite content (ranging from 15 to 30 vol.%). Indeed our 3D data show only localized bubble deformation in mafic scoriae, implying that strain localization (Wrigth and Weinberg, 2009) can occur during magma rising in the conduit, and force melts to cross the glass transition and achieve the fragmentation.

Moreover, calculations taking into account other fragmentation mechanisms (stress-criterion and critical volume fraction criterion) give a wide range of decompression rates that can reach also extreme values (from 6.68-15.95 to 0.63-1.32 x 10^4 MPa/s) and vesicularity values significantly larger compared with those measured in the studied natural samples. It is noteworthy that in these

calculations we have neglected the contribution of CO_2-oversaturation condition possibly derived by the postulated limestone assimilation.
Finally we speculate that latitic-shoshonitic magmas cannot reach classically defined fragmentation conditions and complex mechanisms such as bubble overpressure driven by CO_2-oversaturation (see also Pichavant et al., 2013) and strain localization can concur.

5. Conclusions

In this paper we show that a combination of textural and petro-chemical quantification of the eruptive products can be a powerful tool for reconstructing volcanic conduit dynamics during volcanic eruptions. Our 2D and 3D quantitative textural data combined with Sr and Nd isotopic investigations, demonstrated that explosive behavior during the Pomici di Base Plinian eruption was firstly controlled by rapid decompression under closed-system degassing regime of the uppermost trachytic liquids; subsequently, the inception of the caldera collapse triggered the digestion of detached skarn blocks into the remnant latitic-shoshonitic liquids and in turn the occurrence of rapid vesiculation pulses, that contributed to magnify the intensity of the eruption during the evacuation of the mafic liquids.
To conclude, these results highlight the importance of magma/limestone interaction as a syn-eruptive process able to produce vigorous gas liberation, thus accelerating magma ascent and amplifying eruption intensity. This mechanism of CO_2 fast liberation warrants more detailed consideration as a mechanism driving explosive basaltic volcanism.

Acknowledgements

The authors wish to thank I. Arienzo (INGV-OV), R. de Gennaro (DiSTAR, Università di Napoli) and M. Nazzarini (INGV-Rome) for essential helps during isotopic, SEM and EMPA analyses, respectively. We are thankful to Ciro Sepe (DiSTAR, Università di Napoli) for his fundamental support during fieldwork. Finally, the authors gratefully acknowledge two anonymous reviewers, whose valuable suggestions greatly contributed to improve the manuscript.

Supplementary material

The online version of this article (https://doi.org/10.1007/s00410-018-1486-x) contains supplementary material, which is available to authorized users.

References

Adams NK, Houghton BF, Hildreth W (2006) Abrupt transitions during sustained explosive eruptions: examples from the 1912 eruption of Novarupta, Alaska. Bull Volcanol 69:189–206

Alidibirov M (1994) A model for viscous magma fragmentation during volcanic blasts: Bull of Volcanol 56:459–465. doi:10.1007/s004450050055

Andronico D, Calderoni G, Cioni R, Sbrana A, Sulpizio R, Santacroce R (1995) Geological map of Somma-Vesuvius volcano. Per Min 64 (1–2):77–78

Asimov PD, Ghiorso MS (1998) Algorithmic modifications extending MELTS to calculate subsolidus phase relations. Am Miner 83:1127–1132

ASTM Designation D854-06 (2007) Standard test method for specific gravity of soil solids by water pycnometer: annual book of ASTM standards, Vol. 04.02, ASTM, West Conshohocken, PA

Baker DR, Brun F, O'Shaughnessy C, Mancini L, Fife JL, Rivers M (2012) A four-dimensional X-ray tomographic microscopy study of bubble growth in basaltic foam. Nat Commun 3:1135
Balcone-Boissard H, Villemant B, Boudon G, Michel A (2008) Non-volatile vs volatile behaviours of halogens during the AD 79 Plinian eruption of Mt. Vesuvius, Italy. Earth Planet Sci Lett 269:66–79
Balcone-Boissard H, Villemant B, Boudon G (2010) Behavior of halogens during the degassing of felsic magma. Geochem Geophys Geosyst 11:477–485
Balcone-Boissard H, Boudon G, Ucciani G, Villemant B, Cioni R, Civetta L, Orsi G (2012) Magma degassing and eruption dynamics of the Avellino pumice Plinian eruption of Somma-Vesuvius (Italy). Comparison with the Pompeii eruption. Earth Planet Sci Lett 331–332: 257–268
Balcone-Boissard H, Boudon G, Cioni R, Webster JD, Zdanowicz G, Orsi G, Civetta L (2016) Chlorine as a geobarometer for alkaline magmas: Evidence from a systematic study of the eruptions of Mount Somma - Vesuvius. Sci Rep 6:21726
Bear J (1972) Dynamics of Fluid in Porous Media. Elsevier, New York, NY
Behrens H, Misiti V, Freda C, Vetere F, Botcharnikov RE, Scarlato P (2009) Solubility of H2O and CO2 in ultrapotassic melts at 1200 and 1250C and pressure from 50 to 500 MPa. Am Mineral 94:105–120
Berg SE, Troll VR, Deegan FM, Burchardt S, Krumbholz M, Mancini L, Polacci M, Carracedo JC, Soler V, Arzilli F, Brun F (2016) Heterogeneous vesiculation of 2011 El Hierro xeno-pumice revealed by X-ray computed microtomography. Bull Volcanol 78:85. doi:10.1007/s00445-016-1080-x
Berrino G, Corrado G, Riccardi U (1998) Sea gravity data in the Gulf of Naples: a contribution to delineating the structural pattern of the Vesuvian area. J Volcanol Geoth Res 82:139–150
Bertagnini A, Landi P, Rosi M. and Vigliargio A (1998) The Pomici di Base Plinian eruption of Somma-Vesuvius. J Volcanol Geotherm Res 83:219–239
Blake S (1984) Volatile oversaturation during the evolution of silicic magma chambers as an eruption trigger. J Geophys Res 89:8237–8244
Blower JD, Keating JP, Mader HM and Phillips JC (2002) The evolution of bubble size distributions in volcanic eruptions. J Volcanol Geotherm Res 120(1–2):1–23
Blundy J and Cashman K (2008) Petrologic reconstruction of magmatic system variables and processes. Rev Mineral and Geochem 69:179–239
Blythe LS, Deegan FM, Freda C, Jolis EM, Masotta M, Misiti V, Taddeucci J, Troll VR (2015) CO2 bubble generation and migration during magma–carbonate interaction. Contrib Mineral Petrol 169(4):1–16. doi:10.1007/s00410-015-1137-4
Brocchini DC, Principe D, Castradori M, Laurenzi A, Gorla L (2001) Quaternary evolution of the southern sector of the Campanian Plain and early Somma– Vesuvius activity: insights from the Trecase 1 well. Miner Petrol 73:67–91
Brugger CR, Hammer JE (2010) Crystal size distribution analysis of plagioclase in experimentally decompressed hydrous rhyodacite magma. Earth Planet Sci Lett 300:246–254
Caricchi L, Pommier A, Pistone M, Castro J, Burgisser A, Perugini D (2011) Strain-induced magma degassing: insights from simple-shear experiments on bubble bearing melts. Bull Volcanol 73:1245. doi:10.1007/s00445-011-0471-2
Carr BB, Clarke AB, de' Michieli Vitturi M (2018) Earthquake induced variations in extrusion rate: A numerical modeling approach to the 2006 eruption of Merapi Volcano (Indonesia). Earth Planet Sci Lett 482:377–387
Cashman K, Marsh B (1988). Crystal size distribution (CSD) in rocks and the kinetics and dynamics of crystallization II. Makaopuhi lava lake. Contrib Mineral Petrol 99:292-305
Cashman KV, Mangan MT (1994) Physical aspects of magmatic degassing; II, Constraints on vesiculation processes from textural studies of eruptive products. In: Carroll M (Ed.) Volatiles in Magma. Mineral Soc Am, Washington D.C, pp 447 – 478
Cioni R, Bertagnini A, Santacroce R, Andronico D (2008) Explosive activity and eruption scenarios at Somma-Vesuvius (Italy): Towards a new classification scheme. J Volcanol Geotherm Res 178:331–346
Cnudde V, Boone MN (2013) High-resolution X-ray computed tomography in geosciences: A review of the current technology and applications. Earth Sci Rev 123: 1–17
Cole PD, Scarpati C (2010) The 1944 eruption of Vesuvius, Italy: combining contemporary accounts and field studies for a new volcanological reconstruction. Geol Mag 147:391–415
Couch S, Sparks RSJ, Carroll MR (2003) The kinetics of degassing induced crystallization at Soufrie`re Hills volcano, Montserrat. J Petrol 44:1477–1502
Cubellis E, Marturano A, Pappalardo L (2016) The last Vesuvius eruption in March 1944: reconstruction of the eruptive dynamic and its impact on the environment and people through witness reports and volcanological evidence. Nat Hazards 82:95. doi:10.1007/s11069-016-2182-7
Dallai L, Cioni R, Boschi C, D'Oriano C (2011) Carbonate-derived CO2 purging magma at depth: influence on the eruptive activity of Somma-Vesuvius, Italy. Earth Planet Sci Lett 310:84-95
De Lorenzo S, Di Renzo V, Civetta L, D'Antonio M, Gasparini P (2006) Thermal model of the Vesuvius magma chamber. Geophys Res Lett 33:L17302
De Vivo B, Petrosino P, Lima A, Rolandi G, Belkin HE (2010) Research progress in volcanology in the Neapolitan area, southern Italy: a review and some alternative views. Miner Petrol 99:1-28

Deegan FM, Troll VR, Freda C, Misiti V, Chadwick JP, McLeod CL, Davidson JP (2010) Magma-carbonate interaction processes and associated CO2 release at Merapi volcano, Indonesia: insights from experimental petrology. J Petrol 51:1027-1051
Deegan FM, Troll VR, Freda C, Misiti V, Chadwick JP (2011) Fast and furious: crustal CO2 release at Merapi volcano, Indonesia. Geol Today 27:57-58.
Deer WA, Howie RA, Zussman J (1992) An introduction to the rock-forming minerals. Longman Scientific and Technical, 2nd ed. Wiley, New York, NY
Degruyter W, Bachmann O, Burgisser A (2010) Controls on magma permeability in the volcanic conduit during the climactic phase of the Kos Plateau Tuff eruption (Aegean Arc). Bull Volcanol 72(1):63. doi:10.1007/s00445-009-0302-x
Delibrias G, Di Paola GM, Rosi M, Santacroce R (1979) La storia eruttiva del complesso vulcanico Somma-Vesuvio ricostruita dalle successioni piroclastiche del Monte Somma. Rend Soc It Mineral Petrol 35: 411–438
Devine JD, Gardner JE, Brack HP, Layne GD, Rutherford MJ (1995) Comparison of analytical methods for estimating H2O contents of silicic volcanic glasses. Am Mineral 80:319-328
Di Matteo V, Carroll MR, Behrens H, Vetere F, Brooker RA (2004) Water solubility in trachytic melts. Chem Geol 213:187–196
Di Matteo V, Mangiacapra A, Dingwell DB, Orsi G (2006) Water solubility and speciation in shoshonitic and latitic melt composition from Campi Flegrei Caldera (Italy). Chem Geol 229(1–3):113–124
Dingwell DB, Webb S (1989) Structural relaxation in silicate melts and non-Newtonian melt rheology in geologic processes. Phys Chem Miner 16(5):508–516. doi:10.1007/BF00197020
Duffield WA, Ruiz J (1998) A model that helps explain Sr-isotope disequilibrium between feldspar phenocrysts and melt in largevolume silicic magma systems. J Volcanol Geotherm Res 87:7– 13
Fabbrizio A, Carroll MR (2008) Experimental constraints on the differentiation process and pre-eruptive conditions in the magmatic system of Phlegrean Fields (Naples, Italy). J Volcanol Geotherm Res 171:88–102
Fanara S, Behrens H, Zhang Y (2013) Water diffusion in potassium-rich phonolitic and trachytic melts. Chem Geol 346:149–161
Freda C, Gaeta M, Giaccio B, Marra F, Palladino DM, Scarlato P, Sottili G (2011) CO2-driven large mafic explosive eruptions: The Pozzolane Rosse case study from the Colli Albani Volcanic District (Italy). Bull Volcanol 73(3):241–256. doi:10.1007/s00445-010-0406-3
Gaonac'h H, Lovejoy S, Stix J, Schertzer D (1996) A scaling growth model for bubbles in basaltic lava flows. Earth Planet Sci Lett 139:395–409
Gardner JE, Thomas RME, Jaupart C, Tait S (1996) Fragmentation of magma during Plinian volcanic eruptions. Bull Volcanol 58:144–162
Gebauer SK, Schmitt AK, Pappalardo L, Stockli DF, Lovera OM (2014) Crystallization and eruption ages of Breccia Museo (Campi Flegrei caldera, Italy) plutonic clasts and their relation to the Campanian ignimbrite. Contrib Mineral Petrol 167(1):1–18
Ghiorso MS, Sack RO (1995) Chemical mass transfer in magmatic processes IV. A revised and internally consistent thermodynamic model for the interpolation and extrapolation of liquid-solid equilibria in magmatic systems at elevated temperatures and pressures. Contrib Miner Petrol 119:197–212
Giachetti T, Burgisser A, Arbaret L, Druitt TH, Kelfoun K (2011) Quantitative textural analysis of Vulcanian pyroclasts (Montserrat) using multi-scale X-ray computed microtomography: comparison with results from 2D image analysis. Bull Volcanol 73:1295–1309
Giordano D, Polacci M, Papale P, Caricchi L (2010) Rheological control on the dynamics of explosive activity in the 2000 summit eruption of Mt. Etna. Solid Earth 1:61–69. doi:10.5194/se-1-61-2010
Gonnermann HM, Manga M (2003) Explosive volcanism may not be an inevitable consequence of magma fragmentation. Nature 426:432–435. doi: 10.1038/nature02138
Gonnermann HM, Houghton BF (2012) Magma degassing during the Plinian eruption of Novarupta, Alaska, 1912. Geochem Geophys Geosys 13:Q10009. doi:10.1029/2012GC00427
Gurioli L, Houghton BF, Cashman KV, Cioni R (2005) Complex changes in eruption dynamics during the 79AD eruption of Vesuvius. Bull Volcanol 67:144–159
Gurioli L, Harris A J L, Houghton BF, Polacci M, Ripepe M (2008) Textural and geophysical characterization of explosive basaltic activity at Villarrica volcano. J Geophys Res 113:B08206
Hammer J, Rutherford MJ (2002) An experimental study of the kinetics of decompression-induced crystallization in silicic melt. J Geophys Res 107:1–24
Hammer JE, Cashman KV, Hoblitt RP, Newman S (1999) Degassing and microlite crystallization during pre-climactic events of the 1991 eruption of Mt, Pinatubo, Philippines. Bull Volcanol 60:355– 380
Higgins MD (2000) Measurement of Crystal Size Distributions. Am Mineral 85:1105–1116
Higgins MD (2002) Closure in crystal size distributions (CSD), verification of CSD calculations, and the significance of CSD fans. Am Mineral 87:171-175
Higgins MD (2006) Quantitative textural measurements in igneous and metamorphic petrology. Cambridge University Press

Higgins MD, Chandrasekharam D (2007) Nature of sub-volcanic magma chambers, Deccan province, India: Evidence from quantitative textural analysis of plagioclase megacrysts in the Giant Plagioclase Basalts. J Petrol 48:885-900
Houghton BF, Wilson CJN (1989) A vesicularity index for pyroclastic deposits. Bull Volcanol 51:451–462
Houghton BF, Carey RJ, Cashman KV, Wilson CJN, Hobden BJ, Hammer JE (2010) Diverse patterns of ascent, degassing, and eruption of rhyolite magma during the 1.8 ka Taupo eruption, New Zealand: evidence from clast vesicularity. J Volcanol Geotherm Res 195:31–47
Hughes EC, Neave DA, Dobson KJ, Withers PJ, Edmonds M (2017) How to fragment peralkaline rhyolites: observations on pumice using combined multi-scale 2D and 3D imaging. J Volcanol Geotherm Res 336:179–191
Iacono-Marziano G, Schmidt BC, Dolfi D (2007). Equilibrium and disequilibrium degassing of a phonolitic melt (Vesuvius AD 79 "white pumice") simulated by decompression experiments. J Volcanol Geotherm Res 161:151–164
Improta L, Corciulo M (2006). Controlled source nonlinear tomography: a powerful tool to constrain tectonic models of the Southern Apennines orogenic wedge, Italy. Geology 34:941–944
Jerram DA, Higgins MD (2007) 3D analysis of rock textures: Quantifying igneous microstructures. Elements 3:239-245
Jolis EM, Freda C, Troll VR, Deegan FM, Blythe LS, McLeod CL, Davidson JP (2013) Experimental simulation of magma–carbonate interaction beneath Mt. Vesuvius, Italy. Contrib Mineral Petrol 166(5):1335–1353
Jolis EM, Troll VR, Harris C, Freda C, Gaeta M, Orsi G, Siebe C (2015) Skarn xenolith record crustal CO2 liberation during Pompeii and Pollena eruptions, Vesuvius volcanic system, central Italy. Chem Geol 415: 17-36. doi:10.1016/j.chemgeo.2015.09.003
Kaminski E, Jaupart C (1997) Expansion and quenching of vesicular magma fragments in Plinian eruptions. J Geophys Res 102:12817–12203
Kennedy BM, Wadsworth FB, Vasseur J, Schipper CI, Jellinek AM, von Aulock FW, Hess KU, Russell JK, Lavallée Y, Nichols ARL, Dingwell DB (2016). Surface tension driven processes densify and retain permeability in magma and lava. Earth Planet Sci Lett 433:116–124
Ketcham RA (2005) Computational methods for quantitative analysis of three-dimensional features in geological specimens. Geosphere 1(1):32-41
King PL, Venneman TW, Holloway JR, Hervig RL, Lowenstern JE Forneris JF (2002) Analytical techniques for volatiles: A case study using intermediate (andesitic) glasses. Am Mineral 87:1077-1089
Klebesz R Bodnar RJ, De Vivo B, Török K, Lima A, Petrosino P (2012) Composition and origin of nodules from the ~20 ka Pomici di Base (PB)-Sarno eruption of Mt. Somma - Vesuvius, Italy. Centr Eur J Geosci 4(2): 324-337
Klebesz R, Esposito R, De Vivo B, Bodnar RJ (2015) Constraints on the origin of sub-effusive nodules from the Sarno (Pomici di Base) eruption of Mt. Somma-Vesuvius (Italy) based on compositions of silicate-melt inclusions and clinopyroxene. Am Mineral 100(4):760-77
Klug C, Cashman KV, Bacon C (2002) Structure and physical characteristics of pumice from the climactic eruption of Mount Mazama (Crater Lake), Oregon. Bull Volcanol 64:486–501
Landi P, Bertagnini A, Rosi M (1999) Chemical zoning and crystallization mechanisms in the magma chamber of the Pomici di Base Plinian eruption of Somma-Vesuvius (Italy). Contrib Mineral Petrol 135:179–197
Larsen JF (2008) Heterogeneous bubble nucleation and disequilibrium H2O exsolution in Vesuvius K-phonolite melts. J Volcanol Geotherm Res 175:278-288
Lirer L, Petrosino P, Alberico I (2010) Hazard and risk assessment in a complex multisource volcanic area: the example of the Campania region, Italy. Bull Volcanol 72: 411–429
Mangan MT, Cashman KV (1996) The structure of basaltic scoria and reticulite and inferences for vesiculation, foam formation, and fragmentation in lava fountains. J Volcanol Geotherm Res 73:1–18
Mangan M, Sisson T (2000) Delayed, disequilibrium degassing in rhyolite magma: decompression experiments and implications for explosive volcanism. Earth Planet Sci Lett 183:441-455
Marsh B (1988) Crystal size distribution (CSD) in rocks and the kinetics and dynamics of crystallization I. Theory. Contrib Mineral Petrol 99:277–291
Martel C, Schmidt BC (2003) Decompression experiments as an insight into ascent rates of silicic magmas. Contrib Mineral Petrol 144:397–415
Mastrolorenzo G, Pappalardo L (2006) Magma degassing and crystallization processes during eruptions of high-risk Neapolitan volcanoes: Evidence of common equilibrium rising processes in alkaline magmas. Earth Plan Sci Lett 250:164–181
Mastrolorenzo G, Pappalardo L (2010) Hazard assessment of explosive volcanism at Somma-Vesuvius. J Geophys Res 115:B12212
Mastrolorenzo G, Pappalardo L, Troise C, Panizza A, De Natale G (2008) Probabilistic tephra hazard maps for the Neapolitan area: quantitative volcanological study of Campi Flegrei eruptions. J Geophys Res 113: B07203. doi:10.1029/2007JB004954
Mollo S, Gaeta M, Freda C, Di Rocco T, Misiti V, Scarlato P (2010) Carbonate assimilation in magmas: a reappraisal based on experimental petrology. Lithos 114:503-514
Mourtada-Bonnefoi CC, Laporte D (2002) Homogeneous bubble nucleation in rhyolitic magmas: an experimental study of the effect of H2O and CO2. J Geophys Res 107:B4. doi:10.1029/2001JB00290

Mueller S (2007) Permeability and porosity as constraints on the explosive eruption of magma: laboratory experiments and field investigations. In: Earth and Environment. Ludwig-Maximilians University, Munich, pp 1–149
Namiki A, Manga M (2008) Transition between fragmentation and permeable outgassing of low viscosity magmas. J Volcanol Geotherm Res 169:48–60
Okumura S, Nakamura M, Tsuchiyama A, Nakano T, Uesugi K (2008) Evolution of bubble microstructure in sheared rhyolite: formation of a channel-like bubble network. J Geophys Res 113:B07208
Okumura S, Nakamura M, Nakano T, Uesugi K, Tsuchiyama A (2012) Experimental constraints on permeable gas transport in crystalline silicic magmas. Contrib Mineral Petrol 164:493-504
Otsu N (1979) A threshold selection method from gray level histograms. IEEE Trans. Syst Man Cybern 9:62–66. doi:10.1109/TSMC.1979.4310076
Papale P (1999) Strain-induced magma fragmentation in explosive eruptions. Nature 397:425–428. doi:10.1038/17109
Papale P, Dobran F (1993) Modeling of the ascent of magma during the plinian eruption of Vesuvius in A.D. 79. J Volcanol Geothermal Res 58: 101–132
Pappalardo L, Mastrolorenzo G (2010) Short residence times for alkaline Vesuvius magmas in a multi-depth supply system: Evidence from geochemical and textural studies. Earth Plan Sci Lett 296:133–143
Pappalardo L, Mastrolorenzo G (2012) Rapid differentiation in sill-like magma reservoir: a case study from the Campi Flegrei caldera. Sci Rep 2:712. doi:10.1038/srep00712
Pappalardo L, Piochi M, Mastrolorenzo G (2004) The 3550 YR BP - 1944 AD magma-plumbing system of Somma-Vesuvius, constraints on its behavior and present state through a review of Sr-Nd isotope data. Ann Geophys 47:1471–1483
Pappalardo L, Ottolini L, Mastrolorenzo G (2008) The Campanian Ignimbrite, Southern Italy. geochemical zoning, insight on the generation of a super-eruption from catastrophic differentiation and fast withdrawal. Contrib Mineral Petrol 156:1–26
Pappalardo L, D'Auria L, Cavallo A, Fiore S (2014) Petrological and seismic precursors of the paroxysmal phase of the last Vesuvius eruption on March 1944. Sci Rep 4:6297
Pichavant M, Di Carlo I, Rotolo SG, Scaillet B, Burgisser A, Le Gall N, Martel C (2013) Generation of CO2-rich melts during basalt magma ascent and degassing. Contrib Mineral Petrol 166:545-561
Polacci M, Baker DR, Mancini L, Favretto S, Hill RJ (2009) Vesiculation in magmas from Stromboli and implications for normal Strombolian activity and paroxysmal explosions in basaltic systems. J Geophys Res 114:B01206
Polacci M, Baker DR, La Rue A, Mancini L, Allard P (2012) Degassing behaviour of vesiculated basaltic magmas: an example from Ambrym volcano, Vanuatu Arc. J Volcanol Geotherm Res 233– 234:55–64
Polacci M, Bouvet de Maisonneuve C, Giordano D, Piochi M, Mancini L, Degruyter W, Bachmann O (2014) Permeability measurements of Campi Flegrei pyroclastic products: an example from the Campanian Ignimbrite and Monte Nuovo eruptions. J Volcanol Geotherm Res 272:16-22. doi: 10.1016/j.jvolgeores.2013.12.002
Proussevitch AA, Sahagian DL, Tsentalovich EP (2007a). Statistical analysis of bubble and crystal size distributions: formulations and procedures. J Volcanol Geotherm Res 164:95–111. doi:10.1016/j.jvolgeores.2007.04.007
Proussevitch AA, Sahagian DL, Carlson WD (2007b) Statistical analysis of bubble and crystal size distributions: application to Colorado Plateau basalts. J Volcanol Geotherm Res 164:112–126. doi:10.1016/j.jvolgeores.2007.04.006
Rotella MD, Wilson CJN, Barker SJ, Cashman KV, Houghton BF, Wright IC (2014) Bubble development in explosive silicic eruptions: insights from pyroclast vesicularity textures from Raoul volcano (Kermadec arc). Bull Volcanol 76:826
Rust AC, Cashman KV (2011) Permeability controls on expansion and size distributions of pyroclasts. J Geophys Res 116:B11202
Rutherford MJ, Gardner JE (2000) Rates of magma ascent. In: Sigurdsson H (ed) Encyclopedia of volcanoes. Academic Press, San Diego
Santacroce R, Cioni R, Marianelli P, Sbrana A, Sulpizio R, Zanchetta R Donahued DJ, Joron JL (2008) Age and whole rock–glass compositions of proximal pyroclastics from the major explosive eruptions of Somma-Vesuvius: A review as a tool for distal tephrostratigraphy. J Volcanol Geotherm Res 177:1–18
Scaillet B, Pichavant M Cioni R (2008) Upward migration of Vesuvius magma chamber over the past 20,000 years. Nature 455:216-219. doi:10.1038/nature07232
Scarpati C, Sparice D, Perrotta A (2016) Comparative proximal features of the main Plinian deposits (Campanian Ignimbrite and Pomici di Base) of Campi Flegrei and Vesuvius. J Volcanol Geoth Res 321:149–157
Scheibner B, Heumann A, Wörner G, Civetta L (2008) Crustal residence times of explosive phonolite magmas: U-Th ages of magmatic Ca-garnets of Mt. Somma-Vesuvius (Italy). Earth Planet Sci Lett 276: 293–301. doi:10.1016/j.epsl.2008.09.028
Schneider CA, Rasband WS, Eliceiri KW (2012) NIH Image to ImageJ: 25 years of image analysis, Nat Methods 9(7):671-675
Shea T, Houghton BF, Gurioli L, Cashman KV, Hammer JE, Hobden BJ (2010a) Textural studies of vesicles in volcanic rocks: an integrated methodology. J Volcanol Geotherm Res 190(3–4):271–289
Shea T Gurioli L, Larsen JF, Houghton BF, Hammer JE, Cashman KV (2010b) Linking experimental and natural vesicle textures in Vesuvius 79 AD white pumice. J Volcanol Geotherm Res 192:69–84

Schmidt BC, Behrens H (2008) Water solubility in phonolite melts: influence of melt composition and temperature. Chem Geol 256:259–268
Siani G, Sulpizio R, Paterne M Sbrana A (2004) Tephrostratigraphy study for the last 18,000 14C years in a deep-sea sediment sequence for the South Adriatic. Quat Sci Rev 23:2485–2500
Song SR, Jones KW, Lindquist WB, Dowd BA, Sahagian DL (2001) Synchrotron X-ray computed microtomography: studies on vesiculated basaltic rock. Bull Volcanol 63:252–263
Sottili G, Taddeucci J, Palladino DM, Gaeta M, Scarlato P, Ventura G (2009) Sub-surface dynamics and eruptive styles of maars in the Colli Albani Volcanic District, Central Italy. J Volcanol Geotherm Res 180:189–202
Sottili G, Taddeucci J, Palladino DM (2010) Constraints on magma-wall rock thermal interaction during explosive eruptions from textural analysis of cored bombs. J Volcanol Geotherm Res 192:27–34
Sparks RSJ (1978) The dynamics of bubble formation and growth in magmas: A review and analysis: J Volcanol Geotherm Res 3:1–37. doi:10.1016/ 0377-0273(78)90002-1
Spera FJ, Bohrson WA (2001) Energy-constrained open-system magmatic processes I: general model and energy-constrained assimilation and fractional crystallization (EC-AFC) formulation. J Petrol 42:999–1018
Spieler O, Kenned, B, Kueppers U, Dingwell DB, Scheu B Taddeucci J (2004) The fragmentation threshold of pyroclastic rocks: Earth Planet Sci Lett 226:139–148. doi:10.1016/j.epsl.2004.07.016
Takeuchi S, Tomiya A, Shinohara H (2009) Degassing conditions for permeable silicic magmas: Implications from decompression experiments with constant rates. Earth Planet Sci Lett 283(1–4):101–110
Thomas N, Jaupert C, Vergniolle S (1994) On the vesicularity of pumice. J Geophys Res 99:15,633–15,644
Toramaru A (2006) BND (bubble number density) decompression rate meter for explosive volcanic eruptions. J Volcanol Geotherm Res 154:303–316
Troll VR, Hilton DR, Jolis EM, Chadwick JP, Blythe LS, Deegan FM, Schwarzkopf LM, Zimmer M (2012) Crustal CO2 liberation during the 2006 eruption and earthquake events at Merapi volcano, Indonesia. Geophys Res Lett 39:L11302. doi:10.1029/ 2012GL051307
Verhoogen J (1951) Mechanics of ash formation. Am J Sci 249:729–739
Villemant B (1988) Trace element evolution in the Phlegrean Fields Central Italy: fractional crystallization and selective enrichment. Contrib Mineral Petrol 98:169–183
Voltolini M, Zandomeneghi D, Mancini L, Polacci M (2011) Texture analysis of volcanic rock samples: quantitative study of crystals and vesicles shape preferred orientation from X-ray microtomography data. J Volcanol Geotherm Res 202:83–95
Vona A, Romano C, Dingwell DB, Giordano D (2011) The rheology of crystal-bearing basaltic magmas from Stromboli and Etna. Geochim Cosmochim Acta 75(11):3214–3236
Zandomeneghi D, Voltolini M, Mancini L, Brun F, Dreossi D, Polacci M (2010) Quantitative analysis of X-ray microtomography images of geomaterials: application to volcanic rocks. Geosphere 6:793–804
Zhang Y (1999) A criterion for the fragmentation of bubbly magma based on brittle failure theory. Nature 402:648–650. doi:10.1038/45210
Watson EB (1994) Diffusion in volatile-bearing magmas. Rev Mineral 30:371–411
Webb S (1997) Silicate Melts: Relaxation, Rheology, and the Glass Transition. Rev Geophys 35(2) :191–218
Wright HMN, Weinberg RF (2009) Strain localization in vesicular magma: implications for rheology and fragmentation. Geology 37(11):1023–1026. doi:10. 1130/G30199A.1

3.1.2. Magmatic stoping during caldera-forming Pomici di Base eruption (Somma-Vesuvius, Italy) as a fuel of eruption explosivity

This work is submitted to Lithos under the same title with authors:

Buono G.[a,b], Pappalardo L.[a], Harris C.[c], Edwards B.R.[d], Petrosino P.[b]

a - Istituto Nazionale di Geofisica e Vulcanologia, Osservatorio Vesuviano, Italy
b - University of Naples Federico II, Department of Earth, Environmental and Resources Science, Italy
c - University of Cape Town, Department of Geological Sciences, South Africa
d - Dickinson College, Department of Earth Sciences, USA

I contributed to all phases (field activities, rock characterization, thermodynamic and kinetic calculations, data interpretation, writing) and investigations of the work except the oxygen isotopes analyses, performed at Department of Geological Sciences of the University of Cape Town.

Abstract

Magma-carbonate interaction and the subsequent CO_2 release can occur before and during an eruption, critically affecting magma storage and ascent processes. However, its mechanism and timescale still remain unclear, particularly during the fast magma withdrawal feeding high-intensity eruptions.
We selected as case study the caldera-forming Pomici di Base plinian eruption, the oldest (22 ka) and largest (> 4.4 km^3) explosive event of the Somma-Vesuvius. During this event the emission of trachytic and latitic-shoshonitic (~25% and ~75% of the erupted magma volume respectively) magmas generated a long-lasting plinian column, hypothetically driven by CO_2 liberation during magma-carbonate interaction as inferred in a previous study.
In this study, we reconstruct in detail the evolution of the plumbing system during the Pomici di Base eruption combining geochemical (major/minor elements and radiogenic/stable isotopes) analyses of juvenile products with thermodynamic and kinetic calculations. Our results demonstrate that magmatic stoping (i.e. the formation and transport of host-rock pieces into a magma body) during caldera collapse evolution can promote magma assimilation of carbonate blocks and CO_2-rich fluids resulting from destabilization of the carbonate bedrock, thus triggering CO_2 release and acting as a fuel of the eruption explosivity. Our findings suggest that the accurate knowledge of these processes and their influence on eruptive dynamics can be crucial to improve the hazard assessment of volcanoes with plumbing systems located in carbonate bedrocks.

1. Introduction

Understanding the dynamics of plinian eruptions is challenging. These events are typically driven by silicic high-viscous magmas (e.g. Cioni et al., 2015) but occasionally they can also involve mafic low-viscous melts (e.g. Freda et al., 2011; Houghton et al., 2004). Moreover complex and abrupt variations in intensity and magnitude, including also the transition between explosive and effusive regime, can occur during these eruptions making difficult predictions for the eruption evolution (e.g. Cassidy et al., 2018). Mostly, eruptive dynamics are controlled by: (i) magma storage physico-chemical variables (e.g. temperature, pressure, magma and volatile compositions, rheological

properties) and their temporal changes (Blundy and Cashman, 2008); (ii) conduit degassing (and outgassing) processes (Gonnermann and Manga, 2007 and references therein); (iii) external environmental factors, such as interactions with wall-rock and external water or change in conduit geometry (e.g. Houghton et al., 2004; Liedl et al., 2019). Particularly, since several volcanoes in the world (e.g. Campi Flegrei, Colli Albani Volcanic District, Etna, Merapi, Nisyros, Popocatépetl, Somma-Vesuvius) are settled in carbonate bedrock, analytical and experimental evidences of critical interaction between magma and limestone wall-rock or skarn have been documented. Some authors suggested that limestone assimilation can be an extremely energetic and fast process, especially when hot and low-viscosity mafic magmas are involved, and able to influence the evolution of an eruption. During this reaction, large amounts of CO_2 can be released with possible significant consequences for the eruption explosivity and in some cases potentially acting as an eruption trigger (Cassidy et al., 2018; Deegan et al. 2011). Recently, rapid crustal CO_2 liberation has been invoked as driving mechanism to increase the eruptive intensity during the 2006 and the 2010 eruptions at Merapi volcano, Indonesia (Borisova et al., 2010; Carr et al., 2018; Deegan et al., 2010; Troll et al., 2012). Moreover, syn-eruptive carbonate wall-rock ingestion has been identified as a process able to affect the eruptive dynamics of several explosive eruptions in the Colli Albani Volcanic District, Italy (e.g. Pozzolane Rosse highly explosive eruptions, Freda et al., 2011; Prata Porci and Albano maar eruptions, Cross et al., 2014; Sottili et al., 2009; 2010). However, although experimental studies (e.g. Blythe et al., 2015; Deegan et al. 2010; 2011; Jolis et al. 2013) have demonstrated that decarbonation of limestone can be very rapid (minutes to days), the specific mechanisms by which these processes occur still remain unclear, especially during high-intensity eruptions.

In this study the caldera-forming Pomici di Base plinian eruption (PBE), the oldest (22 ka) and largest (volume > 4.4 km^3) explosive event of the Somma-Vesuvius, has been selected as case study. During the plinian phase of this eruption, 1.3 km^3 of magma with variable composition from trachyte to predominantly latite-shoshonite (~25% and ~75% of the volume respectively) has been emitted, feeding a sustained plume (height = 16-17 km, peak mass discharge rate, MDR = 2-2.5x10^7 kg s^{-1}; Bertagnini et al., 1998), hypothetically driven by CO_2 release during magma transfer through carbonate bedrock (Pappalardo et al., 2018). Here we present a detailed petrological study on PBE products based on geochemical and (radiogenic and stable) isotopic analyses as well as thermodynamic and kinetic calculations in order to reconstruct the magmatic variables, processes and timescales governing this high-energy eruption during magma storage and ascent.

2. Somma-Vesuvius and Pomici di Base plinian eruption

Evidence of earlier volcanic activity in the Mt. Somma-Vesuvius area has been found by Brocchini et al. (2001) and consist of products of effusive eruptions, emitted from small-scattered volcanic centers, formed about 400 ka. The onset of Somma-Vesuvius volcano activity occurred after the Campanian Ignimbrite eruption (the major eruption of Campi Flegrei, ~39 ka, volcanic explosivity index = 7) and was characterized by a dominantly effusive and low-energy explosive volcanism (Brocchini et al., 2001; Di Renzo et al., 2007). This persistent open-conduit activity determined Mt. Somma edifice growth and was interrupted about 22 ka by the Pomici di Base plinian eruption (Bertagnini et al., 1998; Buono et al., 2019; Landi et al., 1999; Pappalardo et al., 2018). The PBE is the largest explosive event of the Somma-Vesuvius (Bertagnini et al., 1998; Santacroce et al., 2008) and marks the beginning of high-explosive activity period during which other three caldera-forming plinian eruptions occurred (Mercato Pumice, 8.9 ka; Avellino Pumice, ca. 4.0 ka; Pompeii Pumice, 79 AD eruptions), alternated with minor events. After the Pompeii Pumice eruption, the new Vesuvius cone (Gran Cono) began to form during periods of effusive and strombolian activity, the last of which manifested in 1631-1944 (Cioni et al., 1999; Santacroce et al., 2008).

Petrological and geophysical studies have suggested that Somma-Vesuvius eruptions were fed by shallower (~2-10 km) magma chambers, developed within a carbonate bedrock extended from 2 to about 10 km depth (Brocchini et al., 2001; De Natale et al., 2006 and references therein), recharged from a deeper (15-30 km) reservoir (Balcone-Boissard et al., 2016; De Natale et al., 2006 and references therein; Mastrolorenzo and Pappalardo, 2006; Pappalardo and Mastrolorenzo, 2010; 2012; Scaillet et al., 2008). In fact, in recent years, numerous geochemical and experimental studies provided evidence of magma-limestone interaction (e.g. Dallai et al., 2011; Iacono-Marziano et al., 2008; Jolis et al., 2013; 2015; Pappalardo et al., 2004; Piochi et al., 2006).
According to Bertagnini et al. (1998), the Pomici di Base eruption (also called the Sarno eruption) occurred from a vent located 1-2.5 km west of the present cone and was characterized by three main phases. PBE started with a short *opening phase* during which a thin trachytic pumice ash and lapilli fallout deposit was formed (U-1, Fig. 1a). The following *plinian phase* was dominated by the emplacement of a thick fall deposit, further separated in three layers with a constant relative thickness of 2:1:5 (U-2): basal trachytic white pumice beds, a transitional trachytic grey pumice bed and upper latitic-shoshonitic black scoria beds. A *phreatomagmatic phase*, marked by an alternation of lithic-rich shoshonitic fall and wet pyroclastic density currents (PDCs) deposits, concluded the eruption and was characterized by a caldera collapse event (U-3 to U-6). The plinian fallout, by far the most significant deposit, has an estimated volume of 4.4 km^3. This was generated by an eruptive plume E-NE dispersed that reached a maximum inferred height of 16-17 km (MDR= 2-2.5x10^7 kg s^{-1}) and remained stable during the whole phase although the strong compositional variation towards mafic terms (Bertagnini et al., 1998). Pappalardo et al. (2018) on the basis of a 3D textural study inferred that during the plinian phase a fast decompression under closed-system degassing regime controlled the uppermost trachytic magma ascent. Subsequently, the emission of the deeper latitic-shoshonitic liquid, under an open-system degassing regime, was likely intensified by a late vesiculation pulse driven by a fast CO_2 liberation during magma migration through the carbonate bedrock, able to maintain high eruptive intensity and magnitude.
The location of magma chamber at the time of PBE has been debated in the literature. Landi et al. (1999) deduced that the magma reservoir was situated at a depth corresponding to a pressure of 3-5 kbar (> 9 km). This depth was used by Scaillet et al. (2008) for a general reconstruction of the Somma-Vesuvius plumbing system evolution, however a more recent analogous scheme of Balcone-Boissard et al. (2016) relocated PBE magma chamber at 3-4 km (1 kbar). Furthermore, Klebesz et al. (2012; 2015) associated melt inclusions hosted in clinopyroxenes of sub-effusive nodules included in the late-stage concentrated PDCs deposit (U-6 in Bertagnini et al., 1998) with pre-PBE magmas, and estimated a clinopyroxene crystallization temperature slightly under 1200 °C and a minimum pressures of 4 (up to 3) kbar.

3. Samples and analytical methods

3.1. Samples

Samples representative of the entire plinian fallout deposit of the Pomici di Base eruption were collected from two distal stratigraphic sections (sections 1 and 2, Fig. 1) located at about 15 km NE of the Somma-Vesuvius (town of Palma Campania). Section 1 changes upward from highly vesicular white pumice lapilli beds to moderate vesicular gray pumice beds to poorly vesicular black scoria lapilli beds, including almost the whole stratigraphic succession recognized by Bertagnini et al. (1998). As shown in Fig. 1 the largest number of samples (from G10 to NN) was taken from this outcrop. Section 2 instead is constituted only by the upper black scoria beds (from which sample S5 and S1 have been collected) that show in the topmost part grain size variations likely linked with a partial instability of the eruptive column in the final stage of plinian phase. Moreover samples (F1) from the wet concentrated PDCs deposit emplaced during the last part of the phreatomagmatic phase (U-6 in Bertagnini et al., 1998) were collected from a proximal outcrop

(section 3, Fig. 1), localized on the NE slope of Mt. Somma (Traianello quarry, town of Somma-Vesuviana). This poorly sorted deposit is composed by poorly vesicular dark scoria lapilli and ash associated to a high content of lithic clasts.
Samples were taken over narrow (5-10 cm) stratigraphic intervals. Seven samples (G10, G80, G160, N170, N200, S1, F1), representative of the whole plinian fallout and of the last phreatomagmatic PDCs, were selected for geochemical and isotopic analyses; further samples (G40, G100, G130, G185, NN, S5) from intermediate heights were chosen for a more exhaustive characterization of stable isotopic trends (Fig. 1a). Thin sections were prepared choosing juvenile clasts with modal density (and vesicularity) values (Balcone-Boissard et al., 2016 and references therein) for geochemical investigations. Instead phenocrysts were separated from groundmasses for isotopic analyses crushing in an agate mortar dozens of juvenile lapilli randomly taken and handpicking fragments with a size between 0 and 1 phi ($\varphi = -log_2 D/D_0$ where D is the diameter of the clasts in mm and D_0 is a reference diameter, equal to 1 mm) under binocular microscope.

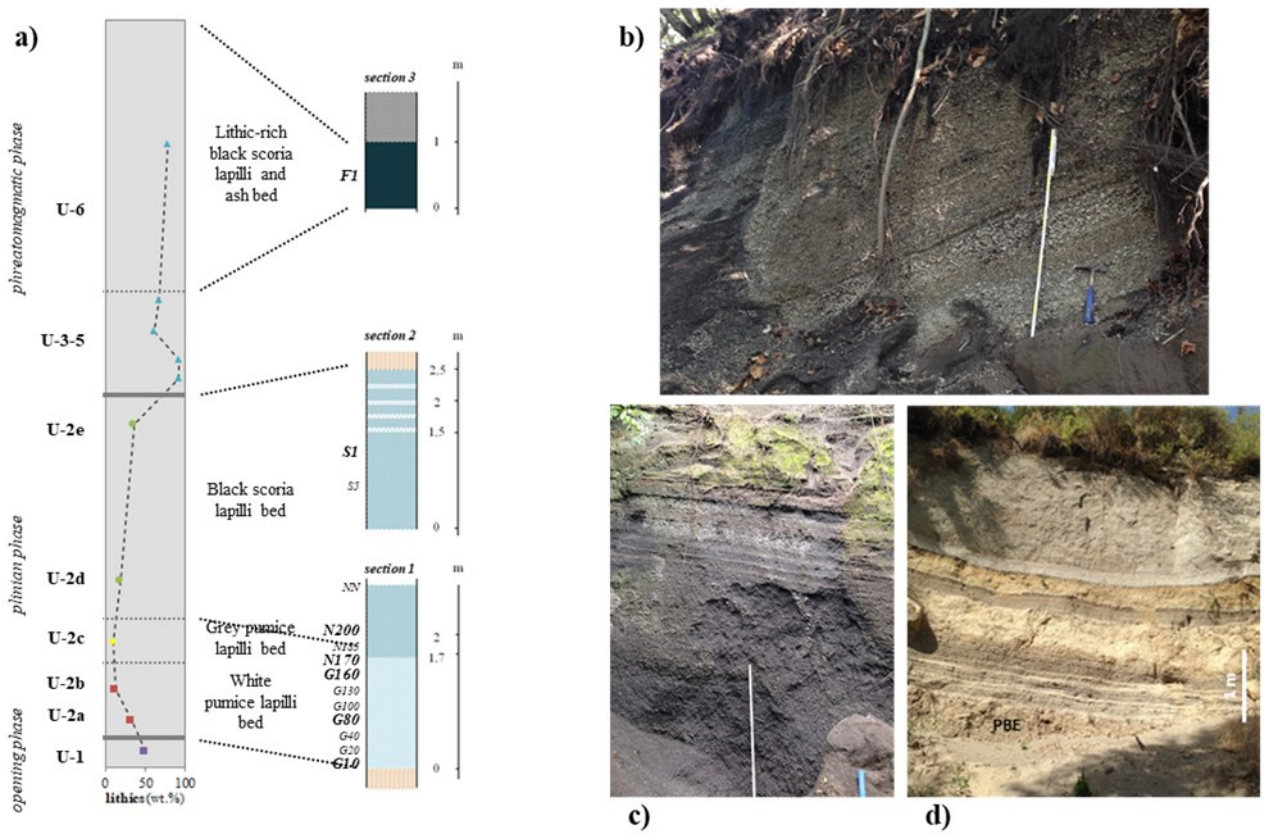

Fig. 1. a) Schematic representation of the sampled stratigraphic sections and correlation with a stratigraphic column (following the reconstruction adapted by Klebesz et al., 2012, based on the descriptions of Bertagnini et al., 1998). Lithic content variation with the stratigraphic height has been also reported using data from Bertagnini et al. (1998). b), c), d) Outcrops of sections 1, 2 and 3 respectively.

3.2. Analytical methods

Bulk density

Following the bulk density measurement procedure described in Pappalardo et al. (2018) we have analyzed, when possible, 100 individual juvenile clasts, coated with a thin film of paraffin wax, for each grain-size classes between -5 to -2 phi using a water pycnometer.

Geochemical and textural analyses
Analyses of major/minor and volatile elements were performed with a JEOL-JXA-8200 electron microprobe (EMPA - WD/ED combined micro analyzer) at the Istituto Nazionale di Geofisica e Vulcanologia (INGV) in Rome for matrix-glasses and a Scanning Electron Microscope (SEM) JEOL-JSM-5310 equipped with EDS at DiSTAR - University of Naples Federico II for crystals (phenocrysts and microlites). EMPA investigation was performed with a 10 μm beam at 15 keV, a beam current of 10 nA and a counting time of 10 s. For each analysis a defocused beam was used to minimize losses of alkalis and volatiles, which were counted first to avoid diffusion effects. Data reduction was carried out using ZAF4/FLS software by Link Analytical. The analytical uncertainty was about 1% for most elements and ≤10% for minor elements. SEM+EDS examination was achieved at 15 kV, using ZAF Correction Routine. Mean precision was < 5% for SiO_2, Al_2O_3, K_2O, CaO, FeO and around 10% for the other elements.
Microlite contents have been estimated acquiring BSE images using SEM, then processed and analyzed with ImageJ software.

Radiogenic isotopes analyses
Isotopic analyses for Sr and Nd of phenocrysts (sanidine and clinopyroxene) and groundmasses were obtained at the INGV – Osservatorio Vesuviano in Naples, using a ThermoFinnigan Triton TI multi-collector thermal ionization mass spectrometer (TIMS). Samples were processed through conventional HF–HNO_3–HCl dissolution before Sr and middle REE (MREE) were separated by standard cation exchange column chemistry, and Nd was further purified on an anion column. Sr and Nd were then loaded onto Ta and Re filaments, respectively. Sr and Nd blanks were negligible for the analyzed samples during the periods of measurements. Measured $^{87}Sr/^{86}Sr$ ratios were normalized for within-run isotopic fractionation to $^{87}Sr/^{86}Sr = 0.1194$, and $^{143}Nd/^{144}Nd$ ratios to $^{143}Nd/^{144}Nd = 0.7219$. The mean measured value of $^{87}Sr/^{86}Sr$ for NIST–SRM 987 was 0.710215 ± 0.000008 (2σ, n = 36) and of $^{143}Nd/^{144}Nd$ for La Jolla was 0.511843 ± 0.000006 (2 σ, n = 11). Each Sr and Nd isotopic analysis reported is a weighted mean of 180 single measurements. The quoted error (internal error) is the standard deviation of the mean (2σ) for n = 180. Instead, the external reproducibility 2σ, which takes into account the uncertainty in the repeated measurements of the standards is calculated according to Goldstein et al. (2003) and is a more reliable estimate of the analytical uncertainty in isotopic measurements. Therefore, the latter has been adopted as an error bar in isotopic diagrams. Sr and Nd isotope ratios have been normalized to the recommended values of NIST SRM 987 ($^{87}Sr/^{86}Sr = 0.71025$) and La Jolla ($^{143}Nd/^{144}Nd = 0.51185$) standards, respectively.

Oxygen isotopes analyses
Oxygen isotopes were determined on phenocrysts (sanidine and clinopyroxene) using the laser fluorination method described by Harris and Vogeli (2010), which employs BrF_5. All O-isotope ratios were measured off-line using a Finnegan DeltaXP mass spectrometer in dual inlet mode at University of Cape Town, and all data are reported in δ-notation, where $\delta^{18}O = (R_{sample}/R_{standard} - 1) \times 1000$; R is the measured $^{18}O/^{16}O$ ratio and SMOW is the standard. Oxygen isotope ratios were measured on O_2 gas. The internal standard MON GT was analysed in duplicates with each batch of 10 samples. MON GT has a $\delta^{18}O$ value of 5.38‰, calibrated against the UWG-2 garnet standard, assuming a $\delta^{18}O$ value of 5.80‰ for UWG-2. The average $\delta^{18}O$ value of the MON GT for each run was used to normalise the raw data to the SMOW scale (Harris and Vogeli, 2010). The minerals gave 100% yields within error. The long-term average difference in $\delta^{18}O$ values of duplicates of MON GT is 0.12‰, which corresponds to a 2σ value of 0.15‰ (n = 283).
The glass was found to decompose partially during pre-fluorination, rendering the analyses by laser fluorination unreliable. All the groundmasses O-isotope analyses were, therefore, made using externally-heated Ni bombs (Harris et al., 2015), employing ClF_3 as reagent at 550 °C, and

converting the liberated O_2 to CO_2. Duplicate splits of the in-house quartz standard MQ were run with each batch of eight samples to monitor analytical precision and convert the raw data to the SMOW scale using the $\delta^{18}O$ value of 10.1‰ for MQ. The long-term variability of MQ suggests a 2σ error of 0.16‰.

4. Results

4.1. Bulk density

Modal clast densities increase upward from 0.57-0.61 g cm^{-3} for white and grey pumice in the lower plinian beds to 1.10-1.51 g cm^{-3} for black scoriae in the upper plinian and phreatomagmatic beds (Table 1). Using dense rock equivalent (DRE) densities of 2.4 and 2.6 g cm^{-3} respectively (Bertagnini et al., 1998) we obtained corresponding modal vesicularities values of 75-76% and 42-57%.

Sample	Modal density (g cm^{-3})	Modal vesicularity (%)	Microlite content (%)
G10	0.59	75	-
G80	0.58	76	-
G160	0.57	76	-
N170	0.61	75	-
N200	1.11	57	15
S1	1.40	46	28
F1	1.51	42	42

Table 1. Modal density/vesicularity and total microlite content of juvenile products sampled from the Pomici di Base plinian fallout.

4.2. Petrographic description

Qualitative textural and mineralogical features of samples have been obtained from preliminary observations under polarizing microscope. All juvenile samples show a porphyritic texture with a low phenocrysts content (< 5 vol.%) dominated by sanidine, plagioclase, clinopyroxene, black mica in order of decreasing abundance and in minor amount by amphibole, magnetite and garnet. The phenocrysts have a maximum size of ≈ 3 mm and are predominantly discrete crystals, however crystal aggregates are also present. Plagioclase and mafic crystals content increases upward towards the black scoria beds, where they are present also as micro-phenocrysts (<< 1 mm). Although phenocrysts are mainly euhedral and sub-euhedral suggesting equilibrium crystallization, sometimes they display disequilibrium textures (i.e. irregular shapes, embayments, zoned plagioclase and clinopyroxene crystals with resorbed cores).

In the plinian lower beds highly vesicular white and grey pumice samples show microlite-free groundmass, while in the plinian and phreatomagmatic upper black scoria beds an increase in microlite cristallinity (from 15 vol.% in N200 to 28 vol.% in S1 to 42 vol.% in F1, mostly clinopyroxene and feldspars, while black mica and oxides only in small amount) and a decrease in vesicularity is observed (Table 1).

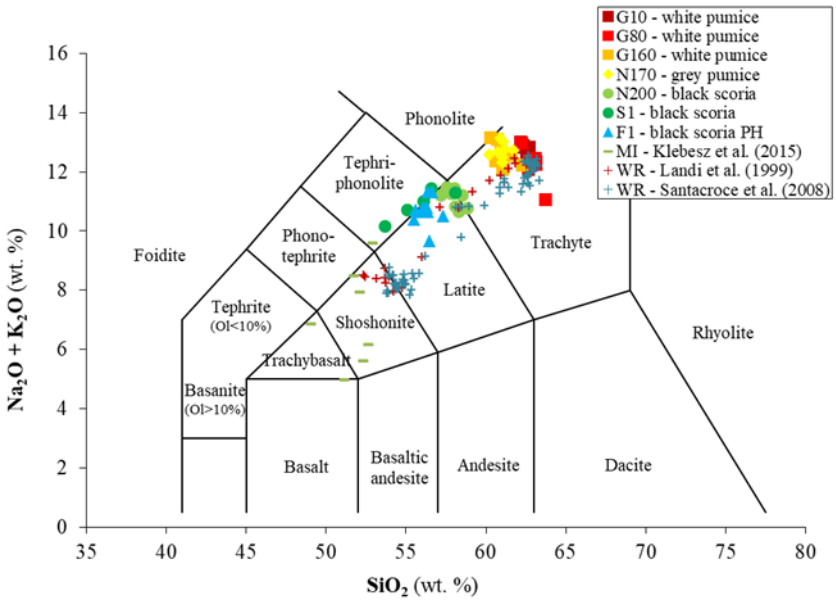

Fig. 2. TAS (Total Alkalies vs. Silica) diagram for volcanic glass compositions of representative Pomici di Base samples. PH = phreatomagmatic phase. Additional data: whole-rocks compositions of Pomici di Base samples from the plinian fallout analyzed by Landi et al. (1999) and Santacroce et al. (2008); compositions of melt inclusions hosted in clinopyroxene of sub-effusive nodules from the late concentrated PDC deposit analyzed by Klebesz et al. (2015).

4.3. Geochemical data

Glass composition

Glass compositions range from trachyte to latite (Fig. 2) moving upward in the stratigraphic succession. Whole-rock compositions reported in Landi et al. (1999) and Santacroce et al. (2008) are generally less-evolved, reaching the shoshonitic field. This difference becomes significant in the black scoriae in which microlites content increases up to 42 vol.% of the groundmass (Table 1). A compositional gap is observed between trachytes and latites-shoshonites, however no evidence of mixing/mingling has been observed (e.g. heterogeneous composition of glasses and crystals).

Harker diagrams (Fig. 3 and supplementary data) show a positive correlation of MgO (min: 0.20 – max: 2.23 wt.%) with TiO_2 (0.16-0.97 wt.%), FeO_{tot} (2.28-9.36 wt.%), CaO (2.42-6.43 wt.%), P_2O_5 (0.01-0.94 wt.%) and a negative correlation with SiO_2 (53.05-63.10 wt.%) and Na_2O (2.64-4.49 wt.%). Al_2O_3 (15.92-18.56 wt.%) and MnO (0.05-0.33 wt.%) concentrations show almost constant values, whereas K_2O (6.67-9.00 wt.%) increases to reach constant values as MgO decreases.

Crystal composition

Phenocrysts: The Or content (from Or_{57} to Or_{92}) in sanidines reaches maximum values in more differentiated trachytes, whereas plagioclases are bytownite and labradorite in composition (An_{49} – An_{92}) and present a general increase in albitic component with the degree of evolution. Clinopyroxenes are close to diopside in composition (Fs_{19} – Fs_{58} and Wo ≈ 50) with decreasing Fs component in the less-evolved terms.

Microlites: Feldspars are only present in samples of the uppermost scoriaceous levels (58% and 71% of the total microlites in S1 and F1 respectively, Table 1) and are essentially composed by plagioclases with composition similar to that of more evolved phenocrysts. Instead mafic crystals are included in samples from the whole scoriaceous deposit (N200, S1 and F1, Table 1) and are basically clinopyroxenes, with average Fs and Wo values slightly higher than those of the corresponding phenocrysts.

Crystals compositions are presented in Fig. 4 and in supplementary data.

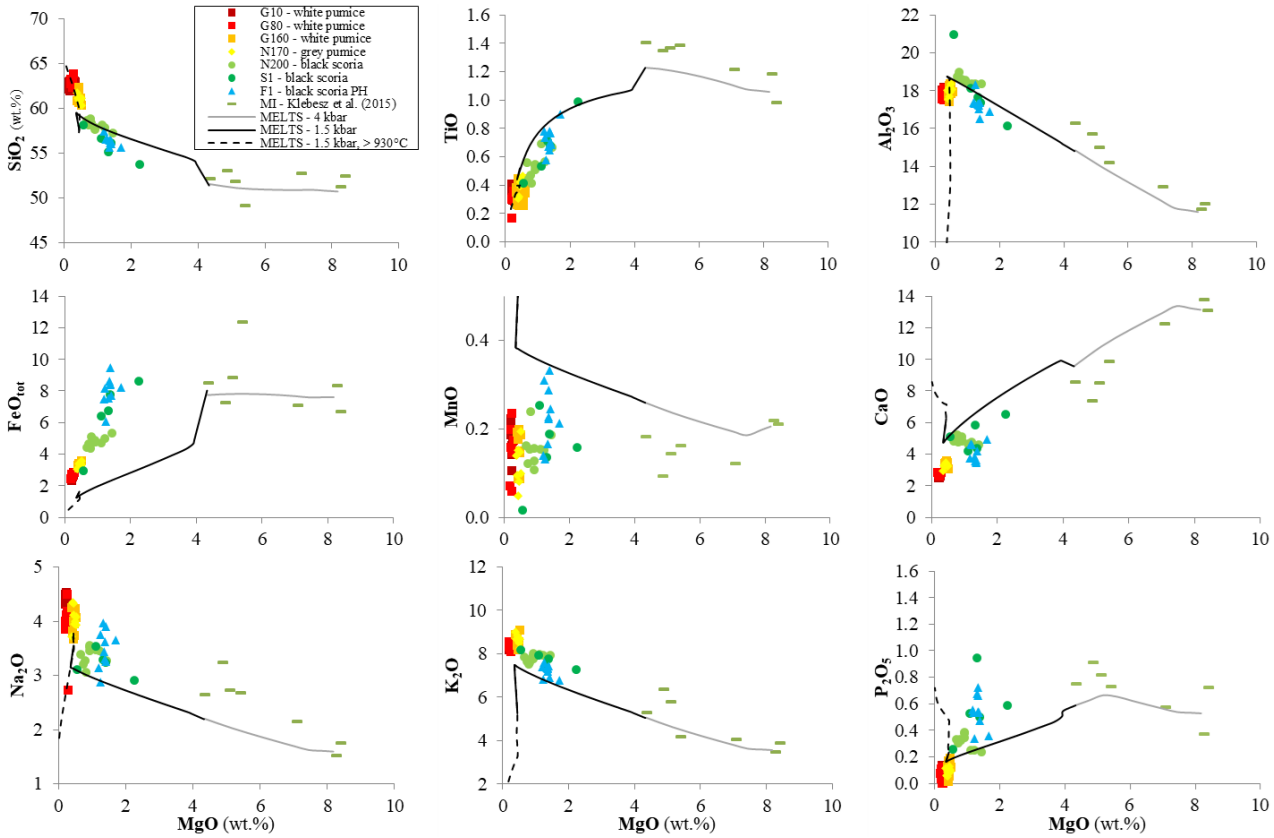

Fig. 3 Harker diagrams of volcanic glasses investigated in the present study and melt inclusions analysed by Klebesz et al. (2015). Best results of the aphaMELTS simulations (P=4 kbar, Ti=1240 °C, fO2=NNO + 1.5, H2Oi + CO2i=1.5 + 0.375 wt.% and P=1.5 kbar, Ti=1150 °C, fO2=NNO + 1.5) are also plotted (see text for details).

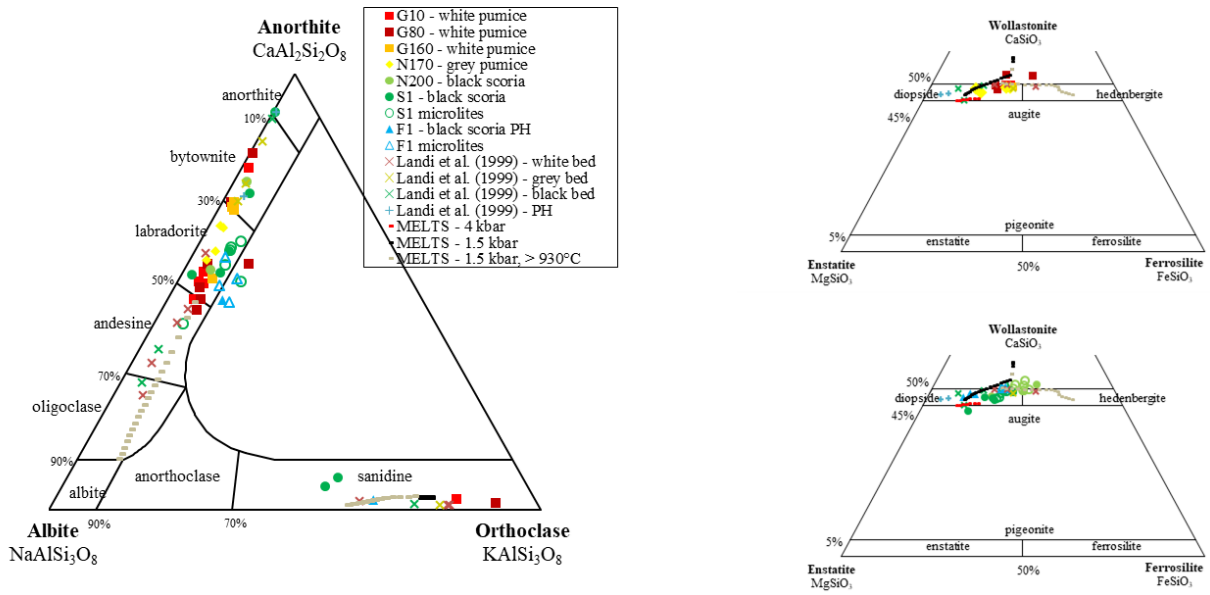

Fig. 4. Compositions of feldspar (left) and clinopyroxene (right: trachytic samples above and latitic-shoshonitic samples below) phenocrysts and microlites. Mineral database of Landi et al. (1999) has been also reported (white, transitional and black beds from plinian fallout, ph. from phreatomagmatic phase). Results of the best-fit aphaMELTS simulations (see text and Fig. 3) performed at 1.5 kbar have been represented separately for data above and below the invariant temperature of 930 °C.

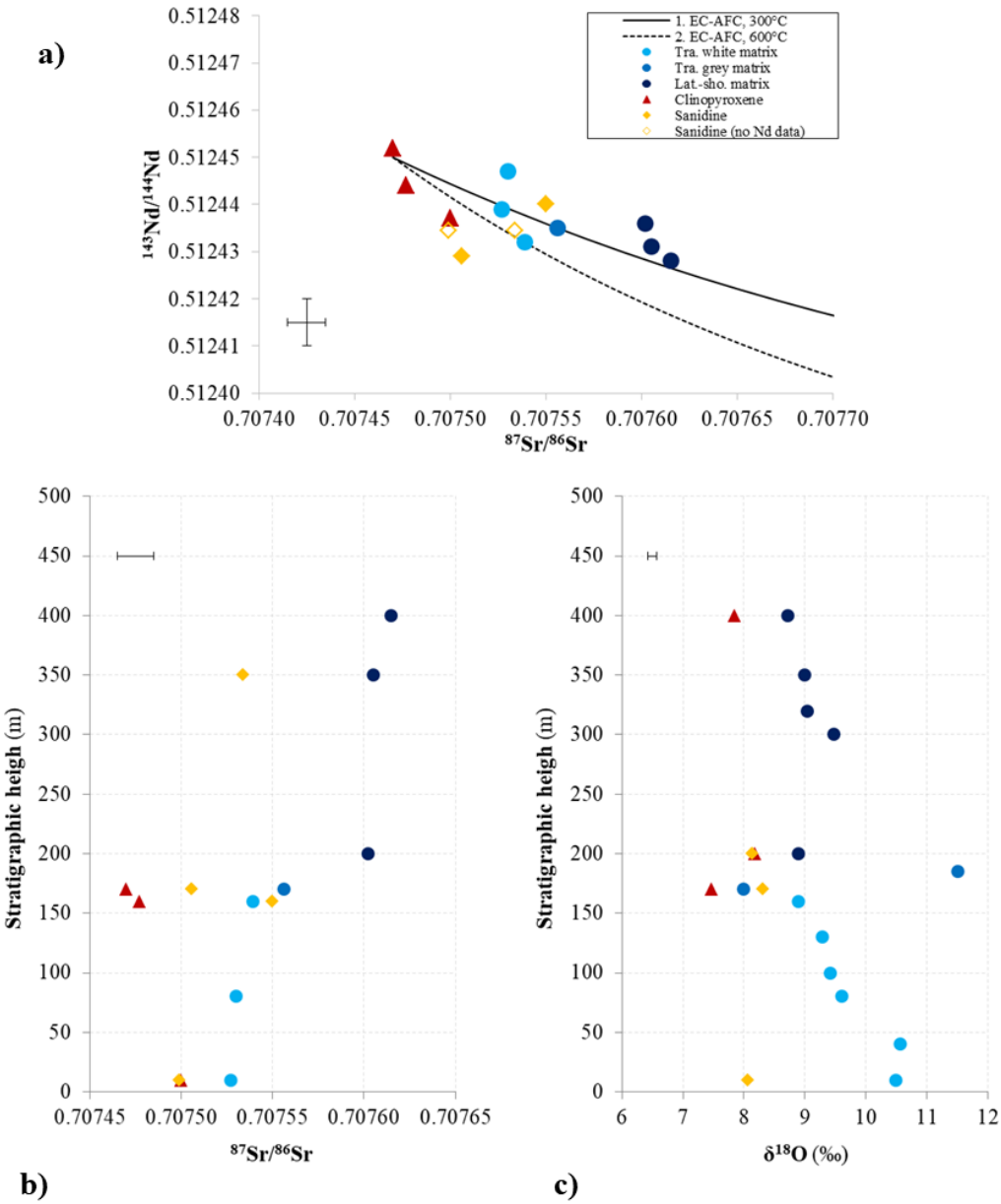

Fig. 5. a) Sr and Nd isotopic ratios of analysed groundmasses and phenocrysts. Best results from EC-AFC simulations are also plotted (see text and Table 4 for details). b) and c) Chemostratigraphy of Sr and oxygen isotopes respectively. Stratigraphic heights for samples NN, S5, S1, F1 are qualitative.

4.4. Isotope data

Radiogenic isotopes

We performed Sr-Nd isotopic analyses on the groundmass of the selected samples and on separated phenocrysts (sanidine and clinopyroxene) in several samples (G10, G160, N170, S1). The obtained results (Fig. 5a, 5b and Table 2) show that $^{87}Sr/^{86}Sr$ ratios progressively increase, according to stratigraphy, from trachytic white to trachytic grey pumice groundmasses (from 0.707527 to 0.707556) and have markedly higher values in latitic-shoshonitic groundmasses (0.707602 – 0.707615). The different mineralogical phases are characterized by specific ranges of $^{87}Sr/^{86}Sr$. Clinopyroxene has the lower values (0.707470 – 0.707500), sanidine instead has higher values

(0.707499 – 0.707550), partially overlapped with trachytic matrix-glasses isotopic ratios. $^{143}Nd/^{144}Nd$ ratios instead are much less variable and show almost constant values (0.512428 - 0.512452) both in groundmasses and phenocrysts. Furthermore, it is important to highlight that latitic-shoshonitic groundmasses samples constitute a cluster with Sr isotopic ratios higher than those of their corresponding phenocrysts as well as of trachyte phenocrysts and matrix-glasses.

	Samples	Glass		Sanidine		Pyroxene	
$^{87}Sr/^{86}Sr$	**G10**	0.707527	±6	0.707499	±6	0.707500	±6
	G80	0.707530	±7				
	G160	0.707539	±6	0.707550	±6	0.707477	±6
	N170	0.707556	±8	0.707506	±6	0.707470	±6
	N200	0.707602	±6				
	S1	0.707605	±7	0.707534	±6	-	±6
	F1	0.707615	±7				
$^{143}Nd/^{144}Nd$	**G10**	0.512439	±7	-		0.512437	±7
	G80	0.512447	±7				
	G160	0.512432	±6	0.512440	±6	0.512444	±6
	N170	0.512435	±6	0.512429	±7	0.512452	±6
	N200	0.512436	±6				
	S1	0.512431	±6	-		0.512452	±7
	F1	0.512428	±7				
$\delta^{18}O$ (‰)	**G10**	10.5		8.1		-	
	G40	10.6					
	G80	9.6					
	G100	9.4					
	G130	9.3					
	G160	8.9					
	N170	8		8.3		7.5	
	N185	11.5					
	N200	8.9		8.1		8.2	
	NN	9.5					
	S5	9					
	S1	9					
	F1	8.7		-		7.8	

Table 2. Strontium, neodymium and oxygen isotopic ratios and 2σ values for groundmasses and phenocrysts in Pomici di Base samples.

Oxygen isotopes

Oxygen isotopes were measured in groundmasses of thirteen samples and in phenocrysts from selected white-pumice, gray-pumice and black-scoria samples (G10, G170, N200 and F1, respectively).

Oxygen isotopic compositions (Fig. 5c and Table 2) of separated clinopyroxene and sanidine phenocrysts are quite uniform, particularly $\delta^{18}O$ ranges from 7.5 to 8.2‰ in clinopyroxenes and from 8.1 to 8.3‰ in sanidines. Separated groundmass material has higher $\delta^{18}O$ values, ranging from 8.0 to 11.5‰ in trachytes, and from 8.7 to 9.5‰ in latites-shoshonites.
Crystal data were converted to melt $\delta^{18}O_{values}$ assuming the per mil difference between melt and minerals Δ(melt-min) reported by Zhao and Zheng (2003) for trachy-andesitic compositions. Moreover, since minerals oxygen isotope diffusion is slow at storage temperature (e.g. Dallai et al., 2011 and references therein), it can be assumed that crystal $\delta^{18}O$ values have remained the same since their formation. It is noteworthy that the lack of correlation between groundmasses $\delta^{18}O$ values and H_2O and CO_2 contents (see supplementary data and Pappalardo et al., 2018) rules out a significant contribution of hydration/alteration processes in the variation of $\delta^{18}O$ values.

5. Discussion

5.1. Magmatic variables and processes

Magma chamber snapshot
The systematic geochemical variation shown by both analyzed matrix-glasses and crystals (Fig. 2 - 4) in representative juvenile samples of Pomici di Base eruption (PBE) suggest that magma differentiated mainly by fractional crystallization. Starting from the measured geochemical data (i.e. glass and mineral compostions, see supplementary data) we have reconstructed the principal pre-eruptive magma chamber variables (Table 3) using several petrological models.
A temperature increment from 904 °C to 1052 °C towards the less-evolved compositions (average value: 965 °C; standard deviation σ: 55 °C; $K_D(Fe\text{-}Mg)^{cpx\text{-}liq}$ range: 0.09-0.32) and an average pressure of 1.51 (σ: 0.29) kbar have been obtained applying the clinopyroxene-liquid geothermobarometer proposed by Masotta et al. (2013) for alkaline differentiated rocks. Similar pressure values were estimated adopting the Cl content measured on volcanic glasses as geobarometer following the model of Balcone-Boissard et al. (2016). In detail, our Cl data on trachytic samples indicate a storage pressure for the chamber top of about 1.05±0.22 kbar (mean value using Cl solubility model from Signorelli and Carrol, 2002 and considering an analytical uncertainty of 10% for Cl concentration, Table 3). We neglected the latitic-shoshonitic terms from this calculation due to the lack of data on Cl solubility for this melt composition and their high microlite content that weaken the estimate.
Initial water-content values of about 5-6 wt.% (Table 3), suggesting saturation of the magma at the pressure estimated above (using Papale et al., 2006), have been obtained using the K-feldspar-liquid hygrometer proposed by Mollo et al. (2015) for trachytic samples (the only PBE melt composition covered by the database) although the few geochemical data available on the PBE sanidines.
Finally, by applying the model of Giordano et al. (2008) and assuming water saturated melts, it was possible to record a gradual increase in melt viscosity η of about one order of magnitude towards the less-differentiated terms (log η from 2.99 to 1.89 Pa s, Table 3).
Assuming a lithostatic system with an average crustal density of 2.5 g cm^{-3} we can convert the constrained storage pressure value of 1.05±0.22 kbar into a depth of the magma chamber top of about 4.29±0.91 km, from which more than 1.3 km^3 (0.34 and 0.96 km^3 of trachytic and latitic-shoshonitic magma respectively, Landi et al., 1999) of magmas have been erupted.

Sample	T (°C)	P (kbar)	Kd_{Fe-Mg}	Cl (wt.%)	P (kbar)(*)	H_2O (wt.%)(**)	Kd_{Or-Ab}	log η (Pa s)(***)
G10	917	-	0.12	0.71	0.76	5.37	0.45	2.91
G80	904	1.43	0.12	0.68	0.87	6.49	0.20	2.99
G160	931	1.43	0.21	0.55	1.32	-	-	2.71
N170	954	1.35	0.14	0.57	1.25	-	-	2.51
N200	972	2.01	0.32					2.54
S1	1023	1.66	0.19					2.07
F1	1052	1.18	0.09					1.89
average value	965	1.51		0.63	1.05	5.93		2.52
Error	55 [a]	0.29 [a]		0.06 [b]	0.22 [b]	0.79 [a]		0.41 [a]
Model	*Masotta et al. (2013)*			*Balcone Boissard et al. (2015)*		*Mollo et al. (2015)*		*Giordano et al. (2008)*

Table 3. Magmatic variables reconstructed using petrological models.
(*) Estimate made using Signorelli and Carroll (2002) experimental dataset; (**) temperature obtained using Masotta et al. (2013); (***) temperature obtained from Masotta et al. (2013) and saturation conditions (using Papale et al., 2006). [a] standard deviation; [b] considering an analytical uncertainty of 10% for Cl concentration.

Magma chamber evolution

Intensive and extensive variables obtained so far suggest the existence, at the time of Pomici di Base eruption, of a reservoir located in the crust at a pressure of about 1-1.5 kbar, including co-genetic chemically, thermally and rheologically zoned magmas generated by fractional crystallization processes. In order to test this hypothesis and to better understand the evolution of key magmatic variables we have performed isobaric fractional crystallization simulations by using alphaMELTS software (Smith and Asimov, 2005) combining sets of independent variables (i.e. T, P, magma composition, fO_2) and comparing measured and modeled melt and crystal compositions. Shoshonitic-trachybasaltic melt inclusions hosted in sub-effusive nodules emitted during PBE (Klebesz et al., 2015, Fig. 2) have been assumed as parental melts and used as starting composition (i.e. average compositions of the two lowest values of Mg#). Since Klebesz et al. (2015) estimated minimum storage pressures of 4 up to 3 kbar for these pre-PBE melts, we speculate that the magmatic evolution occurred in a multi-level plumbing system: a deeper less-differentiated reservoir (represented by melt inclusion compositions in nodules), and a shallower more-evolved chamber (represented by PBE juvenile compositions). To verify this hypothesis, we have performed two sets of simulations, changing pressure in a range between 5 to 1 kbar, initial H_2O concentration from 1 to 3 wt.% and the related CO_2 content (adopting the model of Papale et al., 2006 and assuming saturation conditions) and oxygen fugacity, varying both QMF and NNO from -1 to +3 (with a step of 0.5) buffers.

The best match between measured and calculated compositions (Fig. 3 and 4) has been obtained using as input parameters: P=4 kbar, T_i=1240 °C (i.e. liquidus temperature), fO_2=NNO + 1.5 (values of fO_2 compatible with those used by Mollo et al., 2015 and references therein), H_2O_i + CO_{2i}=1.5 + 0.375 wt.% for the first step in the deeper reservoir and P=1.5 kbar, T_i=1150 °C, fO_2=NNO + 1.5 for the second step in the shallower magmatic layer. These calculations validate our hypothesis and indicate crystal fractionation of about 25 (clinopyroxene >> olivine) and 60 wt.% (sanidine > clinopyroxene > plagioclase ≥ spinel) for the two sets of simulations respectively. Crystal phases reproduced by alphaMELTS are in general agreement with those measured in PBE

products. However the stability of Fe-rich spinel is overestimated (~10 wt.% of solid phase) resulting in a bad fitting of FeO concentrations. Moreover the plagioclase stability field, in particular for the An-rich members, is widely underestimated (Fig. 4) resulting in higher CaO and slightly lower alkalis modeled concentrations and thus a poor fit for the most-evolved terms in some Harker diagrams (Fig. 3).
In conclusion, it is noteworthy that these discrepancies between measured and predicted data for Campanian rocks have been previously observed by Fowler et al. (2007) and interpreted as being due to minor amounts of country-rock (skarn and foid-bearing syenite) assimilation during fractional crystallization. Moreover our obtained data seem to rule out the possibility that mixing events involved these magmas, in agreement with Landi et al. (1999), who also investigated trace elements.
Finally, alphaMELTS simulations show the occurrence of a pseudo-invariant temperature (T_{inv}, definition by Fowler et al., 2007) of ~930 °C, at which residual melt fraction (from ~0.6 to ~0.4) and some magma properties (e.g. dissolved/exolved water, viscosity, magma/melt density) abruptly change, possibly promoting magma eruptability and acting as eruption trigger mechanism. However the drastic increase in crystallization at this pseudo-invariant temperature is in disagreement with the low crystal contents (< 5 wt.%, see also Landi et al. 1999) observed in PBE deposits. We infer that this incongruity can be explained by a mechanism of magma extraction from a crystal-rich mush zone in the magma chamber (simulated crystallinity ≥ 60%, corresponding to the critical value for efficient melt extraction predicted by Bachmann et al., 2007 and references therein; see also Landi et al., 1999).

5.2. Role of crustal contamination

Assimilation and Fractional Crystallization
The obtained radiogenic and stable isotopic data (Fig. 5 and Table 2) support the evidence of a minor crustal contamination in the evolution of PBE magmas, previously invoked to justify several discrepancies between measured and modelled glasses for Campanian rocks (e.g. Fowler et al., 2007).
In fact, radiogenic isotopes show that clinopyroxenes, the first crystallizing phase (as recorded by microscopic textural features and alphaMELTS simulations results), have a narrow range of low Sr isotope ratios (0.707470 – 0.707500) and that the later-formed sanidines have higher Sr-isotope ratios (0.707499 – 0.707550), partially overlapped with those of the trachytic groundmass (0.707527 - 0.707556). Instead, all phenocrysts and groundmasses have almost constant values of Nd isotopic ratios (0.512428 - 0.512452). These features suggest that PBE magmas during fractional crystallization experienced assimilation (AFC) of Mesozoic carbonate, which is extended from 2 to ~10 km beneath the Somma-Vesuvius volcanic complex (see above for details), according to the constrained storage pressures. Mesozoic carbonate beneath Somma-Vesuvius are characterized by $^{87}Sr/^{86}Sr$ and $^{143}Nd/^{144}Nd$ values of 0.70729–0.70924 and 0.51201-0.51214 (Civetta et al 1991; Del Moro et al., 2001; Iannace, 1991; Iannace et al., 2011; Stille et al., 1996) as well as Sr and Nd average concentrations of 500 ppm and 10 ppm (Sr range: 100 – 1000 ppm from Civetta et al., 1991; Jolis et al., 2013 and Nd range = 1 – 50 ppm assumed from Bellanca et al., 1993), whereas PBE magmas have isotopic ratios measured in this study and an average Sr composition that ranges from about 600 ppm in trachytes to 1000 ppm in latites-shoshonites coupled with an almost constant Nd content of 50 ppm (Landi et al., 1999).
In order to test the plausibility of this contamination mechanism, several isenthalpic simulations have been performed with the EC-AFC (Energy-Constrained - Assimilation and Fractional Crystallization) model (Spera and Bohrson, 2001, Fig. 5a), constrained with data calculated in this study and available from the literature. Different simulations sets and results are summarized in Table 4 (see caption of Table 4 for more details). Almost all sets are able to roughly reproduce PBE isotopic evolution from a primitive melt to trachytic compositions with a contamination ≤ 10% of a

magma which has crystallized ≤ 60% of its initial mass. Best results have been obtained considering (Fig. 5a and Table 4): Triassic carbonate isotopic ratios ($^{87}Sr/^{86}Sr$ = 0.709, $^{143}Nd/^{144}Nd$ = 0.512; values typically used for Vesuvian AFC modeling, e.g. Di Renzo et al., 2007; Gebauer et al., 2014; Jolis et al., 2015; Piochi et al. 2006; compatible with global isotopic data, e.g. Iannace et al., 2011 and references therein); Sr and Nd average concentration (Sr = 500 ppm and Nd = 10 ppm); Sr incompatible (K_d ~ 1) and Nd compatible (K_d ~ 0.1) during carbonate melting; an initial wall-rock temperature of 300 °C (following De Lorenzo et al., 2006). In this conditions the Sr and Nd isotopic trend is justified by an assimilation of about 2.5% of a magma which has fractionated ~55% of its mass. These values are consistent with those obtained by Iacono-Marziano et al. (2008) to experimental simulate alkaline compositions similar to PBE. Moreover, we highlight that EC-AFC path is characterized by a sudden radiogenic isotopic variation once a temperature of about 985 °C was reached, quite comparable with the pseudo-invariant temperature obtained with our alphaMELTS simulations (~ 930 °C).

Input parameters				
Thermal parameters		***Compositional parameters***		
Tl,m (°C)	1200	*Element*	Sr	Nd
Tm0 (°C)	1200	*Magma conc.* (ppm)	1004	51
Tl,a (°C)	1000	*bulk D_m*	2.3	0.9
Ta0 limestone (°C)	300 and 600	*Isotopic ratio*	0.70747	0.51245
Ts (°C)	800	*Limestone conc.* (ppm)	100; **500**; 1000	1; **10**; 50
Teq (°C)	900	*bulk D_a*	0.1; 0.5; **1**	**0.1**; 0.5; 1
Cp,m (J kg-1 per K)	1484	*Isotopic ratio*	0.70777; **0.709**	0.51210; **0.512**
Cp,a (J kg-1 per K)	1370			
Δhcry (J kg-1)	396000			
Δhfus (J kg-1)	270000			
Output parameters				
Best fit simulations	*T inv* (°C)	*Magma T* (°C)	*Ma** (%)	*Mc* (%)
1	986	975	2.5 – 3.5	55
2	1050	1035	4.0 - 6.0	40

Table 4. Input and output data for EC-AFC simulations.
Simulations were performed using compositional parameters for Mesozoic carbonate bedrock assimilant (Sr and Nd average values of 500 and 5 ppm; Sr range = 100 – 1000 ppm and Nd range = 1 - 50 ppm; Bellanca et al., 1997; Civetta

et al. 1991; Jolis et al., 2013), assuming two sets of isotopic ratios: $^{87}Sr/^{86}Sr$ and $^{143}Nd/^{144}Nd$ average values for Mesozoic limestones (0.707770 and 0.51210; Civetta et al., 1991; Del Moro et al., 2001; Iannace, 1991; Iannace et al., 2011; Stille et al., 1996) and typical isotopic ratios of the Triassic limestones (0.709 and 0.512; Di Renzo et al., 2007; Piochi et al., 2006 according to Iannace, 1991; Iannace et al., 2011). Sr and Nd wall-rock partition coefficients have been changed from 0.1 to 1 (0.1, 0.5, 1). Magma composition, D_m are from Landi et al. (1999) database and applied with the method of Villemant et al. (1988) using the less differentiated latitic-shoshonitic average Sr and Nd content (1004 ppm and 51 ppm) and assuming the less Sr radiogenic clinopyroxene ($^{87}Sr/^{86}Sr$ = 0.707470, $^{143}Nd/^{144}Nd$ = 0.512452) in isotopic equilibrium with the primitive melts. For thermal parameters initial wall-rock temperatures of 300°C (following the thermal model developed by De Lorenzo et al., 2006 for pressure range constrained) and 600 °C (assumed) were used. Liquidus temperature were obtained from alphaMELTS, wall-rock solidus temperature from Lentz (1999) and Wenzel et al. (2002), and equilibrium temperature from this study and other parameters from Bohrson and Spera (2001).
Almost all simulations are able to reproduce the PBE isotopic evolution from a primitive melt to trachytic compositions with a contamination ≤ 10% of a magma that has crystallized ≤ 60% of its initial mass. Higher percentages of contaminant and crystallized mass are necessary only when carbonate with Sr content near the lower value of the reported range (100 ppm) is used.
Tl,m=magma liquidus T; *Tm0*=initial magma T; *Tl,a*=wallrock liquidus T; *Ta0*=initial wallrock T; *Ts*=wallrock solidus T; *Teq*=equilibration T between magma and assimilant; *Cp,m*=magma isobaric specific heat capacity; *Cp,a*=assimilant isobaric specific heat capacity; *hcry*= crystallization enthalpy; *hfus*=fusion enthalpy; *D*=bulk distribution coefficient
Best fit simulations are shown in Figure 5 and obtained with parameters reported in bold in the table at 300 and 600 °C (see text for further details).

A pure Assimilation and Fractional Crystallization?

The main limitation of a simple AFC model is that it cannot explain the anomalous high Sr isotopic ratios in the groundmasses of the less evolved (latitic-shoshonitic) rocks (0.707602 – 0.707615), in strong isotopic disequilibrium with their corresponding phenocrysts (0.707534) as well as trachytes phenocrysts (0.707470 - 0.707550) and matrix-glasses (0.707527 - 0.707556).
Moreover, combining Sr and oxygen isotopes (Fig. 6a), two different distributions can be observed for trachytic and latitic-shoshonitic liquids, indicating a more complex magma contamination possibly superimposed on the pure AFC. In detail, $\delta^{18}O$ sharply increases and $^{87}Sr/^{86}Sr$ slightly decreases in trachytes towards the lower-stratigraphic samples, while $\delta^{18}O$ is slightly positively correlated with radiogenic Sr in latitic-shoshonitic groundmasses. Taking into account the isotopic composition of the different rock types formed during the progressive magma-limestone country-rock interaction (from weakly-metamorphosed limestone-marble and exoskarn to highly metamorphosed endoskarn aureole) documented in Somma-Vesuvius past deposits (Fig. 6a) we can observe that: the former distribution described by trachytic liquids tends towards typical isotopic compositions of endoskarn aureole (i.e. representing the inner part of the interaction zone, more proximal to magmatic body), while the latter, described by the less-evolved groundmasses, tends towards limestone ($^{87}Sr/^{86}Sr$ = 0.709; $\delta^{18}O$ = 31‰, see Table 4 and Jolis et al., 2015), marble and exoskarn values (i.e. representing the outer part of the interaction zone).
To explain these Sr-O isotopic features we hypothesize two different stages of contamination: (i) A first pre-eruptive stage of interaction between the evolving magmas with the carbonatic host-rocks (i.e. AFC). The subsequent progressive precipitation of the main crystal phases and the formation of metasomatic aureoles, limited (e.g. for thermal barrier, skarn barrier, calcite saturation point) the assimilation of pure-limestone in favor of the growing skarn and/or related metasomatic fluids (Carter and Dasgupta, 2016; Dallai et al., 2011; Gaeta et al., 2009; Jolis et al., 2015; Kerrick, 1977; Watkinson and Wyllie, 1969; Fig. 6a). (ii) A superimposed syn-eruptive stage, during which contamination can be renewed with the outer part of the interaction zone, constituted mainly by pure-limestone, due to creation of fresh reaction surfaces as a consequence of tectono-volcanic activity (see below for details) accompanying the extrusion of the residual less-evolved hotter liquids (Fig. 6a and 6b).

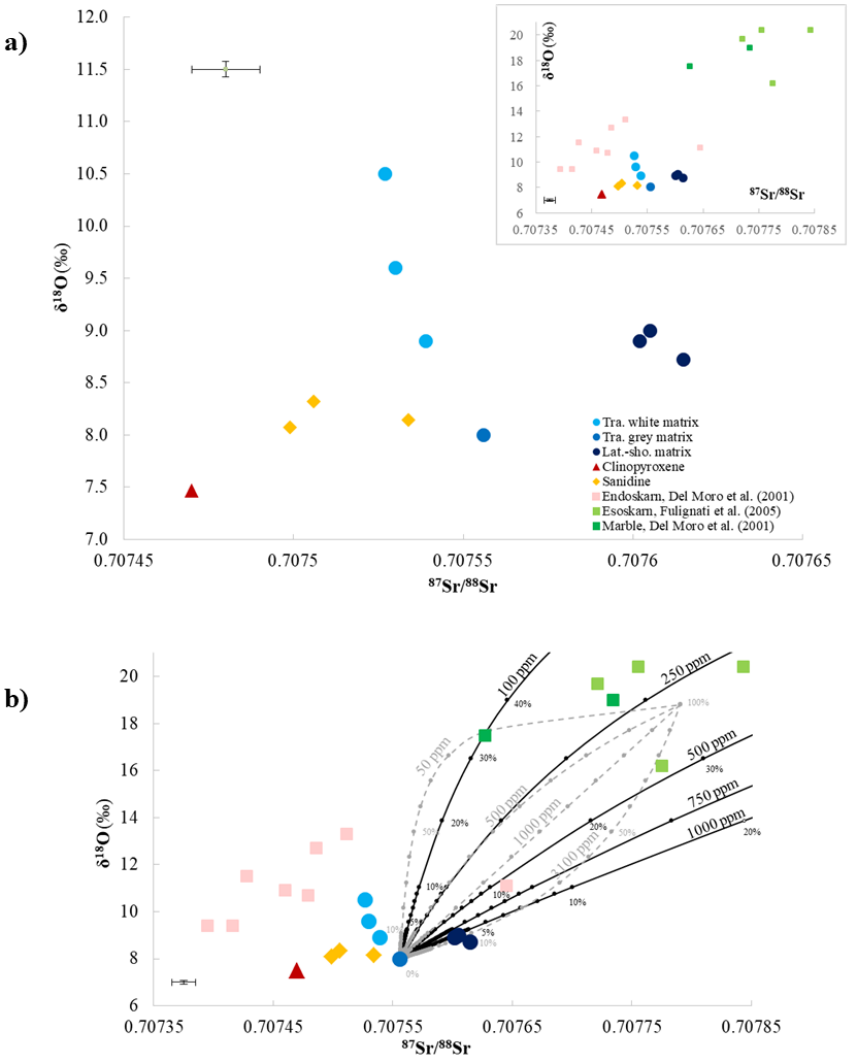

Fig. 6. a) Strontium vs. oxygen isotopes. Two different isotopic distributions are formed by trachytic and latitic-shoshonitic groundmasses. Insert: comparison between $^{87}Sr/^{86}Sr$ and $\delta^{18}O$ (‰) values in our samples and those of the Somma-Vesuvius "skarn environment" reported in the literature (Del Moro et al., 2001; Fulignati et al., 2005). Sanidine of black scoria fallout beds is referred to both N200 and S1 values. b) Curves of binary mixing between the less contaminated melt (sample N170; $^{87}Sr/^{86}Sr$ =0.70756; Sr=1004 ppm; $\delta^{18}O$=8 ‰; O=35 wt.%) and carbonate ($^{87}Sr/^{86}Sr$ =0.7079; $\delta^{18}O$ =31 ‰; O=48 wt.%; black lines) and esoskarn/marble (average values; $^{87}Sr/^{86}Sr$ =0.70779; $\delta^{18}O$ =35 ‰; O=35 wt.%; grey lines) varying Sr content in the range of literature data (carbonate: 100-1000 ppm, average value of 500 ppm; skarn/marble: 50-3100 ppm, average value of 500 ppm; Civetta et al., 1991; Jolis et al., 2013; 2015). See text and Table 4 for additional references. Best fits results for latitic-shoshonitic groundmasses results from mixing with 5% of carbonate or about 15% of esoskarn/marble with Sr content ≥ average value.

5.3. Late-stage carbonate assimilation: mechanism and timescale

Mechanism

We propose that a process of magmatic stoping (i.e. the formation and transport of host-rock pieces into magma bodies, e.g. Blatt et al., 2006; Glazner and Bartley, 2006; Winter, 2001) triggered by the progressive evolution of caldera collapse could have renewed the contamination between residual mafic melts in the emptying chamber with carbonate host-rocks (Fig. 7). Our hypothesis is in agreement with the observations on Somma-Vesuvius deposits of Cioni et al. (1999) suggesting that "As a consequence of the extensive fracturing of the roof rocks accompanying collapse of the magma chamber, many lithic clasts from the outer shell of the chamber and its apophysis (syenitic rocks, skarns and thermometamorphic limestone), as well as from the upper volcanic and

sedimentary pile, are generally found in these (plinian) deposits." Actually, this mechanism can be recorded in the increment of lithic content in the upper latitic-shoshonitic plinian deposit emplaced during the embryonic stage of the PBE caldera collapse (average values from 9 wt.% in U-2c to 19 wt.% and 36 wt.% in U-2d and U-2e, see Fig. 1a), as well as in the uppermost pheatomagmatic deposits (average lithics content values of 60-93 wt.%, data from Bertagnini et al., 1998) formed during the climaxing caldera-formation stage.
According to theoretical models, magma chamber emptying can produce pressure decrease towards a critical value in the reservoir (e.g. Martí et al., 2008 and references therein) and in the volcanic conduit (e.g. Aravena et al., 2017; Macedonio et al., 1994), thus promoting the destabilization of the whole plumbing system. The progressive cracking of the fresh and altered (by decarbonation and thermal microcracking; see Mollo et al., 2013) carbonate bedrocks allows magma contamination due to the production of CO_2-rich fluids and carbonate blocks. The skarn fragments (< 1 wt.%) found inside juvenile clasts of Pomici di Base plinian fallout by Landi et al. (1999) can represent the remnant portion of these ingested stoped blocks. While coarser blocks can sink towards the bottom of the magma chamber and possibly be simultaneously assimilated (using a simplified model of Stokes settling, a 1 m large fragment can sink for 100 m in few minutes also with a density contrast of only 100 kg m^{-3} in a magma with a viscosity of 10^2 Pa s).

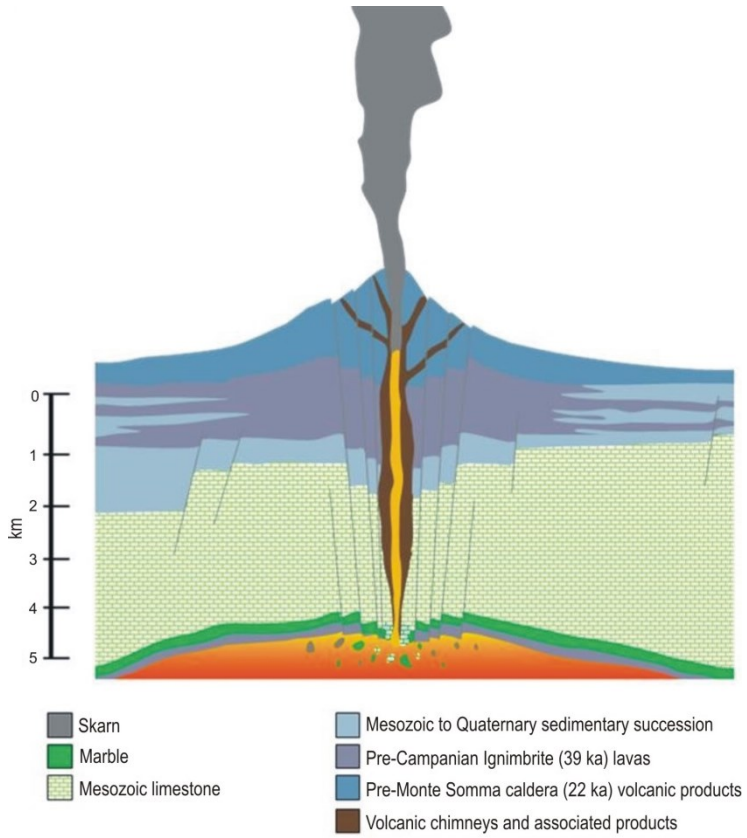

Fig. 7. Cross-section of Mt. Somma at the time of Pomici di Base eruption (22 ka) depicting the incipient caldera collapse due to chamber depressurization during the magma withdrawal, which was able to promote ingestion of carbonate stoped blocks by the residual magmatic liquids and rapid CO_2 liberation.

Timescale

In order to constrain the timescale of this contamination stage we quantified the time lapse needed to conductively heat above its solidus temperature (800 °C; see Table 4) a single (spherical, with a radius *a* from 1 cm to 1 m) carbonate fragment eventually trapped in the latitic-shoshonitic melts.

We started from the theory of heat conduction in solids, regulated by the equation $\nabla^2 T + \frac{q'}{K} = \frac{1}{k}\frac{\partial T}{\partial t}$, where T is the temperature, q' is the generated or consumed heat, K is thermal conductivity and k is thermal diffusivity (for carbonate: K = 1.5 J m^{-1} s^{-1} K^{-1} and k = 5.7 x 10-7 m^2 s^{-1} respectively; Vosteen and Schellschmidt, 2003), solved in spherical coordinates following Rosseel et al. (2006). We assumed homogeneous melt (T_l) and lithic (T_s) temperatures (selected initial latitic-shoshonitic melt temperature: 1050 °C, see Table 3; selected initial lithic temperature: 300-600 °C, see Table 4) and no heat addition or loss. Results (Fig. 8) show that magma can melt carbonate clasts with a radius of 1 cm at an initial T_s of 300 or 600 °C in less than 1 minute. Conversely when particles with a radius of 10 cm are involved, clast rim exceeds the solidus T after few tens of minutes or quite instantly in function of T_s (26.6 minutes or 1 second for T_s of 300 and 600 °C respectively), while the core only after about 1-1.5 hour (55 minutes and 93.3 minutes for 300 and 600 °C). Finally, blocks with a radius of 1 m reach the solidus T at their rim after few days (1.8 days for T_s=300 °C) or quite immediately (1 second for T_s=600 °C) while at their core after several days (6.5 days and 3.8 days for 300 and 600 °C). Instead, small variations of magma temperature (maximum 25 °C in our calculations) are observable in the area surrounding the lithic fragments.
Therefore our results suggest that this stage of assimilation can occur very quickly. Moreover, despite the simplified used model, the obtained timescales can be considered maximum values since potential effects of latent heat liberation during microlites crystallization and mass transfer (i.e. a continuous generation of fresh magma-lithic reaction surfaces by decarbonation of the clasts rim) have been neglected in the calculations as well as higher values of T_s have been inferred especially at the periphery of magma chamber (e.g. Fulignati et al., 2005; Mollo et al., 2013 and references therein).

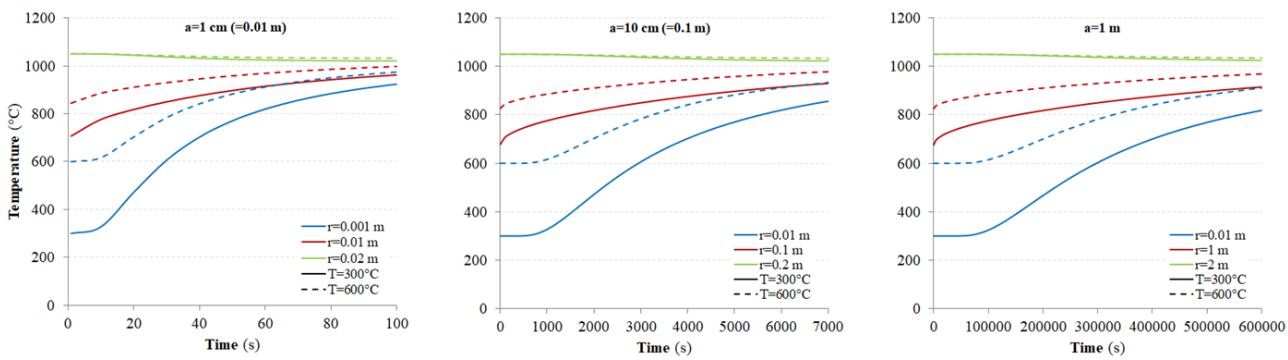

Fig. 8. Temporal temperature variations for conductive heat transfer of spherical carbonate fragments with a radius (a) of 1 cm, 10 cm and 1 m and an initial temperature of 300 °C and 600 °C (solid and dashed lines respectively; see Table 4) embedded in a magma with an initial temperature of 1050 °C (see Table 3). Results for several distances (r) from the clast core are shown, corresponding to: clast core (blue curves), clast rim (red curves), magma melts around the clast (green curves).

A similar timescale (from minutes to days for carbonate clasts with radius from 1 cm to 1 m) has been obtained estimating the calcite dissolution rate (1 x 10^{-3} cm s^{-1}) following Edwards and Russel (1998 and references therein; chemical potentials obtained with alphaMELTS and Berman, 1988 Thermodynamic Properties Calculator), starting from the reaction $CaCO_{3_{solid}} + 2SiO_{2_{melt}} \rightarrow CaSiO_{3_{melt}} + CO_{2\ fluid}$ for our less-evolved compositions.
Our calculated timescales are in agreement with decarbonation time lapse (from minutes to days) observed in several experimental studies (e.g. Blythe et al., 2015; Deegan et al., 2011) as well as clinopyroxene microlites crystallization time (3 h – 18 days) obtained by applying the crystal size distribution (CSD) theory on PBE samples (Pappalardo et al., 2018) using a wide range of growth

rate. The formation of these microcrystals from the latitic-shoshonitic magmas can be the combined effect of degassing-induced crystallization under open-system regime (Pappalardo et al., 2018) and carbonate assimilation, in agreement with the reaction $\mathrm{CaCO_{3}}_{solid} + \mathrm{MgO}_{melt} + 2\mathrm{SiO_{2}}_{melt} \rightarrow \mathrm{CaMgSi_2O_{6}}_{cpx} + \mathrm{CO_{2}}_{\ fluid}$ (Iacono-Marziano et al., 2008). Accordingly, clinopyroxene microlites show an average Ca content slightly higher than the corresponding phenocrysts (Fig. 4).
Finally, it is noteworthy that a comparable time range (hour to days) is necessary to reach the oxygen isotopic equilibrium between basaltic melts and CO_2 according to Dallai et al. (2011). These authors suggest in fact that CO_2 could act as a ^{18}O-rich decarbonation agent able to quickly promote a magma isotopic re-equilibrium without altering significantly other compositional parameters. Moreover, Jolis et al. (2013) reported fast timescale (minutes) necessary for Sr isotope re-equilibrium during experiments of Vesuvian mafic magma-carbonate interaction.

6. Conclusions and implications

Our study on caldera-forming Pomici di Base eruption case study shows that:
(i) Pomici di Base plinian eruption, the first and largest of the four caldera-forming Somma-Vesuvius events, was fed by a chemically (from trachyte to latite-shoshonite), thermally (from ~900 to 1050 °C) and rheologically (from ~1000 to 100 Pa s) zoned shallow (~4.5 km) magma chamber, likely supplied by deep (~16 km) trachybasaltic liquids. Primitive magmas were subjected to progressive AFC (carbonate assimilation and fractional crystallization) process producing metasomatized skarn aureole during magma chamber evolution, until eruptible state has been reached.
(ii) The plinian phase began with the rapid withdrawal of microlite-free and highly-vesicular upper trachytic magmas generating an incipient caldera collapse due to chamber depressurization. This mechanism possibly promoted a pervasive destabilization of the plumbing system, providing hot stoped blocks (i.e. decarbonated limestone and metasomized skarns) and CO_2-rich fluids from renewed outer sectors of the magma-limestone interaction zone. The consequent fast release of CO_2 enhanced the degassing and explosivity of the mafic residual magmas. The concurrent occurrence of massive volatile exolution and degassing-induced microlites precipitation under open-system degassing regime (Pappalardo et al., 2018), caused a rapid change of magma rheological properties and in turn favoured fragmentation.
In conclusion, we propose that magmatic stoping during caldera collapse evolution involving plumbing systems developed in carbonate bedrocks (e.g. Campi Flegrei, Colli Albani Volcanic District, Etna, Merapi, Nisyros, Popocatépetl) can be the source of large amount of CO_2 liberation then acting as a fuel of eruption explosivity. In fact, this rapid mechanism can promote CO_2 bubble nucleation, reduction of water solubility favouring H_2O exolution and decrease in melt density increasing magma buoyancy with severe effects on magma ascent (Blythe et al., 2015; Dallai et al., 2011; Freda et al., 2011; Pappalardo et al. 2018). The subsequent high mass discharge rates can avoid/postpone critical mechanical instabilities in the conduit (Aravena et al., 2017) and create plinian phases with long-lasting sustained plumes.

Acknowledgements

The authors wish to acknowledge I. Arienzo (INGV-OV), M. Nazzarini (INGV-Rome), R. de Gennaro (University of Naples Federico II) for their crucial helps during radiogenic isotopes and geochemical analyses. We thank Sherissa Roopnarain for help with the O-isotope analyses.

Supplementary material

Glass

	G10_1	G10_2	G10_3	G10_4	G10_5	G10_6	G10_7	G10_8	G80_1	G80_2	G80_3	G80_4	G80_5	G80_6	G80_7	G80_8	G160_1	G160_2	G160_3
SiO_2	62.04	61.79	61.74	61.79	61.26	61.36	61.64	61.81	61.95	60.86	61.86	63.10	62.24	60.30	60.68	61.74	58.98	60.17	59.49
TiO_2	0.31	0.40	0.32	0.29	0.34	0.31	0.29	0.35	0.32	0.29	0.31	0.30	0.16	0.34	0.34	0.27	0.26	0.43	0.34
Al_2O_3	17.47	17.73	17.86	17.75	17.54	17.50	17.62	17.77	17.42	17.31	17.70	17.54	17.56	17.42	17.04	17.27	17.59	18.11	17.87
FeO_{tot}	2.51	2.57	2.48	2.70	2.62	2.67	2.62	2.28	2.53	2.59	2.62	2.57	2.40	2.53	2.72	2.72	3.17	3.34	3.13
MnO	0.22	0.20	0.14	0.16	0.19	0.17	0.10	0.18	0.06	0.15	0.15	0.20	0.07	0.23	0.14	0.17	0.08	0.18	0.19
MgO	0.22	0.22	0.26	0.25	0.27	0.27	0.25	0.22	0.26	0.22	0.25	0.23	0.20	0.26	0.27	0.29	0.47	0.45	0.46
CaO	2.47	2.42	2.45	2.53	2.52	2.55	2.42	2.56	2.56	2.71	2.57	2.68	2.79	2.57	2.72	2.72	3.19	3.40	3.44
Na_2O	4.26	4.35	4.36	4.49	4.38	4.35	4.25	4.43	4.10	3.73	4.05	3.99	3.86	3.85	4.38	2.64	3.85	3.96	3.84
K_2O	8.42	8.42	7.95	8.43	8.24	8.00	8.15	8.06	8.12	8.26	8.14	8.35	8.20	7.78	8.27	8.06	7.90	8.32	7.94
P_2O_5	0.08	0.03	0.03	0.09	0.08	0.00	0.13	0.07	0.00	0.10	0.12	0.03	0.07	0.01	0.00	0.02	0.18	0.17	0.05
Cl	0.71	0.70	0.67	0.72	0.73	0.70	0.69	0.74	0.68	0.66	0.65	0.69	0.68	0.69	0.71	0.66	0.55	0.55	0.49
F	0.18	0.26	0.29	0.20	0.27	0.25	0.26	0.19	0.18	0.12	0.14	0.25	0.30	0.24	0.21	0.28	0.25	0.17	0.21
SO_3	0.00	0.04	0.00	0.00	0.02	0.00	0.01	0.01	0.04	0.03	0.00	0.03	0.00	0.03	0.01	0.00	0.03	0.04	0.02
Tot.	98.89	99.12	98.55	99.39	98.45	98.13	98.43	98.66	98.21	97.03	98.56	99.95	98.53	96.23	97.48	96.85	96.51	99.28	97.48
H_2O*	1.11	0.88	1.45	0.61	1.55	1.87	1.57	1.34	1.79	2.97	1.44	0.05	1.47	3.77	2.52	3.15	3.49	0.72	2.52

	G160_4	G160_5	G160_6	G160_7	G160_8	G160_9	N170_1	N170_2	N170_3	N170_4	N170_5	N170_6	N170_7	N170_8	N200_1	N200_2	N200_3	N200_4	N200_5
SiO_2	61.85	59.62	59.69	60.69	60.18	59.43	60.81	60.45	60.87	59.96	60.43	60.87	58.54	60.03	56.68	57.25	56.50	58.78	58.27
TiO_2	0.39	0.38	0.35	0.37	0.27	0.38	0.44	0.29	0.39	0.40	0.31	0.42	0.45	0.42	0.66	0.68	0.55	0.46	0.41
Al_2O_3	17.25	17.41	17.74	17.67	17.40	17.38	17.50	17.64	17.55	17.71	17.74	17.87	17.83	17.94	18.18	18.06	17.93	18.55	18.56
FeO_{tot}	3.05	3.28	3.52	3.27	3.10	3.21	3.35	3.00	3.15	3.28	3.06	3.21	3.42	3.19	5.23	4.59	4.85	4.36	5.07
MnO	0.17	0.14	0.18	0.19	0.08	0.14	0.05	0.14	0.15	0.19	0.09	0.15	0.10	0.08	0.18	0.15	0.15	0.15	0.24
MgO	0.45	0.49	0.53	0.41	0.43	0.48	0.45	0.39	0.45	0.53	0.42	0.50	0.51	0.47	1.44	1.12	1.21	0.80	0.83
CaO	3.27	3.16	3.01	3.37	3.22	3.33	3.28	2.86	3.27	3.17	3.22	3.29	3.18	3.39	4.54	4.57	4.61	5.21	4.76
Na_2O	3.63	4.14	4.02	4.24	3.72	3.63	4.32	3.63	4.08	4.01	4.30	3.98	3.81	3.89	3.24	3.42	3.37	3.26	3.05
K_2O	8.50	8.30	9.00	8.84	8.57	8.31	8.79	8.82	8.59	8.08	8.55	8.46	8.41	8.61	7.86	7.86	7.74	7.50	7.59
P_2O_5	0.09	0.17	0.12	0.12	0.01	0.13	0.05	0.11	0.09	0.08	0.06	0.12	0.09	0.10	0.23	0.25	0.24	0.33	0.32
Cl	0.51	0.57	0.60	0.55	0.56	0.56	0.56	0.46	0.60	0.60	0.59	0.58	0.61	0.56	0.53	0.50	0.50	0.49	0.61
F	0.17	0.15	0.21	0.19	0.16	0.28	0.23	0.14	0.23	0.18	0.12	0.30	0.19	0.06	0.28	0.09	0.15	0.00	0.20
SO_3	0.00	0.04	0.04	0.02	0.02	0.05	0.00	0.01	0.02	0.04	0.01	0.00	0.00	0.02	0.04	0.06	0.06	0.03	0.01
Tot.	99.34	97.84	99.02	99.93	97.72	97.31	99.83	97.94	99.44	98.23	98.90	99.75	97.14	98.75	99.10	98.60	97.86	99.93	99.92
H_2O*	0.66	2.16	0.98	0.07	2.28	2.69	0.17	2.06	0.56	1.77	1.10	0.25	2.86	1.25	0.90	1.40	2.14	0.07	0.08

	N200_6	N200_7	N200_8	N200_9	N200_10	S1_1	S1_2	S1_3	S1_4	F1_1	F1_2	F1_3	F1_4	F1_5	F1_6	F1_7	F1_8	F1_9	F1_10
SiO_2	57.31	57.18	57.80	56.17	56.46	55.26	53.05	55.54	54.84	55.52	55.59	56.80	56.18	55.95	55.92	54.97	55.79	54.97	55.49
TiO_2	0.50	0.54	0.55	0.52	0.43	0.67	0.97	0.52	0.70	0.56	0.67	0.77	0.67	0.76	0.64	0.77	0.72	0.89	0.69
Al_2O_3	18.37	18.28	18.46	18.01	18.41	17.07	15.92	17.75	17.56	17.94	17.11	17.16	17.21	16.97	17.05	17.12	17.09	16.71	16.37
FeO_{tot}	4.72	4.79	4.33	4.62	4.52	7.60	8.49	6.26	6.70	5.95	7.60	7.41	7.48	8.32	8.38	8.50	8.03	8.09	9.36
MnO	0.15	0.10	0.16	0.12	0.12	0.19	0.16	0.25	0.13	0.13	0.24	0.14	0.16	0.29	0.22	0.22	0.30	0.21	0.33
MgO	0.93	0.92	0.67	0.92	0.72	1.39	2.23	1.09	1.33	1.24	1.41	1.20	1.34	1.39	1.38	1.36	1.23	1.70	1.40
CaO	4.79	4.72	4.75	4.94	4.83	4.26	6.43	4.11	5.81	4.50	4.14	3.69	3.74	3.62	3.46	3.52	4.54	4.85	3.39
Na_2O	3.48	3.51	3.34	3.37	3.11	3.18	2.87	3.46	3.26	3.68	3.84	3.11	3.94	3.60	3.28	3.39	2.84	3.61	3.22
K_2O	7.69	7.76	7.72	7.82	7.40	7.65	7.18	7.75	7.40	7.42	6.81	7.29	7.33	7.16	7.28	7.21	6.71	6.67	7.34
P_2O_5	0.37	0.38	0.33	0.34	0.30	0.49	0.58	0.51	0.94	0.33	0.46	0.55	0.67	0.66	0.53	0.71	0.53	0.35	0.53
Cl	0.54	0.59	0.48	0.53	0.64	0.59	0.60	0.67	0.60	0.43	0.57	0.55	0.66	0.72	0.71	0.69	0.77	0.61	0.67
F	0.21	0.17	0.15	0.23	0.22	0.16	0.30	0.20	0.18	0.34	0.27	0.39	0.28	0.31	0.31	0.39	0.22	0.29	0.33
SO_3	0.05	0.06	0.01	0.05	0.05	0.02	0.03	0.02	0.07	0.02	0.03	0.03	0.04	0.03	0.04	0.03	0.03	0.04	0.04
Tot.	99.12	99.01	98.75	97.63	97.21	98.52	98.81	98.13	99.52	98.06	98.75	99.09	99.69	99.76	99.20	98.87	98.80	98.98	99.15
H_2O*	0.88	0.99	1.25	2.37	2.79	1.48	1.19	1.87	0.48	1.94	1.25	0.91	0.31	0.24	0.80	1.13	1.20	1.02	0.85

Clinopyroxene

	G10_1	G10_2	G80_1	G80_2	G80_3	G80_4	G80_5	G160_1	N170_1	N170_2	N170_3	N170_4	N200_1	N200_2	N200_3	N200_4	N200_5	N200_6	N200_7	N200_8	N200_9
																microlite	*Microlite*	*microlite*	*Microlite*	*microlite*	*microlite*
SiO_2	49.38	47.36	44.45	42.94	48.57	44.17	48.43	47.71	46.67	47.02	47.30	46.61	41.26	46.29	41.59	42.77	42.92	43.33	43.79	47.97	49.48
TiO_2	0.58	0.83	2.16	2.02	0.73	1.11	0.66	1.02	0.50	1.17	1.39	1.01	2.21	1.02	1.30	1.48	1.28	1.84	1.76	0.67	1.19
Al_2O_3	3.49	5.05	8.59	9.89	4.49	8.23	3.99	5.55	5.01	6.59	5.79	4.97	9.81	7.09	10.37	11.29	11.70	8.46	10.74	13.30	13.68
FeO_{tot}	12.37	13.26	13.08	11.28	10.93	14.94	11.83	13.34	12.94	7.97	9.19	13.63	16.45	10.69	15.26	14.28	13.73	13.32	12.41	10.84	10.25
MnO	0.50	0.64	0.22	0.27	0.18	1.17	0.10	0.50	0.88	0.10	0.06	0.40	0.22	0.44	0.23	0.12	0.49	0.56	0.38	0.31	0.27
MgO	10.03	9.52	9.03	9.28	11.17	6.51	11.32	9.20	10.25	13.38	13.11	9.84	6.64	11.73	8.22	7.84	7.49	9.11	8.25	5.75	4.99
CaO	23.45	23.24	22.08	24.03	23.38	22.76	23.36	22.28	23.11	23.31	22.85	23.09	23.10	22.58	22.60	21.63	21.89	23.15	22.18	17.99	14.71
Na_2O	0.16	0.09	0.31	0.29	0.55	1.11	0.30	0.39	0.64	0.46	0.32	0.45	0.31	0.17	0.42	0.59	0.51	0.23	0.49	1.09	1.79
K_2O	0.03	0.00	0.08	0.00	0.00	0.00	0.00	0.00	0.00	0.00	0.00	0.00	0.00	0.00	0.00	0.00	0.00	0.00	0.00	2.09	3.63

	S1_1	S1_2	S1_3	S1_4	S1_5	S1_6	S1_7	S1_8	S1_9	S1_10	S1_11	S1_12	S1_13	F1_1	F1_2	F1_3	F1_4	F1_5
							microlite	*microlite*	*microlite*	*microlite*	*microlite*	*microlite*	*microlite*				*microlite*	*microlite*
SiO_2	46.63	46.90	50.49	50.77	44.67	44.70	45.07	43.56	45.02	43.40	42.56	43.16	45.32	48.42	47.94	50.45	44.11	45.09
TiO_2	1.54	2.15	0.97	0.80	1.13	1.46	1.91	1.41	2.38	2.23	2.38	1.61	1.46	1.54	1.24	0.81	1.40	1.44
Al_2O_3	5.94	5.95	3.42	2.93	8.06	8.03	9.58	9.83	8.08	10.12	9.87	10.10	7.43	5.24	6.64	4.16	9.69	8.67
FeO_{tot}	9.74	10.92	8.47	11.51	13.64	13.20	11.24	11.40	11.29	11.71	11.92	12.29	11.91	7.86	6.94	6.34	11.89	11.24
MnO	0.79	0.00	0.16	0.10	0.28	0.08	0.21	0.29	0.08	0.10	0.26	0.39	0.69	0.10	0.00	0.10	0.00	0.22
MgO	12.56	11.65	15.20	11.55	9.33	9.54	10.02	9.66	11.03	9.87	10.06	9.71	10.84	13.45	13.77	14.95	9.80	10.10
CaO	22.64	21.89	21.08	21.73	22.61	22.94	21.12	23.23	21.51	22.27	22.83	22.35	21.96	22.98	23.02	22.82	22.56	22.68
Na_2O	0.15	0.53	0.20	0.61	0.28	0.05	0.33	0.56	0.32	0.30	0.13	0.39	0.38	0.40	0.42	0.34	0.37	0.34
K_2O	0.00	0.00	0.00	0.00	0.00	0.00	0.52	0.06	0.29	0.00	0.00	0.00	0.00	0.00	0.03	0.02	0.18	0.22

Feldspar

	G10_1	G10_2	G10_3	G10_4	G10_5	G10_6	G80_1	G80_2	G80_3	G80_4	G80_5	G80_6	G80_7	G80_8	G160_1	G160_2	G160_3	G160_4	N170_1	N170_2	N170_3	N170_4
	Pl	Pl	pl	Pl	Pl	sn	Pl	pl	pl	Pl	pl	pl	pl	sn	pl	pl	pl	pl	Pl	Pl	pl	Pl
SiO_2	54.39	52.45	47.87	53.71	54.45	64.39	52.36	48.62	54.35	52.86	54.60	45.91	51.49	63.61	50.08	53.05	49.69	49.60	50.87	50.41	51.65	53.55
TiO_2	0.00	0.00	0.43	0.18	0.00	0.00	0.13	0.00	0.00	0.00	0.00	0.00	0.00	0.00	0.09	0.00	0.14	0.00	0.00	0.08	0.25	0.00
Al_2O_3	29.20	30.23	33.01	29.10	28.76	19.39	29.48	32.36	28.79	29.34	28.40	34.20	30.07	18.64	31.77	30.03	31.89	31.58	31.56	31.58	30.45	29.31
FeO_{tot}	0.25	0.57	0.41	0.47	0.51	0.15	0.77	0.31	0.15	0.65	0.33	0.37	0.62	0.00	0.27	0.47	0.96	0.75	0.41	0.75	0.41	0.59
MnO	0.00	0.00	0.00	0.00	0.00	0.07	0.16	0.00	0.00	0.00	0.00	0.00	0.00	0.00	0.00	0.00	0.00	0.26	0.00	0.00	0.00	0.03
MgO	0.00	0.13	0.05	0.12	0.00	0.03	0.00	0.00	0.00	0.00	0.00	0.00	0.00	0.00	0.00	0.05	0.00	0.16	0.26	0.00	0.00	0.00
CaO	11.44	12.19	16.29	11.73	11.04	0.53	12.76	15.85	11.27	12.04	10.87	17.85	12.87	0.33	14.93	11.69	14.41	14.92	13.73	13.86	13.23	12.46
Na_2O	3.86	3.77	1.72	3.99	4.37	1.59	3.69	2.55	4.32	4.24	4.60	1.58	2.93	0.90	2.48	3.65	2.41	2.35	2.82	2.84	3.35	3.50
K_2O	0.87	0.66	0.22	0.70	0.87	13.85	0.66	0.31	1.12	0.88	1.21	0.09	2.02	16.52	0.40	1.06	0.51	0.38	0.35	0.48	0.67	0.55

	N200_1	N200_2	S1_1	S1_2	S1_3	S1_4	S1_5	S1_6	S1_7	S1_8	S1_9	S1_10	S1_11	S1_12	S1_13	F1_1	F1_2	F1_3	F1_4	F1_5	F1_6
										microlite	*microlite*	*microlite*	*microlite*	*microlite*	*microlite*			*microlite*	*microlite*	*microlite*	*Microlite*
	Pl	Pl	Pl	Pl	pl	pl	Pl	sn	sn	Pl	pl	pl	pl	pl	pl	pl	sn	pl	pl	Pl	Pl
SiO_2	47.41	52.35	47.69	51.93	48.43	51.38	51.78	63.03	63.13	50.62	55.31	50.79	50.23	51.90	51.68	53.64	64.86	52.79	51.43	53.21	53.05
TiO_2	0.30	0.00	0.09	0.00	0.00	0.00	0.00	0.00	0.00	0.00	0.00	0.00	0.00	0.00	0.00	0.05	0.00	0.44	0.13	0.00	0.00
Al_2O_3	32.85	29.38	32.26	29.54	10.24	29.96	29.14	21.02	21.31	30.32	27.89	30.23	30.26	28.80	29.27	27.92	19.35	28.06	29.33	27.38	28.19
FeO_{tot}	1.03	0.50	1.08	1.06	15.15	0.99	1.05	0.09	0.36	1.18	0.18	0.66	1.38	1.86	1.30	0.77	0.18	0.95	1.02	1.67	1.45
MnO	0.25	0.00	0.00	0.00	0.00	0.00	0.00	0.00	0.00	0.00	0.00	0.00	0.00	0.00	0.00	0.00	0.00	0.00	0.19	0.00	0.14
MgO	0.00	0.00	0.14	0.00	0.00	0.00	0.00	0.00	0.00	0.00	0.00	0.00	0.00	0.00	0.00	0.20	0.00	0.27	0.17	0.31	0.08
CaO	15.84	13.01	15.95	12.80	25.13	12.74	13.70	1.89	1.33	13.61	10.44	14.02	13.97	12.05	13.03	11.52	0.52	12.15	13.30	11.40	11.94
Na_2O	1.91	3.86	2.07	4.28	0.94	3.66	3.19	3.99	4.32	3.14	5.17	3.15	2.81	3.30	3.43	4.02	3.46	3.86	3.31	3.88	3.28
K_2O	0.41	0.90	0.71	0.39	0.11	1.27	1.15	9.99	9.55	1.13	1.03	1.15	1.34	2.09	1.29	1.89	11.62	1.49	1.12	2.16	1.86

Table S1. Glass and crystal (phenocrysts and microlites) composition.
Values in wt.%. * H_2O by difference. pl = plagioclase, sn = sanidine.

References

Aravena, A., de' Michieli Vitturi, M., Cioni, R., Neri, A., 2017. Stability of volcanic conduits during explosive eruptions. Journal of Volcanology and Geothermal Research 339, 52–62. https://doi.org/10.1016/j.jvolgeores.2017.05.003

Bachmann, O., Miller, C.F., de Silva, S.L., 2007. The volcanic-plutonic connection as a stage for understanding crustal magmatism. Journal of Volcanology and Geothermal Research 167, 1–23. https://doi.org/10.1016/j.jvolgeores.2007.08.002

Balcone-Boissard, H., Boudon, G., Cioni, R., Webster, J.D., Zdanowicz, G., Orsi, G., Civetta, L., 2016. Chlorine as a geobarometer for alkaline magmas: Evidence from a systematic study of the eruptions of Mount Somma-Vesuvius. Scientific Reports 6, 21726. https://doi.org/10.1038/srep21726

Bellanca, A., Masetti, D., Neri, R., 1997. Rare earth elements in limestone/marlstone couplets from the Albian-Cenomanian Cismon section (Venetian region, northern Italy): Assessing REE sensitivity to environmental changes. Chemical Geology 141, 141–152. https://doi.org/10.1016/S0009-2541(97)00058-2

Berman, R.G., 1988. Internally-Consistent Thermodynamic Data for Minerals in the System Na_2O-K_2O-CaO-MgO-FeO-Fe_2O_3-Al_2O_3-SiO_2-TiO_2-H2O-CO_2. Journal of Petrology 29, 445–522. https://doi.org/10.1093/petrology/29.2.445

Bertagnini, A., Landi, P., Rosi, M., Vigliargio, A., 1998. The Pomici di Base plinian eruption of Somma-Vesuvius. Journal of Volcanology and Geothermal Research 83, 219–239. https://doi.org/10.1016/S0377-0273(98)00025-0

Blatt, H., Tracy, R.J., Owens, B.E., 2006. Petrology: Igneous, Sedementary and Metamorphic, third ed. W.H. Freeman and Company, New York

Blundy, J.D., Cashman, K. V., 2008. Petrologic Reconstruction of Magmatic System Variables and Processes. Reviews in Mineralogy and Geochemistry 69, 179–239. https://doi.org/10.2138/rmg.2008.69.6

Blythe, L.S., Deegan, F.M., Freda, C., Jolis, E.M., Masotta, M., Misiti, V., Taddeucci, J., Troll, V.R., 2015. CO_2 bubble generation and migration during magma–carbonate interaction. Contributions to Mineralogy and Petrology 169, 1–16. https://doi.org/10.1007/s00410-015-1137-4

Bohrson, W.A., Spera, F.J., 2001. Energy-Constrained Open-System Magmatic Processes II: Application of Energy-Constrained Assimilation-Fractional Crystallization (EC-AFC) Model to Magmatic Systems. Journal of Petrology 42, 1019–1041. https://doi.org/10.1093/petrology/42.5.1019

Borisova, A.Y., Martel, C., Gouy, S., Pratomo, I., Sumarti, S., Toutain, J., Bindeman, I.N., de Parseval, P., Metaxian, J., Surono, 2013. Highly explosive 2010 Merapi eruption: Evidence for shallow-level crustal assimilation and hybrid fluid. Journal of Volcanology and Geothermal Research 261, 193–208. https://doi.org/10.1016/j.jvolgeores.2012.11.002

Brocchini, D., Principe, C., Castradori, D., Laurenzi, M.A., Gorla, L., 2001. Quaternary evolution of the southern sector of the Campanian Plain and early Somma-Vesuvius activity: Insights from the Trecase 1 well. Mineralogy and Petrology 73, 67–91. https://doi.org/10.1007/s007100170011

Buono, G., Pappalardo, L., Petrosino, P., 2019. Magma storage and ascent during the largest eruption of Somma-Vesuvius volcano: Pomici di Base (22 ka) plinian event. Bollettino Di Geofisica Teorica e Applicata, in press.

Carr, B.B., Clarke, A.B., de' Michieli Vitturi, M., 2018. Earthquake induced variations in extrusion rate: A numerical modeling approach to the 2006 eruption of Merapi Volcano (Indonesia). Earth and Planetary Science Letters 482, 377–387. https://doi.org/10.1016/j.epsl.2017.11.019

Carter, L.B., Dasgupta, R., 2016. Effect of melt composition on crustal carbonate assimilation: Implications for the transition from calcite consumption to skarnification and associated CO_2 degassing. Geochemistry, Geophysics, Geosystems 17, 3893–3916. https://doi.org/10.1002/2016GC006444

Cassidy, M., Manga, M., Cashman, K. V., Bachmann, O., 2018. Controls on explosive-effusive volcanic eruption styles. Nature Communications 9, 2839. https://doi.org/10.1038/s41467-018-05293-3

Chadwick, J.P., Troll, V.R., Ginibre, C., Morgan, D.J., Gertisser, R., Waight, T.E., Davidson, J.P., 2007. Carbonate assimilation at Merapi Volcano, Java, Indonesia: Insights from crystal isotope stratigraphy. Journal of Petrology 48, 1793–1812. https://doi.org/10.1093/petrology/egm038

Cioni, R., Santacroce, R., Sbrana, A., 1999. Pyroclastic deposits as a guide for reconstructing the multi-stage evolution of the Somma-Vesuvius Caldera. Bulletin of Volcanology 61, 207–222. https://doi.org/10.1007/s004450050272

Cioni, R., Pistolesi, M., & Rosi, M. (2015). Plinian and Subplinian Eruptions, in: Sigurdsson, H., Houghton, B., McNutt, S. R., Rymer, H., Stix, J. (Eds.), The Encyclopedia of Volcanoes (Second Edition). Academic Press, London, pp. 519–535. https://doi.org/10.1016/b978-0-12-385938-9.00029-8

Civetta, L., Galati, R., Santacroce, R., 1991. Magma mixing and convective compositional layering within the Vesuvius magma chamber. Bulletin of Volcanology 53, 287–300. https://doi.org/10.1007/BF00414525

Cross, J.K., Tomlinson, E.L., Giordano, G., Smith, V.C., De Benedetti, A.A., Roberge, J., Manning, C.J., Wulf, S., Menzies, M.A., 2014. High level triggers for explosive mafic volcanism: Albano Maar, Italy. Lithos 190–191, 137–153. https://doi.org/10.1016/j.lithos.2013.11.001

Dallai, L., Cioni, R., Boschi, C., D'Oriano, C., 2011. Carbonate-derived CO_2 purging magma at depth: Influence on the eruptive activity of Somma-Vesuvius, Italy. Earth and Planetary Science Letters 310, 84–95. https://doi.org/10.1016/j.epsl.2011.07.013

De Lorenzo, S., Di Renzo, V., Civetta, L., D'Antonio, M., Gasparini, P., 2006. Thermal model of the Vesuvius magma chamber. Geophysical Research Letters 33, L17302. https://doi.org/10.1029/2006GL026587

De Natale, G., Troise, C., Pingue, F., Mastrolorenzo, G., Pappalardo, L., 2006. The Somma-Vesuvius volcano (Southern Italy): Structure, dynamics and hazard evaluation. Earth-Science Reviews 74, 73–111. https://doi.org/10.1016/j.earscirev.2005.08.001

Del Moro, A., Fulignati, P., Marianelli, P., Sbrana, A., 2001. Magma contamination by direct wall rock interaction: Constraints from xenoliths from the walls of a carbonate-hosted magma chamber (Vesuvius 1944 eruption). Journal of Volcanology and Geothermal Research 112, 15–24. https://doi.org/10.1016/S0377-0273(01)00231-1

Deegan, F.M., Troll, V.R., Freda, C., Misiti, V., Chadwick, J.P., McLeod, C.L., Davidson, J.P., 2010. Magma-carbonate interaction processes and associated CO_2 release at Merapi volcano, Indonesia: Insights from experimental petrology. Journal of Petrology 51, 1027–1051. https://doi.org/10.1093/petrology/egq010

Deegan, F.M., Troll, V.R., Freda, C., Misiti, V., Chadwick, J.P., 2011. Fast and furious: Crustal CO_2 release at Merapi volcano, Indonesia. Geology Today 27, 63–64. https://doi.org/10.1111/j.1365-2451.2011.00785.x

Di Renzo, V., Di Vito, M.A., Arienzo, I., Carandente, A., Civetta, L., D'Antonio, M., Giordano, F., Orsi, G., Tonarini, S., 2007. Magmatic history of Somma-Vesuvius on the basis of new geochemical and isotopic data from a deep borehole (Camaldoli della Torre). Journal of Petrology 48, 753–784. https://doi.org/10.1093/petrology/egl081

Edwards, B.R., Russell, J.K., 1998. Time scales of magmatic processes: New insights from dynamic models for magmatic assimilation. Geology 26, 1103–1106. https://doi.org/10.1130/0091-7613(1998)026<1103:TSOMPN>2.3.CO;2

Fowler, S.J., Spera, F.J., Bohrson, W.A., Belkin, H.E., De Vivo, B., 2007. Phase equilibria constraints on the chemical and physical evolution of the campanian ignimbrite. Journal of Petrology 48, 459–493. https://doi.org/10.1093/petrology/egl068

Freda, C., Gaeta, M., Giaccio, B., Marra, F., Palladino, D.M., Scarlato, P., Sottili, G., 2011. CO_2-driven large mafic explosive eruptions: The Pozzolane Rosse case study from the Colli Albani Volcanic District (Italy). Bulletin of Volcanology 73, 241–256. https://doi.org/10.1007/s00445-010-0406-3

Fulignati, P., Panichi, C., Sbrana, A., Caliro, S., Gioncada, A., Del Moro, A., 2005. Skarn formation at the walls of the 79AD magma chamber of Vesuvius (Italy): Mineralogical and isotopic constraints. Neues Jahrbuch Für Mineralogie - Abhandlungen 181, 53–66. https://doi.org/10.1127/0077-7757/2005/0181-0007

Gaeta, M., Di Rocco, T., Freda, C., 2009. Carbonate assimilation in open magmatic systems: The role of melt-bearing skarns and cumulate-forming processes. Journal of Petrology 50, 361–385. https://doi.org/10.1093/petrology/egp002

Gebauer, S.K., Schmitt, A.K., Pappalardo, L., Stockli, D.F., Lovera, O.M., 2014. Crystallization and eruption ages of Breccia Museo (Campi Flegrei caldera, Italy) plutonic clasts and their relation to the Campanian ignimbrite. Contributions to Mineralogy and Petrology 167, 1–18. https://doi.org/10.1007/s00410-013-0953-7

Giordano, D., Russell, J.K., Dingwell, D.B., 2008. Viscosity of magmatic liquids: A model. Earth and Planetary Science Letters 271, 123–134. https://doi.org/10.1016/j.epsl.2008.03.038

Glazner, A.F., Bartley, J.M., 2006. Is stoping a volumetrically significant pluton emplacement process? Bulletin of the Geological Society of America 118, 1185–1195. https://doi.org/10.1130/B25738.1

Goldstein, S.L., Deines, P., Oelkers, E.H., Rudnick, R.L., Walter, L.M., 2003. Standards for publication of isotope ratio and chemical data in Chemical Geology. Chemical Geology 202, 1-4. https://doi.org/10.1016/j.chemgeo.2003.08.003

Gonnermann, H.M., Manga, M., 2007. The Fluid Mechanics Inside a Volcano. Annual Review of Fluid Mechanics 39, 321–356. https://doi.org/10.1146/annurev.fluid.39.050905.110207

Harris, C., Vogeli, J., 2010. Oxygen isotope composition of garnet in the Peninsula Granite, Cape Granite Suite, South Africa: Constraints on melting and emplacement mechanisms. South African Journal of Geology 113, 401–412. https://doi.org/10.2113/gssajg.113.4.401

Harris, C., le Roux, P., Cochrane, R., Martin, L., Duncan, A.R., Marsh, J.S., le Roex, A.P., Class, C., 2015. The oxygen isotope composition of Karoo and Etendeka picrites: High $\delta_{18}O$ mantle or crustal contamination? Contributions to Mineralogy and Petrology 170, 8. https://doi.org/10.1007/s00410-015-1164-1

Houghton, B.F., Wilson, C.J.N., Del Carlo, P., Coltelli, M., Sable, J.E., Carey, R.J., 2004. The influence of conduit processes on changes in style of basaltic Plinian eruptions: Tarawera 1886 and Etna 122 BC. Journal of Volcanology and Geothermal Research 137, 1–14. https://doi.org/10.1016/j.jvolgeores.2004.05.009

Iacono-Marziano, G., Gaillard, F., Pichavant, M., 2008. Limestone assimilation by basaltic magmas: An experimental re-assessment and application to Italian volcanoes. Contributions to Mineralogy and Petrology 155, 719–738. https://doi.org/10.1007/s00410-007-0267-8

Iannace, A., 1991. Ambienti deposizionali e processi diagenetici in successione di piattaforma carbonatica del Trias Superiore nei Monti Lattari e Picentini (Salerno). PhD Thesis, Università di Napoli Federico II, Napoli, Italy, pp. 221.

Iannace, A., Capuano, M., Galluccio, L., 2011. "Dolomites and dolomites" in Mesozoic platform carbonates of the Southern Apennines: Geometric distribution, petrography and geochemistry. Palaeogeography, Palaeoclimatology, Palaeoecology 310, 324–339. https://doi.org/10.1016/j.palaeo.2011.07.025

Jolis, E.M., Freda, C., Troll, V.R., Deegan, F.M., Blythe, L.S., McLeod, C.L., Davidson, J.P., 2013. Experimental simulation of magma-carbonate interaction beneath Mt. Vesuvius, Italy. Contributions to Mineralogy and Petrology 166, 1335–1353. https://doi.org/10.1007/s00410-013-0931-0

Jolis, E.M., Troll, V.R., Harris, C., Freda, C., Gaeta, M., Orsi, G., Siebe, C., 2015. Skarn xenolith record crustal CO_2 liberation during Pompeii and Pollena eruptions, Vesuvius volcanic system, central Italy. Chemical Geology 415, 17–36. https://doi.org/10.1016/j.chemgeo.2015.09.003

Kerrick, D.M., 1977. The genesis of zoned skarns in the sierra nevada, California. Journal of Petrology 18, 144–181. https://doi.org/10.1093/petrology/18.1.144

Klébesz, R., Bodnar, R.J., De Vivo, B., Torok, K., Lima, A., Petrosino, P., 2012. Composition and origin of nodules from the ~20 ka Pomici di Base (PB)-Sarno eruption of Mt. Somma - Vesuvius, Italy. Central European Journal of Geosciences 4, 324–337. https://doi.org/10.2478/s13533-011-0059-6

Klébesz, R., Esposito, R., De Vivo, B., Bodnar, R.J., 2015. Constraints on the origin of sub-effusive nodules from the Sarno (Pomici di Base) eruption of Mt. Somma-Vesuvius (Italy) based on compositions of silicate-melt inclusions and clinopyroxene. American Mineralogist 100, 760–773. https://doi.org/10.2138/am-2015-4958

Landi, P., Bertagnini, A., Rosi, M., 1999. Chemical zoning and crystallization mechanisms in the magma chamber of the Pomici di Base plinian eruption of Somma-Vesuvius (Italy). Contributions to Mineralogy and Petrology 135, 179–197. https://doi.org/10.1007/s004100050505

Lentz, D.R., 1999. Carbonatite genesis: A reexamination of the role of intrusion-related pneumatolytic skarn processes in limestone melting. Geology 27, 335–338. https://doi.org/10.1130/0091-7613(1999)027<0335:CGAROT>2.3.CO;2

Liedl, A., Buono, G., Lanzafame, G., Dabagov, S.B., Della Ventura, G., Hampai, D., Mancini, L., Marcelli, A., Pappalardo, L., 2019. A 3D imaging textural characterization of pyroclastic products from the 1538 AD Monte Nuovo eruption (Campi Flegrei, Italy). Lithos 340–341, 316–331. https://doi.org/10.1016/j.lithos.2019.05.010

Macedonio, G., Dobran, F., Neri, A., 1994. Erosion processes in volcanic conduits and application to the AD 79 eruption of Vesuvius. Earth and Planetary Science Letters 121, 137–152. https://doi.org/10.1016/0012-821X(94)90037-X

Martí, J., Geyer, A., Folch, A., Gottsmann, J., 2008. A Review on Collapse Caldera Modelling. Developments in Volcanology 10, 233–283. https://doi.org/10.1016/S1871-644X(07)00006-X

Masotta, M., Mollo, S., Freda, C., Gaeta, M., Moore, G., 2013. Clinopyroxene-liquid thermometers and barometers specific to alkaline differentiated magmas. Contributions to Mineralogy and Petrology 166, 1545–1561. https://doi.org/10.1007/s00410-013-0927-9

Mastrolorenzo, G., Pappalardo, L., 2006. Magma degassing and crystallization processes during eruptions of high-risk Neapolitan-volcanoes: Evidence of common equilibrium rising processes in alkaline magmas. Earth and Planetary Science Letters 250, 164–181. https://doi.org/10.1016/j.epsl.2006.07.040

Mollo, S., Heap, M.J., Dingwell, D.B., Hess, K.U., Iezzi, G., Masotta, M., Scarlato, P., Vinciguerra, S., 2013. Decarbonation and thermal microcracking under magmatic P-T-fCO_2 conditions: The role of skarn substrata in promoting volcanic instability. Geophysical Journal International 195, 369–380. https://doi.org/10.1093/gji/ggt265

Mollo, S., Masotta, M., Forni, F., Bachmann, O., De Astis, G., Moore, G., Scarlato, P., 2015. A K-feldspar-liquid hygrometer specific to alkaline differentiated magmas. Chemical Geology 392, 1–8. https://doi.org/10.1016/j.chemgeo.2014.11.010

Papale, P., Moretti, R., Barbato, D., 2006. The compositional dependence of the saturation surface of H_2O + CO_2 fluids in silicate melts. Chemical Geology 229, 78–95. https://doi.org/10.1016/j.chemgeo.2006.01.013

Pappalardo, L., Mastrolorenzo, G., 2010. Short residence times for alkaline Vesuvius magmas in a multi-depth supply system: Evidence from geochemical and textural studies. Earth and Planetary Science Letters 296, 133–143. https://doi.org/10.1016/j.epsl.2010.05.010

Pappalardo, L., Mastrolorenzo, G., 2012. Rapid differentiation in a sill-like magma reservoir: A case study from the campi flegrei caldera. Scientific Reports 2, 712. https://doi.org/10.1038/srep00712

Pappalardo, L., Piochi, M., Mastrolorenzo, G., 2004. The 3550 year BP-1944 A.D. magma-plumbing system of Somma-Vesuvius: Constraints on its behaviour and present state through a review of Sr-Nd isotope data. Annals of Geophysics 47, 1471–1483. https://doi.org/10.4401/ag-3354

Pappalardo, L., Buono, G., Fanara, S., Petrosino, P., 2018. Combining textural and geochemical investigations to explore the dynamics of magma ascent during Plinian eruptions: a Somma–Vesuvius volcano (Italy) case study. Contributions to Mineralogy and Petrology 173, 61. https://doi.org/10.1007/s00410-018-1486-x

Piochi, M., Ayuso, R.A., De Vivo, B., Somma, R., 2006. Crustal contamination and crystal entrapment during polybaric magma evolution at Mt. Somma-Vesuvius volcano, Italy: Geochemical and Sr isotope evidence. Lithos 86, 303–329. https://doi.org/10.1016/j.lithos.2005.05.009

Rosseel, J., White, J.D.L., Houghton, B.F., 2006. Complex bombs of phreatomagmatic eruptions: Role of agglomeration and welding in vents of the 1886 Rotomahana eruption, Tarawera, New Zealand. Journal of Geophysical Research: Solid Earth 111, B12205. https://doi.org/10.1029/2005JB004073

Santacroce, R., Cioni, R., Marianelli, P., Sbrana, A., Sulpizio, R., Zanchetta, G., Donahue, D.J., Joron, J.L., 2008. Age and whole rock-glass compositions of proximal pyroclastics from the major explosive eruptions of Somma-Vesuvius: A review as a tool for distal tephrostratigraphy. Journal of Volcanology and Geothermal Research 177, 1–18. https://doi.org/10.1016/j.jvolgeores.2008.06.009

Scaillet, B., Pichavant, M., Cioni, R., 2008. Upward migration of Vesuvius magma chamber over the past 20,000 years. Nature 455, 216–219. https://doi.org/10.1038/nature07232

Signorelli, S., Carroll, M.R., 2002. Experimental study of Cl solubility in hydrous alkaline melts: Constraints on the theoretical maximum amount of Cl in trachytic and phonolitic melts. Contributions to Mineralogy and Petrology 143, 209–218. https://doi.org/10.1007/s00410-001-0320-y

Smith, P.M., Asimow, P.D., 2005. Adiabat-1ph: A new public front-end to the MELTS, pMELTS, and pHMELTS models. Geochemistry, Geophysics, Geosystems 6, Q02004. https://doi.org/10.1029/2004GC000816

Sottili, G., Taddeucci, J., Palladino, D.M., Gaeta, M., Scarlato, P., Ventura, G., 2009. Sub-surface dynamics and eruptive styles of maars in the Colli Albani Volcanic District, Central Italy. Journal of Volcanology and Geothermal Research 180, 189–202. https://doi.org/10.1016/j.jvolgeores.2008.07.022

Sottili, G., Taddeucci, J., Palladino, D.M., 2010. Constraints on magma-wall rock thermal interaction during explosive eruptions from textural analysis of cored bombs. Journal of Volcanology and Geothermal Research 192, 27–34. https://doi.org/10.1016/j.jvolgeores.2010.02.003

Spera, F.J., Bohrson, W.A., 2001. Energy-Constrained Open-System Magmatic Processes I: General Model and Energy-Constrained Assimilation and Fractional Crystallization (EC-AFC) Formulation. Journal of Petrology 42, 999–1018. https://doi.org/10.1093/petrology/42.5.999

Stille, P., Steinmann, M., Riggs, S.R., 1996. Nd isotope evidence for the evolution of the paleocurrents in the Atlantic and Tethys Oceans during the past 180 Ma. Earth and Planetary Science Letters 144, 9–19. https://doi.org/10.1016/0012-821x(96)00157-4

Troll, V.R., Hilton, D.R., Jolis, E.M., Chadwick, J.P., Blythe, L.S., Deegan, F.M., Schwarzkopf, L.M., Zimmer, M., 2012. Crustal CO_2 liberation during the 2006 eruption and earthquake events at Merapi volcano, Indonesia. Geophysical Research Letters 39, L11302. https://doi.org/10.1029/2012GL051307

Villemant, B., 1988. Trace element evolution in the Phlegrean Fields (Central Italy): fractional crystallization and selective enrichment. Contributions to Mineralogy and Petrology 98, 169–183. https://doi.org/10.1007/BF00402110

Vosteen, H.D., Schellschmidt, R., 2003. Influence of temperature on thermal conductivity, thermal capacity and thermal diffusivity for different types of rock. Physics and Chemistry of the Earth 28, 499–509. https://doi.org/10.1016/S1474-7065(03)00069-X

Watkinson, D.H. and Wyllie, P., 1964. The limestone assimilation hypothesis. Nature 204, 1053–1054. https://doi.org/10.1038/2041053a0

Wenzel, T., 2002. Partial Melting and Assimilation of Dolomitic Xenoliths by Mafic Magma: the Ioko-Dovyren Intrusion (North Baikal Region, Russia). Journal of Petrology 43, 2049–2074. https://doi.org/10.1093/petrology/43.11.2049

Winter, J.D., 2001. An Introduction to Igneous and Metamorphic Petrology. Prentice Hall, New Jersey.

Zheng, Y.-F., Zhao, Z.-F., 2003. Calculation of oxygen isotope fractionation in magmatic rocks. Chemical Geology 193, 59–80. https://doi.org/10.1016/S0009-2541(02)00226-7

3.2. Weakly explosive volcanism: the case study of the latest Campi Flegrei eruption

3.2.1. A 3D imaging textural characterization of pyroclastic products from the 1538 AD Monte Nuovo eruption (Campi Flegrei, Italy)

This work is published on Lithos (vol.: 340–341, 316–331; doi: https://doi.org/10.1016/j.lithos.2019.05.010; year: 2019) under the same title with authors:

Liedl A.[a], Buono G.[b,c], Lanzafame G.[d], Dabagov S.B.[a,e], Della Ventura G.[a,f], Hampai D.[a], Mancini L.[d], Marcelli A.[a,g], Pappalardo L[b].

a - Istituto Nazionale di Fisica Nucleare, Laboratori Nazionali di Frascati, Italy
b - Istituto Nazionale di Geofisica e Vulcanologia, Osservatorio Vesuviano, Italy
c - University of Naples Federico II, Department of Earth, Environmental and Resources Science, Italy
d - Elettra - Sincrotrone Trieste S.C.p.A., Italy
e - National Research Nuclear University MEPhI, Russia
f - Università Degli Studi Roma Tre, Italy
g - Rome International Center for Materials Science. Italy

I contributed to all phases (field activities, rock characterization, data interpretation, writing) and investigations of the work except 3D image acquisition, performed at the SYRMEP beamline of the Elettra Sincrotrone Trieste facility.

Abstract

The explosive volcanic event of the 1538 AD Monte Nuovo eruption (Volcanic Explosivity Index, VEI = 2) in the Campi Flegrei high-risk caldera (Italy) has a strategic significance in the framework of volcanology and volcanic hazard of caldera-forming magmatic systems. In fact, it represents the last and unique historical eruption of the highly populated Phlegraean restless-caldera, and its precursory and eruptive phenomena are well-known because they were described in detail by contemporaneous eyewitnesses.
In this study, a set of samples representative of the complete stratigraphic sequence of the Monte Nuovo eruption was characterized using phase-contrast synchrotron radiation computed microtomography and quantitatively investigated through the development of a new protocol for 3D textural analysis of highly-vesiculated volcanic rocks. Previous studies of products from this eruption are available in the literature, mostly based on 2D imaging techniques, and thus provide a useful data set for comparison.
The 3D textural measurements allow us to investigate the subvolcanic processes (mechanisms and timing of magma degassing) that occurred during magma ascent in the conduit for each stage of the eruption and their relationship with the variations in the eruptive style described in the contemporaneous accounts of the eruption. This information is fundamental for the definition of a

volcanic eruption scenario for such low-VEI events, often recurrent in the history of the caldera, and is useful both for hazard assessment and emergency planning.

1. Introduction

In the field of volcanology, quantitative textural studies on rock samples (e.g. scoriae and pumices) represent a fundamental approach in reconstructing the degassing conditions related to magma ascent in volcanic conduits (e.g. Mastrolorenzo and Pappalardo, 2006; Polacci et al., 2010; Shea et al., 2010; Rust and Cashman, 2011; Gonnermann and Houghton, 2012; Baker et al., 2012a; Pappalardo et al., 2014; Rotella et al., 2014), a process that strongly controls the eruption dynamics. These studies constrain the mechanisms and timing of magma degassing in the conduit, thus improving the interpretation of volcano-monitoring signals and, in turn, our ability to perform hazard assessments. Many recent investigations have demonstrated the potential of hard X-ray computed microtomography (X-µCT) to explore complex textures for Earth science applications. Thanks to its non-destructive character, high-resolution X-µCT is a powerful tool to perform three-dimensional (3D) morphological and textural studies at the micron and sub-micron scale of many types of materials (Withers, 2008; Maire & Whithers, 2014) on samples up to the tens of centimeters in size. By using laboratory- and synchrotron-based X-µCT, the sample microstructure can be visualized and further analyzed through the reconstruction of 3D digital maps of either the mass attenuation coefficient (absorption mode) or the refraction index (phase-contrast mode) of X-rays within the sample volume (Cloetens et al., 1997). In the last two decades, this technique has been successfully applied to the study of natural phenomena in volcanic (Polacci et al., 2010; 2018; Baker et al., 2012b), seismic (Zucali et al., 2015) and hydrogeological (Cnudde and Boone, 2013) risk contexts (mechanisms of magma vesiculation, crystallization and fragmentation, fracture propagation in rocks, fluid/rock interactions, rock alteration processes, etc.).
In particular, vesiculated pyroclasts produced during explosive eruptions have been successfully characterized (e.g. Voltolini et al., 2011; Baker et al., 2012a; Polacci et al., 2014; Lanzafame et al., 2017; Moretti et al., 2019, Pappalardo et al., 2018; Polacci et al., 2018). X-µCT allows the direct observation and quantitative characterization of the number, size, orientation and shape of vesicles, as well as their degree of connectivity and permeability, which are impossible to determine using conventional two-dimensional (2D) techniques (Zandomeneghi et al., 2010). However, many issues are still open in 3D quantitative textural analysis, especially for volcanic rocks with a complex network of highly interconnected vesicles. In this case, one of the main challenges is to find efficient procedures for the separation of the pore network into individual vesicles, in order to restore the magma to pre-fragmentation conditions (e.g. Shea et al., 2010; Baker et al., 2012a). The reconstruction of the tiny glass walls separating vesicles is particularly complex because 1) they can break during the latter stages of bubble interconnection in the volcanic conduit (e.g. Rust and Cashman, 2011), 2) they may not be properly detected during image acquisition (e.g. unresolved walls smaller than the imaging resolution available) or 3) they can disappear during image processing (Shea et al., 2010; Lanzafame et al., 2018; Pappalardo et al., 2018).
We selected, as a case study, the Monte Nuovo eruption, representing the only historical event of the high-risk Campi Flegrei caldera (Italy) (e.g. Mastrolorenzo and Pappalardo, 2006; Mastrolorenzo et al., 2008; 2017 and references therein), where signs of unrest are currently observed (Chiodini et al., 2012; 2015; 2016; D'Auria et al., 2015). This small eruption (Volcanic Explosivity Index, VEI = 2) occurred in 1538 AD after a rest period of about 3000 years and represents the most recent event of the caldera. The chronicles from the time provide a detailed description of the event (Guidoboni and Ciuccarelli, 2011 and references therein), thus an accurate chronology of pre-eruptive (e.g. ground deformation, earthquakes), as well as eruptive, phenomena is available. In particular, the eruption was characterized by the gradual shift from initial phreato-magmatic activity to a subsequent magmatic low-explosivity phase. We performed a 3D textural

characterization of a set of samples from the different eruptive phases by means of synchrotron X-μCT in phase-contrast mode. The application of software tools dedicated to 3D processing and analysis of reconstructed tomographic images allowed i) definition of a specific protocol for 3D image processing and analysis that can be applied to highly-vesiculated, volcanic samples and ii) retrieval of quantitative parameters such as vesicle sizes and number density, connectivity and tortuosity of the pore network. These 3D textural measurements have been used to infer degassing mechanisms during magma ascent in the volcanic conduit and their influence on the eruption dynamics, such as the transition between phreato-magmatic and magmatic activity.

2. The Phlegraen Volcanic District

The Phlegraean Volcanic District (PVD) (west of Naples, southern Italy), is a densely populated active volcanic area including the Campi Flegrei (CF) caldera and the volcanic islands of Procida-Vivara and Ischia (Fig. 1). The CF is dominated by a 12-km wide caldera depression formed during two high-magnitude events: the ca 40 ka-BP (e.g. Gebauer et al., 2014) Campanian Ignimbrite (VEI = 7) and the ca 15 ka-BP (Deino et al., 2004) Neapolitan Yellow Tuff (VEI = 6) eruptions (Fig. 1a).
Volcanic activity at CF began >60 ka BP (Pappalardo, et al., 1999; Wu et al., 2015) and produced potassic volcanic rocks ranging in composition from trachybasalt, to latite, to trachyte and phonolite (e.g. Pappalardo et al., 2002). Evidence of ancient volcanic activity has been found in the heart of Naples (Chiaia district; Scarpati, et al., 2015), as testified by the presence of monogenetic edifices constituting the so-called Paleoflegrei activity (> 78 ka). After this period, the volcanism at CF is divided into three cycles (e.g. Vitale and Isaia, 2014; Scarpati et al., 2015; Mastrolorenzo et al., 2017).
During the first cycle (78-39 ka), several volcanic edifices were formed in different sectors of the caldera, including lava domes of San Martino, Cuma and Punta Marmolite, as well as tuff cones located at Monte di Procida and in the city of Naples (Rosi and Sbrana 1987; Scarpati et al., 2015). This activity culminated with the Campanian Ignimbrite super-eruption, probably the largest volcanic event of the whole Mediterranean area in the last 200 ka, during which 300 km^3 of trachytic magma was emitted (e.g. Pappalardo et al., 2008). There are different hypotheses about possible vent(s) locations for this eruption, possibly in the Campi Flegrei caldera or in a fracture system north of Naples (Pappalardo et al., 2008 and references therein).
The volcanic activity during the second cycle (40-15 ka) produced thick pyroclastic deposits (Whitish Tuffs) localized in the western part of Naples and two monogenetic vents: Chiatamone and Trentaremi. At least eleven low- to moderate-scale (VEI = 2-5) explosive events have been reconstructed on the basis of the stratigraphic sequences (Pappalardo et al., 1999). A new caldera-forming eruption that produced the Neapolitan Yellow Tuff (15 ka; Deino et al., 2004), ends this period of activity.
The third cycle is the most studied one of the sequence. At least seventy explosive eruptions occurred, ranging in VEI between 2 and 5 (Rosi and Sbrana, 1987; Di Vito et al., 1999; Orsi et al., 2004 and references therein). These recent events, including the last 1538 AD Monte Nuovo eruption (VEI 2, Di Vito et al., 1987), typically produced monogenetic tuff rings and tuff cones, and subordinate spatter cones, scattered throughout the caldera. According to different authors (e.g. Di Vito et al., 1999, Isaia et al., 2009) this cycle can be divided into three epochs of intense activity, separated by periods of quiescence. In the first epoch, from ca 15 ka to about 10.6 ka, 34 explosive (magmatic or phreato-magmatic) eruptions occurred, with an average repose interval of about 70 years. The second volcanic epoch, dating between 9.6 and 9.1 ka produced six explosive eruptions, approximately every 65 years. The last epoch, from 5.5 to 3.5 ka produced 20 eruptions with a mean interval of 50 years (e.g. Di Vito et al., 1999).
Geophysical anomalies detected by seismic tomography (Zollo et al., 2008) indicate that a partial melting zone is currently present at 7–8 km depth beneath the CF as well as beneath neighboring

Vesuvius volcano. This evidence, that is consistent with the similarity in petrological features of the products from these volcanoes, suggests that a widely distributed magma source may be active beneath the entire Neapolitan volcanic district (Pappalardo et al., 2004, 2008; Pappalardo and Mastrolorenzo, 2010; 2012; Fedi et al., 2018).

The most recent unrest of CF caldera has been characterized by short-term ground deformation (or bradyseism), culminating in unrest between 1950-1952, 1969–1972 and 1982–1984. The last two major unrest episodes consisted of uplifts of ~1.7 and ~1.8 m, respectively, accompanied by M < 4 seismicity in the central part of the caldera, clustered below the Pozzuoli - Solfatara area (Dvorak and Mastrolorenzo 1991). In the last decades, the CF caldera has been undergoing moderate and localized uplift associated with significant variations in the temperature and geochemical parameters monitored at the Solfatara-Pisciarelli fumaroles (Chiodini et al., 2012, 2015, 2016), as well as episodic seismic swarms (D'Auria et al., 2015). This behavior led Italian Civil Protection to raise the alert level of the volcano from "background" to "attention" in 2012.

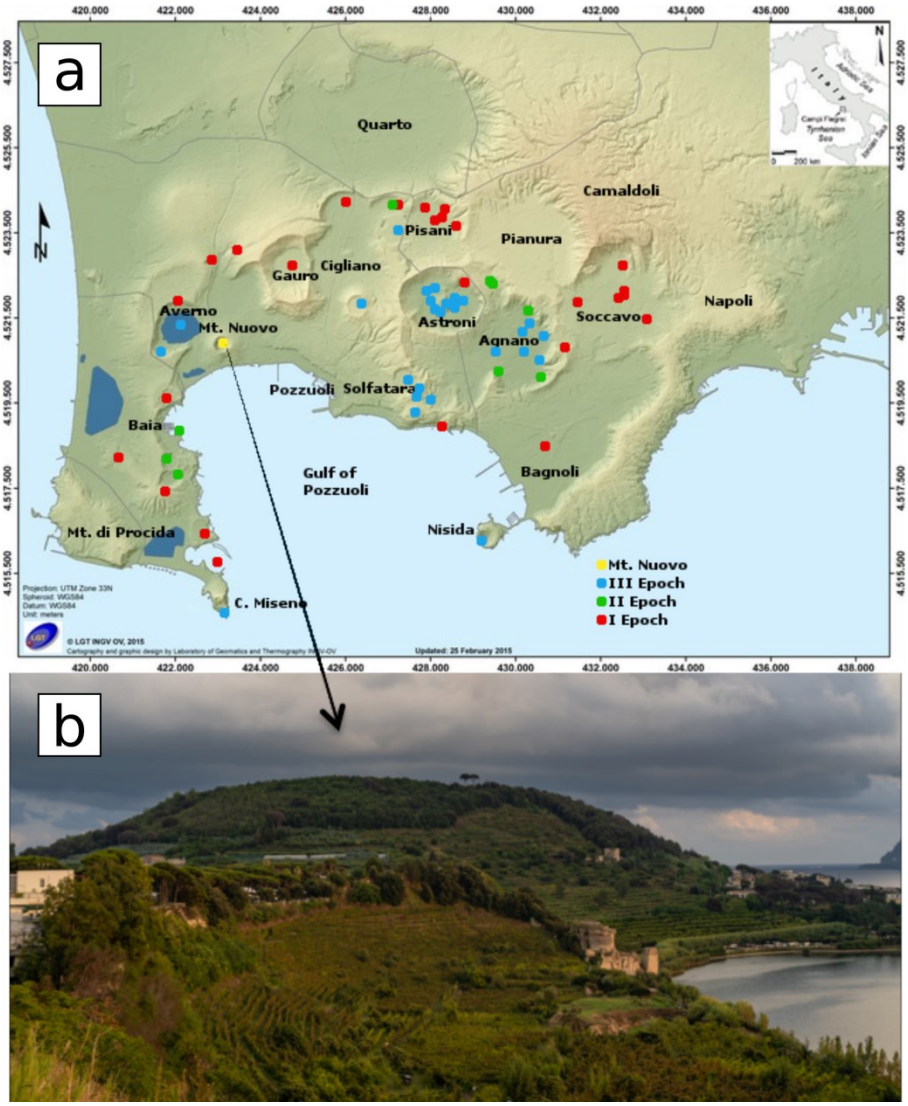

Fig. 1. a) Topographic map of the Campi Flegrei volcanic field and location of the eruptive vents during the last 15 ka of activity (upper panel); b) View of the Monte Nuovo tuff cone from the Averno lake (photo courtesy of Max Schanofski) (lower panel).

3. The Monte Nuovo eruption

Monte Nuovo is a 132-m-high, 800-m-wide and 100–120 m deep monogenetic tuff cone, with a 250 m diameter summit crater (Fig. 1b). The Monte Nuovo tuff cone originates from the most recent volcanic event of the CF that occurred in historical times (1538 AD) in the north-west sector of the caldera. The eruption was directly followed and described by several eyewitnesses, thus accounts of the events immediately before and during the eruption are available (Guidoboni and Ciuccarelli, 2011 and references therein). The historical accounts were examined by later authors, including Parascandola (1946), Rosi and Santacroce (1984), Di Vito et al. (1987) and Dvorak and Gasparini (1991).

According to these reports, the eruption was preceded by significant seismic activity and ground uplift that started in the 1536–1538 period and increased in the autumn of 1538. On September 27th –28th, rapid uplift occurred in a small zone around the vent and was accompanied by an increase of seismic activity and strong gas emissions. On September 29th, about half an hour before opening of the main eruptive vent, a fracture opened on the seabed about 40–100 m from the coast. The eruption started in the night between September 29th and 30th, with the opening of an eruptive vent located at Le Tripergole village, which was completely destroyed by the construction of a new tuff cone.

The first opening phases were characterized by phreato-magmatic activity with the emplacement of two small-scale pyroclastic flow units in a small area around the vent (units I and II, from Di Vito et al., 1987, also labeled lower-member, LM, by D'Oriano et al., 2005) that built the main cone. These units consist of thick ash-supported beds (maximum thickness of 7 and 60–70 m respectively, Di Vito et al., 1987) with fine planar and cross lamination containing lithic clasts, pottery and pumice fragments with sizes >4 cm, sometimes forming discontinuous lenses (Piochi et al., 2005). After two days (October 1st–2nd) of decreasing magmatic activity, a fire fountaining event produced scoria deposits radially distributed around the vent (unit III, from Di Vito et al., 1987 and upper member 1, UM1, of D'Oriano et al., 2005). These products (maximum thickness of 2-3 m, Di Vito et al., 1987) are separated by a phreato-magmatic grey ash layer indicating that during the magmatic activity the external water supply was not totally exhausted. The magmatic activity was followed by two days of quiescence, then the eruption renewed and ended on October 6th with a violent explosive phase and the emplacement of a small pyroclastic flow (unit IV, from Di Vito, et al., 1987 and upper member 2, UM2, in D'Oriano et al., 2005) alternating with fall-out products covering the southern slope of the cone (maximum thickness of 25 m, Di Vito et al., 1987). The scoria deposits of units III and IV contain lava with hydrothermal lithic clasts, and black juvenile fragments up to 10 cm in size. This last activity caused the death of >24 people who were on the slopes of the new volcano watching the eruption. The total volume of pyroclastic deposits was 4.4 x 10^7 m^3 corresponding to 2.5 x 10^7 m^3 dense-rock equivalent (Di Vito al., 1987).

In spite of the distinct colors and textures, the products of Monte Nuovo show a nearly homogeneous composition plotting in the K-rich phonolite - trachyte field (Fig. 2), with SiO_2 = 58.7–59.6 wt%, Na_2O+K_2O = 13.8–14.7 wt%, and K_2O/Na_2O ~1.0 (Piochi et al., 2005). The higher Fe^{3+}/Fe^{2+} ratio in the upper products with respect to the lower products suggests that the dark color of the clasts could be an effect of increased fO_2 that can facilitate Fe^{3+} oxide precipitation (D'Oriano et al., 2005), affecting the crystallization sequence (Kolzenburg et al., 2018), increasing magma viscosity (Di Genova et al., 2017) and thus modifying the eruptive style. All clasts contain both phenocrysts (<3% in volume) and feldspar microlites. The magmatic scoriae contain a greater abundance of microlites (average content 30-40%) than the phreato-magmatic pumice samples (about 10-30%) (D'Oriano et al., 2005; Piochi et al., 2005).

Recently, Di Vito et al. (2016), on the basis of the historical, archaeological and geological record, suggested that the emplacement of magma may have begun as early as ~300 years before the eruption at ~4.7 km depth below the caldera center.

Pre- and syn-eruptive processes have been studied on the basis of geochemical and 2D textural evidence by Piochi et al. (2005) and D'Oriano et al. (2005). Piochi et al. (2005) concluded that magma decompression occurred in two distinct phases: a first conduit-opening phase characterized by a slow (lasting months) magma ascent from a depth of 4-5 km to shallow levels (about 1 km), and a second, fast-rising stage (lasting a few hours) occurring in the upper part of the eruptive conduit. According to Piochi et al., the transition from the phreato-magmatic to the magmatic phase was related to the exhaustion of the aquifer. D'Oriano et al. (2005), instead, assume the formation of a plug in the conduit during the time interval separating the two eruptive phases, allowing an increase in magma viscosity due to syn-eruptive crystallization (Caricchi et al., 2008; Vona et al., 2013; Di Genova, 2017; Kolzenburg et al., 2018).
This hypothesis was reappraised by Arzilli et al. (2016a), who constrained the pre-eruptive conditions and timescale of magma ascent by comparing natural and experimental samples. These authors inferred that magma transfer from the pre-eruptive storage chamber (150-135 MPa) to shallowers levels (50-70 MPa), followed by a fast ascent to 30 MPa (fragmentation point), lasted a few hours to several days. Changes in the eruptive style from the early to late eruptive phases must be attributed to a decrease in the magma ascent rate that promoted crystallization and more efficient degassing in the shallow levels of the volcanic conduits.

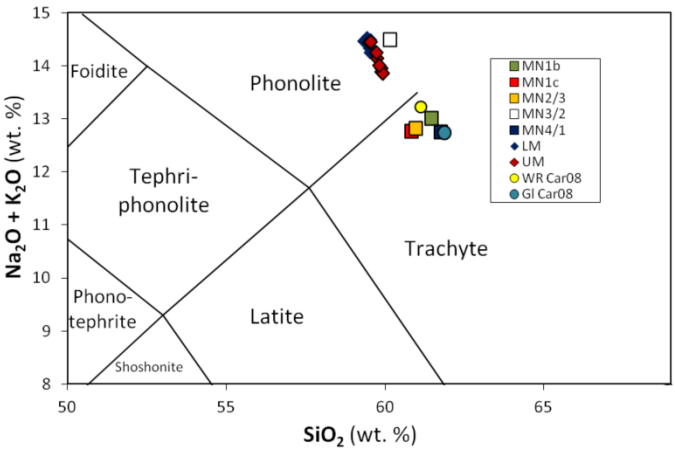

Fig. 2. Total Alkali versus Silica (TAS) classification diagram for the Monte Nuovo whole-rocks. Data from: MN (Piochi et al., 2005), LM/UM (D'Oriano et al., 2005), WR/GI (Caricchi et al., 2008).

4. Materials and Methods

4.1. Sampling

We selected eight samples representative of the whole stratigraphic sequence of the Monte Nuovo eruption, displayed in Fig. 3 following Di Vito et al. (1987). Three samples are from Unit I (MN1a, MN1b, MN1c), two from Unit II (MN2/2, MN2/3), two from Unit III (MN3/1, MN3/2), and one from Unit IV (MN4/1) (Fig. 3). The clasts chosen for the 3D textural analysis were selected on the basis of data reported by Piochi et al. (2005). In detail, Units I and II consist of juvenile vesicular white pumices, while Units III and IV contain juvenile black scoriae. Samples have been selected from different stratigraphic levels for each unit, except for Unit I, in which clasts are less homogenous; the main clast types have been distinguished as banded pumice (MN1b), with dark and light glassy components separated by sharp contacts, associated with white pumices of differing porosity (MN1a, MN1c).

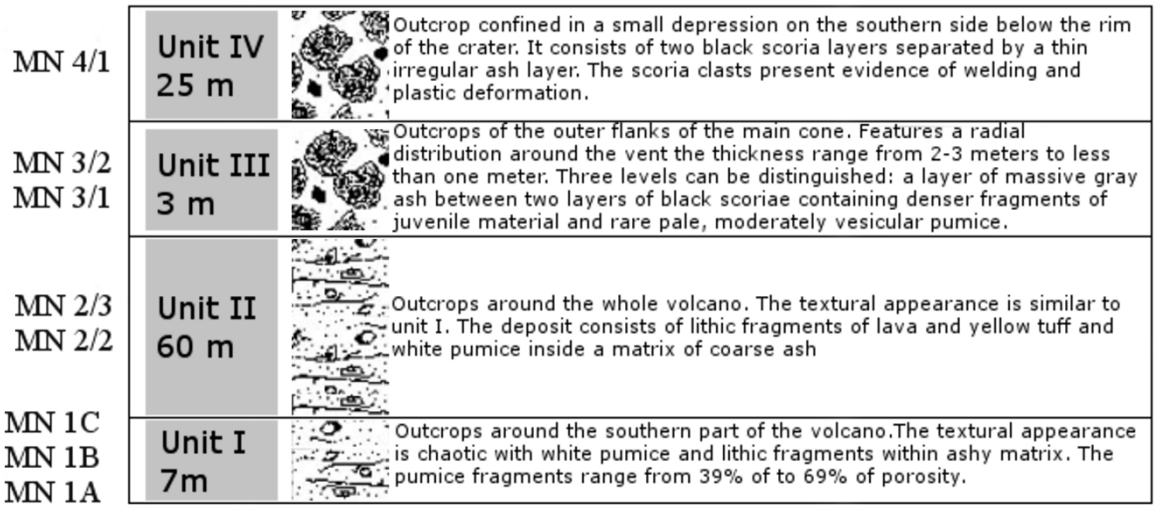

Fig. 3. Schematic stratigraphic section of the Monte Nuovo deposit and location of the studied samples.

4.2. Synchrotron X-ray computed microtomography (SX-µCT) measurements

An X-µCT scan is based on the acquisition, through a digital X-ray camera, of the 2D radiographs (projections) of the sample at different angular views. Projections are recorded at regular steps over a total angular scan of 180 or 360°. Then, a virtual tomographic reconstruction of the imaged sample volume is obtained by applying mathematical algorithms. The process is well described in previous works (Baruchel, 2000; Ketcham & Carlson, 2001; Zandomeneghi et al., 2010).

The investigation of the Monte Nuovo samples was performed by using high-resolution synchrotron X-µCT (SX-µCT) at the SYRMEP beamline of the Elettra Sincrotrone Trieste facility (Basovizza - Trieste, Italy) (Polacci et al., 2010). The nearly-parallel X-ray beam delivered by a bending magnet source features a high photon flux and a high spatial coherence, allowing exploitation of propagation-based phase-contrast imaging (Cloetens et al., 1997; Baruchel et al., 2000; Arzilli et al. 2016b). This technique, based on the detection of phase modulations produced by the sample on the X-ray beam, is extremely advantageous because it enhances the visibility of fine microstructural features or small discontinuities within materials characterized by similar X-ray absorptions. Following the approach of Arzilli et al. (2016b), phase-contrast SX-µCT scans of Monte Nuovo samples were recorded in a white-beam configuration: a filtered polychromatic X-ray beam (filters: 1.5 mm Si + 1 mm Al) was used, with a mean X-ray energy of ca. 25 keV. The detector was an air-cooled, 16 bit, sCMOS camera (Hamamatsu C11440-22C) with a 2048 × 2048 pixel chip coupled to a 17 µm-thick LSO:Tb scintillator screen and high numerical aperture optics. Since the aim of this study was the separation and quantitative analysis of the different phases constituting the rock samples, the sample-to-detector distance was optimized depending on the sample microstructure in the range between 80 and 150 mm. This allowed increasing the contrast of the different phases present in the samples thanks to an edge-enhancement effect at their rim (Cloetens et al., 1997; Polacci et al., 2010; Arzilli et al. 2016b). The effective pixel size of the detector was set to 2.0 × 2.0 μm^2, yielding a maximum field-of-view of ca. 4.1 × 4.1 mm^2. Because the lateral size of the samples was larger than the horizontal field of view of the detector, the SX-µCT scans were acquired in *local* or *region-of-interest* mode (Maire and Withers 2014). A series of 1800 projections were acquired over a total angular range of 180° with an exposure time/projection between 1000 and 2000 ms. The detailed experimental conditions used for the acquisition of the SX-µCT scans are summarized in Table 1.

The tomographic reconstruction was carried out by using the SYRMEP Tomo Project (STP) software suite (Brun et al., 2017) based on a Filtered Back-Projection algorithm (Herman et al., 1980). This software allows the pre-processing of data to remove ring artifacts caused by imperfect

detector elements that appear on CT images as concentric elements (Brun et al. 2011). Because the application of the phase-contrast imaging modality does not automatically provide a quantitative reconstruction of the refraction index, the application of phase-retrieval algorithms to the projection images is necessary prior to the tomographic reconstruction. In this study, a single-distance phase-retrieval algorithm based on the Transport of Intensity algorithm (Paganin et al., 2002) was applied to the sample projections. For each sample, a value varying between 20 and 70 was set for the $\delta / \beta = \gamma$ parameter (ratio between the real and imaginary parts of the complex refractive index of the investigated material) after a manual optimization, with the goal of removing the phase-contrast 'artifacts' and enhancing the contrast in the reconstructed images, while preserving the microstructural fine features of interest visible in the reconstructed slices without phase-retrieval (see Table 1). Selected reconstructed axial slices of all samples are shown in Fig. 4.

Samples	Pixel size (µm)	Exposure Time/Projection (ms)	Total Angular Range (degree)	Number of Projections	Sample-Detector Distance (mm)	Phase retrieval (γ ratio)
MN1a	2.0	1000	180	1800	80	50
MN1b	2.0	2000	180	1800	150	20
MN1C	2.0	2000	180	1800	150	50
MN2/2	2.0	2000	180	1800	150	50
MN2/3	2.0	2000	180	1800	150	70
MN3/1	2.0	1250	180	1800	150	70
MN3/2	2.0	1250	180	1800	150	50
MN4/1	2.0	1250	180	1800	150	50

Table 1. Parameters used for the tomographic scan and for the reconstruction process.

	VOI = 1000x1000x1000 (voxel)	VOI = 400x400x400 (voxel)		VOI = 640x640x950 (voxel)		
Sample	**Porosity (%)**	**Tortuosity**	**Connectivity Density (mm^{-3})**	**Number Density ($\#/m^3$)**	**Volume ratio of vesicles to melt ($=V_G/V_L$)**	**Power Low Exp**
MN1a	69	1.31	22433	4.98×10^{12}	2.23	4.99
MN1b	43	2.13	41	6.72×10^{11}	0.75	1.93
MN1c	39	2.23	2883	3.22×10^{12}	0.64	4.72
MN2/2	42	2.29	6153	4.08×10^{12}	0.72	5.05
MN2/3	55	1.74	12517	3.77×10^{12}	1.22	5.67
MN3/1	29	2.05	3070	1.61×10^{13}	0.41	3.45
MN3/2	41	2.83	6113	5.29×10^{12}	0.69	3.81
MN4/1	31	2.32	1902	7.44×10^{12}	0.45	3.72

Table 2. Key textural features of the analyzed samples.

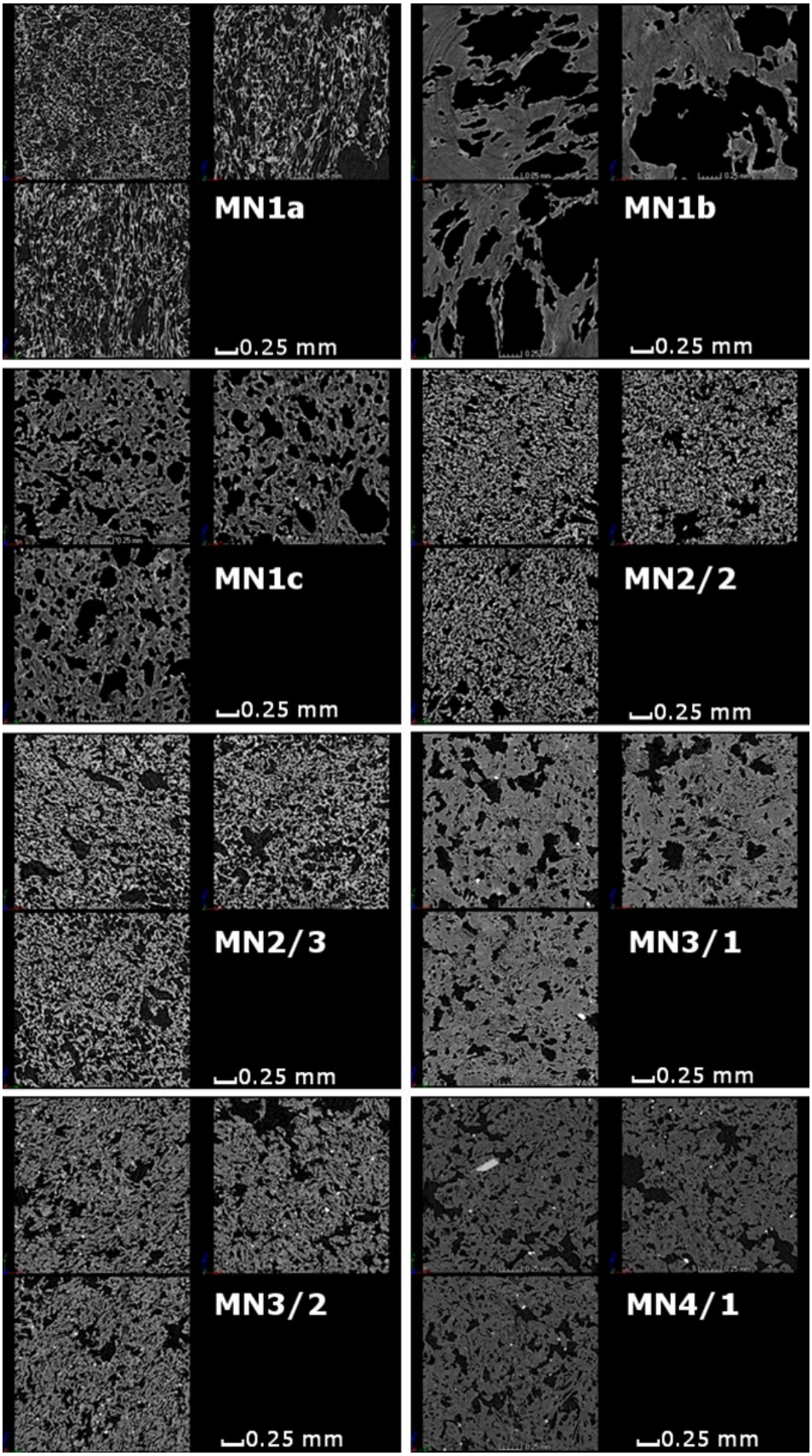

Fig. 4. Selected reconstructed sagittal, coronal and axial slices of all investigated samples (size = 1000 x 1000 pixels^2 corresponding to 2.0 x 2.0 mm^2).

4.3. Image processing and analysis

The data obtained by SX-µCT experiments were processed and then analyzed to extract the morphological characteristics of vesicles. 3D textural analysis of rocks with a complex network of large interconnected pores is a challenging task, and no shared software routines are available to study samples for volcanological applications. Here we developed a new protocol useful for both the investigation of (i) individual vesicles (after 3D reconstruction of the glass walls) and (ii) the pore network features, starting from images segmented using automatic tools. A schematic view of the image processing and analysis pipeline is reported in Fig. 5.

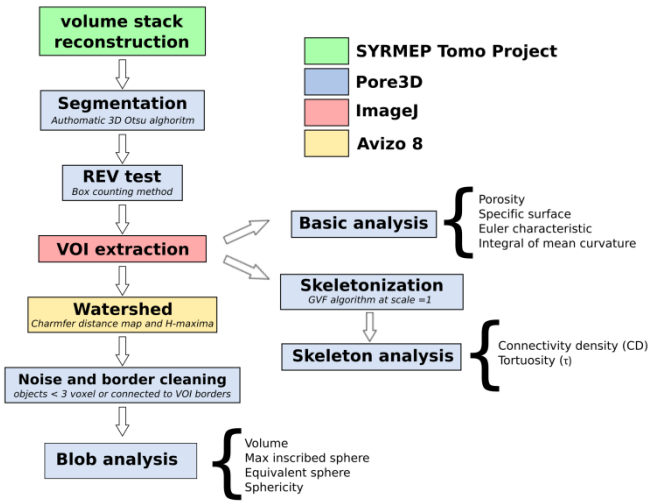

Fig. 5. Schematic representation of the image processing and analysis pipeline, highlighting the used software packages and the extracted quantitative parameters.

The first step was the segmentation of the vesicle phase from 3D images by using the automatic 3D Otsu method (Otsu, 1979), manually adjusting the thresholds when necessary. Then representative Volumes Of Interest (VOIs) of the original image stacks were selected. In order to verify the suitability of the selected VOIs, Representative Elementary Volumes (REVs) tests were performed using the box-counting method applied on the vesicle density (or porosity), specific surface area and Euler characteristic (Table 2 and Fig. 6), by means of the *Pore3D* software library developed at Elettra (Brun et al., 2010; https://github.com/ElettraSciComp/Pore3D). Results indicate that, for each sample, a cubic VOI with size of 400x400x400 voxels (0.512 mm^3) can be considered representative of the entire volume. Using a VOI equal to the REV ensures the minimization of the computational cost while maintaining the representativeness of the analysis. However, when it was possible, we used a VOI larger than the REV in order to produce a more accurate analysis.

Vesicles in the studied samples are characterized by extensive coalescence, leading to the formation of highly connected networks. In order to restore magma pre-fragmentation conditions, a marker-based watershed algorithm using a Chamfer distance map and H-maxima with a marker extent between 4 and 5 was applied using Separate Object tool in the commercial software Avizo 8® (Thermo Fisher Scientific, USA) (Fig. 7). Due to computational limitations, this procedure was applied to VOIs of 640x640x950 voxels. The watershed algorithm (Soille, 2004) was chosen because it preserves the original volume and shape of the vesicles, in contrast to erosion-dilation operations (e.g. Ketcham et al., 2001), which is sometimes inefficient in separating these highly-interconnected pores. Other protocols such as skeletonization combined with maximal inscribed sphere method also provide accurate results for the measurement of vesicle size (Baker et al. 2012a), especially for low-porosity rocks. However the watershed approach needs a shorter

computational time, allowing analysis of larger VOIs, which reduce the uncertainties in the measurements.
After the vesicle separation, images were processed by removing isolated objects smaller than 3 voxels and objects connected to the VOI borders that may be truncated and thus not show their original shape. Then, a quantitative analysis of the processed images allowed retrieval of a series of parameters:
1) Vesicle Number Density (VND), that is the number of vesicles normalized to the investigated volume of groundmass, which usually includes glass or glass plus microlites. The vesicle number density can change significantly among pyroclasts from various kinds of eruption (e.g. Shea et al., 2010). VND is commonly linked to magma ascent rate (Toramaru, 2006): high values (i.e. many small bubbles) are associated with high decompression rates, and low values (i.e. few large bubbles) are related to slow, or staged ascent (e.g. Cashman and Mangan, 1994). Shea et al. (2010) reported VND values between 10^{11} and 10^{12} m^{-3} for slowly ascening magmas (VEI from 0 to 2) and up to 10^{16} m^{-3} for rapidly ascending magmas (e.g. Vesuvius 79 AD VEI 6 Plinian eruption).
2) Vesicle Size Distribution (VSD) and Vesicle Volume Distribution (VVD) being, respectively, the number density of the vesicles at their equivalent diameter and the volume fraction of the vesicles at their equivalent volume. VSD values are used commonly to infer kinematics of nucleation density and growth rates of bubbles. Specifically, cumulative VSD (CVSD) log plots have been observed to follow either exponential or power law distributions. Power law trends occur both in natural and experimental samples. It has been predicted that pure cascading coalescence produces a power law distribution with a fractal dimension $d = 4$, while continuous bubble nucleation yields lower d values that increase with the intensity of nucleation events or the length of the nucleation period up to a limit of $d = 2.45$ (Gonnermann and Houghton, 2012 and references therein). Exponential bubble size distributions are widely interpreted to reflect nucleation and viscosity-limited diffusional bubble growth (e.g., Toramaru 2006). Generally, pumices generated by purely magmatic processes show CVSD values that follow power law distributions for larger vesicles, while the smallest bubble sizes (e.g., Carey et al., 2009) show exponential trends that are interpreted to represent the bubble populations generated during ascent and eruption (e.g. Gonnermann and Houghton, 2012; Rotella et al., 2014).
The connectivity properties within the network of vesicles were investigated by the elaboration and analysis of their skeleton. This approach represents a powerful method for describing the structure, connectivity and tortuosity of a network, as demonstrated by recent applications to pore networks in carbonates (Zambrano et al., 2018) and volcanic rocks (Lanzafame et al., 2017). In detail, tortuosity (τ) is a crucial parameter to globally describe numerous features of the network (e.g. pore-throat size, organization and topology, see Baker et al., 2012a and references therein). We applied the *GVF* skeletonization algorithm (Brun et al. 2010), implemented in the *Pore3D* software, to VOIs of 400x400x400 voxels. Within the skeleton analysis, the vesicles are classified as "nodes" if connected with more than one vesicle or as "ends" if connected with only one vesicle. A further analysis of the skeletons allowed evaluation of the connectivity density (CD) parameter, a scalar representing the number of redundant connections normalized to the analyzed volume (V); it is computed as $(1 - (a - b))/V$), where a is the number of vesicles and b the number of connections between nodes (Brun et al., 2010; Zandomeneghi et al., 2010). The CD parameter can assume values from $-\infty$ to $+\infty$. Highly connected networks are characterized by positive values, whereas negative or close to zero values indicate the predominance of isolated objects. In general, CD increases with the degree of connectivity of the vesicles. In this study tortuosity has been computed as the ratio between the measured shortest path from one vesicle to another and their line distance with a minimum of 1 (straight line); the higher this value, the higher the complexity of the sample skeleton.
The 3D visualization of the reconstructed and processed images was performed by volume rendering procedures by means of the commercial software VGStudio MAX 2.0® (Volume Graphics, Germany).

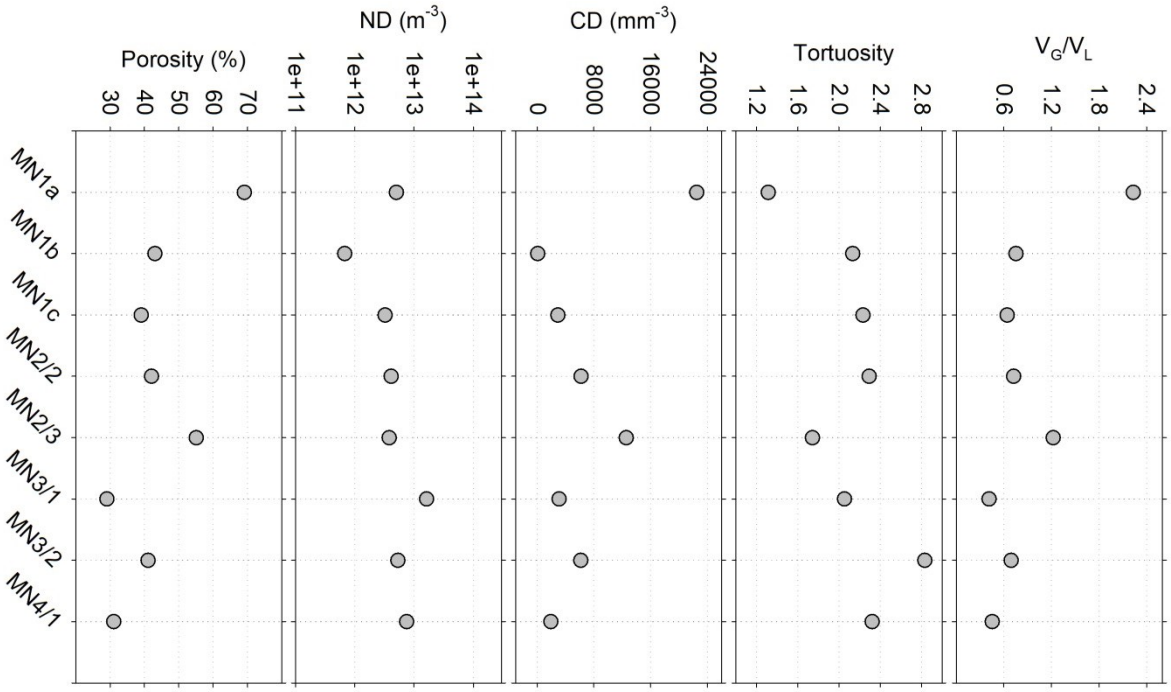

Fig. 6. Variation of porosity, number density (ND), connectivity density (CD), tortuosity (□) and VG/CL along the investigated stratigraphic sequence.

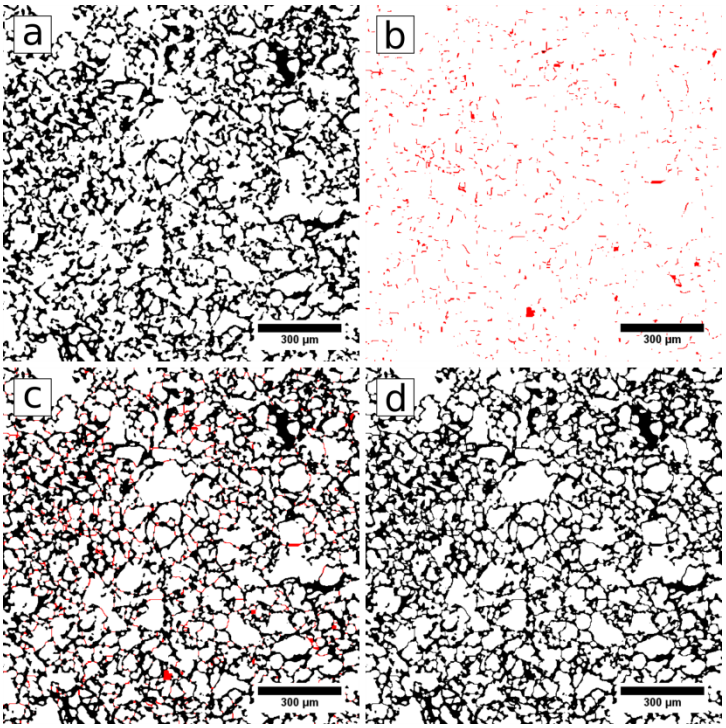

Fig. 7. Example of vesicle separation using the marker-based watershed algorithm of the Avizo 8® software. a) original slice (400 × 400 pixels^2) from MN1a sample after segmentation of pores (in white); b) calculated watershed lines; c) result of (a) + (b); d) final image showing separated vesicles.

5. Results

As stressed above, the observation of vesicle textures is a key method to assess conditions related to nucleation, growth and coalescence of gas bubbles and magma fragmentation (e.g. Cashman and Mangan, 1994).
In the following, we describe key textural features of vesicles investigated in representative pumice clasts, including porosity, vesicle number density, size and volume distribution, as well as pore structure (connectivity and tortuosity) for each unit of this eruption.

5.1. Porosity, Vesicle number density and Pore structure

Phreato-magmatic phase (Units I and II)
A main feature of the clasts from Unit I and II is the variety of textures suggesting complex degassing and fragmentation histories.
The most vesiculated clasts (MN1a-MN2/3) represent the most abundant pumice type of this phase of the eruption. This kind of clast is characterized by vesicle populations ranging from small (diameter <25 μm) spherical vesicles (Fig. 8) to irregular-shaped intermediate-to-large vesicles (> 25 μm) showing many stages of coalescence and separated by relatively thin (< 100 μm) films of glass (Fig. 9 and 10). On the other hand, dense clasts (MN1c, MN2/2) display more mature textures characterized by large, flattened, and generally oriented vesicles, possibly due to coalescence along the direction of maximum stretching as well as compaction. These vesicles range in size between 200 and 500 μm and are separated by thick glass walls (<500 μm). Unit I also includes fragments (e.g. banded pumice, MN1b) with intermediate morphological and textural characteristics between dense and high-vesiculated clasts, characterized by sharp contacts between vesicle-free and vesicle-rich zones.
The pumice samples (MN1a, b, c) of Unit I show the widest range of values in textural parameters (Fig. 6 and Table 2). In particular, porosity ranges from 69 (MN1a) to 39% (MN1c) and is positively correlated to connectivity density values ranging from 22433 to 2883 mm^{-3}. On the contrary, the two pumice samples from the Unit II have moderate porosity (42% for MN2/2 and 55% for MN2/3) as well as CD values of 6153 and 12517 mm^{-3}, respectively (Table 2).
The VND shows moderate values in both Units I and II ranging from 3.22 x 10^{12} m^{-3} to 4.98 x 10^{12} m^{-3}. With the exception of MN1b, all samples show a complex vesicle network, with high values of CD indicating a high degree of coalescence. Tortuosity values (from 1.31 to 2.29) are close to the minimum ($\tau = 1$ indicating a straight path, see section above) for the samples with a high number of vesicles, indicating a moderate (and similar) degree of complexity of the vesicle network (Fig. 6 and Table 2). The banded-pumice shows a decrease in the values of vesicle number density (0.67 x 10^{12} m^{-3}) as well as porosity (43%) and connectivity density. In particular, the CD value for this sample (41 mm^{-3}) differs by two or three orders of magnitude from the others, implying moderate coalescence of vesicles.

Magmatic phase (Unit III and IV)
Scoria sample textures from the magmatic phase (Unit III and IV) are relatively uniform and are characterized by zones of large (>100 μm) and intermediate vesicle sizes (50-100 μm) with polylobate and convoluted shapes, reflecting coalescence in variable directions. Evidence of flattening is also present in the larger vesicles, possibly as a consequence of vesicle collapse and reduction of porosity during permeable outgassing (see Fig. 10). Matrix-glass, ranging in thickness between 10 and 100 μm, is characterized by numerous small (< 25 μm in diameter) round vesicles (Fig. 8).
Textural parameters show a narrow range of values with respect to those of samples erupted in the first phase of the eruption (Fig. 6 and Table 2). Particularly, vesicularity ranges from 29 to 41%,

connectivity density from 1902 to 6113 mm^{-3}, and tortuosity from 2.05 to 2.83. Number density reaches higher values, ranging from 0.53 to 1.61 x 10^{13} m^{-3}.

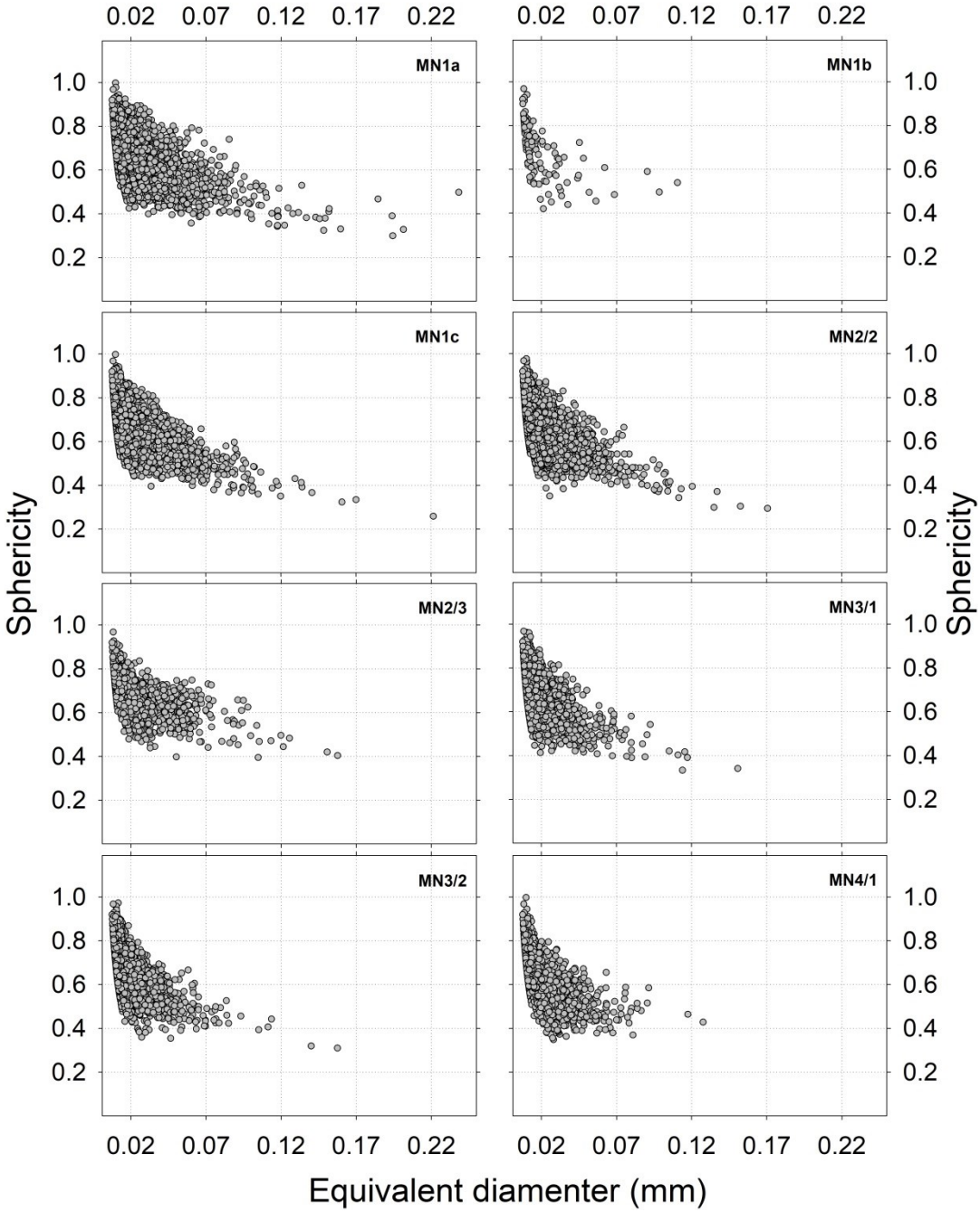

Fig. 8. Vesicle size vs. sphericity diagram for the different investigated samples. Parameters were extracted using the "Blob analysis" function of Pore3D. The vesicle size is calculated as the diameter of a sphere (D_{eq}) having an equivalent volume of the vesicle, sphericity is calculated as D_{max}/D_{eq}, where D_{max} is the diameter of the maximum inscribed sphere in the vesicle.

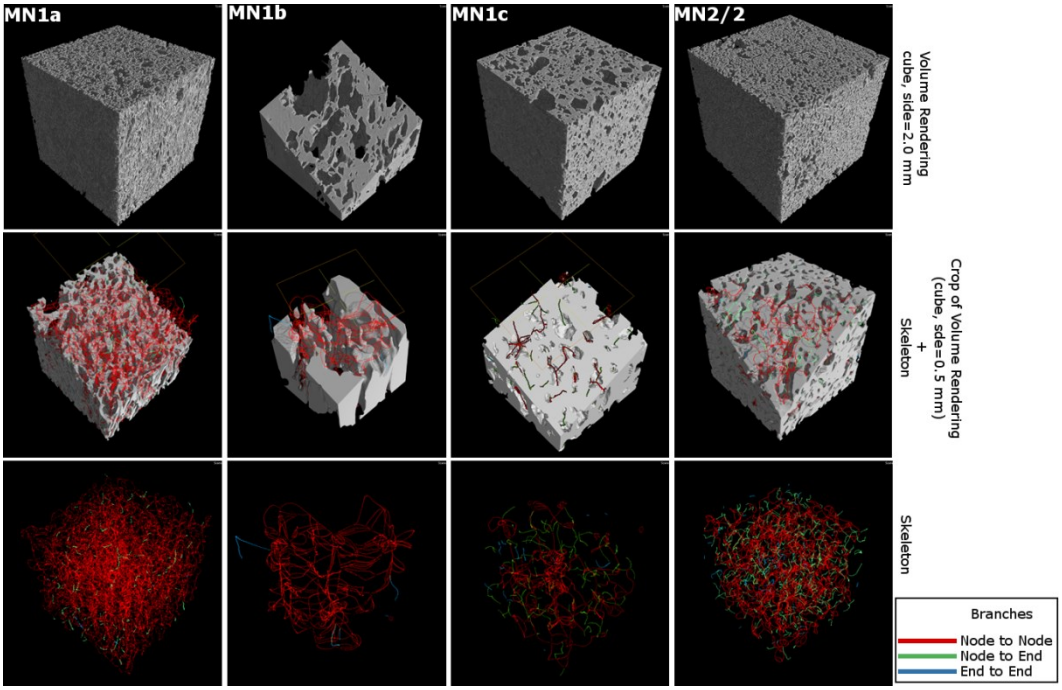

Fig. 9. Volume renderings and computed pore skeleton of selected VOI for MN1a, MN1b, MN1c and MN2/2 samples. Top row: renderings of the as reconstructed volume. Middle row: crop of the rendered volumes by an oblique plane with the whole skeleton represented. Bottom Row: only the skeleton is showed.

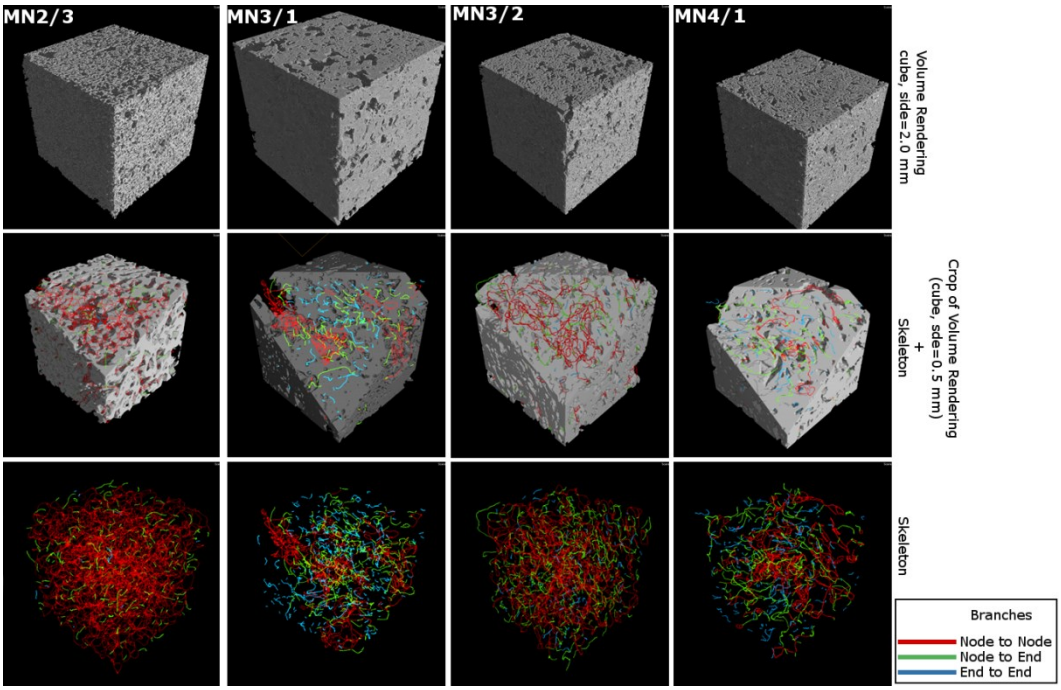

Fig. 10. Volume renderings and computed pore skeleton of selected VOI for MN2/3, MN3/1, MN3/2 and MN4/1 samples. Top row: renderings of the reconstructed volume. Middle row: crop of the rendered volumes by an oblique plane with the whole skeleton represented. Bottom Row: only the skeleton is shown.

5.2. Vesicle size and volume distributions

The CVSD values of the samples show a different behavior for the various stages of the eruption (Fig. 11). In pumice samples from phreato-magmatic phases (Unit I and II) CVSDs exhibit

continuous curved trends with small bubbles following an exponential distribution and larger bubbles following a power law distribution. The transition between exponential and power law distributions is generally observed for bubble sizes in the range of 20–50 μm, corresponding to the range of sizes commonly observed in silicic pyroclasts worldwide (e.g. Carey et al., 2009). Banded-pumices show CVSD curves that rapidly decrease towards low VND values and become less steep towards large-size classes.

On the contrary, the CVSDs of scoria samples from the last magmatic phases of the eruption (Unit III and IV) follow irregular trends formed by multiple curved segments (Fig. 11). These sorts of distributions have been previously recognized in both experimental and natural samples and interpreted as due to a) discrete vesiculation pulses driven by limestone assimilation (Blythe et al., 2015; Pappalardo et al., 2018) or b) a continuous vesiculation process characterized by fast rates of coalescence (Masotta and Keppler, 2014).

The different trends in the CVSD curves between phreato-magmatic and magmatic samples is also reflected in dissimilarity between VVD values. The VVDs of pumices of phreato-magmatic Units I and II show bimodality with a principal peak at <25 μm and a broad mode at 50-75 μm. The scoria samples from magmatic Units III and IV have very different vesicle volume distributions, showing narrow, relatively unimodal VVDs dominated by small sized vesicles (< 25 μm) (see Fig. 12).

Plots representing the ratio of vesicle volume (VG) to melt volume (VL) versus the vesicle number density (Fig. 13 and Table 2) show that phreato-magmatic pumice samples are characterized by fairly uniform VND despite slight variations in VG/VL. On the contrary, the scoria magmatic samples display a wider range in VND and more uniform VG/VL ratio.

The different VG/VL ratios versus VND between phreato-magmatic (MN1 and 2) and magmatic samples (MN3 and 4) suggests that the two types of samples experienced contrasting degassing histories in the shallow plumbing system. In particular the phreato-magmatic pumice samples show a large range of VG/VL values and constant VND, generally attributed to continuous nucleation and progressive free bubble growth causing an increase in the volume ratio of gas over melt. The magmatic pumice clasts show lower VG/VL values consistent with volatile loss through outgassing causing the collapse of large vesicles and a drop in VG/VL. In this latter case the increment in VND can be indicative of a further event of bubble nucleation.

5.3. Comparison with previous textural studies on Monte Nuovo eruption

The products of 1538 AD Monte Nuovo eruption were previously investigated by means of 2D textural analysis on thin sections (D'Oriano et al., 2005; Piochi et al. 2005, 2008; Mastrolorenzo and Pappalardo 2006) and permeability measurements on cm-sized samples (Polacci et al. 2014) of representative pumices and scoriae. To our knowledge, few 3D data are available (one pumice and one scoria, Piochi et al., 2008). However it's noteworthy that, until the present study, no 2D or 3D data existed on vesicle size distributions and pore network descriptors of pyroclasts emitted during this event. Our study found vesicle contents ranging from 39 to 69 vol% in pumices of Unit I and II, respectively. These results are in agreement with data obtained by 2D analysis of SEM images and density measurements reported in the literature (54-64 vol% - D'Oriano et al. (2005); 31-64 area% - Piochi et al. 2005; 33-83 area% - Piochi et al., 2008; 50 vol% - Mastrolorenzo and Pappalardo 2006). Piochi et al. (2008) report a vesicle content of 38 vol% from 3D analyses, whereas permeability measurements performed by Polacci et al. (2014) on pumices indicate connected porosity of 48 vol% and permeability values between 2.8 x 10^{-12} m^2. 2D literature data from scoriae of the Upper Member (Unit III and IV of this work) indicate vesicle contents of 40-55 vol% (D'Oriano et al. 2005), 40-41 area% (Piochi et al. 2005) and 41-63 area% (Piochi et al. 2008). Permeability measurements by Polacci et al. (2014) and 3D analysis by Piochi et al. (2008) report values of 1.6-9.3 x 10^{-11} m^2 with 51-62 vol% of connected porosity and 46 vol%, respectively. These data are slightly higher than those obtained in this work, ranging from 29 to 41 vol%. Vesicle number density determined in this study (10^{11}–10^{12} m^{-3} in pumices and 10^{12}–10^{13} m^{-3} in scoriae)

overlap those obtained by 2D and 3D investigations reported by Piochi et al. (2005, 2008) and Mastrolorenzo and Pappalardo (2006) (10^{11}-10^{13} m^{-3} in Unit I-II and in Units III-IV).

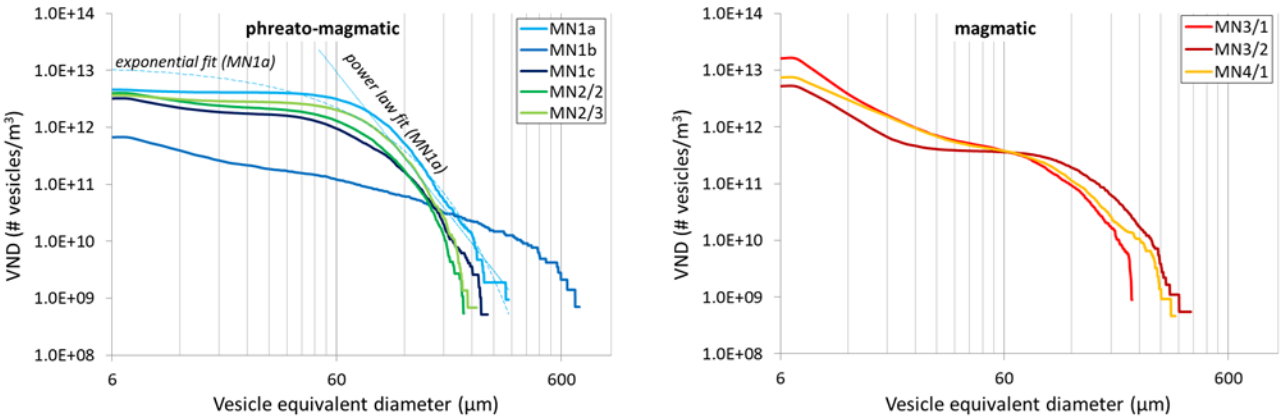

Fig. 11. Cumulative vesicle-size distributions (CVSD) for Monte Nuovo samples, represented as the number of vesicles, in the groundmass volume, larger than the equivalent diameter indicated in the abscissa. (log–log plot).

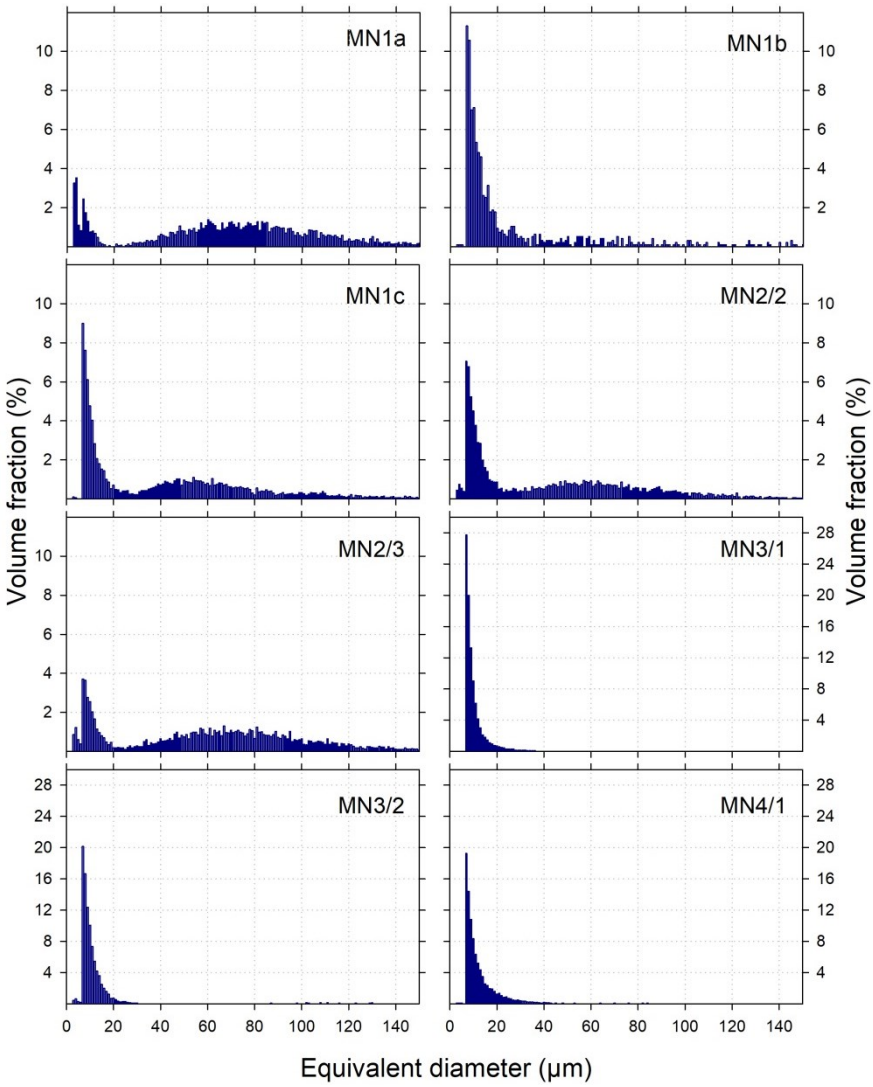

Fig. 12. Vesicle volume distributions (VVD) for studied samples of the Monte Nuovo eruption.

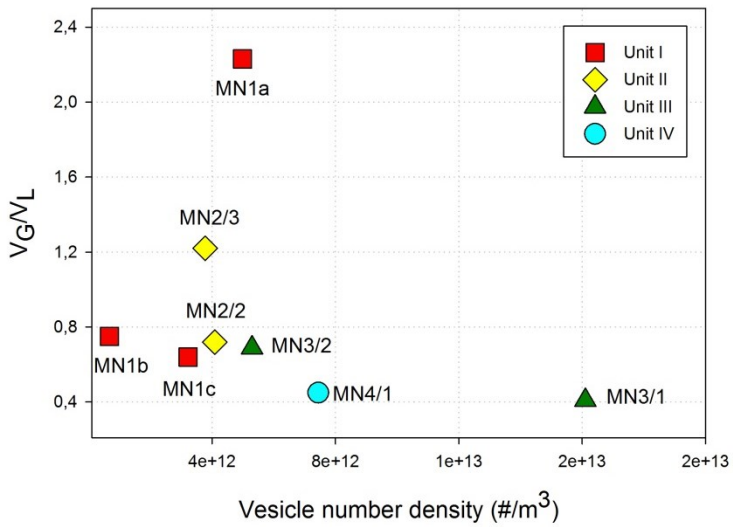

Fig. 13. Ratio of vesicles to melt volumes (VG/VL) against Vesicle Number Density (VND).

6. Discussion

The detailed description of the eruption given in the historical chronicles allows the reconstruction of the eruptive style evolution as observed on the surface during the different stages; thus in the following discussion we will use our 3D textural data to characterize the subvolcanic processes that occurred during magma ascent in the conduit for each stage and their relationship with the variations in the eruptive style observed by the contemporaries and described in the chronicles.

A complex dynamic mechanism characterized the beginning of the Monte Nuovo eruption. Historical chronicles report the opening of a new fracture on the seabed about 40–100 m from the coast and its subsequent propagation in the region between Lake Averno and Monte Barbaro, where the development of ground uplift, cracks and water springs preceded the opening of the main vent. Then "*continuous and violent expulsions with the development of columns of smoke (white and black) associated with incandescent material (flames, fire), stones, pumice, earth and muddy ash*" was described in the first two days of activity (29th and 30th September 1538, Guidoboni and Ciuccarelli, 2011). These accounts correspond well to the development of a limited eruption column and the generation of the ash-bearing pyroclastic density currents that originated the first two phreato-magmatic units (Unit I and II, Di Vito et al., 1987).

Our three-dimensional textural data of juvenile clasts from lower deposits (Units I and II) indicate that the volcanic products emitted during the first phreato-magmatic phase show highly variable textural characteristics, with porosities ranging from about 69 to 39 vol.% and a low-to-moderate microlite content (13 and 32 vol.%, Piochi et al., 2005; D'Oriano et al., 2005). However, the prevalence of the most vesiculated and microlite-poor clasts, dominating the phreato-magmatic deposits (see also D'Oriano et al., 2005), suggests that the water/magma interaction is predominantly a late process that occurs shallower within the conduit, when the magma is almost completely vesiculated. The co-existence of both exponential and power-law trends in CVSDs of these high-vesicularity pumices linked to the presence of bimodal VVDs distributions (Fig. 12) and a large range of VG/VL values at constant VND (Fig. 13) indicates a continuous vesiculation process during decompression (Gonnermann and Houghton, 2012 and references therein).

In this condition, the large bubbles' power-law trend can be attributed to the expansion and coalescence of earlier formed bubbles, while the small bubbles were formed during the last

nucleation event (exponential trend) in the shallow conduit (e.g., Gonnermann and Houghton, 2012; Rotella et al., 2014). Moreover vesicle populations are best fit by power laws with d = 4.72-5.67 (Table 2), quite close to prediction for the cascading coalescence mechanism.
These CVSD data, and the presence of a higher number of oriented vesicles with flattened shapes that become more evident in the dense clasts (MN1c, MN2/2 samples) from the same stratigraphic level (Units I and II), suggests the occurrence of progressive clast densification induced by outgassing. Coalescing bubbles may in fact promote high levels of interconnectivity (bubbles channels) allowing the gas to escape and the foam to collapse.
The complex shapes observed in the larger bubble population indicate that coalescence occurred on a time scale shorter than the characteristic viscous relaxation time scale (at least of 30 to 300 s for magma viscosity of 10^5 Pa s, according to the formulation reported in Carey et al., 2012), preventing bubbles from returning to spherical shapes prior to fragmentation (Janebo et al., 2016). This evidence could suggest quite rapid magma ascent, as also supported by the measured Vesicle Number Density values (0.67 to 4.98 x 10^{12} m^{-3}) corresponding to maximum mass eruption rates of 10^6 to 10^7 kg s^{-1} using the empirical relation from Mangan et al. (2014). Although this relationship has been defined for mafic compositions, it provides the same result on mass discharge rates (minimum value of 10^6 kg s^{-1}, D'Oriano et al., 2005) calculated for the trachytic melts emitted during the Monte Nuovo eruption. Numerical simulations (Aravena et al., 2018) demonstrated that such mass eruption rates for phonolitic and trachytic magmas produced unstable conditions favoring the access of external water into the conduit. In this scenario, the presence of bubbles in the magma causes a reduction in strength, thus making the magma more susceptible to breakage and promoting efficient phreato-magmatic fragmentation (e.g. Heap et al., 2014; Liu et al., 2017).
This mechanism of shallow magma/water interaction could also justify the presence in the lower Units of poorly-vesicular as well as banded-pumice clasts, associated with dominant highly-vesicular pumice. These denser clasts can be derived by the disruption, during the initial vent-opening phreato-magmatic explosions, of magma degassed by shear-related permeability along the conduit margins. Shear zones were possibly generated during the slow magma intrusion that triggered the development and propagation of the new fractures (dyke propagation) during the unrest that preceded the eruptions (e.g. "*progressive intensification of the earthquake frequency three months before the eruption*" by Guidoboni and Ciuccarelli, 2011) as well as by the development of horizontal gradients along the conduit (i.e., maximum velocity at the center, minimum at both conduit margins) during magma ascent.
On the morning of Tuesday 1 October, the activity decreased and then stopped completely. A new strong explosion occurred the 3th of October generating "*dark globular clouds which overran the sea for a few miles, along with a scattered shower of blocks*" (Guidoboni and Ciuccarelli, 2011). This phase of the eruption produced scoria deposits radially distributed around the vent (Unit III). After two more days of pause, a new explosion occurred on October 6th. The scoria deposits formed during this phase (Unit IV) covered a very limited area on the southern side of the cone, suggesting directional emplacement (Di Vito et al., 1987).
Samples collected from the scoria-bearing pyroclastic density currents of the upper Unit III and IV show more uniform characteristics with porosities around 30-40% and high contents of microlites (30-40%; D'Oriano et al., 2005; Piochi et al., 2005).
The volume ratio of vesicles to melt (VG/VL) (Fig. 13), low porosity and high crystallinity measured in the glass of these samples indicate an open-system degassing process under conditions of slow ascent or stasis, in the conduit, favoring the separation and removal of the gaseous phase (outgassing), the consequent lowering of the solidus temperature and the crystallization of microlites. This in turn led to a strong increase of the magma viscosity and the formation of a plug obstructing the conduit that triggered the last explosive phase of the eruption (Caricchi et al. 2008). Notably, results of crystallization experiments (Arzilli et al., 2016a) on trachy-phonolitic melts indicate an increase in crystal fraction between 30 and 50 MPa with timescales between several hours to ~3 days. The textural features observed in natural samples are then consistent with the

repose intervals of days reported by chronicles before the magmatic explosions. During the prolonged residence time (days) in the shallower conduit, extended connectivity and coalescence favored protracted outgassing and bubble collapse. In these open-system degassing conditions, experimental studies show a reduction in the number of small vesicles due to the collapse of micro-bubbles networks during outgassing, as a consequence of magma densification driven by surface tension stresses (Kennedy et al., 2016).

In contrast, the scoria samples analyzed in this study, despite their connectivity density and tortuosity values that fall in the range of those measured in pumices, show an increase in the number density associated with a unimodal pattern of vesicle volume distributions (VVDs). These observations suggest the occurrence of a late event of rapid nucleation with the generation of a large number of small and spherical bubbles (Fig. 8). The multiple trends of CVSDs of these scoriae also could be indicative of discrete nucleation events. We infer that during the stasis of the eruptive activity the degassed magma (coarse part of the CVSD curve, with larger coalesced and collapsed bubbles) was forced to erupt due to a rapid decompression event (smaller bubbles) induced by internal (disruption of a highly viscous magma plug) or external (the collapse of a flank of the volcanic edifice) triggering factors. The last process can justify the sharp scar, well visible in the southern sector of the volcano, where the magmatic deposit reaches its maximum thickness.

However in both cases (internal or external triggering) the rapid decompression-induced nucleation (of small and spherical bubbles) could be attributed to different processes (in heterogeneous or homogeneous conditions): (i) second boiling driven by rapid crystallization; (ii) a sharp change in the decompression rate during the ascent of already vesiculated melts near the fragmentation level; and (iii) downward propagation of a rarefaction wave into the conduit generated by plug rupture/flank collapse. In the Monte Nuovo case study, it is arduous to discriminate between homogeneous versus heterogeneous nucleation. However, no correspondence is observed between the small spherical bubbles and petrographically-observable microlites (especially Fe-Ti oxides, Fig. 4) acting as nucleation sites; despite this observation we cannot exclude the influence of nano-scale crystals on bubbles nucleation. Actually, Preuss et al. (2016) found a maximum supersaturation pressure of 76 MPa for trachyte for homogeneous nucleation. This value corresponds to that found for microlite crystallization by decompression experiments (Arzillli et al., 2016a) on Monte Nuovo magmas, thus supporting the hypothesis that a stationary magma could occur at this depth in the conduit (≤ 3 km of depth). In this state, the crystallization of elongated microlites contributes to increasing melt viscosity (Caricchi et al., 2008; and Vona et al., 2013), enhancing fragmentation during the subsequent bubble nucleation event.

7. Conclusions

The three-dimensional textural characterization of pyroclasts erupted during the Monte Nuovo event has been conducted defining a new protocol for 3D image analysis of highly-vesiculated volcanic rocks.

Our results indicate that considerable vesiculation took place prior to magma-water interaction during the opening phreato-magmatic activity. In particular, magma vesiculation in this phase occurred under quasi-closed system degassing at a critical mass eruption rate that produced unstable conditions favoring the access of external water into the conduit. This mechanism of shallow magma/water interaction can also explain the presence in the lower Units of low vesicularity scoria as well as banded-pumice clasts. These denser clasts can be derived by the disruption, during the initial vent-opening phreatic explosions, of the magma degassed by shear-related permeability along the conduit margins during syn-eruptive dyke propagation and magma ascent. The seismic activity as well as the ground uplift that preceded the eruption suggest the gradual activation of the hydrothermal system by the recurrent intrusion of magma at shallow levels (arrested dykes, Fig. 14). This process possibly caused the weakening (heating) of the crustal rocks, thus favoring the

propagation of fractures towards the surface (feeder dykes, Fig. 14). The rapid decompression of the hydrothermal fluid could be the cause of the phreatic activity (e.g. formation of water springs associated with cracks opening) described in the chronicles and the fast expulsion of most of the magma volume present in the chamber (phreato-magmatic phase). The subsequent ascent of small magma batches from the remnant, deeper, portion of the storage zone fed the last purely magmatic phases. The textural features in the resulting rocks indicate open system degassing conditions (outgassing) during slow magma ascent or a pause during ascent in the conduit. This is consistent with the rest interval of days reported by chronicles before magmatic explosions were triggered by internal or external factor (plug disruption and/or flank collapse). Notably, these results confirm those obtained on crystallization experiments of trachy-phonolitic melts indicating extensive crystallization between 30-50 MPa in response to magma degassing during ascent in the conduit.
The reconstructed syn-eruptive scenario suggests that long-lasting episodes of unrest that characterize calderas can be the consequence of the recurrent migration of magma at shallower levels that occasionally can fracture overlying country-rocks, reach the surface and erupt. In this view, information on magma ascent processes and timescale inferred from 3D analyses of eruption products could thus help decipher geophysical and geochemical signals recorded by monitoring networks at Campi Flegrei and active calderas worldwide.

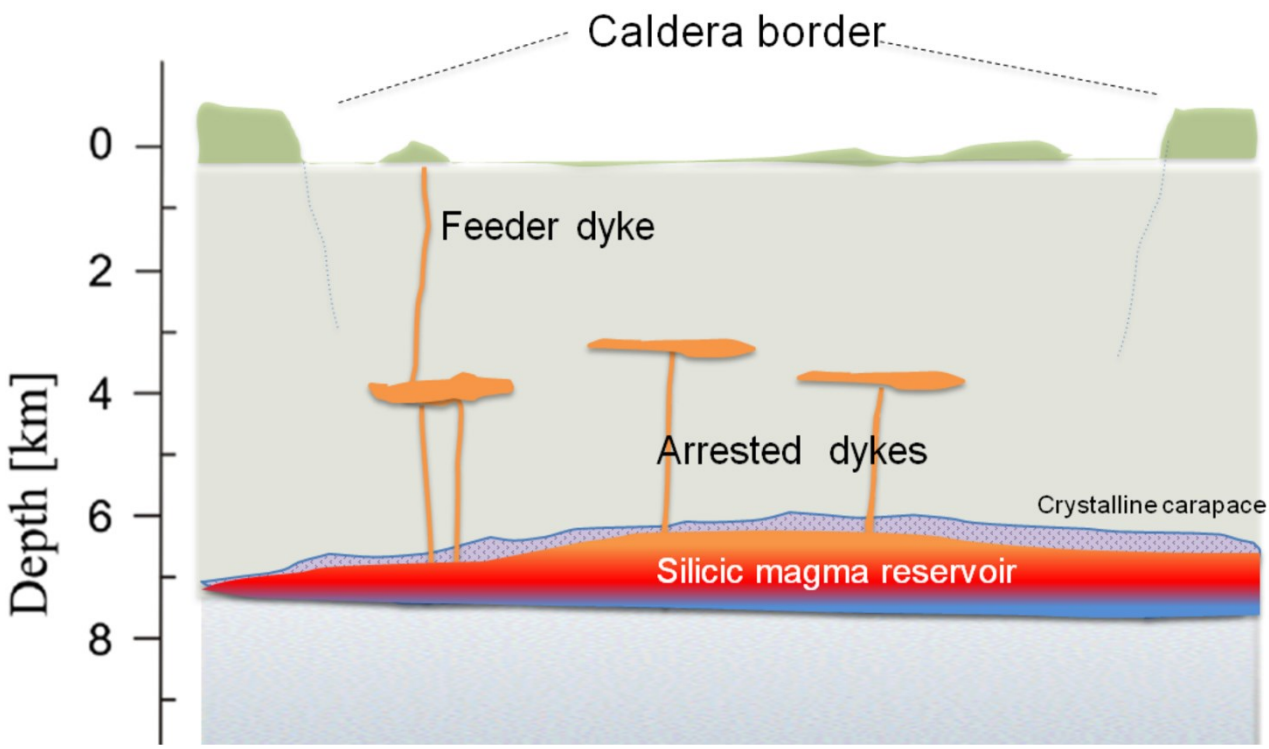

Fig. 14. Geological model of the plumbing system of the Campi Flegrei caldera during the Monte Nuovo eruption. The syn-eruptive scenario reconstructed on the basis of 3D textural data of emitted pyroclasts and historical chronicles suggests the possible recurrent migration of magma at shallower level (arrested dykes) before the eruption. This process possibly caused the weakening (heating) of the crustal rocks, thus favoring the propagation of fractures towards the surface (feeder dyke) triggering the eruption (see the text for further explanation).

Acknowledgements

We thank Stephan Kolzenburg and an anonymous reviewer for comments that greatly improved the manuscript. We gratefully acknowledge the critical reading of the manuscript by Don Baker.

The Grant to Department of Science, Roma Tre University (MIUR-Italy Dipartimenti di Eccellenza, ARTICOLO 1, COMMI 314 – 337 LEGGE 232/2016) is gratefully acknowledged.

References

Aravena, Á., Cioni, R., De'michieli Vitturi, M., Neri, A., 2018. Conduit stability effects on intensity and steadiness of explosive eruptions. Sci. Rep. 8, 1–9. https://doi.org/10.1038/s41598-018-22539-8

Arzilli, F., Piochi, M., Mormone, A., Agostini, C., Carroll, M.R. (2016a). Constraining pre-eruptive magma conditions and unrest timescales during the Monte Nuovo eruption (1538 AD; Campi Flegrei, Southern Italy): integrating textural and CSD results from experimental and natural trachy-phonolites. Bull Volcanol (2016) 78: 72, DOI 10.1007/s00445-016-1062-z

Arzilli, F., Polacci, M., Landi, P., Giordano, D., Baker, D.R., Mancini, L. (2016b). A novel protocol for resolving feldspar crystals in synchrotron X-ray microtomographic images of crystallized natural magmas and synthetic analogs. American Mineralogist, Volume 101, pages 2301–2311, DOI: http://dx.doi.org/10.2138/am-2016-5788 2301

Baker, D.R., Brun, F., O'Shaughnessy, C., Mancini, L., Fife, J.L., Rivers, M., 2012a. A four-dimensional X-ray tomographic microscopy study of bubble growth in basaltic foam, Nat. Commun., 3, 1135. https://doi.org/10.1038/ncomms2134

Baker, D.R., Mancini, L., Polacci, M., Higgins, M.D., Gualda, G.A.R., Hill, R.J., Rivers, M.L., 2012b. An introduction to the application of X-ray microtomography to the three-dimensional study of igneous rocks. Lithos 148, 262–276. https://doi.org/10.1016/j.lithos.2012.06.008

Baruchel, J., Cloetens, P., Hartiw, J., Ludwig, W., Mancini, L., Pernot, P., Schlenker, M., 2000. Phase imaging using highly coherent X-rays : radiography, tomography , diffraction topography. J. Synchrotron Radiat. 7, 196–201. https://doi.org/10.1107/S0909049500002995

Blythe, L.S., Deegan, F.M., Jolis, C.F.E.M., Misiti, M.M.V, 2015. CO 2 bubble generation and migration during magma–carbonate interaction. Contrib. Mineral. Petrol. https://doi.org/10.1007/s00410-015-1137-4

Brun, F., Mancini, L., Kasae, P., Favretto, S., Dreossi, D., Tromba, G., 2010. Nuclear Instruments and Methods in Physics Research A Pore3D : A software library for quantitative analysis of porous media. Nucl. Inst. Methods Phys. Res. A 615, 326–332. https://doi.org/10.1016/j.nima.2010.02.063

Brun, F., Kourousias, G., Dreossi, D., Mancini, L. & Tromba, G. (2011). A comparative evaluation of ring artifacts reduction filters for X-ray computed microtomography images. Proceedings of the International Conference on Image Processing, ICP 6116535, 405–408

Brun, F., Massimi, L., Fratini, M., Dreossi, D., Billé, F., Accardo, A., Pugliese, R., Cedola, A., 2017. SYRMEP Tomo Project : a graphical user interface for customizing CT reconstruction workflows. Adv. Struct. Chem. Imaging. https://doi.org/10.1186/s40679-016-0036-8

Carey, R.J., Houghton, B.F., Thordarson, T., 2009. Abrupt shifts between wet and dry phases of the 1875 eruption of Askja Volcano : Microscopic evidence for macroscopic dynamics. J. Volcanol. Geotherm. Res. 184, 256–270. https://doi.org/10.1016/j.jvolgeores.2009.04.003

Carey, R.J., Manga, M., Degruyter, W., Swanson, D., Houghton, B., Orr, T., Patrick, M., 2012. Externally triggered renewed bubble nucleation in basaltic magma: The 12 October 2008 eruption at Halemaumau Overlook vent, Klauea, Hawai'i, USA. J. Geophys. Res. B Solid Earth 117, 1–10. https://doi.org/10.1029/2012JB009496

Caricchi, L., Giordano, D., Burlini, L., Ulmer, P., Romano, C., 2008. Rheological properties of magma from the 1538 eruption of Monte Nuovo (Phlegrean Fields , Italy): An experimental study. Chem. Geol. 256, 157–170. https://doi.org/10.1016/j.chemgeo.2008.06.035

Cashman, K.V. and Mangan, M.T. (1994). Physical Aspects of Magmatic Degassing II. Constraints on Vesiculation Processes from Textural Studies of Eruptive Products. In: Carroll, M.R. and Holloway, J.R., Eds., Volatiles in Magmas, Mineralogical Society of America, Chantilly, 447-478

Chiodini, G., Caliro, S., De Martino, P., Avino, R., Gherardi, F., 2012. Early signals of new volcanic unrest at Campi Flegrei caldera? Insights from geochemical data and physical simulations. Geology 40, 943–946. https://doi.org/10.1130/G33251.1

Chiodini, G., Pappalardo, L., Aiuppa, A., and Caliro, S., 2015. The geological CO2 degassing history of a long-lived caldera. Geology 43, 767-770. doi:10.1130/G369051

Chiodini, G., Paonita, A., Aiuppa, A., Costa, A., Caliro, S., Martino, P. De, Acocella, V., Vandemeulebrouck, J., 2016. Magmas near the critical degassing pressure drive volcanic unrest towards a critical state. Nat. Commun. 7, 1–9. https://doi.org/10.1038/ncomms13712

Cloetens, P., Buffière, J.Y., Peix, G., Baruchel, J., 1997. Observation of microstructure and damage in materials by phase sensitive radiography and tomography radiography and tomography. J. Appl. Phys. 81, 5878. https://doi.org/10.1063/1.364374

Cnudde V. and Boone M.N., 2013: High-resolution X-ray computed tomography in geosciences: a review of the current technology and applications. Earth-Sci. Rev. 123, 1–17

D'Auria, L., Pepe, S., Castaldo, R., Giudicepietro, F., Macedonio, G., Ricciolino, P., Tizzani, P., Casu, F., Lanari, R., Manzo, M., Martini, M., Sansosti, E., Zinno, I., 2015. Magma injection beneath the urban area of Naples: A new mechanism for the 2012-2013 volcanic unrest at Campi Flegrei caldera. Sci. Rep. 5, 1–11. https://doi.org/10.1038/srep13100

Deino, A.L., Orsi, G., Vita, S. De, Piochi, M., 2004. The age of the Neapolitan Yellow Tuff caldera-forming eruption (Campi Flegrei caldera - Italy) assessed by Ar / 39 Ar dating method. J. Volcanol. Geotherm. Res. 133, 157–170. https://doi.org/10.1016/S0377-0273(03)00396-2

Di Genova, D., Kolzenburg, S., Wiesmaier, S., Dallanave, E., Neuville, D.R., Hess, K.U., Dingwell, D.B. (2017) A compositional tipping point governing the mobilization and eruption style of rhyolitic magma. Nature 552, pp. 235–238

Di Vito, M., Lirer, L., Mastrolorenzo, G., Rolandi, G., 1987. The 1538 Monte Nuovo eruption (Campi Flegrei, Italy) Mauro. Bull. Volcanol. 49, 608–615

Di Vito, M., Isaia, R., Orsi, G., Southon, J., De Vita, S., D'Antonio, M., Pappalardo, L., Piochi, M., 1999. Volcanism and deformation since 12,000 years at the Campi Flegrei caldera (Italy). J. Volcanol. Geotherm. Res. 91, 221–246

Di Vito, M., Acocella, V., Aiello, G., Barra, D., Battaglia, M., Carandente, A., Del Gaudio, C., De Vita, S., Ricciardi, G.P., Ricco, C., Scandone, R., Terrasi, F., 2016. Magma transfer at Campi Flegrei caldera (Italy) before the 1538 AD eruption. Sci. Rep. 6, 1–9. https://doi.org/10.1038/srep32245

D'Oriano, C., Poggianti, E., Bertagnini, A., Cioni, R., Landi, P., Polacci, M., Rosi, M., 2005. Changes in eruptive style during the A .D. 1538 Monte Nuovo eruption (Phlegrean Fields , Italy): the role of syn-eruptive crystallization. Bull. Volcanol. 67, 601–621. https://doi.org/10.1007/s00445-004-0397-z

Dvorak, J.J. and Gasparini, P., 1991. History of earthquakes and vertical ground movement in Campi Flegrei caldera, Southern Italy : comparison of precursory events to the A. D. 1538 eruption of Monte Nuovo and of activity since 1968. J. Volcanol. Geotherm. Res. 48, 77–92

Dvorak, J.J. and Mastrolorenzo, G., 1991. The Mechanism of Recent Vertical Crustal Movements in Campi Flegrei Caldera, Southern Italy. The Geological Society of America, 263

Fedi, M., Cella, F., D'Antonio, M., Florio, G., Paoletti, V., Morra, V., 2018. Gravity modeling finds a large magma body in the deep crust below the Gulf of Naples, Italy. Sci. Rep. 8, 1–19. https://doi.org/10.1038/s41598-018-26346-z

Gebauer, S.K., Schmitt, A.K., Pappalardo, L., Stockli, D.F., Lovera, O.M., 2014. Crystallization and eruption ages of Breccia Museo (Campi Flegrei caldera , Italy) plutonic clasts and their relation to the Campanian ignimbrite. Contrib. Mineral. Petrol. 167, 953. https://doi.org/10.1007/s00410-013-0953-7

Gonnermann, H.M., Houghton, B.F., 2012. Magma degassing during the Plinian eruption of Novarupta, Alaska, 1912. Geochemistry Geophys. Geosystems 13, 1–20. https://doi.org/10.1029/2012GC004273

Guidoboni, E., Ciuccarelli, C., 2011. The Campi Flegrei caldera: historical revision and new data on seismic crises, bradyseisms, the Monte Nuovo eruption and ensuing earthquakes (twelfth century 1582 AD). Bull. Volcanol., 73, 655–677. DOI: http://doi.org/10.1007/s00445-010-0430-3

Heap, M.J., Xu, T., Chen, C., Feng, 2014. The influence of porosity and vesicle size on the brittle strength of volcanic rocks and magma. Bull. Volcanol. 76, 1–15. https://doi.org/10.1007/s00445-014-0856-0

Herman, G.T., 1980. Image Reconstruction from Projections: The Fundamentals of Computerized Tomography. Academic Press, New York

Isaia, R., Marianelli, P., Sbrana, A., 2009. Caldera unrest prior to intense volcanism in Campi Flegrei (Italy) at 4.0 ka B. P.: Implications for caldera dynamics and future eruptive scenarios. Geophys. Res. Lett. 36, 1–6. https://doi.org/10.1029/2009GL040513

Janebo, M.H., Houghton, B.F., Thordarson, T., Larsen, G., 2016. Shallow conduit processes during the ad 1158 explosive eruption of Hekla volcano, Iceland. Bull. Volcanol. 78. https://doi.org/10.1007/s00445-016-1070-z

Kennedy, B.M., Wadsworth, F.B., Vasseur, J., Ian Schipper, C., Mark Jellinek, A., von Aulock, F.W., Hess, K.U., Kelly Russell, J., Lavallée, Y., Nichols, A.R.L., Dingwell, D.B., 2016. Surface tension driven processes densify and retain permeability in magma and lava. Earth Planet. Sci. Lett. 433, 116–124. https://doi.org/10.1016/j.epsl.2015.10.031

Ketcham, R.A., and Carlson, W.D., 2001, Acquisition, optimization and interpretation of X-ray computed tomographic imagery: Applications to the geosciences: Comput. Geosci., 27, 381–400, https://doi.org/10.1016/S0098-3004(00)00116-3

Kolzenburg, S., Di Genova, D., Giordano, D., Hess, K.U., Dingwell, D.B., (2018). The effect of oxygen fugacity on the rheological evolution of crystallizing basaltic melts. Earth and Planet. Sci. Lett., 487, 21-32. https://doi.org/10.1016/j.epsl.2018.01.023

Lanzafame, G., Iezzi, G., Mancini, L., Lezzi, F., Mollo, S., Ferlito, C., 2017. Solidification and turbulence (non-laminar) during magma ascent: insights from 2D and 3D analyses of bubbles and minerals in an Etnean dyke. J. Petrol. 58, 1511–1533

Lanzafame, G., Ferlito, C., Donato, S., 2018. Combining chemical and X-Ray microtomography investigations on crustal xenoliths at Mount Etna: evidence of volcanic gas fluxing. Annals of Geophysics 61, https://doi.org/10.4401/ag-7740.

Liu, E.J., Cashman, K.V., Rust, A.C., Höskuldsson, A., 2017. Contrasting mechanisms of magma fragmentation during coeval magmatic and hydromagmatic activity: the Hverfjall Fires fissure eruption, Iceland. Bull. Volcanol. 79. https://doi.org/10.1007/s00445-017-1150-8

Maire, E., Withers, P.J., 2014. Quantitative X-ray tomography. Int. Mater. Rev. 59, 1–43. https://doi.org/10.1179/1743280413Y.0000000023

Mangan, M.T., Cashman, K.V., Swanson, D.A., 2014. The dynamics of Hawaiian-style eruptions: a century of study. In: Poland, M.P., Takahashi, T.J. and Landowski, C.M. (ed). Characteristics of Hawaiian volcanoes. US Geological Survey, pp. 323–35

Masotta, M., Ni, H., Keppler, H., 2014. In situ observations of bubble growth in basaltic, andesitic and rhyodacitic melts. Contrib. to Mineral. Petrol. 976. https://doi.org/10.1007/s00410-014-0976-8

Mastrolorenzo, G. and Pappalardo, L., 2006. Magma degassing and crystallization processes during eruptions of high-risk Neapolitan-volcanoes : Evidence of common equilibrium rising processes in alkaline magmas. Earth Planet. Sci. Lett. 250, 164–181. https://doi.org/10.1016/j.epsl.2006.07.040

Mastrolorenzo, G., Pappalardo, L., Troise, C., Panizza, A., Natale, G. De, 2008. Probabilistic tephra hazard maps for the Neapolitan area : Quantitative volcanological study of Campi Flegrei eruptions. J. Geophys. Res. 113, 1–14. https://doi.org/10.1029/2007JB004954

Mastrolorenzo, G., Palladino, D.M., Pappalardo, L., Rossano, S., 2017. Probabilistic-numerical assessment of pyroclastic current hazard at Campi Flegrei and Naples city : Multi-VEI scenarios as a tool for "full-scale" risk management. PLoS ONE 12(10): e0185756. https://doi.org/10.1371/journal.pone.0185756

Moretti, R., Arienzo, I., Di Renzo, V., Orsi, G., Arzilli, F., Brun, F., D'Antonio, M., Mancini, L., Deloule, E., 2019. Volatile segregation and generation of highly vesiculated explosive magmas by volatile-melt fining processes: the case of the Campanian Ignimbrite eruption. Chem. Geol. 503, 1-14

Orsi, G., Di Vito, M.A., Isaia, R., 2004. Volcanic hazard assessment at the restless Campi Flegrei caldera. Bull. Volcanol. 66, 514–530. https://doi.org/10.1007/s00445-003-0336-4

Otsu, N., 1979. A Threshold Selection Method from Gray-Level Histograms. IEEE Trans. Syst. Man Cybern. 20, 62–66.

Paganin D., Mayo S.C., Gureyev T.E., Wilkins P.R., and Wilkins S.W.. 2002. Simultaneous phase and amplitude extraction from a single defocused image of a homogeneous object, J. Microsc. 206, 33–40

Pappalardo, L. and Mastrolorenzo, G., 2010. Short residence times for alkaline Vesuvius magmas in a multi-depth supply system, Evidence from geochemical and textural studies. Earth Plan. Sci. Lett. 296, 133–143

Pappalardo, L. and Mastrolorenzo, G., 2012. Rapid differentiation in a sill-like magma reservoir: A case study from the campi flegrei caldera. Sci. Rep. 2, Article number, 712. https://doi.org/10.1038/srep00712

Pappalardo, L., Civetta, L., D'Antonio, M., Deino, A.L., Di Vito, M., Orsi, G., Carandente, A., De Vita, S., Isaia, R., Piochi, M., 1999. Chemical and Sr-isotopical evolution of the Phlegraean magmatic system before the Campanian Ignimbrite and the Neapolitan Yellow Tuff eruptions. J. Volcanol. Geotherm. Res. 91, 141–166

Pappalardo, L., Piochi, M., D'Antonio, M., Civetta, L., Petrini, R., 2002. Evidence for Multi-stage Magmatic Evolution during the past 60 kyr at Campi Flegrei (Italy) Deduced from Sr, Nd and Pb Isotope Data. J. Petrol. 43, 1415–1434. https://doi.org/10.1093/petrology/43.8.1415

Pappalardo, L, Piochi, M, Mastrolorenzo, G., 2004. The 3550 YR BP - 1944 AD magma-plumbing system of Somma-Vesuvius: constraints on its behavior and present state through a review of Sr-Nd isotope data. Annals of Geophysics 47, 4, 1471-1483

Pappalardo, L., Ottolini, L., Mastrolorenzo, G., 2008. The Campanian Ignimbrite (southern Italy) geochemical zoning : insight on the generation of a super-eruption from catastrophic differentiation and fast withdrawal. Contrib. Mineral. Petrol. 156, 1–26. https://doi.org/10.1007/s00410-007-0270-0

Pappalardo, L., D'Auria, L., Cavallo, A., Fiore, S., 2014. Petrological and seismic precursors of the paroxysmal phase of the last Vesuvius eruption on March 1944. Scientific Reports 4, Article number: 6297. https://doi.org/10.1038/srep06297

Pappalardo, L., Buono, G., Fanara, S., Petrosino, P., 2018. Combining textural and geochemical investigations to explore the dynamics of magma ascent during Plinian eruptions: a Somma–Vesuvius volcano (Italy) case study. Contrib. Mineral. Petrol. 173, 61

Parascandola, A., 1946. Il Monte Nuovo e Il lago Lucrino. Boll. Soc. Nat. 55, 173–175

Piochi, M., Mastrolorenzo, G., Pappalardo, L., 2005. Magma ascent and eruptive processes from textural and compositional features of Monte Nuovo pyroclastic products, Campi Flegrei , Italy. Bull. Volcanol. 67, 663–678. https://doi.org/10.1007/s00445-005-0410-1

Piochi, M., Polacci, M., De Astis, G., Zanetti, A., Mangiacapra, A., Vannucci, R., Giordano, D., 2008. Texture and composition of pumices and scoriae from the Campi Flegrei caldera (Italy): Implications on the dynamics of explosive eruptions. Geochem. Geophys. Geosyst. 9, 3

Polacci, M., Mancini, L., Baker, D.R., 2010. The contribution of synchrotron X-ray computed microtomography to understanding volcanic processes soil and geosciences. J. Synchrotron Radiat. 17, 215–221. https://doi.org/10.1107/S0909049509048225

Polacci, M., Maisonneuve, C.B. De, Giordano, D., Piochi, M., Mancini, L., Degruyter, W., Bachmann, O., 2014. Permeability measurements of Campi Flegrei pyroclastic products : an example from the Campanian Ignimbrite and Monte Nuovo eruptions. J. Volcanol. Geotherm. Res. 272, 16–22. https://doi.org/10.1016/j.jvolgeores.2013.12.002

Polacci, M., Arzilli, F., La Spina, G., Le Gall, N., Cai, B., M.E. Hartley, Di Genova D., Vo, N.T., Nonni S., Atwood, R.C., Llewellin, E.W., Lee, P.D. and Burton, M.R., 2018. Crystallisation in basaltic magmas revealed via in situ 4D synchrotron X-ray microtomography. Sci. Rep., 8, 8377. https://www.nature.com/articles/s41598-018-26644-6

Preuss, O., Marxer, H., Ulmer, S., Wolf, J., Nowak, M., 2016. Degassing of hydrous trachytic Campi Flegrei and phonolitic Vesuvius melts: experimental limitations and chances to study homogeneous bubble nucleation. Am. Mineral. 101, 859–875

Rosi, M. and Santacroce, R., 1984. Volcanic Hazard Assessment in the Phlegraean Fields: a Contribution Based on Stratigraphic and Historical Data. Bull. Volcanol. 47, 359–370

Rosi, M. and Sbrana, A., 1987. Phlegrean Fields. Quad. della Ric. Sci. 114, 175

Rotella, M.D., Wilson, C.J.N., Barker, S.J., Cashman, K.V., Houghton, B.V., Wright, I.C., 2014. Bubble development in explosive silicic eruptions : insights from pyroclast vesicularity textures from Raoul volcano (Kermadec arc). Bull. Volcanol. 76, 826. https://doi.org/10.1007/s00445-014-0826-6

Rust, A.C. and Cashman, K.V., 2011. Permeability controls on expansion and size distributions of pyroclasts. J. Geophys. Res. Solid Earth 116, 1–17. https://doi.org/10.1029/2011JB008494

Scarpati, C., Sparice, D., Perrotta, A., 2015. The ground layer of the Campanian Ignimbrite : an example of deposition from a dilute pyroclastic density current. Bull. Volcanol. 77, 1–10. https://doi.org/10.1007/s00445-015-0985-0

Shea, T., Houghton, B.F., Gurioli, L., Cashman, K.V., Hammer, J.E., Hobden, B.J., 2010. Textural studies of vesicles in volcanic rocks: An integrated methodology. J. Volcanol. Geotherm. Res. 190, 271–289. https://doi.org/10.1016/j.jvolgeores.2009.12.003

Soille, S., 2003. Morphological Image Analysis, Principles and Applications- 2nd edition. Springer

Toramaru, A., 2006. BND (bubble number density) decompression rate meter for explosive volcanic eruptions. J. Volcanol. Geotherm. Res. 154, 303–316. https://doi.org/10.1016/j.jvolgeores.2006.03.027

Vitale, S., Isaia, R., 2014. Fractures and faults in volcanic rocks (Campi Flegrei , southern Italy): insight into volcano - tectonic processes. Int. J. Earth Sci. 103, 801–819. https://doi.org/10.1007/s00531-013-0979-0

Voltolini, M., Zandomeneghi, D., Mancini, L., Polacci, M., 2011. Texture analysis of volcanic rock samples : Quantitative study of crystals and vesicles shape preferred orientation from X-ray microtomography data. J. Volcanol. Geotherm. Res. 202, 83–95. https://doi.org/10.1016/j.jvolgeores.2011.02.003

Vona, A., Romano, C., Giordano, D., Russell, J.K., 2013. The multiphase rheology of magmas from Monte Nuovo (Campi Flegrei, Italy). Chem. Geol. 346, 213–227. https://doi.org/10.1016/j.chemgeo.2012.10.005

Withers, P.J. (2008). X-ray nanotomography. Mater. Today 10, 12, pp. 26-34

Wu, W.N., Schmitt, A.K., Pappalardo, L., 2015. U-Th baddeleyite geochronology and its significance to date the emplacement of silica undersaturated magmas. Am. Mineral. 100, 2082–2090

Zambrano, M., Tondi E., Mancini, L., Lanzafame, G., Trias, X.F., Arzilli, F., Materazzi, M., Torrieri, S., 2018. Fluid flow simulation and permeability computation in deformed porous carbonate grainstones. Advan. Wat. Res. 115, 95-111

Zandomeneghi, D., Voltolini, M., Mancini, L., Brun, F., Dreossi, D., Polacci, M., 2010. Quantitative analysis of X-ray microtomography images of geomaterials : Application to volcanic rocks. Geosphere 6, 793–804. https://doi.org/10.1130/GES00561.1

Zollo, A., Maercklin, N., Vassallo, M., Dello Iacono, D., Virieux, J., Gasparini, P., 2008. Seismic reflections reveal a massive melt layer feeding Campi Flegrei caldera. Geophys. Res. Lett. 35, 0–5. https://doi.org/10.1029/2008GL034242

Zucali, M., Barberini, V., Voltolini, M., Ouladiaff, B., Chateigner, D., Mancini, L. and Lutterotti, L., 2015. Quantitative 3D microstructural analysis of naturally deformed amphibolite from the Southern Alps (Italy): microstructures, LPO and seismic anisotropies from a fossil passive margin, Geological Society, London, Special Publications, 409, 201-222. http://sp.lyellcollection.org/content/early/2014/08/01/SP409.5

3.2.2. Eruptive dynamics during low-magnitude events at Campi Flegrei (Italy): the 1538 AD Monte Nuovo eruption case study

In this section is summarized the work presented at CoV (Cities on Volcanoes) 10 Conference (Napoli, Italy; 2018) under the same title with authors:

Buono G.[a,b], Macedonio G.[a], Pappalardo L.[a]

a - Istituto Nazionale di Geofisica e Vulcanologia, Osservatorio Vesuviano, Italy
b - University of Naples Federico II, Department of Earth, Environmental and Resources Science, Italy

I contributed to all phases (numerical fluid-dynamics simulations, data interpretation, conference presentation) and investigations of the work.

1. Introduction

In the last decades the high-risk Campi Flegrei caldera (CFc) was affected by several volcanic unrests contributing to increase the scientific interest on this volcanic area. About 70 eruptions of different Volcanic Explosivity Index (VEI) occurred inside the caldera during the last 15 ka. Probabilistic approaches allowed to estimate a probability of occurrence particularly high (i.e. 60%) for low-magnitude events with respect to both medium and large magnitude or effusive eruptions (Orsi et al., 2009). Therefore in this study we explored the magma ascent dynamics in the volcanic conduit during the Monte Nuovo eruption by using numerical (fluid-dynamics) simulations, combined with petrological (Liedl et al., 2019 and references therein) and historical (Guidoboni and Ciuccarelli, 2011) data available in literature.
The AD 1538 Monte Nuovo eruption (VEI~2) was the last CFc eruptive episode. During this event a small 130-m-high tuff cone was formed and a deposit with a volume of about 0.05 km^3 was emplaced. The eruption started with a violent quasi-sustained phreatomagmatic activity (*phreatomagmatic phase*: September 29th – 30th, 3-6 x 10^7 m^3, MDR=10^6 kg/s), subsequently attenuated and then vigorously resumed in two magmatic events (*magmatic phase*: October 3rd and 6th, 1-4 x 10^6 m^3) of less intensity and magnitude (Di Vito et al., 1987; D'Oriano et al., 2005).

2. Methods

Numerical simulations were made using CPIUC code (Macedonio et al., 2005) in order to explore the parameters that governed the magma ascent during Monte Nuovo eruption in the volcanic conduit, despite some simplifications. CPIUC is a one-dimensional model able to simulate conduit flow under steady-state and isothermal conditions, It solves the transport equations of mass and momentum conservation (see Chapter 1) using as boundary conditions an initial pressure P_i at the conduit bottom and choked flow conditions at the conduit exit as well as setting a critical vesicularity (75%) as fragmentation criteria. Magmatic variables used as input data were reconstructed using several petrological models (Papale et al., 2006; Giordano et al., 2008; Masotta et al., 2013; Mollo et al., 2015) starting from published geochemical and textural data (D'Oriano et al., 2005; Piochi et al., 2005; Liedl et al., 2019). Instead, Mass Discharge Rates (MDRs) obtained from field studies (see above) were used to constrain the simulations.

3. Results and discussion

3.1. Magma storage conditions

The reconstructed initial magmatic variables (Table 1) suggest that Monte Nuovo eruption was fed by a magma chamber consisting of a homogeneous trachy-phonolitic magma at a temperature of 900 °C and a pressure of about 100 MPa (using Masotta et al., 2013) and saturated or slightly oversaturated conditions (H_2O ~ 5 wt.%, using Mollo et al., 2015; solubility data from Papale et al., 2006) with with a density of 2.6 g/cm^3 (D'Oriano et al., 2005) and a viscosity of 10^3 Pa s (using Giordano et al., 2008). Assuming a lithostatic system with an average crustal density of 2.5 g/cm^3 a storage depth (and thus a conduit length) of about 4.08 km were estimated using the constrained storage pressure.

Composition	**trachy-phonolitic**
T (°C)	900 (*)
P (MPa)	100 (*)
H_2O (wt.%)	5 (**)
ρ (kg/m3)	2600 [a]
log η (Pa s)	3 (***)
Crystal content (vol.%)	25 – 40 [a]

Table 1. Input data.
(*) using Masotta et al. (2013) with melt and mineral composition from Piochi et al., 2005; (**) using Mollo et al. (2010) with melt and mineral composition from Piochi et al., 2005 and temperature obtained from Masotta et al. (2013); (***) using Giordano et al. (2008) with melt composition from Piochi et al., 2005, temperature obtained from Masotta et al. (2013) and saturation conditions obtained from Mollo et al. (2010). [a] Data from D'Oriano et al. (2005) and Piochi et al. (2005).

3.2. Magma ascent dynamics

Simulation best fits for the phreatomagmatic phase have been obtained with a cylindrical conduit diameter between 20 and 30 m (Table 2, runs 1 and 2). Moreover results suggest that the decrease in the intensity (i.e. MDR) of the eruption of about one order of magnitude during the magmatic phase was controlled by the decrease in conduit diameter to values of less than 10 m (Table 2, runs 3 and 4). In fact, a parametric study shows that the conduit diameter plays the dominant role in the variation of MDRs, whereas other factors (such as magma viscosity, density etc) have only minor effects.

Therefore during the phreatomagmatic phase the conduit was relatively narrow compared with more explosive eruptions from the Neapolitan alkaline volcanism (e.g. conduit diameters between 40 and 100 m have been estimated for 79 AD Plinian eruption of Somma-Vesuvius; e.g. Shea et al., 2011). This result, together with 3D textural evidences described by Liedl et al. (2019), suggests that during this low-magnitude eruption the shear stress along the conduit margins could play a fundamental role, strongly affecting magma degassing (e.g. promoting magma autobrecciation with the subsequent formation of denser clasts, like banded pumices) and ascent velocity, thus reducing eruption explosivity. This process likely contributed to the formation of a plug, able to strongly reduce the conduit diameter and promote intense outgassing (e.g. rocks with low porosity, collapsed

vesicles, microlite content up to 95 vol.%; D'Oriano et al., 2005; Liedl et al., 2019), leading to an eruptive stasis. Finally, eruptive activity resumed with two magmatic explosions probably driven by rapid decompression induced by plug disruption and/or other external factors (e.g. flank collapse).

#	D (m)	Crystal content (vol.%)	MDR (kg/s)
1	30	0.25	6.9×10^6
2	20	0.25	3.0×10^6
3	10	0.4	8.2×10^5
4	5	0.4	2.0×10^5

Table 2. Best fits.

References

Di Vito, M., Lirer, L., Mastrolorenzo, G., Rolandi, G. (1987). The 1538 Monte Nuovo eruption (Campi Flegrei, Italy). Bull. Volcanol. 49, 608–615. https://doi.org/10.1007/BF01079966.

D'Oriano, C., Poggianti, E., Bertagnini, A., Cioni, R., Landi, P., Polacci, M., Rosi, M. (2005). Changes in eruptive style during the A.D. 1538 Monte Nuovo eruption (Phlegrean Fields , Italy): the role of syn-eruptive crystallization. Bull. Volcanol. 67, 601–621. https://doi.org/10.1007/s00445-004-0397-z.

Giordano, D., Russell, J.K., Dingwell, D.B., 2008. Viscosity of magmatic liquids: a model. Earth Planet. Sci. Lett. 271, 123–134. https://doi.org/10.1016/j.epsl.2008.03.038.

Guidoboni, E., Ciuccarelli, C. (2011). The Campi Flegrei caldera: historical revision and new data on seismic crises, bradyseisms, the Monte Nuovo eruption and ensuing earthquakes (twelfth century 1582 AD). Bull. Volcanol. 73, 655–677. https://doi.org/10.1007/s00445-010-0430-3.

Liedl, A., Buono, G., Lanzafame, G., Dabagov, S.B., Della Ventura, G., Hampai, D., Mancini, L., Marcelli, A., Pappalardo, L. (2019). A 3D imaging textural characterization of pyroclastic products from the 1538 AD Monte Nuovo eruption (Campi Flegrei, Italy). Lithos, 340–341, 316–331. https://doi.org/10.1016/j.lithos.2019.05.010.

Macedonio, G., Neri, A., Martí, J., Folch, A. (2005). Temporal evolution of flow conditions in sustained magmatic explosive eruptions. J. Volcanol. Geotherm. Res. 143, 153–172. https://doi.org/10.1016/j.jvolgeores.2004.09.015.

Masotta, M., Mollo, S., Freda, C., Gaeta, M., Moore, G. (2013) Clinopyroxene–liquid thermometers and barometers specific to alkaline differentiated magmas. Contrib. Mineral. Petrol. 166, 1545–1561. https://doi.org/10.1007/s00410-013-0927-9.

Mollo, S., Masotta, M., Forni, F., Bachmann, O., De Astis, G., Moore, G., Scarlato, P. (2015). A K-feldspar-liquid hygrometer specific to alkaline differentiated magmas. Chem. Geol. 392, 1–8. https://doi.org/10.1016/j.chemgeo.2014.11.010.

Orsi, G., Di Vito, M.A., Selva, J., Marzocchi, W. (2009). Long-term forecast of eruption style and size at Campi Flegrei caldera (Italy). Earth Planet. Sci. Lett. 287, 265-276. https://doi.org/10.1016/j.epsl.2009.08.013.

Papale, P., Moretti, R., Barbato, D. (2006). The compositional dependence of the saturation surface of H_2O+CO_2 fluids in silicate melts. Chem. Geol. 229, 78–95. https://doi.org/10.1016/j.chemgeo.2006.01.013.

Shea, T., Gurioli, L., Houghton, B.F., Cashman, K.V., Cioni, R. (2011). Column collapse and generation of pyroclastic density currents during the A.D. 79 eruption of Vesuvius: the role of pyroclast density. Geology 39, 695–698. https://doi.org/10.1130/G32092.1.

3.3. A conceptual model of magma storage and ascent for the Neapolitan alkaline volcanism

3.3.1. Insights into processes and time-scales of magma storage and ascent from textural and geochemical investigations: case studies from high-risk Neapolitan volcanoes (Italy)

This work is published as a chapter of an AGU (American Geophysical Union) Monograph (Title: Magma Dynamics and Timescales in Volcanic Systems; Eds.: Masotta M., Mollo M., Bizimis M., Scarlato P., Beier C.; in press) under the same title with authors:

Pappalardo L.[a], Buono G.[a,b]

a - Istituto Nazionale di Geofisica e Vulcanologia, Osservatorio Vesuviano, Italy
b - University of Naples Federico II, Department of Earth, Environmental and Resources Science, Italy

I contributed to all phases (data review and interpretation, writing) of the work. Particularly, I contributed mainly to the examination of processes and timescales during magma ascent in volcanic conduit.

Abstract

Mechanisms and timescales of magmatic evolution during storage in crustal reservoirs and ascent in the volcanic conduit exert an important control on both the evolution of precursory phenomena recorded during volcanic crises as well as the style and intensity of the impending eruption. The improvement of our knowledge on this topic is therefore of paramount importance for better assessment of hazard for active high-risk volcanoes.
The densely populated Neapolitan volcanic area (Italy) is one of the places most at risk of volcanic disaster in Europe. To reconstruct the magma plumbing system and its evolution towards critical conditions close to eruption, we employed petrological data on past eruptive products representative of the entire volcanic history.
Our results are consistent with the possible existence of a long-term magmatic sill-shaped storage zone beneath the whole Neapolitan volcanic area, with its maximum volume under the Campi Flegrei supervolcano, where the largest eruptions occurred in the last 40 ka. Moreover, slow magma transfer, an open degassing regime and stasis at shallow level (ephemeral storage zones) characterize magma ascent during small-scale events, while fast magma rise and continuous closed degassing mechanism drive violent large-scale eruptions. These distinctive dynamics could imply different time-depth patterns of precursory unrest.

1. Introduction

The size and frequency of volcanic eruptions mostly depend on the mechanisms and timescales of magmatic evolution during storage in crustal reservoirs as well as ascent in the volcanic conduit.
In the last decades, the great development of geophysical exploration techniques, such as seismic tomography, allowed the detection of partially melted horizons within the crust, while advanced monitoring networks provided warnings for variations in volcano dynamics at depth (e.g. Roman & Cashman, 2019); however, a further crucial step is the consistent interpretation of geophysical events and geochemical signals in terms of magma transfer from reservoirs towards the surface and its influence on the eruptive style.
A powerful tool to investigate the evolution of magma plumbing systems at active volcanoes, is the study of petrological (textural and geochemical) features of natural volcanic rocks representative of the entire volcano history. Particularly, the obtained information on the depth, shape and chemico-physical conditions of the volcano magma supply systems is essential for forecasting the future behavior of high-risk volcanoes. Moreover, these studies, applied to the products of recent well-monitored eruptions, have revealed crucial relationships between the petrology of emitted rocks and the pre-/syn-eruptive geophysical signals (e.g. Cashman et al., 2005; Hammer et al., 1999; Pappalardo et al., 2014; Preece et al., 2013; Saunders et al., 2012).
In this chapter we select as a case study the Campi Flegrei caldera and Somma-Vesuvius volcanic complex, situated in the densely populated Naples metropolitan area (Italy), one of the places most at risk of natural disaster in Europe. Combining new and previous evaluations of available petrological data, we reconstruct the conditions of magma chambers and volcanic conduits prior and during eruptions, to obtain new constrains on the possible state of the current plumbing system and on its possible evolution towards critical state.
In Neapolitan area, geophysical anomalies as well as petrological evidence indicate the presence of a laterally extensive magma source beneath the Campi Flegrei volcanic district and Somma-Vesuvius volcano. However, the conditions leading to magma chamber opening, conduit propagation and eruption remain poorly constrained and debated in the recent literature (e.g. Chiodini et al., 2016; Di Vito et al., 2016; Kilburn et al., 2017; Liedl et al., 2019; Lima et al., 2009; Vanorio & Kanitpanyacharoen, 2015). This knowledge is crucial for improving prediction of future eruptive activity and thus it is essential for the mitigation of volcanic risk in the densely urbanized metropolitan area of Naples.

2. Volcanological background of Neapolitan area

The Naples metropolitan area is situated between two active volcanoes: the Campi Flegrei (CF) volcanic district, including also the volcanic islands of Ischia and Procida-Vivara, to the west and the Somma-Vesuvius stratovolcano (SV) to the east (Fig. 1).
The volcanism in this area started about 1.5 Ma with a widespread effusive activity characterized by calc-alkaline andesitic and basaltic compositions as revealed by geothermal boreholes drilled NW of the Campi Flegrei caldera (Barbieri et al., 1979). Subsequently, from about 300 ka, new volcanic activity, fed by alkaline magmas, has generated the CF and SV volcanic complexes (Fig. 2).
The substructure of these two volcanoes has been investigated through several geophysical surveys (e.g. De Natale et al., 2006a, 2006b and references therein). Geophysical data, constrained by deep boreholes (Brocchini et al., 2001; Di Renzo et al., 2007; Rosi & Sbrana, 1987), showed that the deep structure of this volcanic area comprises 1.5-3 km of interbedded lavas and volcanoclastic, marine, and fluvial sedimentary rocks of Pleistocene age. These sequences overlie the Mesozoic carbonate sequences that extend from 2-4 to roughly 8-11 km depth (Berrino et al., 1998, 2008; Improta & Corciulo, 2006) on the Ercinian crystalline basement. The Moho discontinuity occurs at about 30 and 25 km depth beneath SV and CF respectively (e.g. De Natale et al., 2006b; Nunziata, 2010); whereas a low velocity layer, interpreted as the top of a magmatic body, was detected by

seismic tomography at 7-8 km depth beneath the Campi Flegrei caldera and the neighboring Vesuvius volcano (Auger et al., 2001; Zollo et al., 2008).

The CF caldera produced at least six large-scale explosive eruptions in the last 250 ka (e.g. Albert et al., 2019; De Vivo et al., 2001) at intervals of 20.000 – 60.000 years. The largest of these events are the two large ignimbrite eruptions of the Campanian Ignimbrite (CI, 300 km^3 DRE, 40 ka, Gebauer et al., 2014) and the Neapolitan Yellow Tuff (40 km^3, 14.9 ka, Deino et al., 2004) that caused the collapse of the 12 km-wide Campi Flegrei caldera. In the last 15 ka this nested collapse structure was the site of a monogenetic volcanic activity producing about 70 eruptions (with variable Volcanic Explosivity Index, VEI, spanning from 0 to 5), until the last Monte Nuovo event (VEI 2) occurred in 1538 AD. After a long period of subsidence following this last event, the caldera showed signs of potential reactivation characterized by episodes of ground uplift, shallow seismicity, significant increase in hydrothermal degassing and changes in fluid-geochemistry. A first inversion of the subsidence occurred between 1945-53 (0.5 m of uplift), followed by the two main bradyseismic crises of 1970-72 and 1982-84 (1.7 and 1.8 m of uplift respectively), which led to a total elevation of the ground of about 3.5 m in the central sector of the caldera. An ongoing unrest phase started in 2005, prompted the Civil Protection to move the Campi Flegrei volcano from base level (green) to warning (yellow) alert level since the end of 2012.

The volcanic activity of SV was, on the contrary, mostly polygenetic and characterized by the shift from a quiescent (closed-conduit) state, generally interrupted by large-explosive eruptions (at least tens of VEI 4 or 5 eruptions staggered with minor events occurred in the last 22 ka), to open-conduit periods producing mixed effusive/low-explosivity events. The latest of these periods started after the subplinian 1631 eruption and lasted ca 300 years until the last eruption on March 1944. Since that time, the volcano has entered a new state of closed-conduit repose, with very modest fumarolic activity, low-magnitude seismicity and rare earthquakes swarms. The volcano is at its base level of alert (green) due to the absence of variation in monitored parameters.

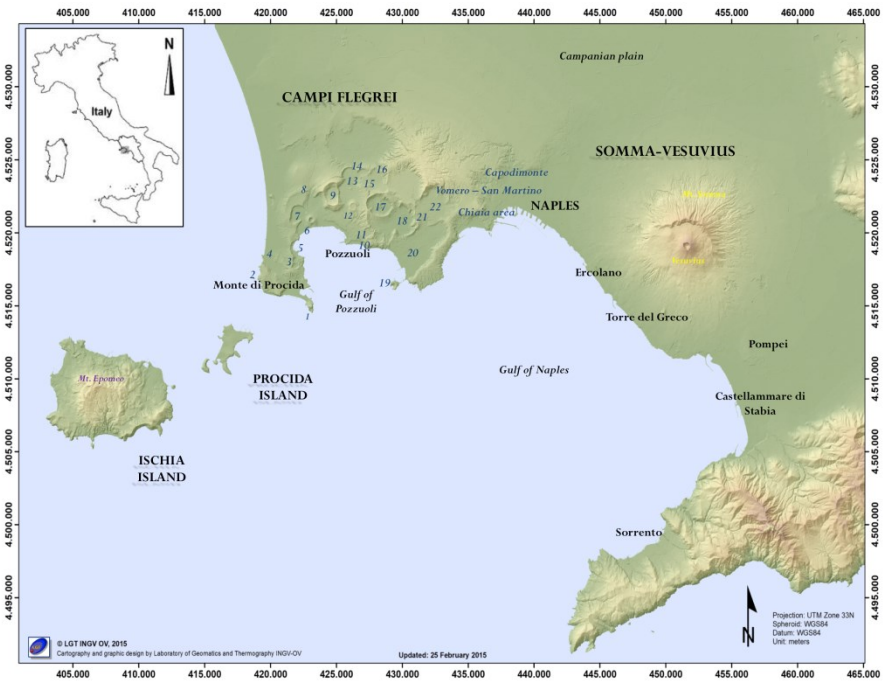

Fig. 1. The Neapolitan volcanic area (Campi Flegrei district and Somma-Vesuvius complex). Numbers refer to some of the well-preserved craters in CF: 1) Capo Miseno, 2) Acqua Morta, 3) Fondi di Baia, 4) Torregaveta, 5) Baia, 6) Mt. Nuovo, 7) Averno, 8) Fondo Riccio, 9) Gauro, 10) Accademia, 11) Solfatara, 12) Cigliano, 13) S. Martino, 14) Montagna Spaccata, 15) Fossa Lupara, 16) Pisani, 17) Astroni, 18) Agnano, 19) Nisida, 20) S. Teresa, 21) Mt. S. Angelo, 22) Minopoli.

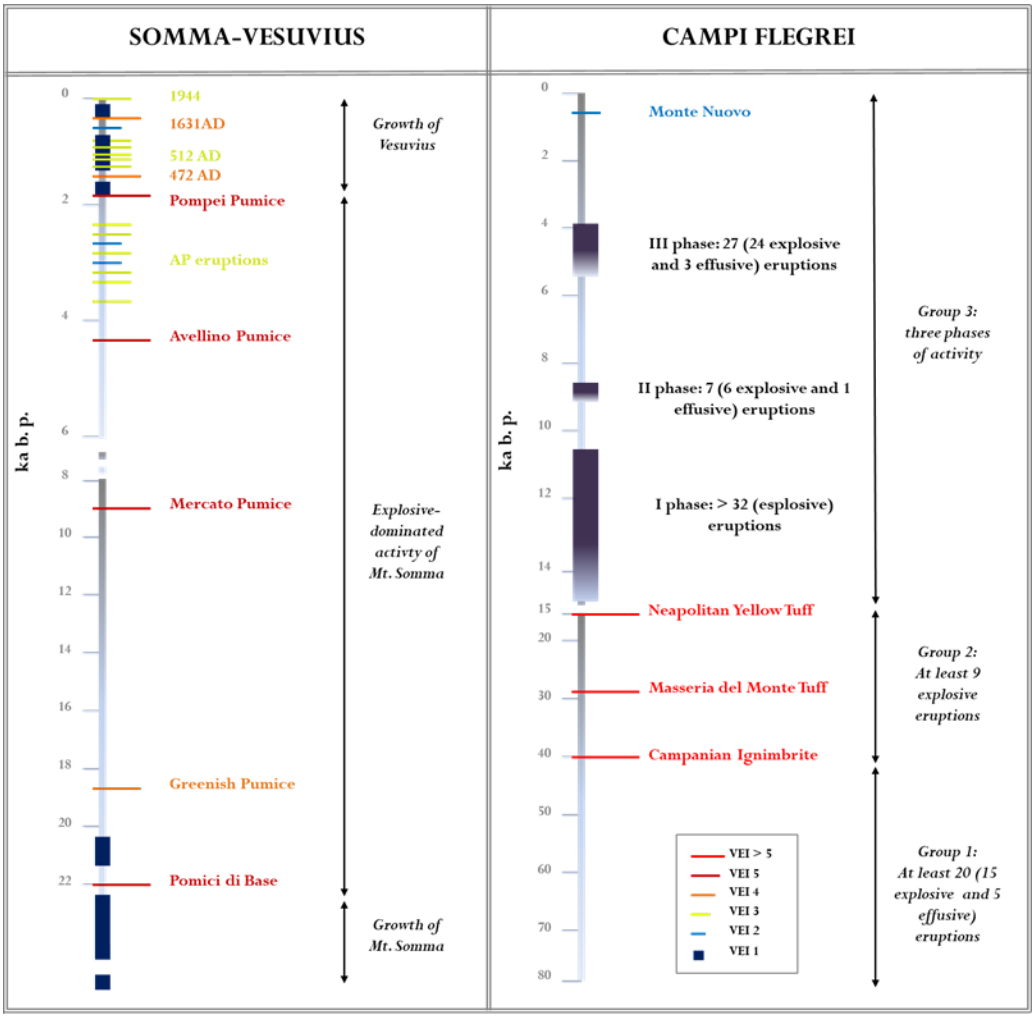

Fig. 2. Schematic chronograms of volcanoes activity as recorded by stratigraphic successions.

3. Magma evolution in crustal reservoirs

Deciphering mechanisms and timescales of generating magmas rich in silica and volatile constituents, which in turn drive the style and frequency of the eruptions, remain a major challenge for igneous petrology. In the last few decades the ideas on the architecture and evolution of magmatic systems were profoundly modified, also due to the significant progresses in analytical techniques as well as geophysical exploration methods (e.g. Marsh 1989, 2015). Several hypotheses have been advocated during time: 1) settling of crystals was shown to play a significant role in the generation of continuous chemical zoning (Bowen, 1928); 2) convective fractionation at the chamber walls in a crystallizing double-diffusive boundary layer (e.g. McBirney et al., 1985; Spera et al., 1995) was proposed to explain the decrease of the liquid density at the top of magma chambers; 3) extraction of silicic melts from a crystal rich-mush deriving by the in-situ crystallization of parental liquid was suggested to justify the abrupt chemico-physical gap observed in some volcanic series (e.g. Brophy, 1991; Hildreth & Wilson, 2007; Marsh, 2002); 4) periodic rejuvenation of previously intruded high-crystallinity (> 50% crystals) magma bodies, possibly subject to rapid heating and remobilization (Andersen et al., 2017; Cooper & Kent, 2014); hypothesis (4) could explain the lack of geophysical evidence of extended magmas-rich portions in

the current upper crust beneath some volcanic systems in the world (e.g. Bachmann & Bergantz, 2003, 2004, 2008a, 2008b, 2008c); 5) incremental assembly of magmatic bodies (e.g. Annen, 2009; Gelman et al., 2013) has been proposed to maintain magma reservoirs in a mush-state for long periods (several hundreds of thousands of years). A most recent view considers the development of magma reservoirs by stacking of sill-like magma intrusions that correspond to crustal heterogeneities (e.g. density, rigidity and/or rheology contrasts; stress concentration); the progression of this mechanism could lead to the formation of large layered intrusion complex in the crust (e.g. Bachmann & Huber, 2016; Cashman & Giordano, 2014; Edmonds et al., 2019; Holness et al., 2019; Sparks et al., 2019). Actually geophysical data have recently shown fast sill propagation before eruptive events in different geodynamic contexts (e.g. Rubin et al., 1998; Sigmundsson et al., 2015) as well as the presence of a large sill containing a significant amount of melt beneath active calderas (e.g. Somma-Vesuvius volcano, Auger et al., 2001; Campi Flegrei caldera, Fedi et al., 2018; Nunziata, 2010; Zollo et al., 2008; Toba caldera, Jaxybulatov et al., 2014; Long Valley caldera, Flinders et al., 2018).

A variety of different approaches (e.g. zircon dating of silicic plutons and volcanic rocks, crystal size distributions theory, diffusion modeling of chemical gradients in minerals) have yielded timescale for magmatic processes on the order of 10^1 - 10^6 years depending on the evolution mechanism as well as size and shape of the system (e.g. Annen & Zellmer, 2008; Cooper, 2019; Cooper & Kent, 2014; Hawkesworth et al., 2000, 2004; Morgan & Blake, 2006; Turner et al., 2000; Zellmer et al., 2005). This apparent discrepancy in age determination actually mirrors the difference between the radiometrically determined absolute ages of crystals and the time interval that the crystals spend at high temperature, recorded by diffusion and crystal growth (e.g. Till et al. 2015).

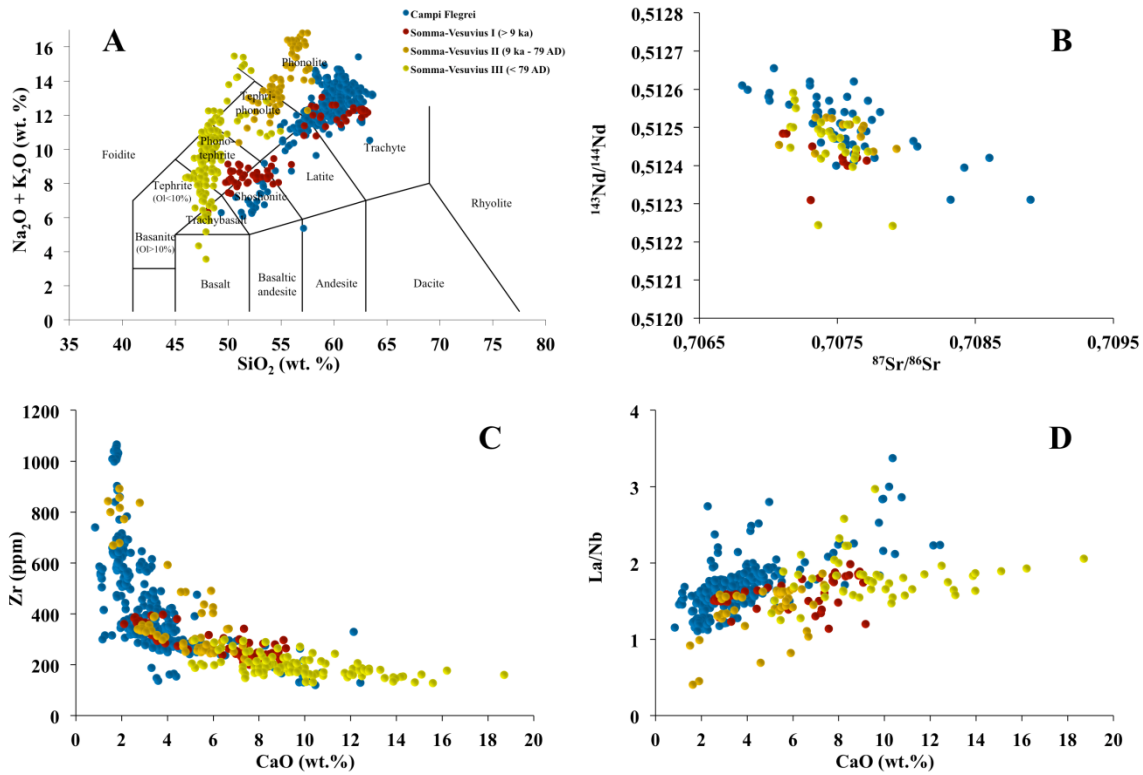

Fig. 3. A) Plot of Total Alkalis vs. Silica (TAS), B) Sr and Nd isotopic ratios and C and D) Examples of variation diagrams of Campi Flegrei and Somma-Vesuvius volcanic bulk-rocks. Data from: Peccerillo (2017) and references therein.

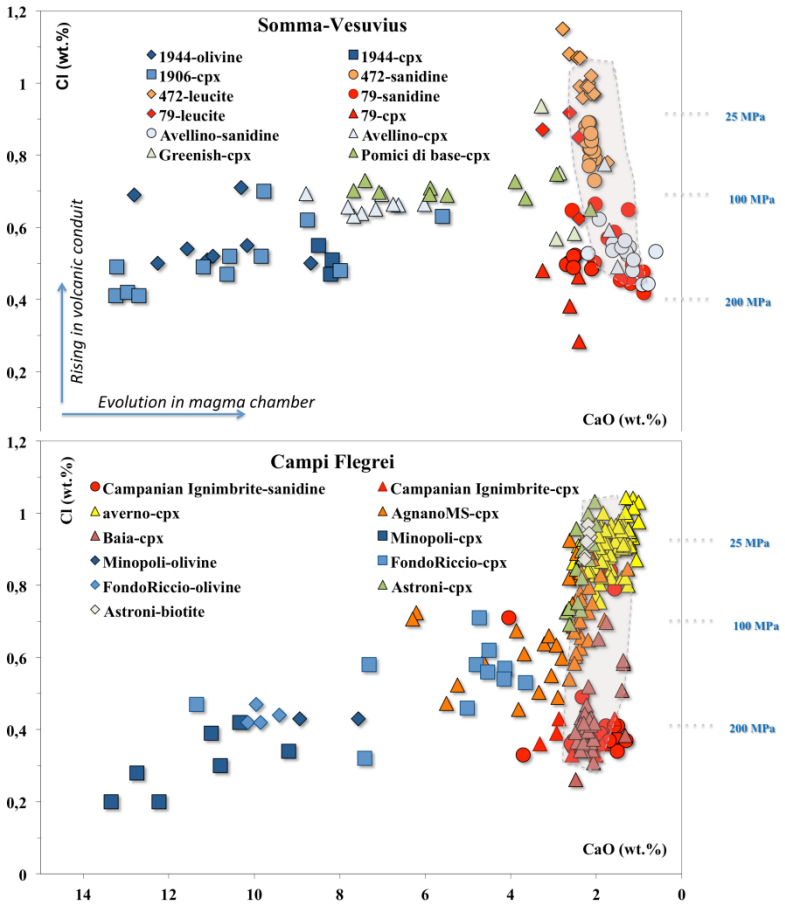

Fig. 4. Cl versus CaO content of melt inclusions in mineral phases. Horizontal lines on the right axis denote saturation pressure for different Cl contents (solubility model by Signorelli & Carroll, 2002). Fields represent degassed matrix-glasses composition. Data from: CF: Arienzo et al. (2010), Cannatelli et al. (2007), Esposito et al. (2018) Fourmentraux et al. (2012), Lima et al. (2017), Mangiacapra et al. (2008), Marianelli et al. (2006), Signorelli & Carroll (2002); SV: Balcone-Boissard et al. (2008, 2012, 2016), Lima et al. (2003), Marianelli et al. (1999, 2005), Webster & De Vivo (2002).

Table 1 - Magmatic intensive variables for Campi Flegrei and Somma-Vesuvius reservoirs

		Campi Flegrei				
Methods	**References**	***Composition***	***Pressure***	***Liquidus T***	***Initial water content***	***CO_2 content***
MELTS						
	Fowler et al., 2007	Trachyte	150 Mpa	1235 °C	3 wt%	-
	Pappalardo et al., 2008	Trachyte	250 Mpa	1199 °C	4 wt%	-
GEOTHERMOBAROMETRY cpx-melt thermometers and barometers	Masotta et al., 2013	Trachyte	127-58 Mpa	> 884-983 °C	-	-
cpx-melt thermometry and K-feld-melt hygrometry	Forni et al., 2018	Trachyte	200 Mpa	1100 °C	4 wt%	-
PHASE-EQUILIBRIUM EXP						
	Fabbrizio & Carroll, 2008	Trachyte	250-200 Mpa	> 800°C	satutation condition	-
		Somma - Vesuvius				
Methods	**References**	***Composition***	***Pressure***	***Liquidus T***	***Initial water content***	***CO_2 content***
MELTS						
	Pappalardo & Mastrolorenzo, 2010	Tephrite	400-350 Mpa	1212 °C	5 wt%	-
	Pappalardo & Mastrolorenzo, 2010	Phonolite	250-200 Mpa	986 °C	7.7 wt%	-
	Pappalardo et al., 2014	Tephrite	400 Mpa	1150 °C	saturation	-
GEOTHERMOBAROMETRY cpx-melt thermometers and barometers	Masotta et al., 2013	Phonolite	157-186 Mpa	800-770 °C	-	-
	Balcone-Boissard et al., 2016	Phonolite	200-180 Mpa	-	5.1 wt%	-
PHASE-EQUILIBRIUM EXP						
	Scaillet et al., 2008	Phonolite	200 Mpa	815-785 °C	6 wt%	-
	Pichavant et al., 2014	Trachybasalt	300 Mpa	1200 °C	1.5-4.5 wt%	600-4500 ppm

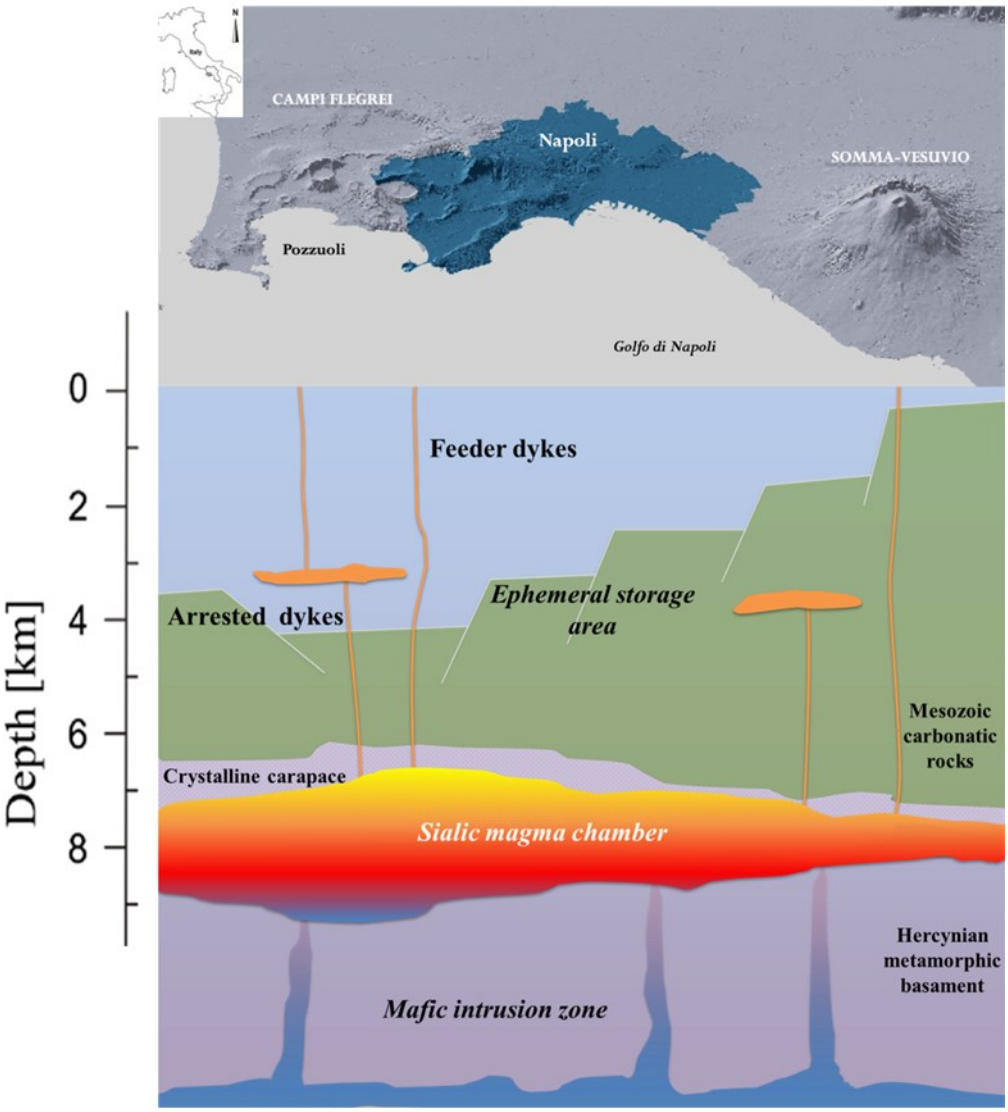

Fig. 5. Geological model of the deep structure of the Neapolitan volcanoes based on both petrological and geophysical data.

Magma storage processes and timescales for Neapolitan volcanoes

The volcanic products emitted from Neapolitan volcanoes belong to the potassic series of Central-Southern Italy Province. Slightly silica-undersaturated rocks, ranging in composition from trachy-basalt to trachy-phonolite, were erupted throughout the history of Campi Flegrei volcanic district as well as at Somma-Vesuvius from 25 to 9 ka. Moderately to strongly undersaturated rocks, from leucite-bearing foidites to phono-tephrites to phonolites, were erupted at SV between 9 ka and 79 AD and after 79 AD, respectively (Fig. 3).

The magmatic system architecture of the Neapolitan volcanoes has been explored by petrological studies on products from past eruptions representative of the whole volcanic history (e.g. Di Renzo et al., 2007; Forni et al., 2018; Pappalardo & Mastrolorenzo, 2010, 2012; Pappalardo et al., 2002, 2004, 2008; Santacroce et al., 2008; Stock et al., 2018).

The MELTS (Ghiorso & Sack, 1995) thermodynamic approach (e.g. CF: Fowler et al., 2007; Pappalardo et al., 2008; SV: Pappalardo & Mastrolorenzo, 2010), geothermobarometry (e.g. CF:

Forni et al., 2018; Masotta et al., 2013; Mollo & Masotta, 2014; SV: Balcone-Boissard et al., 2016) as well as phase-equilibrium experiments (e.g. CF: Fabbrizio & Carroll, 2008; SV: Dolfi & Trigila, 1978; Pichavant et al., 2014; Scaillet et al., 2008) were used to estimate temperature, pressure and volatile content conditions during the crystallization of mafic and sialic melts.

Generally, volatile content measured in melt inclusions is a key tool used to provide information on initial volatile content and crystal equilibration pressure during magma storage, when post-entrapment modification can be excluded. Additionally, the inclusion-bearing crystals can have a wide range of origins and ages, further complicating the interpretation of magmatic processes (Ruth et al., 2018). Data summarised in Fig. 4 demonstrates that, in many studied cases, melt inclusions entrapped in phenocrysts of Campi Flegrei and Somma-Vesuvius samples (CF: Arienzo et al., 2010; Cannatelli et al., 2007; Esposito et al., 2018; Fourmentraux et al., 2012; Lima et al., 2017; Mangiacapra et al., 2008; Marianelli et al., 2006; Signorelli & Carroll, 2002; SV: Balcone-Boissard et al., 2008, 2012, 2016; Lima et al., 2003; Marianelli et al., 1999, 2005; Webster & De Vivo, 2002) have similar volatile contents to the corresponding degassed matrix glasses. This suggests that melt inclusions volatile content does not univocally record pre-eruptive storage depth (horizontal trends characterized by constant values of Cl buffered concentration, despite a strong variations in CaO content) but can follow syn-eruption degassing paths (vertical trends with a variation in Cl content following pressure decrement versus constant values of CaO concentration) (Fig. 4).

The existence of two main magma storage depths active under CF and SV volcanoes have been postulated based on the complete petrological results (Table 1 and Fig. 4), (Pappalardo & Mastrolorenzo, 2010, 2012): a deeper mafic (liquidus T ~ 1200 °C, viscosity ~ 10^0–10^1 Pa s at saturation condition, volatile content ~ 5-9 wt. %) reservoir at pressure of > 400–200 MPa (16 - 8 km depth) extended towards the Moho discontinuity (25-30 km) and a shallower (150-200 MPa, 6-8 km depth) felsic (liquidus T ~ 1000 °C, viscosity ~ 10^2-10^3 Pas at saturation condition, volatile content ~ 4.5-6 wt. %) magma layer at the inferred carbonatic/metamorphic rocks transition.

The geochemical variations of major, trace and volatile elements (Figs. 3 and 4) on separated minerals, glass as well as melts inclusions define systematic trends, suggesting a cogenetic nature of the various magmas at different degree of evolution. However Sr-Nd isotopic variations indicate that contamination with host-rocks and mixing/mingling processes occurred at different depths and timescales (e.g. Dallai et al., 2011; Pappalardo et al., 2004; Piochi et al., 2006). Diffusion chronometry yields mixing timescale on the order of several tens of years before the eruptions (Iovine et al., 2017; Morgan et al., 2006). Furthermore Iacono Marziano et al. (2008) indicated that the massive Ca-rich clinopyroxene crystallization induced by progressive carbonate assimilation may explain the transition from slightly (CF and SV rocks older then 9 ka) to moderately (SV rocks erupted between 9 ka and 79AD) and to strongly silica-undersaturated (SV rocks younger then 79AD) residual melts observed on Neapolitan magmas during time. It has also been proposed that fast magma/limestone interaction, accompanied by the generation of CO_2-fluid phases, could be an important process in controlling the eruption explosivity (e.g. Jolis et al., 2013, 2015; Pappalardo et al., 2018).

Pappalardo and Mastrolorenzo (2010, 2012) applied crystal size distributions theory (Marsh, 1988) on phenocrysts included in the Somma-Vesuvius and Campi Flegrei rocks, and obtained a relatively short crystallization time on the order of few hundreds years, in agreement with pre-eruptive crystal residence time obtained by uranium decay series data for zircon and garnet (Gebauer et al., 2014; Wotzlaw et al., 2019; Wu et al., 2015). This suggests that alkaline magmas could evolve toward a critical state of explosive behavior over a relatively short time span comparable to the repose time of most volcanic systems.

The similar pressure and temperature conditions estimated, as well as timescale of residence time between the magmatic systems of the two Neapolitan volcanic districts, suggest the existence of a wide sill-shaped magmatic chamber (Pappalardo & Mastrolorenzo, 2012) consisting mainly of crystal-poor melts and fed by a deeper storage zone of mafic crystal-rich magmas (Fig. 5).

A unique magmatic source for the two Neapolitan volcanic areas is also supported by the similarity in the Sr and Nd isotopic compositions in both silicic and mafic rocks of Campi Flegrei volcanic district and Somma-Vesuvius (Fig. 3B). Whereas the increase in the degree of magma/wall rock interaction with time (Iacono Marziano et al., 2008) explains the growth of silica-undersaturation, and precipitation of leucite in younger SV melts. Gebauer et al. (2014) have hypothesized that the development of a crystalline carapace at the boundary magma/crustal rocks during CI super-eruption isolated the subsequent CF magmas by extensive assimilation of country rocks (Fig. 5).
Some authors suggested that the absence of Mesozoic carbonate succession beneath CF caldera, due to the lack of calcareous lithic clasts in the Phlegraean stratigraphic volcanic successions (e.g. D'Antonio, 2011). However we observe that the CF caldera is located towards the center of the Campanian graben, in proximity of its maximum depression, where possibly the Mesozoic carbonate series is dislocated at deeper level (> 4 and < 8 km according to geophysical data; e.g. Zollo et al., 2008) compared to the Somma-Vesuvius, placed towards the eastern border of the graben (where the carbonatic succession is reached by boreholes at a depth of 1-2 km; Brocchini et al., 2001). This condition implies that the depth of limestone at CF is always below the surface of magmatic fragmentation (1-2 km, Pappalardo & Mastrolorenzo, 2012) at which the main production of lithic clasts is expected (Macedonio et al., 1994) (Fig. 5).
The occurrence of ancient (> 40 ka) volcanic centers in the heart of the city of Naples, identified in the Chiaia area (Scarpati et al., 2012), halfway between the two volcanoes might be evidence for the long-lived nature of a unique magmatic source for the two Neapolitan volcanic areas . However its persistence today can be postulated on the basis of the heat flow distribution showing a single positive anomaly (> 100 mW/m^2) extended below the entire Neapolitan area, with the maximum value corresponding to the Phlegraean supervolcano (600 mW/m^2, Carlino et al., 2012; Della Vedova et al., 2013), where most of the magma volume is probably stored (the CF caldera emitted ca 400 km^3 of magmas in the last 40 ka compared to the ca 50 km^3 erupted in the last 25 ka at Somma-Vesuvius).

4. Magma ascent in volcanic conduit

Degassing and crystallization mechanisms and timescales accompanying magma ascent in volcanic conduit exert an important control on both the evolution of geochemical and geophysical signals recorded during volcanic crises as well as the style and intensity of impending eruption.
In particular, decompression during magma ascent is associated with a decrease in pressure-dependent solubility, thus causing exsolution of volatiles (mainly H_2O and CO_2) forming a separated gas phase (i.e. bubbles). Exolution in ascending melts increases the magmas liquidus temperature and may trigger extensive crystallization of microlites (i.e. crystals smaller than about 50–100 μm). As a consequence, decompression-induced degassing and crystallization cause significant changes in the chemistry and physical properties of the ascending magma with drastic effects on the eruptive behavior (e.g. Gonnermann & Manga, 2007 and references therein).
Generally, high-intensity explosive activity is expected to result from rapid (average) magma decompression and ascent (> 0.1 m/s; Cassidy et al., 2018) during which the gas remains trapped in the melt (closed-system degassing), causing magma expansion and leading to explosive fragmentation through volatile overpressure in bubbles, high-strain rates due to rapid acceleration, or at a critical vesicularity threshold. On the other hand, low-intensity volcanic activity is associated to slow magma ascent (< 0.1 m/s; Cassidy et al., 2018) that yields sufficient time to the gas to escape (open-system degassing) and microlites to growth (Rutherford & Gardner, 2000).
Classically, it is considered that volatile exolution follows solubility laws (near-equilibrium condition) in low viscosity melts regardless of decompression rate, whereas bubble–melt equilibrium is not maintained (disequilibrium degassing) in highly viscous melts at rapid ascent rate (e.g. Couch et al., 2003; Mangan & Sisson, 2000; Mangan et al., 2004; Mourtada-Bonnefoi &

Laporte, 2004). However several observations do not fit easily in such a simple model (e.g. Larsen & Gardner, 2004; Iacono Marziano et al., 2007; Mastrolorenzo & Pappalardo, 2006) suggesting a more complex relationship between the degassing regime and melts composition and/or ascent rate. Actually, how the different internal (pre-eruptive volatile content, magma injection, magma rheology etc) and external (tectonic regime, stress field, conduit and vent geometry, flanks collapse of volcanic edifice, CO_2 liberation by limestone ingestion, magma/water interaction etc) factors interact controlling the speed of magma ascent is still poorly constrained (e.g. Cassidy et al., 2018; Gonnermann & Houghton, 2012; Rust & Cashman, 2011).

A powerful tool for reconstructing magma decompression history is the 2D and 3D textural characterization of natural volcanic rocks. In particular, in the last decades 3D textural investigation (e.g. X-ray microtomography; μCT) has become an increasingly important tool in both qualitatively and quantitatively assessing rocks textures in in three dimensions, thus entirely avoiding mathematical corrections needed for measurements made in conventional 2D techniques. Many recent studies have demonstrated the power of μCT in the understanding complex textures, such as those of pyroclasts produced during explosive eruptions. In fact, μCT allows the direct observation and accurate quantification of important textural parameters (such as the content, number, orientation, shape and distributions of the crystals and vesicles, as well as of their degree of connectivity and permeability) that strongly influence nucleation, growth and coalescence of gas bubbles, magma fragmentation and crystallization (e.g. Baker et al., 2012; Degruyter et al., 2010a, 2010b; Gurioli et al., 2015; Lanzafame et al., 2017; Liedl et al., 2019; Pappalardo et al., 2018; Polacci et al., 2014, 2018; Voltolini et al., 2011).

In detail, vesicle number densities (VNDs; i.e., the number of vesicles per unit melt or bulk volume) of natural volcanic rocks are correlated with the intensity of the examined eruptions as well as with the decompression rate simulated by experiments (Mangan et al., 2004; Mourtada-Bonnefoi & Laporte, 2004) and numerical models (Toramaru, 2006). In general high VND values are associated with high rate of decompression; low values are related to slow, or staged ascent (e.g. Cashman & Mangan, 1994). Shea et al. (2010a) reported VND values between 10^{11} to 10^{12} m^{-3} for slow ascent magmas (VEI from 0 to 2) and up to 10^{16} m^{-3} for fast ascent magmas (e.g. Vesuvius 79 AD VEI 6 plinian eruption).

Vesicle size distributions (VSDs; i.e. the number of vesicles in each size class per unit melt or bulk volume) and Vesicle Volume Distributions (VVDs; i.e. volume fraction of the vesicles at their equivalent volume) are used commonly to infer kinematics of bubble nucleation and growth rate. Particularly, cumulative VSDs (CVSDs) log-log plots have been observed to follow either exponential or power law distributions both in natural and experimental samples. Generally, pumices generated by purely magmatic processes show CVSDs that follow power law distributions for larger vesicles, while exponential trends for the smallest bubble sizes (e.g. Carey et al., 2009; Klug et al., 2002); these trends are interpreted as representing the bubble populations generated by continuous nucleation events and/or growth and coalescence during ascent (Blower et al., 2003; Gaonac'h et al., 1996) and by a last nucleation event, respectively (Gonnermann & Houghton, 2012; Rotella et al., 2014).

An additional important parameter is the vesicle-to-melt volume ratio (Vg/Vl after Gardner et al., 1996; i.e. ratio between volume of vesicles corrected for phenocrysts, Vg, and volume of melt and microlites, Vl). In particular following Stovall et al. (2011) different vesiculation processes impart a characteristic signature on a plot of Vg/Vl vs. VND. New nucleation of small bubbles leads to increased VND and only a slight increase in Vg/Vl. Bubble growth by diffusion and/or gas expansion leads to increased Vg/Vl at constant VND. Bubble coalescence causes a decrease in VND while Vg/Vl increases, and bubbles collapse leads to a reduction in both parameters. Intermediate trends on the diagram reflect combinations of more than one of these processes. Moreover, the plot of Vg/Vl vs. H_2O content dissolved in the matrix-glass of volcanic rocks can be indicative of different degassing regime (open- versus closed-system regime; e.g. Villemant & Boudon 1998).

Vesicularity and permeability are further important parameters that may have a considerable impact on the characteristics of a volcanic eruption. Theoretically, a veiscularity threshold (percolation threshold) exists because bubbles at low volume fractions are sufficiently distant from one another to prevent pervasive coalescence; however results of numerical simulations and experiments as well as measurements on natural samples indicate that the percolation threshold can range largely from 30 to 78% with no unique relationship with other compositional or textural parameters (e.g. Giacchetti et al., 2019 and references therein).
Likewise crystal content, number density (CND), size (CSD) and volume (CVD) distribution as well as shape of microlites are strictly related to mechanisms and time of magma decompression in volcanic conduit (e.g. Befus et al., 2014; Clarke et al., 2007; Couch et al., 2003; Hammer et al., 1999; Kennedy et al., 2005; Noguchi et al., 2006; Martel, 2012). Particularly decompression experiments (e.g. Blundy & Cashman 2008; Martel et al., 2017) demonstrated that under conditions of rapid ascent, due to high rate of undercooling (defined as the difference between the liquidus temperature and that of the magma) the crystallization is controlled by nucleation of new sites (nucleation-dominated regime), thus resulting in many tiny skeletal (e.g. hopper, shallow-tail, acicular shape) microlites (e.g. Browne & Gardner, 2006; Couch et al., 2003; Geschwind & Rutherford, 1995; Hammer & Rutherford, 2002; Hammer et al., 2002; Martel & Schmidt, 2003; Rutherford & Hill, 1993). On the contrary, in slow ascending magmas, growth of existing crystals prevails (growth-dominated regime) over nucleation due to the reduction over time of the degree of undercooling, thus resulting in fewer but larger (e.g. tabular, prismatic) microlites. Moreover, recent studies (Brugger & Hammer, 2010a, 2010b; Melnik et al., 2011) have determined that during decompression at high-pressure, crystallization occurs under a growth-dominated regime, whereas at low-pressure decompression crystal nucleation prevails. It is worth noting that decompression experiments show the absence of microlites in the groundmass of pumices from highly explosive eruptions; thus indicating that the magma decompression time was too short (up to tens of hours) to generate microlites (e.g. Couch et al., 2003; Martel, 2012).

Degassing and crystallization of ascending alkaline Neapolitan magmas

Degassing and crystallization processes and timescales during magma ascent in volcanic conduits for Neapolitan volcanoes have been investigated by several authors measuring textural and geochemical features on natural sialic and mafic rocks (Cioni et al., 2011; D'Oriano et al., 2005; Mastrolorenzo & Pappalardo, 2006; Mastrolorenzo et al., 2001; Pappalardo & Mastrolorenzo, 2010, 2012; Pappalardo et al., 2008, 2014, 2018; Piochi et al., 2005, 2008; Pistolesi et al., 2017; Shea et al., 2012; Zdanowicz et al., 2018) as well as through decompression experiments (trachyte: Arzilli et al., 2016; Calzolaio et al., 2010; Mastrolorenzo & Pappalardo 2006; Preuss et al., 2016; phonolite: Allabar & Nowak, 2018; Iacono Marziano et al., 2007; Larsen, 2008; Marxer et al., 2015; Preuss et al., 2016; Shea et al., 2010b). Significant differences are apparent between natural rocks from high-explosive events respect to those from moderately-explosive/effusive eruptions (e.g. Mastrolorenzo & Pappalardo, 2006), reflecting different conditions of magma ascent. The only exception is the VND whose value in natural samples ranges from ca 10^{10} to 10^{15} m^{-3} (Mastrolorenzo and Pappalardo, 2006; Mastrolorenzo et al., 2001) apparently regardless of the eruptive style and composition, consistently with VND values produced by heterogeneous nucleation in Neapolitan trachytes ($7.2 \times 10^{12} – 2.9 \times 10^{14}$ m^{-3}, Mastrolorenzo & Pappalardo, 2006) and phonolites ($4.3 \times 10^{13} – 3.8 \times 10^{14}$ m^{-3}, Larsen, 2008; $3.6 \times 10^{14} – 9.9 \times 10^{15}$ m^{-3}, Shea et al., 2010b) as well as by homogeneous nucleation in alkaline melts ($3.0 \times 10^{9} – 1.3 \times 10^{14}$, Marxer et al., 2015; $6.8 \times 10^{13} – 2.5 \times 10^{14}$, Allabar & Nowak, 2018 and references therein) during experiments at different decompression rates.
Moreover, residual water contents measured on trachytic and phonolitic samples obtained by decompression experiments (Larsen, 2008; Larsen & Gardner, 2004; Marxer et al., 2015; Mastrolorenzo & Pappalardo, 2006; Shea et al., 2010b) suggest that ascending alkaline water-saturated magmas generally follow degassing path controlled by near-equilibrium solubility in a

wide range of ascent rate. On the contrary water under-saturated (Allabar & Nowak, 2018; Iacono Marziano et al., 2007; Preuss et al., 2016) experiments on phonolitic compositions indicate that degassing can deviate from equilibrium solubility trends.
In general, trachytic to phonolitic pumice samples (e.g. Mastrolorenzo & Pappalardo, 2006) from large explosive eruptions have highly-vesicular glassy matrix (60–80%) and moderate to high residual water content (1–2 wt.%). These clasts have abundant small spherical vesicles and coalesced large vesicles in microlite-poor (feldspar) to microlite-free (0-5 vol.%) groundmass glass (Fig. 6). Crystal size distributions on microlites are steep (-300 mm^{-1}) with high intercept values (18 mm^{-4}). Textural (vesicularity, Vg/Vl, CSDs, CNDs) and geochemical (water content) features of pumices indicate rapid decompression (hours to days) and degassing under closed-system condition, producing explosive fragmentation possibly when the volume of expanding bubbles reaches a fixed vesicularity threshold (70-80%) at a inferred fragmentation pressure of 10–30 MPa.

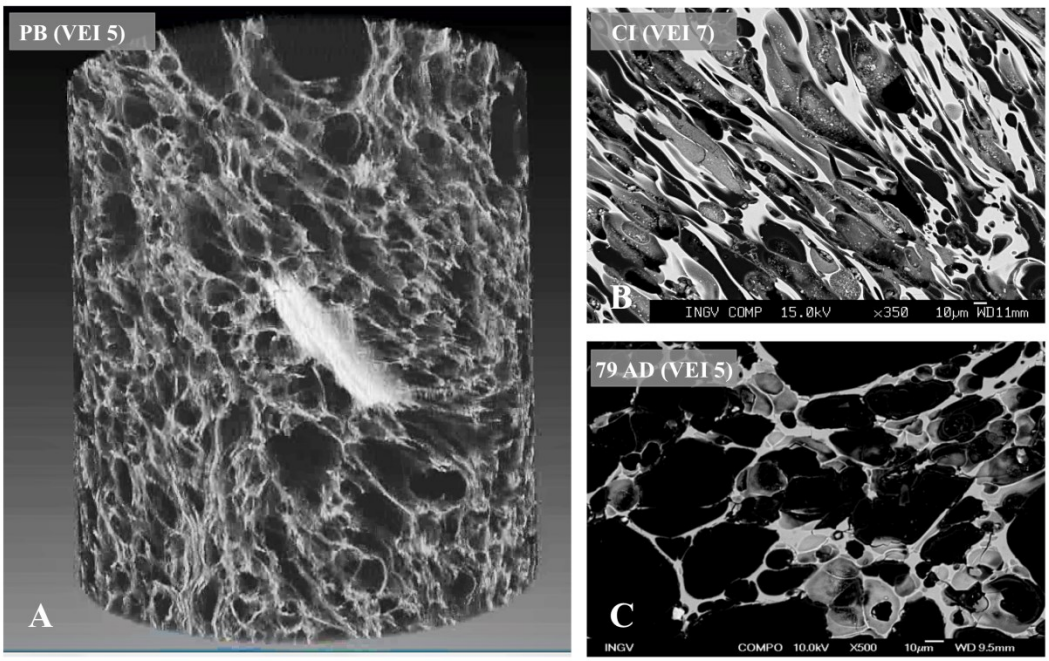

Fig. 6. Example of volume rendering obtained by computed X-ray microtomography (Carl Zeiss Xradia Versa-410) at INGV-NA laboratory and backscattered electron images of selected rocks, performed at INGV-Rome laboratory, showing the high vesicular and microlite-free texture of pumices from high explosive eruptions of Campi Flegrei and Somma Vesuvius. A) Pomici di Base plinian eruption (22 ka) from SV, diameter of cylinder=1mm; B) Campanian Ignimbrite supereruption from CF; C) Pompei plinian eruption (79 AD) from SV.

The only case of a high-explosive event fuelled by mafic magmas in the Neapolitan area is the caldera-forming Pomici di Base plinian eruption, that occurred at 22 ka at Somma-Vesuvius. A recent 3D textural study (Buono et al., 2019; Pappalardo et al., 2018) hypothesized that the explosive character of this mostly shoshonitic-latitic eruption was linked to the rapid release of CO_2, due to the interaction of hot mafic ascending magmas with the limestone substratum. The CVSDs (Fig. 7) in the scoriae erupted during this Vesuvian event suggest a double degassing episode correlated to both water exsolution in a deeper part of the conduit (first vesiculation event) and subsequent CO_2 liberation (second event of vesiculation) at shallow level.

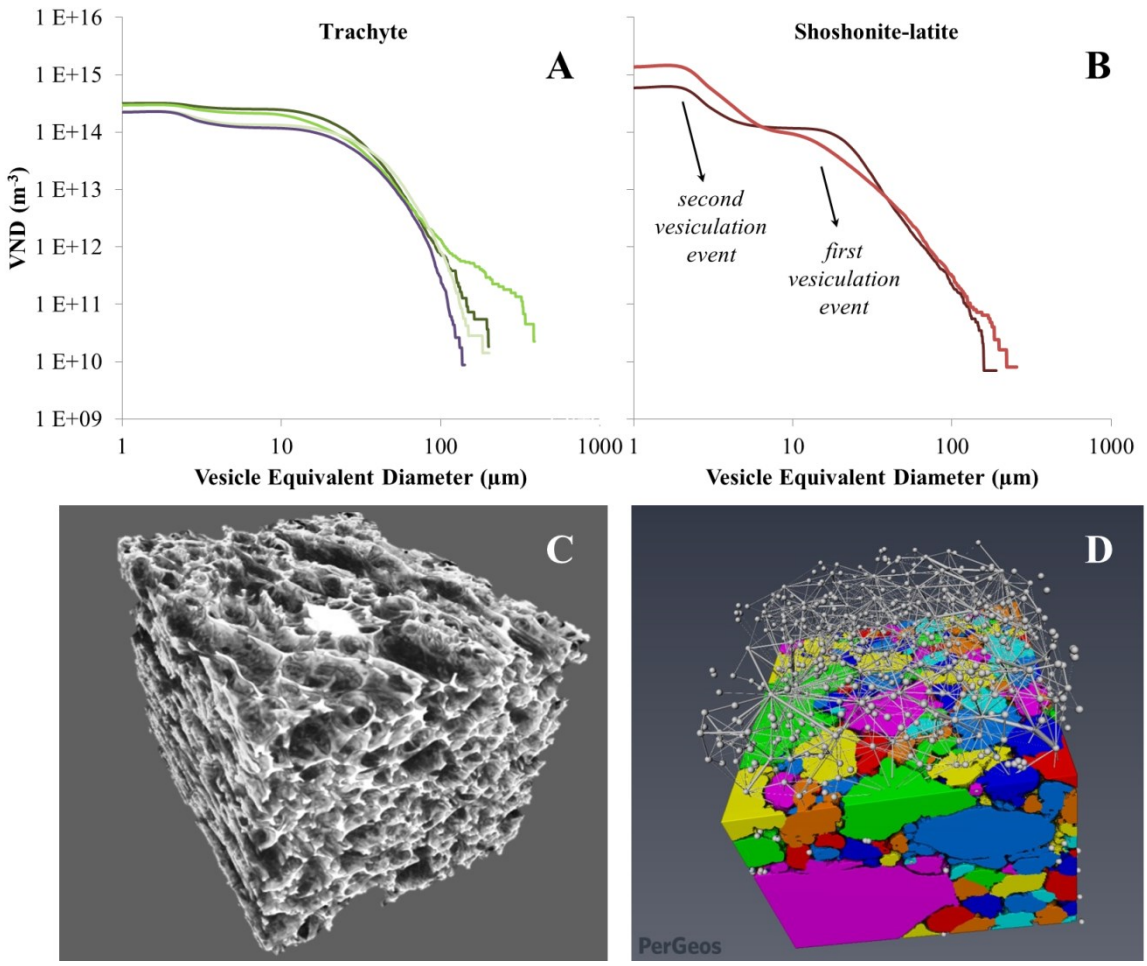

Fig. 7. Example of Cumulative Vesicles volume distributions (CVSDs) for A) trachytic and B) shoshonitic-latitic Somma-Vesuvius rocks. CVSDs of trachytic pumices show a curved continuous trend characterized by exponential distribution for the smaller bubbles and power law distribution for the larger bubbles, indicating a continuous nucleation process. On the contrary CVSDs of scoria latitic samples show irregular trends formed by multiple curved segments suggesting discrete vesiculation events, attributed to multiple nucleation pulses driven by fast CO_2 release during the ongoing decarbonation process (please see text for further explanation). C) Example of 3D micro-CT image (INGV-NA laboratory) of Somma-Vesuvius trachyte. Cube side: 300 pixels (pixel=1 micron). and D) Example of Pore Network Model obtained by Avizo FEI software. A PNM is composed of branching or endpoints of the network called pores (or vesicles for volcanic rocks) and lines connecting pores called throats. Pores are displayed using spheres, and throats are displayed using cylinders. Cube side: 300 pixels (pixel=1 micron). Data from Pappalardo et al. (2018).

In contrast, low-explosive and effusive eruptions (e.g. 1538 AD Monte Nuovo eruption from Campi Flegrei and 1944 eruption from Somma-Vesuvius) produced scoriae and/or lavas characterized by moderate vesicularity (40-60%), moderate to high microcrystalline groundmass (30-40 vol.%) and low glass water content (below 1 wt.%). Scoriae show large vesicles with polylobate and convoluted shapes, reflecting coalescence in variable directions. Evidence of flattening is also present possibly as a consequence of vesicle collapse and reduction of vesicularity during permeable outgassing (Fig. 8). CSDs on microlites show gentle slope (between -80 and -25 mm^{-1}) and low intercept values (15-12 mm^{-4}) and in most cases distinct inflections (hyperbolic CSDs) that are interpreted as different crystal populations growing in distinct magma ascent steps (Fig. 8). The textural and geochemical features of rocks indicate moderate to long magma ascent times (days to months) that favors permeable outgassing (open-system degassing) and in turn bubble collapse as well as extensive degassing-induced microlite crystallization (Fig. 8). Hyperbolic crystal size distributions data reveal that in the case of small eruptions magma ascent occurred by steps, thus

melts can reside at shallower level (ephemeral shallower storage zone) for short periods before erupting or cooling/crystallizing (plug development) in the case of failed eruption.

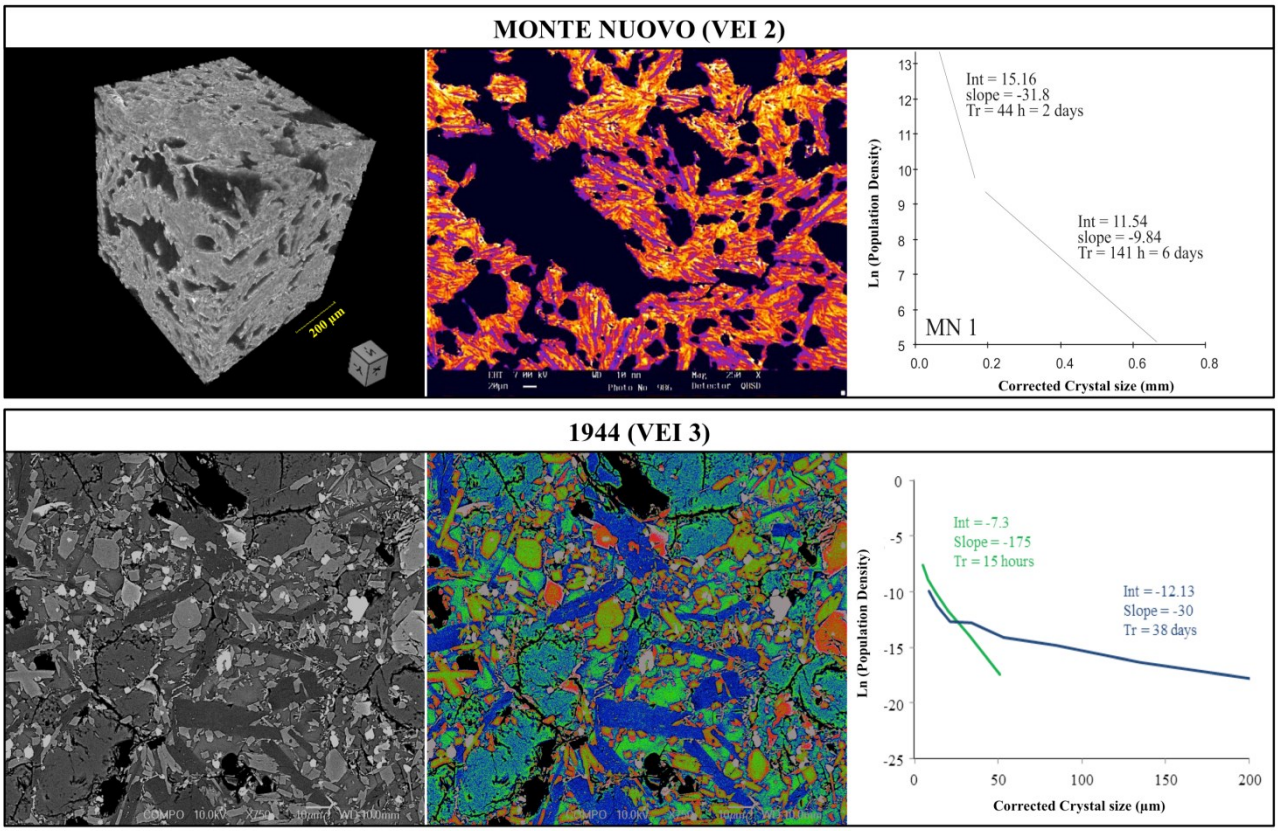

Fig. 8. 3D micro-CT image (INGV-NA laboratory) and 2D backscattered-electron images (INGV-Rome laboratory) of selected rocks from small-scale/effusive eruptions of Campi Flegrei and Somma Vesuvius and corresponding CSD curves obtained by plotting population density (number of crystals per unit volume) versus crystal size (maximum length). In the upper panels samples from the (phreatomagmatic) opening phase of the last CF Monte Nuovo eruption (1538 AD, VEI 2), in violet: sanidine microlite; data from Piochi et al. (2005). In the lower panels sample from the (effusive) opening phase of the last SV eruption (1944 AD, VEI 2), data from Pappalardo et al. (2014). CSDs show hyperbolic trend characterized by distinct inflections that are interpreted as different crystal populations growing in distinct magma ascent steps during conduit opening and propagation. In blue: plagioclase microlite; in green: cpx microlite.

An example of this behavior is represented by the last CF Monte Nuovo eruption, occurred in 1538 AD after a quiescent period lasted ca 3 ka. This eruption, although of low magnitude (VEI 2), was preceded by a long period of unrest, which became more intense few months before the eruption as inferred by the description of historical chronicles (Di Vito et al., 2016; Guidoboni & Ciuccarelli, 2011). A recent study Liedl et al. (2019) revealed that the ground deformations and earthquakes that preceded the eruption could be the result of recurrent magma migrations from a long-lived deep source (6-8 km) towards a shallower (3-4 km) temporary storage area (Fig. 5). The progression of this process possibly caused the weakening (heating) of the crustal rocks, thus favoring the subsequent propagation of fractures towards the surface triggering the eruption.
Eruptive style transitions have been frequently documented in past eruptions of Neapolitan volcanoes (e.g. Mastrolorenzo et al., 2017 and reference therein). Fig. 9 shows Vg/Vl versus water content (Fig. 9A) and vesicularity versus permeability (Fig. 9B) for the two case studies

representative of small-scale (Monte Nuovo strombolian eruption) and high-intensity (Pomici di Base plinian eruption) events fed by alkaline Campanian magmas. Textural data show values of increase permeability at about 55-60% of vesicularity at the passage from scoriae- to pumice-bearing layers, marking the transition from closed- (Vg/Vl and water content near equilibrium conditions, Fig. 9B) to open-system degassing (low Vg/Vl and water content, Fig. 9B). The highest vesicularity and permeability values are observed in the pumice-forming phase of MN eruption, possibly as a consequence of a sudden depressurization event driven by magma/water interaction characterizing the opening phase of this event.

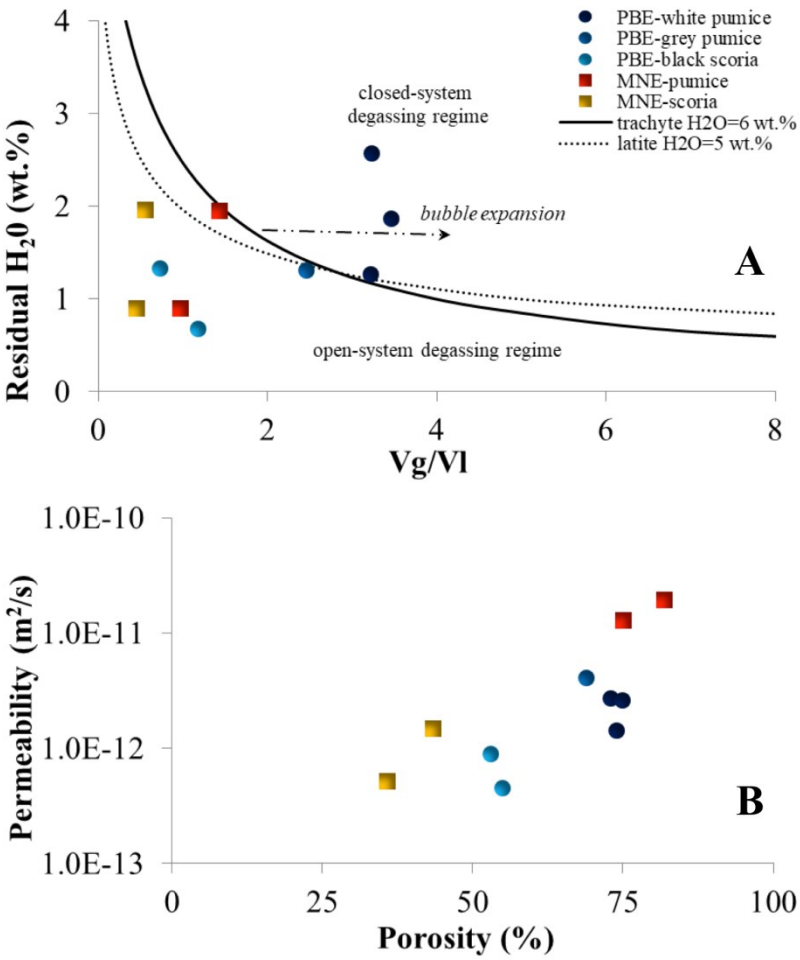

Fig. 9. A) Vg/Vl vs H_2O content and B) vesicularity vs permeability for small-scale Monte Nuovo eruption and for vesuvian plinian Pomici di Base eruption. Data from: Pappalardo et al. (2018) for PBE; Liedl et al. (2019), Piochi et al. (2005) for MNE.

5. Conclusions: Implications for Future hazards

In this chapter we used new and previous evaluation of available petrological (geochemical and textural) data of volcanic rocks representative of the eruptive history of Neapolitan volcanoes to reconstruct the architecture of their plumbing system and its evolution towards critical conditions close to eruption.

The results show the possible existence of a wide sill-like felsic magma layer beneath the whole Neapolitan volcanic area at 7–9 km depth (at the transition between sedimentary and metamorphic successions) fed by a deeper (> 8-10 km) mafic reservoir extending towards the Moho discontinuity (25-30 km of depth). Generally the shallow chamber fuelled mainly intermediate and highly explosive eruptions whereas the deep mafic magma reservoir was the source of less violent eruptions. Crystal Size Distribution data on feldspar phenocrysts (Pappalardo & Mastrolorenzo, 2010; 2012) reveal that primitive magmas can evolve, during the migration in the upper part of the reservoir, toward less-dense felsic liquids in a relatively short time span comparable with the hundreds of years of volcanos repose. This plumbing system could represent a long-term magmatic sills intrusion and storage zone, with its maximum volume under the CF supervolcano (where the huge volume of magmas was erupted in the last 40 ka and the maximum value of heat flux is currently measured).

Textural data (e.g. high vesicularity, Vesicle Size Distributions trends, absence of microlites etc) of rocks erupted during highly explosive eruptions indicate a single-stage volatile degassing under closed-system conditions during fast magma ascent in the volcanic conduit. These features could be indicative of rapid conduit propagation, thus suggesting short, and possibly initially, deep (in proximity of the inferred magma chamber top) precursory signals.

By contrast textural characters of volcanic rocks erupted from small-scale eruptions show evidence of degassing under open system conditions during slow magma migration and storage at shallower depth (ephemeral storage zones) where it resided until erupting or cooling (failed eruption), thus indicating slow conduit propagation and long period of unrest characterized by shallow earthquakes, ground deformation and gas emission.

Acknowledgements

We thank Francesca Forni and an anonymous reviewer for comments that greatly improved the manuscript. We gratefully acknowledge the critical reading of the manuscript by Chris Harris.

References

Albert, P.G., Giaccio, B., Isaia, R., Costa, A., Niespolo, E.M., Nomade, S., Pereira, A., et al. (2019). Evidence for a large-magnitude eruption from Campi Flegrei caldera (Italy) at 29 ka. Geology, 47(7), 595–599. doi: https://doi.org/10.1130/G45805.1

Allabar, A., & Nowak, M. (2018). Message in a bottle: Spontaneous phase separation of hydrous Vesuvius melt even at low decompression rates. Earth and Planetary Science Letters, 501, 192–201. https://doi.org/10.1016/j.epsl.2018.08.047

Andersen, N. L., Jicha, B. R., Singer, B. S., & Hildreth, W. (2017). Incremental heating of Bishop Tuff sanidine reveals preeruptive radiogenic Ar and rapid remobilization from cold storage. Proceedings of the National Academy of Sciences, 114(47), 12407–12412. https://doi.org/10.1073/pnas.1709581114

Annen, C. (2009) From plutons to magma chambers: Thermal constraints on the accumulation of eruptible silicic magma in the upper crust. Earth and Planetary Science Letters, 284, 409–416. https://doi.org/10.1016/j.epsl.2009.05.006

Annen, C., & Zellmer, G. F. (2008). Dynamics of Crustal Magma Transfer, Storage and Differentiation. Geological Society, London. https://doi.org/10.1144/SP304

Arienzo, I., Moretti, R., Civetta, L., Orsi, G., & Papale, P. (2010). The feeding system of Agnano-Monte Spina eruption (Campi Flegrei, Italy): Dragging the past into present activity and future scenarios. Chemical Geology, 270(1–4), 135–147. https://doi.org/10.1016/j.chemgeo.2009.11.012

Arzilli, F., Piochi, M., Mormone, A., Agostini, C., & Carroll, M. R. (2016). Constraining pre-eruptive magma conditions and unrest timescales during the Monte Nuovo eruption (1538 AD; Campi Flegrei, Southern Italy): integrating textural and CSD results from experimental and natural trachy-phonolites. Bulletin of Volcanology, 78(10), 72. https://doi.org/10.1007/s00445-016-1062-z

Auger, E., Gasparini, P., Virieux, J., & Zollo, A. (2001). Seismic evidence of an extended magmatic sill under Mt. Vesuvius. Science, 294(5546), 1510–1512. https://doi.org/10.1126/science.1064893

Bachmann, O., & Bergantz, G. W. (2003). Rejuvenation of the Fish Canyon magma body: A window into the evolution of large-volume silicic magma systems. Geology, 31(9), 789–792. https://doi.org/10.1130/G19764.1
Bachmann, O., & Bergantz, G. W. (2004). On the origin of crystal-poor rhyolites: Extracted from batholithic crystal mushes. Journal of Petrology, 45(8), 1565–1582. https://doi.org/10.1093/petrology/egh019
Bachmann, O., & Bergantz, G. W. (2008a). Deciphering Magma Chamber Dynamics from Styles of Compositional Zoning in Large Silicic Ash Flow Sheets. Reviews in Mineralogy and Geochemistry, 69(1), 651–674. https://doi.org/10.2138/rmg.2008.69.17
Bachmann, O., & Bergantz, G. W. (2008b). Rhyolites and their source mushes across tectonic settings. Journal of Petrology, 49(12), 2277–2285. https://doi.org/10.1093/petrology/egn068
Bachmann, O., & Bergantz, G. W. (2008c). The magma reservoirs that feed supereruptions. Elements, 4(1), 17–21. https://doi.org/10.2113/GSELEMENTS.4.1.17
Bachmann, O., & Huber, C. (2016). Silicic magma reservoirs in the Earth's crust. American Mineralogist, 101(11), 2377–2404. https://doi.org/10.2138/am-2016-5675
Baker, D. R., Mancini, L., Polacci, M., Higgins, M. D., Gualda, G. A. R., Hill, R. J., & Rivers, M. L. (2012). An introduction to the application of X-ray microtomography to the three-dimensional study of igneous rocks. Lithos, 148, 262–276. https://doi.org/10.1016/j.lithos.2012.06.008
Balcone-Boissard, H., Boudon, G., Cioni, R., Webster, J. D., Zdanowicz, G., Orsi, G., & Civetta, L. (2016). Chlorine as a geobarometer for alkaline magmas: Evidence from a systematic study of the eruptions of Mount Somma-Vesuvius. Scientific Reports, 6, 21726. https://doi.org/10.1038/srep21726
Balcone-Boissard, H., Boudon, G., Ucciani, G., Villemant, B., Cioni, R., Civetta, L., & Orsi, G. (2012). Magma degassing and eruption dynamics of the Avellino pumice Plinian eruption of Somma-Vesuvius (Italy). Comparison with the Pompeii eruption. Earth and Planetary Science Letters, 331–332, 257–268. https://doi.org/10.1016/j.epsl.2012.03.011
Balcone-Boissard, H., Villemant, B., Boudon, G., & Michel, A. (2008). Non-volatile vs volatile behaviours of halogens during the AD 79 plinian eruption of Mt. Vesuvius, Italy. Earth and Planetary Science Letters, 269(1–2), 66–79. https://doi.org/10.1016/j.epsl.2008.02.003
Barbieri, M., Di Girolamo, P., Locardi, E., Lombardi, G. & Stanzione, D. (1979). Petrology of the calc-alkaline volcanics of the Parete 2 well (Campania, Italy). Periodico di Mineralogia, 48, 53–74
Befus, K. S., Zinke, R. W., Jordan, J. S., Manga, M., & Gardner, J. E. (2014). Pre-eruptive storage conditions and eruption dynamics of a small rhyolite dome: Douglas Knob, Yellowstone volcanic field, USA. Bulletin of Volcanology, 76(3), 1–12. https://doi.org/10.1007/s00445-014-0808-8
Berrino, G., Corrado, G., & Riccardi, U. (1998). Sea gravity data in the Gulf of Naples: a contribution to delineating the structural pattern of the Vesuvian area. Journal of Volcanology and Geothermal Research, 82(1–4), 139–150. https://doi.org/10.1016/S0377-0273(97)00061-9
Berrino, G., Corrado, G., & Riccardi, U. (2008). Sea gravity data in the Gulf of Naples. A contribution to delineating the structural pattern of the Phlegraean Volcanic District. Journal of Volcanology and Geothermal Research, 175(3), 241–252. https://doi.org/10.1016/j.jvolgeores.2008.03.007
Blower, J. D., Keating, J. P., Mader, H. M., & Phillips, J. C. (2003). The evolution of bubble size distributions in volcanic eruptions. Journal of Volcanology and Geothermal Research, 120(1–2), 1–23. https://doi.org/10.1016/S0377-0273(02)00404-3
Blundy, J. D., & Cashman, K. V. (2008). Petrologic Reconstruction of Magmatic System Variables and Processes. Reviews in Mineralogy and Geochemistry, 69(1), 179–239. https://doi.org/10.2138/rmg.2008.69.6
Bowen, N. L. (1928). Evolution of the Igneous Rocks. Dover Publications, New York
Brocchini, D., Principe, C., Castradori, D., Laurenzi, M. A., & Gorla, L. (2001). Quaternary evolution of the southern sector of the Campanian Plain and early Somma-Vesuvius activity: Insights from the Trecase 1 well. Mineralogy and Petrology, 73(1–3), 67–91. https://doi.org/10.1007/s007100170011
Brophy, J. G. (1991). Composition gaps, critical crystallinity, and fractional crystallization in orogenic (calc-alkaline) magmatic systems. Contributions to Mineralogy and Petrology, 109(2), 173–182. https://doi.org/10.1007/BF00306477
Browne, B. L., & Gardner, J. E. (2006). The influence of magma ascent path on the texture, mineralogy, and formation of hornblende reaction rims. Earth and Planetary Science Letters, 246(3–4), 161–176. https://doi.org/10.1016/j.epsl.2006.05.006
Brugger, C. R., & Hammer, J. E. (2010a). Crystal size distribution analysis of plagioclase in experimentally decompressed hydrous rhyodacite magma. Earth and Planetary Science Letters, 300(3–4), 246–254. https://doi.org/10.1016/j.epsl.2010.09.046
Brugger, C. R., & Hammer, J. E. (2010b). Crystallization kinetics in continuous decompression experiments: Implications for interpreting natural magma ascent processes. Journal of Petrology, 51(9), 1941–1965. https://doi.org/10.1093/petrology/egq044
Buono, G., Pappalardo, L. & Petrosino, P. (2019). Magma storage and ascent during the largest eruption of Somma-Vesuvius volcano: Pomici di Base (22 ka) plinian event. Bollettino Di Geofisica Teorica e Applicata, in press.
Calzolaio, M., Arzilli, F., & Carroll, M. R. (2010). Growth rate of alkali feldspars in decompression-induced crystallization experiments in a trachytic melt of the Phlegraean Fields (Napoli, Italy). European Journal of Mineralogy,

22(4), 485–493. https://doi.org/10.1127/0935-1221/2010/0022-2012
Cannatelli, C., Lima, A., Bodnar, R. J., De Vivo, B., Webster, J. D., & Fedele, L. (2007). Geochemistry of melt inclusions from the Fondo Riccio and Minopoli 1 eruptions at Campi Flegrei (Italy). Chemical Geology, 237(3–4), 418–432. https://doi.org/10.1016/j.chemgeo.2006.07.012
Carey, R. J., Houghton, B. F., & Thordarson, T. (2009). Abrupt shifts between wet and dry phases of the 1875 eruption of Askja Volcano: Microscopic evidence for macroscopic dynamics. Journal of Volcanology and Geothermal Research, 184(3–4), 256–270. https://doi.org/10.1016/j.jvolgeores.2009.04.003
Carlino, S., Somma, R., Troise, C., & De Natale, G. (2012). The geothermal exploration of Campanian volcanoes: Historical review and future development. Renewable and Sustainable Energy Reviews, 16(1), 1004–1030. https://doi.org/10.1016/j.rser.2011.09.023
Cashman, K. V., & Giordano, G. (2014). Calderas and magma reservoirs. Journal of Volcanology and Geothermal Research, 288, 28–45. https://doi.org/10.1016/j.jvolgeores.2014.09.007
Cashman, K. V., & Mangan, M. T. (1994). Physical aspects of magmatic degassing: II. Constraints on vesiculation processes from textural studies of eruptive products. Reviews in Mineralogy, 30, 447–478
Cashman, K. V. & McConnell, S. M. (2005). Multiple levels of magma storage during the 1980 summer eruptions of Mount St. Helens, WA. Bulletin of Volcanology, 68, 57–75. https://doi.org/10.1007/s00445-005-0422-x
Cassidy, M., Manga, M., Cashman, K.V, & Bachmann, O. (2018). Controls on explosive-effusive volcanic eruption styles. Nature Communications, 9(1), 2839. https://doi.org/10.1038/s41467-018-05293-3
Chiodini, G., Paonita, A., Aiuppa, A., Costa, A., Caliro, S., De Martino, P., et al. (2016). Magmas near the critical degassing pressure drive volcanic unrest towards a critical state. Nature Communications, 7, 13712. https://doi.org/10.1038/ncomms13712
Cioni, R., Bertagnini, A., Andronico, D., Cole, P. D., & Mundula, F. (2011). The 512 AD eruption of Vesuvius: Complex dynamics of a small scale subplinian event. Bulletin of Volcanology, 73(7), 789–810. https://doi.org/10.1007/s00445-011-0454-3
Clarke, A. B., Stephens, S., Teasdale, R., Sparks, R. S. J., & Diller, K. (2007). Petrologic constraints on the decompression history of magma prior to Vulcanian explosions at the Soufrière Hills volcano, Montserrat. Journal of Volcanology and Geothermal Research, 161(4), 261–274. https://doi.org/10.1016/j.jvolgeores.2006.11.007
Cooper, K. M. (2019). Time scales and temperatures of crystal storage in magma reservoirs: implications for magma reservoir dynamics. Philosophical Transactions of the Royal Society A: Mathematical, Physical and Engineering Sciences, 377(2139), 20180009. https://doi.org/10.1098/rsta.2018.0009
Cooper, K. M., & Kent, A. J. R. (2014). Rapid remobilization of magmatic crystals kept in cold storage. Nature, 506(7489), 480–483. https://doi.org/10.1038/nature12991
Couch, S., Sparks, R. S. J., & Carroll, M. R. (2003). The Kinetics of Degassing-Induced Crystallization at Soufriere Hills Volcano, Montserrat. Journal of Petrology, 44(8), 1477–1502. https://doi.org/10.1093/petrology/44.8.1477
Dallai, L., Cioni, R., Boschi, C., & D'Oriano, C. (2011). Carbonate-derived CO2 purging magma at depth: Influence on the eruptive activity of Somma-Vesuvius, Italy. Earth and Planetary Science Letters, 310(1–2), 84–95. https://doi.org/10.1016/j.epsl.2011.07.013
D'Antonio, M. (2011). Lithology of the basement underlying the Campi Flegrei caldera: Volcanological and petrological constraints. Journal of Volcanology and Geothermal Research, 200(1–2), 91–98. https://doi.org/10.1016/j.jvolgeores.2010.12.006
Degruyter, W., Bachmann, O., & Burgisser, A. (2010a). Controls on magma permeability in the volcanic conduit during the climactic phase of the Kos Plateau Tuff eruption (Aegean Arc). Bulletin of Volcanology, 72(1), 63–74. https://doi.org/10.1007/s00445-009-0302-x
Degruyter, W., Burgisser, A., Bachmann, O., & Malaspinas, O. (2010b). Synchrotron X-ray microtomography and lattice Boltzmann simulations of gas flow through volcanic pumices. Geosphere, 6(5), 470–481. https://doi.org/10.1130/ges00555.1
Deino, A. L., Orsi, G., de Vita, S., & Piochi, M. (2004). The age of the Neapolitan Yellow Tuff caldera-forming eruption (Campi Flegrei caldera - Italy) assessed by 40Ar/39Ar dating method. Journal of Volcanology and Geothermal Research, 133(1–4), 157–170. https://doi.org/10.1016/S0377-0273(03)00396-2
Della Vedova, B., Bellani, S., Pellis, G., & Squarci, P. (2013). Deep temperatures and surface heat flow distribution. In G. B. Vai & L. P. Martini (Eds.), Anatomy of an Orogen: the Apennines and Adjacent Mediterranean Basins (pp. 65–76). Springer, Dordrecht. https://doi.org/10.1007/978-94-015-9829-3_7
De Natale, G., Troise, C., Pingue, F., Mastrolorenzo, G., & Pappalardo, L. (2006a). The Somma-Vesuvius volcano (Southern Italy): Structure, dynamics and hazard evaluation. Earth-Science Reviews, 74(1–2), 73–111. https://doi.org/10.1016/j.earscirev.2005.08.001
De Natale, G., Troise, C., Pingue, F., Mastrolorenzo, G., Pappalardo, L., Battaglia, M., & Boschi, E. (2006b). The Campi Flegrei caldera: unrest mechanisms and hazards. Geological Society, London, Special Publications, 269(1), 25–45. https://doi.org/10.1144/gsl.sp.2006.269.01.03
De Vivo, B., Rolandi, G., Gans, P. B., Calvert, A., Bohrson, W. A.,Spera,F. J. & Belkin, H. E. (2001). New constraints on the pyroclastic eruptive history of the Campanian volcanic Plain (Italy). Mineralogy and Petrology, 73, 47– 65. https://doi.org/10.1007/s007100170010

Di Renzo, V., Di Vito, M. A., Arienzo, I., Carandente, A., Civetta, L., D'Antonio, M., et al. (2007). Magmatic history of Somma-Vesuvius on the basis of new geochemical and isotopic data from a deep borehole (Camaldoli della Torre). Journal of Petrology, 48(4), 753–784. https://doi.org/10.1093/petrology/egl081

Di Vito, M. A., Acocella, V., Aiello, G., Barra, D., Battaglia, M., Carandente, A., et al. (2016). Magma transfer at Campi Flegrei caldera (Italy) before the 1538 AD eruption. Scientific Reports, 6, 32245. https://doi.org/10.1038/srep32245

Dolfi, D., & Trigila, R. (1978). The role of water in the 1944 Vesuvius eruption. Contributions to Mineralogy and Petrology, 67(3), 297–304. https://doi.org/10.1007/BF00381457

D'Oriano, C., Poggianti, E., Bertagnini, A., Cioni, R., Landi, P., Polacci, M., & Rosi, M. (2005). Changes in eruptive style during the A.D. 1538 Monte Nuovo eruption (Phlegrean Fields, Italy): The role of syn-eruptive crystallization. Bulletin of Volcanology, 67(7), 601–621. https://doi.org/10.1007/s00445-004-0397-z

Edmonds, M., Cashman, K. V., Holness, M., & Jackson, M. (2019). Architecture and dynamics of magma reservoirs. Philosophical Transactions of the Royal Society A: Mathematical, Physical and Engineering Sciences, 377(2139), 20180298. https://doi.org/10.1098/rsta.2018.0298

Esposito, R., Badescu, K., Steele-MacInnis, M., Cannatelli, C., De Vivo, B., Lima, A., et al. (2018). Magmatic evolution of the Campi Flegrei and Procida volcanic fields, Italy, based on interpretation of data from well-constrained melt inclusions. Earth-Science Reviews, 185, 325–356. https://doi.org/10.1016/j.earscirev.2018.06.003

Fabbrizio, A., & Carroll, M. R. (2008). Experimental constraints on the differentiation process and pre-eruptive conditions in the magmatic system of Phlegraean Fields (Naples, Italy). Journal of Volcanology and Geothermal Research, 171(1–2), 88–102. https://doi.org/10.1016/j.jvolgeores.2007.11.002

Fedi, M., Cella, F., D'Antonio, M., Florio, G., Paoletti, V., & Morra, V. (2018). Gravity modeling finds a large magma body in the deep crust below the Gulf of Naples, Italy. Scientific Reports, 8(1), 8229. https://doi.org/10.1038/s41598-018-26346-z

Flinders, A. F., Shelly, D. R., Dawson, P. B., Hill, D. P., Tripoli, B., & Shen, Y. (2018). Seismic evidence for significant melt beneath the Long Valley Caldera, California, USA. Geology, 46(9), 799–802. https://doi.org/10.1130/G45094.1

Forni, F., Degruyter, W., Bachmann, O., De Astis, G., & Mollo, S. (2018). Long-term magmatic evolution reveals the beginning of a new caldera cycle at Campi Flegrei. Science Advances, 4(11), eaat9401. https://doi.org/10.1126/sciadv.aat9401

Fourmentraux, C., Métrich, N., Bertagnini, A., & Rosi, M. (2012). Crystal fractionation, magma step ascent, and syn-eruptive mingling: The Averno 2 eruption (Phlegraean Fields, Italy). Contributions to Mineralogy and Petrology, 163(6), 1121–1137. https://doi.org/10.1007/s00410-012-0720-1

Fowler, S. J., Spera, F. J., Bohrson, W. A., Belkin, H. E., & De Vivo, B. (2007). Phase equilibria constraints on the chemical and physical evolution of the campanian ignimbrite. Journal of Petrology, 48(3), 459–493. https://doi.org/10.1093/petrology/egl068

Gaonac'h, H., Lovejoy, S., Stix, J., & Scherzter, D. (1996). A scaling growth model for bubbles in basaltic lava flows. Earth and Planetary Science Letters, 139(3–4), 395–409. https://doi.org/10.1016/0012-821X(96)00039-8

Gardner, J. E., Thomas, R. M. E., Jaupart, C., & Tait, S. (1996). Fragmentation of magma during Plinian volcanic eruptions. Bulletin of Volcanology, 58(2–3), 144–162. https://doi.org/10.1007/s004450050132

Gebauer, S. K., Schmitt, A. K., Pappalardo, L., Stockli, D. F., & Lovera, O. M. (2014). Crystallization and eruption ages of Breccia Museo (Campi Flegrei caldera, Italy) plutonic clasts and their relation to the Campanian ignimbrite. Contributions to Mineralogy and Petrology, 167(1), 1–18. https://doi.org/10.1007/s00410-013-0953-7

Gelman, S.E., Gutierrez, F.J., & Bachmann, O. (2013) On the longevity of large upper crustal silicic magma reservoirs. Geology, 41, 759–762. https://doi.org/10.1130/G34241.1

Geschwind, C. H., & Rutherford, M. J. (1995). Crystallization of microlites during magma ascent: the fluid mechanics of 1980-1986 eruptions at Mount St Helens. Bulletin of Volcanology, 57(5), 356–370. https://doi.org/10.1007/BF00301293

Ghiorso, M. S., & Sack, R. O. (1995). Chemical mass transfer in magmatic processes IV. A revised and internally consistent thermodynamic model for the interpolation and extrapolation of liquid-solid equilibria in magmatic systems at elevated temperatures and pressures. Contributions to Mineralogy and Petrology, 119(2–3), 197–212. https://doi.org/10.1007/BF00307281

Giachetti, T., Gonnermann, H. M., Gardner, J. E., Burgisser, A., Hajimirza, S., Earley, T. C., et al. (2019). Bubble coalescence and percolation threshold in expanding rhyolitic magma. Geochemistry, Geophysics, Geosystems, 20, 1054– 1074. https://doi.org/10.1029/2018GC008006

Gonnermann, H. M., & Houghton, B. F. (2012). Magma degassing during the Plinian eruption of Novarupta, Alaska, 1912. Geochemistry, Geophysics, Geosystems, 13(10), Q10009. https://doi.org/10.1029/2012GC004273

Gonnermann, H. M. & Manga, M. (2007). The Fluid Mechanics Inside a Volcano. Annual Review of Fluid Mechanics, 39, 321–356. https://doi.org/10.1146/annurev.fluid.39.050905.110207

Guidoboni, E., & Ciuccarelli, C. (2011). The Campi Flegrei caldera: Historical revision and new data on seismic crises, bradyseisms, the Monte Nuovo eruption and ensuing earthquakes (twelfth century 1582 AD). Bulletin of Volcanology, 73(6), 655–677. https://doi.org/10.1007/s00445-010-0430-3

Gurioli, L., Andronico, D., Bachelery, P., Balcone-Boissard, H., Battaglia, J., Boudon, G., et al. (2015). MeMoVolc consensual document: a review of cross-disciplinary approaches to characterizing small explosive magmatic eruptions.

Bulletin of Volcanology, 77(6), 49. https://doi.org/10.1007/s00445-015-0935-x
Hammer, J. E., Cashman, K. V., Hoblitt, R. P., & Newman, S. (1999). Degassing and microlite crystallization during pre-climactic events of the 1991 eruption of Mt. Pinatubo, Philippines. Bulletin of Volcanology, 60(5), 355–380. https://doi.org/10.1007/s004450050238
Hammer, J. E., & Rutherford, M. J. (2002). An experimental study of the kinetics of decompression-induced crystallization in silicic melt. Journal of Geophysical Research: Solid Earth, 107(B1), ECV 8-1-ECV 8-24. https://doi.org/10.1029/2001jb000281
Hammer, J. E., Rutherford, M. J., & Hildreth, W. (2002). Magma storage prior to the 1912 eruption at Novarupta, Alaska. Contributions to Mineralogy and Petrology, 144(2), 144–162. https://doi.org/10.1007/s00410-002-0393-2
Hawkesworth, C., Blake, S., Evans, P., Hughes, R., Macdonald, R., Thomas, L. E., et al. (2000). Time scales of crystal fractionation in magma chambers-integrating physical, isotopic and geochemical perspectives. Journal of Petrology, 41(7), 991–1006. https://doi.org/10.1093/petrology/41.7.991
Hawkesworth, C., George, R., Turner, S., & Zellmer, G. (2004). Time scales of magmatic processes. Earth and Planetary Science Letters, 218(1–2), 1–16. https://doi.org/10.1016/S0012-821X(03)00634-4
Hildreth, W., & Wilson, C. J. N. (2007). Compositional Zoning of the Bishop Tuff. Journal of Petrology, 48(5), 951–999. https://doi.org/10.1093/petrology/egm007
Holness, M. B., Stock, M. J., & Geist, D. (2019). Magma chambers versus mush zones: constraining the architecture of sub-volcanic plumbing systems from microstructural analysis of crystalline enclaves. Philosophical Transactions of the Royal Society A: Mathematical, Physical and Engineering Sciences, 377(2139), 20180006. https://doi.org/10.1098/rsta.2018.0006
Iacono Marziano, G., Gaillard, F., & Pichavant, M. (2008). Limestone assimilation by basaltic magmas: An experimental re-assessment and application to Italian volcanoes. Contributions to Mineralogy and Petrology, 155(6), 719–738. https://doi.org/10.1007/s00410-007-0267-8
Iacono Marziano, G., Schmidt, B. C., & Dolfi, D. (2007). Equilibrium and disequilibrium degassing of a phonolitic melt (Vesuvius AD 79 “white pumice”) simulated by decompression experiments. Journal of Volcanology and Geothermal Research, 161(3), 151–164. https://doi.org/10.1016/j.jvolgeores.2006.12.001
Improta, L., & Corciulo, M. (2006). Controlled source nonlinear tomography: A powerful tool to constrain tectonic models of the Southern Apennines orogenic wedge, Italy. Geology, 34(11), 941–944. https://doi.org/10.1130/G22676A.1
Iovine, R. S., Fedele, L., Mazzeo, F. C., Arienzo, I., Cavallo, A., Wörner, G., et al. (2017). Timescales of magmatic processes prior to the ~4.7 ka Agnano-Monte Spina eruption (Campi Flegrei caldera, Southern Italy) based on diffusion chronometry from sanidine phenocrysts. Bulletin of Volcanology, 79(2), 18. https://doi.org/10.1007/s00445-017-1101-4
Jaxybulatov, K., Shapiro, N. M., Koulakov, I., Mordret, A., Landès, M., & Sens-Schönfelder, C. (2014). A large magmatic sill complex beneath the Toba caldera. Science, 346(6209), 617–619. https://doi.org/10.1126/science.1258582
Jolis, E. M., Freda, C., Troll, V. R., Deegan, F. M., Blythe, L. S., McLeod, C. L., & Davidson, J. P. (2013). Experimental simulation of magma-carbonate interaction beneath Mt. Vesuvius, Italy. Contributions to Mineralogy and Petrology, 166(5), 1335–1353. https://doi.org/10.1007/s00410-013-0931-0
Jolis, E. M., Troll, V. R., Harris, C., Freda, C., Gaeta, M., Orsi, G., & Siebe, C. (2015). Skarn xenolith record crustal CO2 liberation during Pompeii and Pollena eruptions, Vesuvius volcanic system, central Italy. Chemical Geology, 415, 17–36. https://doi.org/10.1016/j.chemgeo.2015.09.003
Kennedy, B., Spieler, O., Scheu, B., Kueppers, U., Taddeucci, J., & Dingwell, D. B. (2005). Conduit implosion during Vulcanian eruptions. Geology, 33(7), 581–584. https://doi.org/10.1130/G21488.1
Kilburn, C. R. J., De Natale, G., & Carlino, S. (2017). Progressive approach to eruption at Campi Flegrei caldera in southern Italy. Nature Communications, 8, 15312. https://doi.org/10.1038/ncomms15312
Klug, C., Cashman, K. V., & Bacon, C. (2002). Structure and physical characteristics of pumice from the climactic eruption of Mount Mazama (Crater Lake), Oregon. Bulletin of Volcanology, 64(7), 486–501. https://doi.org/10.1007/s00445-002-0230-5
Lanzafame, G., Iezzi, G., Mancini, L., Lezzi, F., Mollo, S., & Ferlito, C. (2017). Solidification and Turbulence (Non-laminar) during magma ascent: Insights from 2D and 3D analyses of bubbles and minerals in an Etnean dyke. Journal of Petrology, 58(8), 1511–1534. https://doi.org/10.1093/petrology/egx063
Larsen, J. F. (2008). Heterogeneous bubble nucleation and disequilibrium H 2 O exsolution in Vesuvius K-phonolite melts. Journal of Volcanology and Geothermal Research, 175(3), 278–288. https://doi.org/10.1016/j.jvolgeores.2008.03.015
Larsen, J. F., Gardner, J.E. (2004). Experimental study of water degassing from phonolite melts: implications for volatile oversaturation during magmatic ascent. Journal of Volcanology and Geothermal Research, 134, 109-124. https://doi.org/10.1016/j.jvolgeores.2004.01.004
Liedl, A., Buono, G., Lanzafame, G., Dabagov, S. B., Della Ventura, G., Hampai, D. et al. (2019). A 3D imaging textural characterization of pyroclastic products from the 1538 AD Monte Nuovo eruption (Campi Flegrei, Italy). Lithos, 340–341, 316–331. https://doi.org/10.1016/j.lithos.2019.05.010
Lima, A., Danyushevsky, L. V., De Vivo, B., & Fedele, L. (2003). A model for the evolution of the Mt. Somma-

Vesuvius magmatic system based on fluid and melt inclusion investigations. Developments in Volcanology, 5(C), 227–249. https://doi.org/10.1016/S1871-644X(03)80032-3
Lima, A., De Vivo, B., Spera, F. J., Bodnar, R. J., Milia, A., Nunziata, C., et al. (2009). Thermodynamic model for uplift and deflation episodes (bradyseism) associated with magmatic-hydrothermal activity at the Campi Flegrei (Italy). Earth-Science Reviews, 97(1–4), 44–58. https://doi.org/10.1016/j.earscirev.2009.10.001
Lima, A., Esposito, R., & De Vivo, B. (2017). Fluid and melt inclusions from subvolcanic to surface environment in the Campi Flegrei (Napoli, Italy) active volcanic system. Journal of the Geological Society of India, 90(5), 515–523. https://doi.org/10.1007/s12594-017-0747-z
Macedonio, G., Dobran, F., & Neri, A. (1994). Erosion processes in volcanic conduits and application to the AD 79 eruption of Vesuvius. Earth and Planetary Science Letters, 121(1–2), 137–152. https://doi.org/10.1016/0012-821X(94)90037-X
Mangan, M. T, & Sisson, T. (2000). Delayed, disequilibrium degassing in rhyolite magma: Decompression experiments and implications for explosive volcanism. Earth and Planetary Science Letters, 183(3–4), 441–455. https://doi.org/10.1016/S0012-821X(00)00299-5
Mangan, M. T., Sisson, T.W., & Hankins, W. B. (2004). Decompression experiments identify kinetic controls on explosive silicic eruptions. Geophysical Research Letters, 31(8), L08605. https://doi.org/10.1029/2004GL019509
Mangiacapra, A., Moretti, R., Rutherford, M., Civetta, L., Orsi, G., & Papale, P. (2008). The deep magmatic system of the Campi Flegrei caldera (Italy). Geophysical Research Letters, 35(21), L21304. https://doi.org/10.1029/2008GL035550
Marianelli, P., Métrich, N., & Sbrana, A. (1999). Shallow and deep reservoirs involved in magma supply of the 1944 eruption of Vesuvius. Bulletin of Volcanology, 61(1–2), 48–63. https://doi.org/10.1007/s004450050262
Marianelli, P., Sbrana, A., Métrich, N., & Cecchetti, A. (2005). The deep feeding system Vesuvius involved in recent violent strombolian eruptions. Geophysical Research Letters, 32(2), 1–4. https://doi.org/10.1029/2004GL021667
Marianelli, P., Sbrana, A., & Proto, M. (2006). Magma chamber of the Campi Flegrei supervolcano at the time of eruption of the Campanian Ignimbrite. Geology, 34(11), 937–940. https://doi.org/10.1130/G22807A.1
Marsh, B. D. (1988). Crystal size distribution (CSD) in rocks and the kinetics and dynamics of crystallization I. Theory. Contributions to Mineralogy and Petrology, 99(3), 277–291. https://doi.org/10.1007/BF00375362
Marsh, B. D. (1989). Magma Chambers. Annual Review of Earth and Planetary Sciences, 17(1), 439–474. https://doi.org/10.1146/annurev.earth.17.1.439
Marsh, B. D. (2002). On bimodal differentiation by solidification front instability in basaltic magmas, part 1: Basic mechanics. Geochimica et Cosmochimica Acta, 66(12), 2211–2229. https://doi.org/10.1016/S0016-7037(02)00905-5
Marsh, B. D. (2015). Magma Chambers. In H. Sigurdsson, B. Houghton, S. R. McNutt, H. Rymer, & J. Stix (Eds.), The Encyclopedia of Volcanoes (Second Edition) (pp. 185–201). Academic Press, London. https://doi.org/10.1016/B978-0-12-385938-9.00008-0
Martel, C. (2012). Eruption dynamics inferred from microlite crystallization experiments: Application to plinian and dome-forming eruptions of Mt. Pelée (martinique, lesser antilles). Journal of Petrology, 53(4), 699–725. https://doi.org/10.1093/petrology/egr076
Martel, C., Brooker, R. A., Andújar, J., Pichavant, M., Scaillet, B., & Blundy, J. D. (2017). Experimental Simulations of Magma Storage and Ascent. In J. Gottsmann, J. Neuberg, & B. Scheu (Eds.), Volcanic Unrest (pp. 101–110). Springer, Cham. https://doi.org/10.1007/11157_2017_20
Martel, C., & Schmidt, B. C. (2003). Decompression experiments as an insight into ascent rates of silicic magmas. Contributions to Mineralogy and Petrology, 144(4), 397–415. https://doi.org/10.1007/s00410-002-0404-3
Marxer, H., Bellucci, P., & Nowak, M. (2015). Degassing of H2O in a phonolitic melt: A closer look at decompression experiments. Journal of Volcanology and Geothermal Research, 297, 109–124. https://doi.org/10.1016/j.jvolgeores.2014.11.017
Masotta, M., Mollo, S., Freda, C., Gaeta, M., & Moore, G. (2013). Clinopyroxene-liquid thermometers and barometers specific to alkaline differentiated magmas. Contributions to Mineralogy and Petrology, 166(6), 1545–1561. https://doi.org/10.1007/s00410-013-0927-9
Mastrolorenzo, G., Brachi, L., & Canzanella, A. (2001). Vesicularity of various types of pyroclastic deposits of Campi Flegrei volcanic field: Evidence of analogies in magma rise and vesiculation mechanisms. Journal of Volcanology and Geothermal Research, 109(1–3), 41–53. https://doi.org/10.1016/S0377-0273(00)00303-6
Mastrolorenzo, G., Palladino, D. M., Pappalardo, L. & Rossano, S. (2017) Probabilistic-numerical assessment of pyroclastic current hazard at Campi Flegrei and Naples city: Multi-VEI scenarios as a tool for “full-scale” risk management. PLoS ONE, 12(10), e0185756. https://doi.org/10.1371/journal.pone.0185756
Mastrolorenzo, G., & Pappalardo, L. (2006). Magma degassing and crystallization processes during eruptions of high-risk Neapolitan-volcanoes: Evidence of common equilibrium rising processes in alkaline magmas. Earth and Planetary Science Letters, 250(1–2), 164–181. https://doi.org/10.1016/j.epsl.2006.07.040
McBirney, A. R., Baker, B. H., & Nilson, R. H. (1985). Liquid fractionation. Part I: Basic principles and experimental simulations. Journal of Volcanology and Geothermal Research, 24(1–2), 1–24. https://doi.org/10.1016/0377-0273(85)90026-5
Melnik, O. E., Blundy, J. D., Rust, A. C., & Muir, D. D. (2011). Subvolcanic plumbing systems imaged through crystal

size distributions. Geology, 39(4), 403–406. https://doi.org/10.1130/G31691.1
Mollo, S., & Masotta, M. (2014). Optimizing pre-eruptive temperature estimates in thermally and chemically zoned magma chambers. Chemical Geology, 368, 97–103. https://doi.org/10.1016/j.chemgeo.2014.01.007
Morgan, D. J., & Blake, S. (2006). Magmatic residence times of zoned phenocrysts: Introduction and application of the binary element diffusion modelling (BEDM) technique. Contributions to Mineralogy and Petrology, 151(1), 58–70. https://doi.org/10.1007/s00410-005-0045-4
Mourtada-Bonnefoi, C. C., & Laporte, D. (2004). Kinetics of bubble nucleation in a rhyolitic melt: An experimental study of the effect of ascent rate. Earth and Planetary Science Letters, 218(3–4), 521–537. https://doi.org/10.1016/S0012-821X(03)00684-8
Noguchi, S., Toramaru, A., & Shimano, T. (2006). Crystallization of microlites and degassing during magma ascent: Constraints on the fluid mechanical behavior of magma during the Tenjo Eruption on Kozu Island, Japan. Bulletin of Volcanology, 68(5), 432–449. https://doi.org/10.1007/s00445-005-0019-4
Nunziata, C. (2010). Low shear-velocity zone in the Neapolitan-area crust between the Campi Flegrei and Vesuvio volcanic areas. Terra Nova, 22(3), 208–217. https://doi.org/10.1111/j.1365-3121.2010.00936.x
Pappalardo, L., Buono, G., Fanara, S., & Petrosino, P. (2018). Combining textural and geochemical investigations to explore the dynamics of magma ascent during Plinian eruptions: a Somma–Vesuvius volcano (Italy) case study. Contributions to Mineralogy and Petrology, 173(7), 61. https://doi.org/10.1007/s00410-018-1486-x
Pappalardo, L., Civetta, L., De Vita, S., Di Vito, M., Orsi, G., Carandente, A., & Fisher, R. V. (2002). Timing of magma extraction during the Campanian Ignimbrite eruption (Campi Flegrei Caldera). Journal of Volcanology and Geothermal Research, 114(3–4), 479–497. https://doi.org/10.1016/S0377-0273(01)00302-X
Pappalardo, L., D'Auria, L., Cavallo, A., & Fiore, S. (2014). Petrological and seismic precursors of the paroxysmal phase of the last Vesuvius eruption on March 1944. Scientific Reports, 4, 6297. https://doi.org/10.1038/srep06297
Pappalardo, L. & Mastrolorenzo, G. (2010). Short residence times for alkaline Vesuvius magmas in a multi-depth supply system: Evidence from geochemical and textural studies. Earth and Planetary Science Letters, 296(1–2), 133–143. https://doi.org/10.1016/j.epsl.2010.05.010
Pappalardo, L. & Mastrolorenzo, G. (2012). Rapid differentiation in a sill-like magma reservoir: A case study from the campi flegrei caldera. Scientific Reports, 2, 712. https://doi.org/10.1038/srep00712
Pappalardo, L., Ottolini, L., & Mastrolorenzo, G. (2008). The Campanian Ignimbrite (southern Italy) geochemical zoning: Insight on the generation of a super-eruption from catastrophic differentiation and fast withdrawal. Contributions to Mineralogy and Petrology, 156(1), 1–26. https://doi.org/10.1007/s00410-007-0270-0
Pappalardo, L. Piochi, M., & Mastrolorenzo, G. (2004). The 3550 year BP-1944 A.D. magma-plumbing system of Somma-Vesuvius: Constraints on its behaviour and present state through a review of Sr-Nd isotope data. Annals of Geophysics, 47(4), 1471–1483. https://doi.org/10.4401/ag-3354
Peccerillo, A. (2017). Cenozoic Volcanism in the Tyrrhenian Sea Region. Springer, Cham. http://doi.org/10.1007/978-3-319-42491-0
Pichavant, M., Scaillet, B., Pommier, A., Iacono-Marziano, G., & Cioni, R. (2014). Nature and Evolution of Primitive Vesuvius Magmas: an Experimental Study. Journal of Petrology, 55(11), 2281–2310. https://doi.org/10.1093/petrology/egu057
Piochi, M., Ayuso, R. A., De Vivo, B., & Somma, R. (2006). Crustal contamination and crystal entrapment during polybaric magma evolution at Mt. Somma-Vesuvius volcano, Italy: Geochemical and Sr isotope evidence. Lithos, 86(3–4), 303–329. https://doi.org/10.1016/j.lithos.2005.05.009
Piochi, M., Mastrolorenzo, G., & Pappalardo, L. (2005). Magma ascent and eruptive processes from textural and compositional features of Monte Nuovo pyroclastic products, Campi Flegrei, Italy. Bulletin of Volcanology, 67(7), 663–678. https://doi.org/10.1007/s00445-005-0410-1
Piochi, M., Polacci, M., De Astis, G., Zanetti, A., Mangiacapra, A., Vannucci, R., & Giordano, D. (2008). Texture and composition of pumices and scoriae from the Campi Flegrei caldera (Italy): Implications on the dynamics of explosive eruptions. Geochemistry, Geophysics, Geosystems, 9(3), Q03013. https://doi.org/10.1029/2007GC001746
Pistolesi, M., Bertagnini, A., Di Roberto, A., Isaia, R., Vona, A., Cioni, R., & Giordano, G. (2017). The Baia–Fondi di Baia eruption at Campi Flegrei: stratigraphy and dynamics of a multi-stage caldera reactivation event. Bulletin of Volcanology, 79(9), 67. https://doi.org/10.1007/s00445-017-1149-1
Polacci, M., Arzilli, F., La Spina, G., Le Gall, N., Cai, B., Hartley, M. E., et al. (2018). Crystallisation in basaltic magmas revealed via in situ 4D synchrotron X-ray microtomography. Scientific Reports, 8(1), 8377. https://doi.org/10.1038/s41598-018-26644-6
Polacci, M., Bouvet de Maisonneuve, C., Giordano, D., Piochi, M., Mancini, L., Degruyter, W., & Bachmann, O. (2014). Permeability measurements of Campi Flegrei pyroclastic products: An example from the Campanian Ignimbrite and Monte Nuovo eruptions. Journal of Volcanology and Geothermal Research, 272, 16–22. https://doi.org/10.1016/j.jvolgeores.2013.12.002
Preece K., Barclay J., Gertisser R. & Herd R. A. (2013). Textural and micro-petrological variations in the eruptive products of the 2006 dome-forming eruption of Merapi volcano, Indonesia: Implications for sub-surface processes. Journal of Volcanology and Geothermal Research, 261, 98–120. https://doi.org/10.1016/j.jvolgeores.2013.02.006
Preuss, O., Marxer, H., Ulmer, S., Wolf, J., & Nowak, M. (2016). Degassing of hydrous trachytic Campi Flegrei and

phonolitic Vesuvius melts: Experimental limitations and chances to study homogeneous bubble nucleation. American Mineralogist, 101(4), 859–875. https://doi.org/10.2138/am-2016-5480
Roman, D. C. & Cashman, K. V. (2018) Top–Down Precursory Volcanic Seismicity: Implications for 'Stealth' Magma Ascent and Long-Term Eruption Forecasting. Frontiers in Earth Science, 6, 124. https://doi.org/10.3389/feart.2018.00124
Rosi, M., & Sbrana, A. (1987). The Phlegraean fields. CNR Quaderni della Ricerca Scientifica, Roma.
Rotella, M. D., Wilson, C. J. N., Barker, S. J., Cashman, K. V., Houghton, B. F., & Wright, I. C. (2014). Bubble development in explosive silicic eruptions: Insights from pyroclast vesicularity textures from Raoul volcano (Kermadec arc). Bulletin of Volcanology, 76(8), 1–24. https://doi.org/10.1007/s00445-014-0826-6
Rubin, A. M., Gillard, D., & Got, J.-L. (1998). A reinterpretation of seismicity associated with the January 1983 dike intrusion at Kilauea Volcano, Hawaii. Journal of Geophysical Research: Solid Earth, 103(B5), 10003–10015. https://doi.org/10.1029/97jb03513
Rust, A. C., & Cashman, K. V. (2011). Permeability controls on expansion and size distributions of pyroclasts. Journal of Geophysical Research: Solid Earth, 116(11), B11202. https://doi.org/10.1029/2011JB008494
Ruth, D. C. S., Costa, F., Bouvet De Maisonneuve, C., Franco, L., Cortés, J. A., & Calder, E. S. (2018). Crystal and melt inclusion timescales reveal the evolution of magma migration before eruption. Nature Communications, 9(1), 2657. https://doi.org/10.1038/s41467-018-05086-8
Rutherford, M. J., & Gardner, J. E. (2000). Rates of Magma Ascent. In H. Sigurdsson, B. Houghton, H. Rymer, J. Stix, & S. R. McNutt (Eds.), The encyclopedia of volcanoes (pp. 207–218). Academic Press, London.
Rutherford, M. J., & Hill, P. M. (1993). Magma ascent rates from amphibole breakdown: An experimental study applied to the 1980-1986 Mount St. Helens eruptions. Journal of Geophysical Research: Solid Earth, 98(B11), 19667–19685. https://doi.org/10.1029/93jb01613
Santacroce, R., Cioni, R., Marianelli, P., Sbrana, A., Sulpizio, R., Zanchetta, G., et al. (2008). Age and whole rock-glass compositions of proximal pyroclastics from the major explosive eruptions of Somma-Vesuvius: A review as a tool for distal tephrostratigraphy. Journal of Volcanology and Geothermal Research, 177(1), 1–18. https://doi.org/10.1016/j.jvolgeores.2008.06.009
Saunders, K. E., Blundy, J. D., Dohmen, R. G. & Cashman, K.V. (2012). Linking petrology and seismology at an active volcano. Science, 336(6084), 1023–1027. https://doi.org/10.1126/science.1220066
Scaillet, B., Pichavant, M., & Cioni, R. (2008). Upward migration of Vesuvius magma chamber over the past 20,000 years. Nature, 455(7210), 216–219. https://doi.org/10.1038/nature07232
Scarpati, C., Perrotta, A., Lepore, S., & Calvert, A. (2012). Eruptive history of Neapolitan volcanoes: Constraints from 40Ar-39Ar dating. Geological Magazine, 150(3), 412–425. https://doi.org/10.1017/S0016756812000854
Shea, T., Gurioli, L., & Houghton, B. F. (2012). Transitions between fall phases and pyroclastic density currents during the AD 79 eruption at Vesuvius: Building a transient conduit model from the textural and volatile record. Bulletin of Volcanology, 74(10), 2363–2381. https://doi.org/10.1007/s00445-012-0668-z
Shea, T., Gurioli, L., Larsen, J. F., Houghton, B. F., Hammer, J. E., & Cashman, K. V. (2010b). Linking experimental and natural vesicle textures in Vesuvius 79AD white pumice. Journal of Volcanology and Geothermal Research, 192(1–2), 69–84. https://doi.org/10.1016/j.jvolgeores.2010.02.013
Shea, T., Houghton, B. F., Gurioli, L., Cashman, K. V., Hammer, J. E., & Hobden, B. J. (2010a). Textural studies of vesicles in volcanic rocks: An integrated methodology. Journal of Volcanology and Geothermal Research, 190(3–4), 271–289. https://doi.org/10.1016/j.jvolgeores.2009.12.003
Sigmundsson, F., Hooper, A., Hreinsdóttir, S., Vogfjörd, K. S., Ófeigsson, B. G., Heimisson, E. R., et al. (2015). Segmented lateral dyke growth in a rifting event at Bárðarbunga volcanic system, Iceland. Nature, 517(7533), 191–195. https://doi.org/10.1038/nature14111
Signorelli, S., & Carroll, M. R. (2002). Experimental study of Cl solubility in hydrous alkaline melts: Constraints on the theoretical maximum amount of Cl in trachytic and phonolitic melts. Contributions to Mineralogy and Petrology, 143(2), 209–218. https://doi.org/10.1007/s00410-001-0320-y
Sparks, R. S. J., Annen, C., Blundy, J. D., Cashman, K. V., Rust, A. C., & Jackson, M. D. (2019). Formation and dynamics of magma reservoirs. Philosophical Transactions of the Royal Society A: Mathematical, Physical and Engineering Sciences, 377(2139), 20180019. https://doi.org/10.1098/rsta.2018.0019
Spera, F. J., Oldenburg, C. M., Christensen, C., & Todesco, M. (1995). Simulations of convection with crystallization in the system KAlSi2O6-CaMgSi2O6: Implications for compositionally zoned magma bodies. American Mineralogist, 80(11–12), 1188–1207. https://doi.org/10.2138/am-1995-11-1210
Stock, M. J., Humphreys, M. C. S., Smith, V. C., Isaia, R., Brooker, R. A., & Pyle, D. M. (2018). Tracking volatile behaviour in sub-volcanic plumbing systems using apatite and glass: Insights into pre-eruptive processes at Campi Flegrei, Italy. Journal of Petrology, 59(12), 2463–2492. https://doi.org/10.1093/petrology/egy020
Stovall, W. K., Houghton, B. F., Gonnermann, H., Fagents, S. A., & Swanson, D. A. (2011). Eruption dynamics of Hawaiian-style fountains: The case study of episode 1 of the Kilauea Iki 1959 eruption. Bulletin of Volcanology, 73(5), 511–529. https://doi.org/10.1007/s00445-010-0426-z
Till, C.B., Vazquez, J.A., & Boyce, J.W. (2015). Months between rejuvenation and volcanic eruption at Yellowstone caldera, Wyoming. Geology, 43, 695–698. https://doi.org/10.1130/G36862.1

Toramaru, A. (2006). BND (bubble number density) decompression rate meter for explosive volcanic eruptions. Journal of Volcanology and Geothermal Research, 154(3–4), 303–316. https://doi.org/10.1016/j.jvolgeores.2006.03.027

Turner, S. P., George, R. M. M., Evans, P. J., Hawkesworth, C. J., & Zellmer, G. F. (2000). Time-scales of magma formation, ascent and storage beneath subduction-zone volcanoes. Philosophical Transactions of the Royal Society A: Mathematical, Physical and Engineering Sciences, 358(1770), 1443–1464. https://doi.org/10.1098/rsta.2000.0598

Vanorio, T., & Kanitpanyacharoen, W. (2015). Rock physics of fibrous rocks akin to Roman concrete explains uplifts at Campi Flegrei caldera. Science, 349(6248), 617–621. https://doi.org/10.1126/science.aab1292

Villemant, B., & Boudon, G. (1998). Transition from dome-forming to plinian eruptive styles controlled by H 2 O and Cl degassing. Nature, 392(6671), 65–69. https://doi.org/10.1038/32144

Voltolini, M., Zandomeneghi, D., Mancini, L., & Polacci, M. (2011). Texture analysis of volcanic rock samples: Quantitative study of crystals and vesicles shape preferred orientation from X-ray microtomography data. Journal of Volcanology and Geothermal Research, 202(1–2), 83–95. https://doi.org/10.1016/j.jvolgeores.2011.02.003

Webster, J. D., & De Vivo, B. (2002). Experimental and modeled solubilities of chlorine in aluminosilicate melts, consequences of magma evolution, and implications for exsolution of hydrous chloride melt at Mt. Somma-Vesuvius. American Mineralogist, 87(8–9), 1046–1061. https://doi.org/10.2138/am-2002-8-902

Wotzlaw, J.F., Guillong, M., Balashova, A., Fornia, F., Dunkl, I., Mattssona, H.B. & Bachmann, O. (2019). In-situ garnet 238U-230Th geochronology of Holocene silica-undersaturated volcanic tuffs at millennial-scale precision. Quaternary Geochronology, 50, 1-7. https://doi.org/10.1016/j.quageo.2018.10.004

Wu, W. N., Schmitt, A. K., & Pappalardo, L. (2015). U-Th baddeleyite geochronology and its significance to date the emplacement of silica undersaturated magmas. American Mineralogist, 100(10), 2082–2090. https://doi.org/10.2138/am-2015-5274

Zdanowicz, G., Boudon, G., Balcone-Boissard, H., Cioni, R., Mundula, F., Orsi, G., et al. (2018). Geochemical and textural constraints on degassing processes in sub-Plinian eruptions: case-study of the Greenish Pumice eruption of Mount Somma-Vesuvius. Bulletin of Volcanology, 80(4), 38. https://doi.org/10.1007/s00445-018-1213-5

Zellmer, G. F., Annen, C., Charlier, B. L. A., George, R. M. M., Turner, S. P., & Hawkesworth, C. J. (2005). Magma evolution and ascent at volcanic arcs: Constraining petrogenetic processes through rates and chronologies. Journal of Volcanology and Geothermal Research, 140(1–3), 171–191. https://doi.org/10.1016/j.jvolgeores.2004.07.020

Zollo, A., Maercklin, N., Vassallo, M., Dello Iacono, D., Virieux, J., & Gasparini, P. (2008). Seismic reflections reveal a massive melt layer feeding Campi Flegrei caldera. Geophysical Research Letters, 35(12), L12306. https://doi.org/10.1029/2008GL034242

4. Degassing of evolved alkaline melts: insights from HT-HP decompression experiments and numerical modeling of magma vesiculation

This work is in preparation to be submitted. I contributed to all phases (experiments, sample characterization, numerical modeling, data interpretation, writing) and investigations of the work. Particularly, the experiments were performed during a period of research activity spent at the Department of Experimental and Applied Mineralogy of the Georg-August University of Göttingen and the numerical modeling was developed in collaboration with Dr. Giovanni Macedonio (Istituto Nazionale di Geofisica e Vulcanologia – Osservatorio Vesuviano).

1. Introduction

Predicting the evolution of surface-monitored signals at active volcanoes in terms of magma transfer dynamic processes is challenging. In this framework, understanding how magma degassing works is fundamental as this process strongly controls magma ascent in Earth's crust from magma chamber toward the surface, resulting in different eruptive styles, tephra transport and emplacement as well as atmospheric impacts in the case of eruption (e.g. Cashman and Mangan, 1994; Sparks et al., 1994). Particularly, magma degassing is intimately connected with magma vesiculation (where vesicles refer to frozen bubbles within tephra; Cashman and Scheu, 2015), in fact decompression of a rising magma leads to volatile exolution allowing nucleation, growth and coalescence of bubbles, which change magma compressibility and buoyancy, promoting its ascent. These processes can be investigated using different approaches, such as measurement of textural and chemical parameters in natural volcanic rocks (e.g. Gurioli et al. 2015 and references therein), high temperature and pressure (HT-HP) decompression experiments (e.g. Shea, 2017 and references therein) as well as numerical modeling (e.g. Toramaru, 1989; 1995; Huber et al., 2016). In particular, HT-HP decompression experiments, together with numerical models, permit to study magma degassing under controlled conditions and thus to better constrain field observations (from natural erupted rocks and monitoring signals).

In the last decades this kind of approaches was widely applied to rhyolitic melts allowing to propose a well-recognized paradigm of their degassing (e.g. Hurwitz and Navon, 1994; Mourtada-Bonnefoi and Laporte, 2004; Mangan et al., 2004; Toramaru, 2006; Cashman and Scheu, 2015 and references in these studies). These studies suggest, for example, that homogeneous bubble nucleation is significantly delayed occurring under very high (> 100 MPa) supersaturation pressures (ΔP_{HoN}) in H_2O-rich rhyolitic melts. Under these conditions degassing style typically evolves in disequilibrium, despite equilibrium can be promoted by low decompression rates and heterogeneous bubble nucleation (which reduce ΔP_{HoN}), and the resulting bubble number density is strongly dependent on decompression rate. Consequently, faster decompressions were often associated to explosive eruptions, in which the fragmentation of these highly viscous melts is thought to be driven by the large bubble overpressures.

Only recently some investigations have been focused on evolved, low-viscous, H_2O-rich alkaline magmas, however numerous open questions still remain on how their degassing works, expecially in the case of homogeneous bubble nucleation. In fact, for example, a wide range of ΔP_{HoN} (from 50

to ≥ 100 MPa) was estimated, whereas different degassing styles and bubble number density values were found, also independent on decompression rate. Moreover, the lack of evidences of bubble overpressure suggest in many cases alternative fragmentation criteria for these low-viscous melts (Iacono-Marziano et al., 2007; Gardner, 2012; Gardner et al., 2013; Marxer et al., 2015; Preuss et al., 2016; Allabar and Nowak, 2018).
Therefore expanding the knowledge on kinetics and dynamics of degassing to a wider composition spectrum could be crucial for volcanic hazard assessment, especially in the case of silicic alkaline melts which feed many active high-explosive volcanoes, despite their low viscosity (e.g. Campi Flegrei, Somma-Vesuvius, Azores islands).
Magma decompression (and ascent) rate as well as volatile content can be identified among the parameters that mainly control degassing in ascending magmas and then conduit as well as surficial (i.e. transport in pyroclastic plume and flow) processes. Particularly, despite CO_2 is the second most abundant volatile component after H_2O in natural magmas and has a strong relevance on physico-chemical properties of melts (e.g. Wallace et al., 2015), only few studies were focused on its influence on magma vesiculation (e.g. Gardner and Webster, 2016; Le Gall and Pichavant, 2016b and references in these works; Gonnermann and Manga, 2005; Su and Huber, 2017). Due to its relatively low solubility, carbon dioxide controls the (deep) magma degassing at high pressures (e.g. Wallace et al., 2015) as well as can have a strong impact on volcanic explosivity as a consequence of external CO_2 assimilation during magma storage or ascent (such as magma-crustal carbonate interaction; e.g. Pappalardo et al., 2018; Buono et al., 2019).
In this study, HT-HP isothermal decompression experiments were performed on alkaline trachytic melts at super-liquidus temperature (1200 °C), in order to attain homogeneous bubble nucleation, at variable decompression rates (from 0.01 to 1 MPa s^{-1}) and H_2O-CO_2 volatile content. Experimental samples were 3D texturally (i.e. bubble and Fe-Ti oxide parameters) and chemically (i.e. glass volatile content) characterized. Particularly, 3D textural examination was carried out using X-ray computed microtomography, a powerful tool for the 3D quantitative analysis of large sample volume at high resolution, not directly (i.e. without mathematical corrections to convert 2D data in 3D) provided by 2D conventional techniques. The obtained results were then combined with experimental data available in literature and numerical modeling of magma vesiculation trying to reconstruct a general scheme on degassing of evolved alkaline magmas.

2. HT-HP isothermal decompression experiments

2.1. Experimental set-up

Decompression experiments allow the investigation of magma degassing and vesiculation using natural or (quasi-natural) synthetic melts without spatial and temporal scaling because these processes are not strongly influenced by large-scale interactions (Mader et al., 2004). Here, a trachytic melt (typical of Neapolitan explosive volcanism; sample G10 from Pappalardo et al., 2018) was selected since very few systematic decompression experiments have been performed using this composition (e.g. Preuss et al., 2016; see also Mastrolorenzo and Pappalardo, 2006; Fanara et al., 2017; Sottili et al., 2017). We chose a super-liquidus temperature of 1200 °C to promote homogeneous bubble nucleation, according to phase equilibria of Fanara et al. (2012) showing crystallization of Fe-Ti oxide phenocrysts in trachytic melts at least up to 1100 °C. In order to examine degassing evolution, several decompression steps were obtained starting from an initial pressure (P_i) of 200 MPa (typical of magma storage in many volcanic systems; e.g. see Pappalardo and Mastrolorenzo 2010; 2012 for Neapolitan volcanoes) to a final pressure (P_f) of 200 (i.e. directly quenched at $P_f = P_i$, without decompression), 150, 100, 50 and 25 MPa. In detail, we selected continuous decompression rates of 1 and 0.01 MPa s^{-1}. In fact several works suggested that the transition from "fast" highly- to "slower" moderately- or weakly-explosive eruptions occurs between these average values (e.g. Cassidy et al., 2018; Plank et al, 2018 and references therein).

Moreover we changed H_2O-CO_2 volatile content using X_{H2O}=1 (series A), X_{H2O}=X_{CO2}=0.5 (series B) and X_{CO2}=1 (series C) saturated fluids at P_i (where X is the mole fraction of the fluids dissolved in the melt) to investigate degassing behaviour going from one end-member to the other. It is noteworthy to mention that no systematic HT-HP decompression experiments based on homogeneous bubble nucleation exist for evolved alkaline melts with CO_2 in the fluid phase, despite in alkali-rich liquids its content can reach very high values (e.g. Fanara et al., 2015; Schanofski et al., 2019). As far as we know this kind of experiments was made here for the first time using pure CO_2 fluids, with the aim of isolating the effect of individual volatile species to better examine the degassing of natural magmas (with mixed H_2O-CO_2 fluids). We also used melts with X_{H2O}=1 oversaturated fluids (series A2; corresponding to saturation at 300 MPa) at P_i, indicated as one of the main condition to internally trigger an eruption (e.g. Blake, 1984).

2.2. Methods

2.2.1. Experimental methods

Starting material

A synthetic, trachytic glass was used as starting material. The glass was synthesized by melting a mixture of oxides and carbonates in a Pt crucible at 1600 °C and 1 atm in three cycles (1h + 1h + 4h) for a total of 6 h. The obtained melt was rapidly quenched by submerging the bottom of the crucible in water and then crushed at the end of each cycle to improve its homogeneity. The composition (SiO_2: 61.56, TiO_2: 0.32, Al_2O_3: 18.95, Fe_2O_3: 2.85, MnO: 0.17, MgO: 0.22, CaO: 2.62, Na_2O: 4.52, K_2O: 8.81 wt.%) and homogeneity of the glass were verified by a Bruker M4 Tornado micro-X-ray fluorescence (μ-XRF) spectrometer using polished glass pieces (see Schanofski et al., 2019 for additional information).

Hydration/carbonation experiments

Hydration/carbonation experiments were performed using $Au_{75}Pd_{25}$ capsules (diameter: 4 mm, wall thickness: 0.2 mm, height: 30 mm) containing layers of compacted glass powder (with a total weight of about 300 mg) alternated with deionized water and/or silver oxalate ($Ag_2C_2O_4$), sources for H_2O and CO_2 respectively. The weight of the capsules was determined before and after welding to check for volatile loss. Moreover, the welded capsules were then heated (overnight at 150 °C and 1 atm) and check for leaks. All the experiments were run at the University of Göttingen with an internally heated pressure vessel (IHPV) pressurized with Ar for 24-48 h, at intrinsic oxygen fugacity conditions (f_{O2} = NNO + 3 ± 1), 1200 °C and 300 MPa. A pressure higher than P_i was selected to dissolve the entire volatile content, reducing the probability to form hydration bubbles. The IHPV operates vertically and has a rapid drop-quench device like that of Roux and Lefèvre (1992), which allows a cooling rate of ~ 150 °C s^{-1}, determined in similar experiments by Benne and Behrens (2003). The operation of this kind of equipment was described in detail by Schanofski et al. (2019). Before each experiment two cycles of flushing (i.e. valve opening from 10 MPa at 100 °C) were done to reduce air content in the vessel and avoid Fe reduction reactions. Run conditions for each hydration/carbonation experiment are listed in Table1.

Sample	T (°C)	P (MPa)	H_2O FTIR (wt.%)	H_2O_m FTIR (wt.%)	OH^- FTIR (wt.%)	H_2O TGA (wt.%) [a]	CO_2 FTIR (ppm)
Series A (X_{H2O}=1, saturated fluids at P_i)							
A-1	1200	300	5.82 (0.06)	4.08 (0.06)	1.74 (0.03)	4.86 (0.09)	
A-2	1200	300	6.30 (0.07)	4.66 (0.06)	1.65 (0.03)	5.00 (0.11)	
A-3	1200	300	6.17 (0.08)	4.60 (0.07)	1.5 (0.04)	6.02 (0.01)	
A-4	1200	300	7.08 (0.11)	5.43 (0.10)	1.65 (0.06)	5.22 (0.07) 5.51 (0.01)	
Series A2 (X_{H2O}=1, oversaturated fluids at P_i)							
A2-1	1200	300	7.17 (0.08)	5.46 (0.08)	1.71 (0.04)	6.19 (0.13)	
A2-2	1200	300	7.26 (0.09)	5.52 (0.08)	1.74 (0.04)	-	
A2-3	1200	300	7.22 (0.08)	5.47 (0.07)	1.76 (0.03)	-	
A2-4	1200	300	9.74 (0.15)	7.58 (0.13)	2.16 (0.07)	6.59 (0.01)	
A2-5	1200	300	-	-	-	-	
Series B (X_{H2O}=X_{CO2}=0.5, saturated fluids at P_i)							
B-1	1200	300	3.34 (0.05)	2.02 (0.04)	1.32 (0.03)	3.25 (0.09)	670 (90)
B-2	1200	300	3.08 (0.04)	1.74 (0.03)	1.34 (0.02)	3.28 (0.01)	740 (110)
B-3	1200	300	3.45 (0.04)	2.04 (0.03)	1.41 (0.02)	3.51 (0.01)	560 (90)
B-4	1200	300	3.45 (0.05)	2.06 (0.04)	1.39 (0.03)	3.41 (0.09)	610 (160)
B-5	1200	300	3.88 (0.04)	2.49 (0.04)	1.39 (0.02)	3.41 (0.09)	800 (200)
Series C (X_{CO2}=1, saturated fluids at P_i)							
C-1	1200	300	0.06 (0.01)	0.00	0.06 (0.01)	0.32 (0.07)	970 (160)
C-2	1200	300	0.07 (0.01)	0.00	0.07 (0.01)	0.45 (0.01)	1050 (150)
C-3	1200	300	0.07 (0.01)	0.00	0.07 (0.01)	0.36 (0.07)	850 (90)
C-4	1200	300	0.04 (0.01)	0.00	0.04 (0.01)	0.02 (0.05)	1500 (160)

Table 1. Run conditions and (chemical) results of hydration/carbonation experiments.
Calculated errors are shown in brackets near values. [a] In series B and C corresponds to the total fluids content.

Decompression experiments

The obtained hydrated/carbonated glass cylinders were checked for their volatile content (see below) and subsequently used for decompression experiments. In detail, they were cut in smaller pieces (with a weight of about 100 mg) and placed in $Au_{75}Pd_{25}$ capsules (diameter: 4 mm, wall thickness: 0.2 mm, height: 15 mm; with ~5 mm long void space above the cylinder to accommodate gas expansion during decompression) under vacuum (using a vacuum pump) in order to avoid the possible formation of air bubbles during this experimental stage. Decompression experiments were run using the same IHPV, equipped with a continuous decompression system. Melts were first equilibrated at 1200 °C and 200 MPa for 24-48 h, then isothermally decompressed up to final pressures of 150, 100, 50 and 25 MPa and rapidly quenched at isobaric conditions. Pressure was released (i) manually to achieve decompression rates of 1 MPa s^{-1}, (ii) with quasi-continuous decompression steps (< 1 MPa) by opening automatically a motor driven micrometering valve to obtain rates of 0.01 MPa s^{-1} (see also Fanara et al., 2017; Sottili et al., 2017). Moreover, capsules for each experimental series were also directly quenched at 200 MPa after the equilibration (i.e. without decompressing) to examine the melts prior to decompression. Each capsule was weighted before and after decompression experiments to test for possible leakage. Run conditions for each decompression experiment are listed in Table 2.

Sample	Starting sample	T (°C)	dP/dt (MPa s^{-1})	P_i (MPa)	P_f (MPa)	H_2O FTIR (wt.%)	H_2O_m FTIR (wt.%)	OH^- FTIR (wt.%)	H_2O TGA (wt.%) [a]	CO_2 FTIR (ppm)	Analyzed volume (mm^3)	Porosity (%)	BND (mm^{-3})	BSD D_m (µm)	BSD σ (µm)	Microlite content (%)	CND (mm^{-3})	CSD D_m (µm)	CSD σ (µm)
Series A (X_{H2O}=1, saturated fluids at P_i)																			
a-0	A-1	1200		200	200	5.07 (0.06)	3.50 (0.05)	1.57 (0.03)	-		16	0.03	1.1×10^{11}	17	4	0.002	3.6×10^{9}	19	6
a-1f	A-3	1200	1	200	150	6.08 (0.08)	4.48 (0.07)	1.60 (0.04)	5.06 (0.09)		28	0.24	3.8×10^{11}	20	7	0.012	2.6×10^{10}	17	7
a-2f (*)	A-2	1200	1	200	100	4.32 (0.08)	2.97 (0.07)	1.35 (0.04)	3.92 (0.07)		28	2.60	1.9×10^{12}	27	8	0.017	2.6×10^{10}	20	7
											6	*4.33*	*2.8×10^{12}*	*29*	*9*				
a-3f	A-4	1200	1	200	50	-	-	-	3.82 (0.01)		11	12.92	4.8×10^{11}	70	34	0.036	5.0×10^{9}	22	26
a-4f	A-2	1200	1	200	25	-	-	-	0.65 (0.13)		26	18.27	9.3×10^{11}	64	31	0.006	1.2×10^{10}	19	8
a-1s	A-4	1200	0.01	200	150	-	-	-	-		13	0.16	3.8×10^{11}	19	5	0.003	5.8×10^{9}	19	6
a-2s (*)	A-4	1200	0.01	200	100	-	-	-	4.47 (0.01)		29	0.75	1.3×10^{12}	19	7	0.022	5.1×10^{10}	18	6
											8	*0.43*	*2.1×10^{12}*	*13*	*6*				
a-3s	A-1	1200	0.01	200	50	2.98 (0.03)	1.70 (0.02)	1.28 (0.02)	2.96 (0.05)		5	7.75	1.7×10^{11}	68	50	0.006	1.2×10^{10}	19	7
a-4s	A-1	1200	0.01	200	25	-	-	-	1.92 (0.09)		8	0.31	2.2×10^{10}	42	33	0.018	1.2×10^{10}	24	13
-	-	-	-	-	-	-	-	-	-	-	-	-	-	-	-				
Series A2 (X_{H2O}=1, oversaturated fluids at P_i)																			
a2-0	A2-5	1200		200	200	-	-	-	3.34 (0.08)		7	0.30	3.3×10^{11}	21	10	0.003	7.5×10^{9}	19	5
a2-1f (*)	A2-3	1200	1	200	150	5.64 (0.07)	4.02 (0.06)	1.63 (0.04)	7.89 (0.11) 4.97 (0.07)		14	0.76	2.9×10^{12}	16	3	0.005	1.3×10^{10}	18	6
											5	*1.17*	*5.5×10^{12}*	*15*	*4*				
a2-2f	A2-5	1200	1	200	100	-	-	-	4.10 (0.10)		15	4.28	4.6×10^{12}	24	8	0.008	1.7×10^{10}	19	6
a2-3f	A2-3	1200	1	200	50	2.59 (0.06)	1.46 (0.04)	1.13 (0.04)	2.46 (0.10)		7	4.35	4.9×10^{12}	22	9	0.106	1.5×10^{10}	26	27
a2-4f	A2-4	1200	1	200	25	2.33 (0.05)	1.21 (0.04)	1.13 (0.04)	2.50 (0.01)		14	17.59	4.5×10^{10}	162	99	0.022	4.0×10^{10}	18	8
a2-1s	A2-1	1200	0.01	200	150	5.04 (0.06)	3.53 (0.05)	1.51 (0.03)	5.45 (0.10)		19	1.23	2.8×10^{12}	19	5	0.044	1.0×10^{11}	18	6
a2-1s_2 (*)	A2-3	1200	0.01	200	150	-	-	-	4.81 (0.01)		7	0.78	2.8×10^{12}	17	4	0.011	2.3×10^{10}	19	6
											5	*0.52*	*4.2×10^{12}*	*12*	*4*				
a2-2s	A2-1	1200	0.01	200	100	2.22 (0.04)	1.44 (0.03)	0.78 (0.02)	3.79 (0.06)		19	4.73	2.2×10^{12}	31	11	0.023	7.4×10^{9}	21	18
a2-2s_2	A2-4	1200	0.01	200	100	-	-	-	4.70 (0.01)		5	0.30	1.2×10^{10}	65	34	0.026	9.2×10^{10}	17	4
a2-3s (**)	A2-2	1200	0.01	200	50	2.59 (0.03)	1.49 (0.02)	1.10 (0.02)	2.96 (0.04)		3	27.94	7.9×10^{10}	88	143	0.007	2.3×10^{10}	17	5
											7	2.41	5.4×10^{10}	39	49	0.030	8.4×10^{9}	27	20
a2-4s	A2-2	1200	0.01	200	25	1.94 (0.04)	0.90 (0.03)	1.04 (0.02)	-		14	3.32	1.0×10^{10}	105	113				

Series B (X_{H2O}=X_{CO2}=0.5, saturated fluids at P_i)																			
b-0	B-1	1200		200	200	3.46 (0.05)	1.98 (0.04)	1.49 (0.03)	-	670 (90)	16	0.09	3.5×10^{11}	16	4	0.004	3.6×10^{9}	23	11
b-1f	B-2	1200	1	200	150	3.44 (0.04)	2.08 (0.03)	1.36 (0.02)	3.07 (0.08)	137 (90)	10	0.08	3.1×10^{11}	16	4	0.040	2.6×10^{10}	19	14
b-2f	B-4	1200	1	200	100	1.63 (0.03)	0.62 (0.02)	1.01 (0.02)	1.69 (0.08) 1.91 (0.06)	60 (90)	10	0.78	2.6×10^{12}	16	5	0.031	8.1×10^{9}	25	20
b-3f	B-5	1200	1	200	50	-	-	-	2.44 (0.01)	0 (90)	28	1.29	2.9×10^{12}	18	6	0.006	9.2×10^{9}	19	8
b-4f	B-3	1200	1	200	25	2.71 (0.06)	1.50 (0.05)	1.21 (0.04)	2.50 (0.06) 2.70 (0.07)	0 (90)	3	10.97	2.4×10^{12}	35	20	0.045	6.0×10^{10}	20	10
b-1s (***)	B-2	1200	0.01	200	150	1.38 (0.02)	0.48 (0.01)	0.89 (0.01)	1.40 (0.07)	150 (110)	21	0.34	1.3×10^{12}	16	4				
b-1s_2	B-5	1200	0.01	200	150	2.00 (0.04)	0.87 (0.03)	1.12 (0.02)	2.09 (0.01)	130 (110)	17	0.34	1.3×10^{12}	16	4	0.025	3.2×10^{10}	20	9
b-2s	B-2	1200	0.01	200	100	1.54 (0.02)	0.48 (0.01)	1.06 (0.02)	1.75 (0.08)	0 (90)	9	1.23	3.2×10^{12}	18	5	0.003	4.1×10^{9}	19	9
b-2s_2	B-5	1200	0.01	200	100	-	-	-	2.21 (0.05) 2.27 (0.15)	0 (90)	9	0.80	3.3×10^{12}	15	4	0.002	3.7×10^{9}	20	7
b-3s	B-1	1200	0.01	200	50	2.33 (0.03)	1.34 (0.02)	1.00 (0.02)	2.76 (0.07)	0 (90)	7	3.25	3.9×10^{12}	21	9	0.006	9.3×10^{9}	19	8
b-4s	B-1	1200	0.01	200	25	-	-	-	1.94 (0.10)	0 (90)	12	6.19	7.9×10^{12}	21	9	0.009	6.5×10^{9}	23	13
Series C (X_{CO2}=1, saturated fluids at P_i)																			
c-0	C-1	1200		200	200	0.05 (0.00)	0.00	0.05 (0.00)	-	770 (160)	21	0.18	2.1×10^{11}	21	10	0.003	5.8×10^{9}	18	7
c-1f	C-4	1200	1	200	150	-	-	-	-	476 (120)	15	0.20	2.9×10^{11}	20	9	0.017	1.7×10^{10}	21	10
c-2f	C-4	1200	1	200	100	-	-	-	-	340 (100)	29	1.30	1.4×10^{12}	19	11	0.008	1.0×10^{10}	20	9
c-3f	C-4	1200	1	200	50	-	-	-	0.26 (0.08)	220 (100)	9	2.89	3.0×10^{12}	20	11	0.014	7.2×10^{9}	24	15
c-4f	C-4	1200	1	200	25	-	-	-	0.04 (0.08)	80 (100)	10	4.64	5.0×10^{12}	21	9	0.002	5.0×10^{9}	18	4
c-1s	C-2	1200	0.01	200	150	-	-	-	-	430 (110)	23	0.51	7.8×10^{11}	19	8	0.011	1.1×10^{10}	21	10
c-2s	C-3	1200	0.01	200	100	-	-	-	-	310 (100)	26	0.83	1.4×10^{12}	19	8	0.013	1.6×10^{10}	21	9
c-3s	C-1	1200	0.01	200	50	-	-	-	0.28 (0.06)	230 (90)	8	1.84	2.1×10^{12}	19	10	0.001	2.1×10^{9}	18	6
c-4s	C-3	1200	0.01	200	25	-	-	-	0.18 (0.09)	110 (90)	17	5.07	6.7×10^{12}	20	9	0.004	9.7×10^{9}	17	6

Table 2. Run conditions and (chemical and textural) results of decompression experiments.
Calculated errors are shown in brackets near values. [a] In series B and C corresponds to the total fluids content; (*) results from 3D images at resolution of 3-4 µm (above) and 2 µm below); (**) results from decoalesced (above) and isolated (below) bubbles; (***) microlite analysis affected by the presence of residual portions of $Ag_2C_2O_4$.

2.2.2. Analytical methods

3D imaging textural characterization

3D textural parameters (e.g. content, number density, size distribution) of bubbles and microlite crystals (i.e. Fe-Ti oxides, see below) for each decompressed sample were quantified through X-ray computed microtomography (μCT) using a ZEISS Xradia Versa 410 microscope at the Istituto Nazionale di Geofisica e Vulcanologia – Osservatorio Vesuviano, Naples. μCT imaging of the whole sample was performed in absorption mode acquiring 1601 2D radiographs (projections) over a total angular scan of 360° at 80 kV and 7 W. Effective resolutions between 3 and 4 μm/pixel were attained opportunely setting geometrical and optical (4X lens) magnification. The tomographic reconstruction was carried out using XRM Reconstructor software based on a filtered back-projection algorithm. The obtained 3D digital maps were processed with Avizo software manually thresholding the grey-level histogram (proportional to the mass attenuation coefficients) in order to segment the objects of interest (i.e. bubbles or microlites), which were then labelled and quantified for their morphological parameters. For each sample both total and cropped volumes were analysed to maximize the investigated size, eventually removing the possible effect on the measurement of the bubbles heterogeneously nucleated at the melt-capsule interface (i.e. fringe bubbles). Moreover since the uncertainty significantly increases when objects smaller than 3 pixels are quantified (Hughes et al., 2017; Pappalardo et al., 2018; Liedl et al, 2019), we filtered the data excluding bubbles or crystals with a diameter less than 12 μm. Four samples were also analysed at higher resolution (2 μm/pixel) using more time-consuming scans (4001 projections over 360° at 60 kV and 5 W; 10X lens) to check possible variation in sample texture (filtering data with diameters below 6 μm). Moreover, only one sample (i.e. a2-3s) was characterized by a highly interconnected network of vesicles, from which individual bubbles were decoalesced with a marker-based watershed algorithm and permeability was measured with appropriate simulations following the procedure described by Pappalardo et al. (2018).

Bubble and crystal size distributions (BSD and CSD) were examined estimating their total number density, mean diameter and standard deviation (obtained also from numerical modeling, see below and Appendix A), assuming spherical shape. Bubble and crystal number densities (BND and CND) were calculated on volume of melt (see Proussevitch et al., 2007).

Glass volatile content

H_2O and CO_2 concentrations in hydrated/carbonated and decompressed glasses were determined by Fourier transform infrared (FTIR) spectroscopy. The spectra were collected in transmission using an IR microscope (Bruker Hyperion 3000) connected to a FTIR spectrometer (Bruker Vertex 70) and a liquid N_2 cooled MCT detector (range 600–12000 cm−1) at University of Göttingen. W lamp and CaF_2 beam splitter or Globar light source and KBr beam splitter were used for near-infrared (NIR) and mid-infrared (MIR) spectra, respectively. In fact, H_2O and CO_2 were analysed in the NIR region (2000–6000 cm^{-1}) and in the MIR region (600–4000 cm^{-1}) using doubly polished thin sections about 250 and 100 μm thick respectively. In detail for H_2O, heights of the absorption peaks 4500 (structurally bonded hydroxyl groups, OH^-) and 5200 (molecular H_2O, H_2O_{mol}) cm^{-1} were measured applying a TT (two-tangent) baseline. Instead for CO_2, heights of the absorption peaks 1430 and 1510 (carbonate doublet, CO_3^{2-}) as well as 2350 (molecular CO_2, CO_{2mol}) cm^{-1} were determined subtracting a spectrum normalized to the same thickness from a glass with the same composition and also water content following the method described by Schanofski et al. (2019). At least three NIR and MIR spectra were collected from each sample, any of which resulting from 100 scans with a resolution of 4 cm^{-1}. A square focus area with side between 30 and 50 μm was used depending on the abundance of bubbles in the sample. Volatile concentration was then calculated through the Lambert-Beer law, measuring thin section thickness with a Mitutoyo digital micrometer (3 μm accuracy), glass density from Richet et al. (2000), assuming the effect of CO_2 on melt density negligible, and using absorption coefficients for the NIR and MIR bands from Fanara et al. (2015).

H_2O content was also determined by thermogravimetry using a Setaram™ TGA 92 at University of Göttingen and recording the weight loss of a dehydrating sample during its heating. For each sample at least 15 mg of glass powder were loaded into a Pt crucible (diameter: 4 mm, height: 10 mm) and covered with a Pt lid. Crucible was then suspended at a balance in a graphite tube furnace filled with helium to avoid Fe-oxidation. It was heated with a rate of 10 °C min^{-1} to 1200 °C, at which was dwelled for 30 min and then cooled with a rate of 30 °C min^{-1}. Blank measurements (i.e. a second heating and cooling cycle directly after the first one) were done once per day to correct for the buoyancy changes of the crucible and sample with temperature. More details are furnished by Schmidt and Behrens (2008). Because glass powder used in these analyses was sometime linked to bubbles heterogeneously nucleated at the melt-capsule interface, some TGA data could potentially underestimate water content.
Solubility values reported along the whole text were calculated using the model of Ghiorso and Gualda (2015).

2.3. Results

2.3.1. Pre-decompression samples

(i) Glasses hydrated/carbonated show slightly variable H_2O and CO_2 content, with average values generally in agreement with solubility concentrations predicted by Ghiorso and Gualda (2015) model for each series (Table 2). In particular, for melts with saturated fluids at P_i of 200 MPa, hydrated glasses of series A (X_{H2O}=1) show an H_2O content (average: 6.34 wt.%) slightly higher than the solubility value (6.03 wt.%); hydrated/carbonated glasses of series B (X_{H2O}=X_{CO2}=0.5) have H_2O and CO_2 concentration (average H_2O and CO_2: 3.44 wt.%, 676 ppm) close to equilibrium solubility values (H_2O: 3.35 wt.%, CO_2: 680 ppm); carbonated samples in series C (X_{CO2}=1), show dissolved CO_2 (average: 1093 ppm) only slightly higher (close to the error threshold) than the corresponding solubility value (872 ppm). Instead melts with oversaturated fluids at P_i of series A2 (X_{H2O}=1) have dissolved H_2O (average: 7.85 wt.%) compatible with the equilibrium solubility value at 300 MPa (7.89 wt.%).
(ii) Glasses directly quenched at P_f = P_i from series A, series B and series C show a very low porosity (0.03, 0.09, 0.18% respectively) constituted by small (mean diameter D_m: 17, 16, 21 μm) and homogeneous (standard deviation σ: 4, 4, 10 μm) hydration/air bubbles, far from each other (Fig. 1, Table 2). Their bubble number density (BND: 1.1 x 10^{11}, 3.5 x 10^{11}, 2.1 x 10^{11} m^{-3}) was used as background value to study vesiculation evolution for each series (Table 2). The relative larger BND in CO_2-rich melts can be a consequence of their higher viscosity due to the low H_2O content, able to prevent bubble buoyancy towards the void space at the top of the capsules. Instead in series A2 as expected from melts with oversaturated fluids at P_i, glasses directly quenched at P_f = P_i have porosity (0.30%; with BND: 3.3x10^{11} m^{-3}, D_m: 21 μm and σ: 10 μm) one order of magnitude higher than series A. Moreover, glasses directly quenched at P_f = P_i of all series show low content of Fe-Ti oxide microlites (0.002 - 0.004%; D_m: 18 - 23 μm and σ: 5 - 11 μm; Table 2) with crystal number density (CND: 3.6 -7.5 x 10^9 m^{-3}; Table 2) three order of magnitude lower than peak BND in decompressed samples (see below).

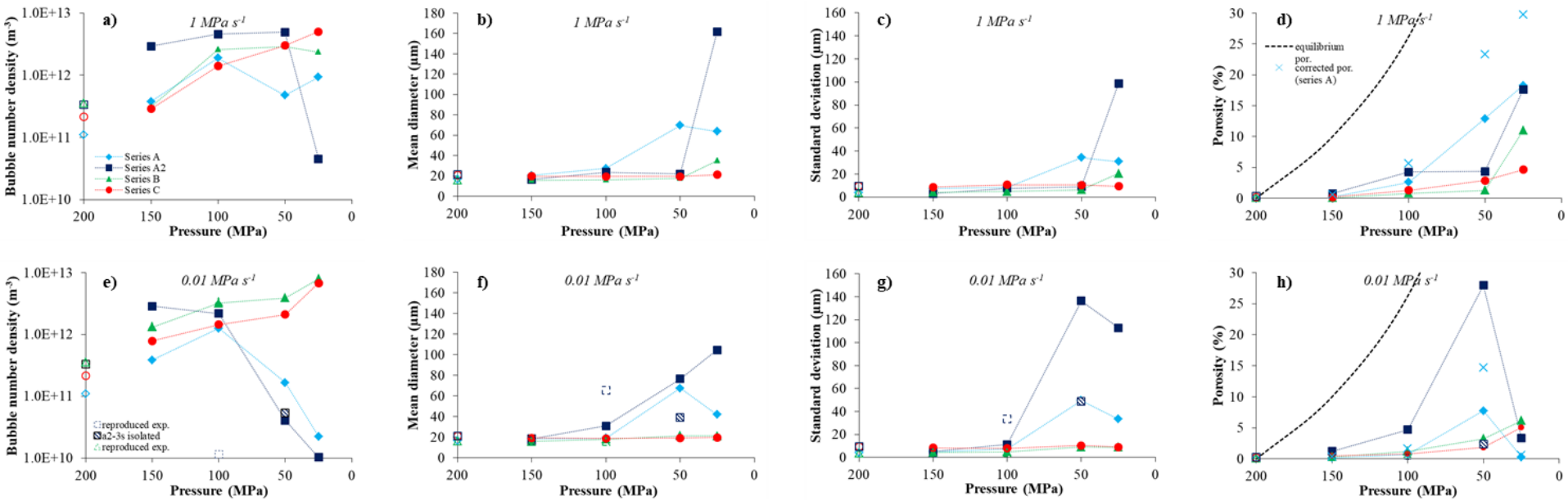

Fig.1. Final pressures vs. bubble number density (a, e), bubble mean diameter (b, f), standard deviation (c, g) and porosity (d, h) of decompressed samples at 1 MPa s-1 (a-d; upper panels) and 0.01 MPa s-1 (e-h; botton panels). Equilibrium and corrected porosity were calculated respectively using Eq. 5 in Gardner et al. (1999) for melts with pure H_2O fluids and shrinking factor correction proposed by Marxer et al. (2015). Sample a2-3s (from the series A2 decompressed at 1 MPa s-1 and quenched at Pf 50 MPa) contain both isolated bubbles and a network of high interconnected bubbles (opportunely decolaesced, see methods).

2.3.2. Decompressed samples

Bubbles

Decompression of H_2O-rich melts (series A and A2) at 1 and 0.01 MPa s^{-1}

(i) In all the experiments performed on H_2O-rich melts at both decompression rates homogeneous bubble nucleation can occur with a pressure decrease (ΔP) equal or less than 50 MPa during a stage of bubble nucleation-dominated degassing (Fig. 1, Table 2). In detail:

- In series A our results indicate that nucleation was incipient after a pressure decrease (ΔP) of 50 MPa at both rates. In fact, BND slightly increases (to 3.8 x 10^{11} and 1.9 x 10^{12} m^{-3} at 1 MPa s^{-1}, Fig. 1a; to 3.8 x 10^{11} and 1.3 x 10^{12} m^{-3} at 0.01 MPa s^{-1}, Fig. 1e) as pressures decreases to 150 and 100 MPa, whereas D_m, σ and porosity only weakly change (from 20 µm, 7 µm, 0.24% to 27 µm, 8 µm, 3% at 1 MPa s^{-1}, Fig. 1b-d; from 19 µm, 5 µm, 0.16% to 19 µm, 7 µm, 0.75% at 0.01 MPa s^{-1}, Fig. 1f-h) between 150 and 100 MPa.
- In series A2 our data suggest that nucleation was developed at ΔP of 50 MPa at both rates. In fact, BND sharply rises (to 2.9 x 10^{12} m^{-3} at 1 MPa s^{-1}, Fig. 1a; to 2.8 x 10^{12} m^{-3} at 0.01 MPa s^{-1}, Fig. 1e) at P_f of 150 MPa, after which only slightly changes (to 4.6 x 10^{12} m^{-3} at 1 MPa s^{-1}; to 2.2 x 10^{12} m^{-3} at 0.01 MPa s^{-1}) at P_f of 100 MPa. At the same time D_m, σ and porosity slowly grow (to 16 µm, 3 µm, 0.76% and to 24 µm, 8 µm, 4% at at 1 MPa s^{-1}, Fig. 1b-d; to 19 µm, 5 µm, 1.23% and to 31 µm, 11 µm, 5%, Fig. 1f-h) as pressure falls towards 150 and 100 MPa.

(ii) Subsequently, starting from pressures of 100 - 50 MPa evidences of transition from bubble nucleation- to growth and coalescence dominated-degassing were observed (Fig. 1, Table 2). In detail:

- At 0.01 MPa s^{-1}, in both series this transition starts at P_f of 100 MPa. In fact, a BND rapid decrease of two order of magnitude (to 1.7 x 10^{11} and 2.2 x 10^{10} m^{-3} in series A; to 7.9 x 10^{10} and 1.0 x 10^{10} m^{-3} in series A2; Fig. 1e) is coupled with a sharp BSD widening (σ from 7 to 50 µm in series A; from 11 to 143 µm in series A2; Fig. 1g) as well as an increase in mean diameter (from 19 to 68 µm in series A, from 31 to 88 µm in series A2; Fig. 1f) and porosity (from 0.75 to 8% in series A, from 5 to 28% in series A2; Fig. 1h) going toward a P_f of 50 and 25 MPa. Morover an extensive bubble interconnection is observed in series A2 at 50 MPa (isolated porosity: 2.5% and connected porosity: 28%, which constitutes the 92% of the total porosity, Fig. 1h; permeability: 6.0 x 10^{-13} m^2), likely achieved between 50 and 25 MPa also in series A. Moreover, samples decompressed to a final pressure of 25 MPa at this slower rate appear fragmented in both series, resulting in glass fragments with a low (0.31% in series A and 3% in series A2; Fig. 1h) apparent (i.e. ratio between total bubbles and fragments volumes) porosity.
- At 1 MPa s^{-1}, similar transition is observed in series A at 100 MPa, where BND decreases (to a value of 3.8 x 10^{11} m^{-3}, Fig. 1a), BSD widens (D_m: 70 µm and σ: 34 µm; Fig. 1b-c) and porosity rapidly increases (to 13%; Fig. 1d), whereas in series A2 at 50 MPa, where BND sharply decreases of two order of magnitude (4.5 x 10^{10} m^{-3}; Fig. 1a) as well as D_m, σ and porosity rapid increase (up to 162 µm, 99 µm and 18%; Fig.b-d).

In series A from 50 to 25 MPa, porosity continues to increase (up to 18%; Fig. 1d), while BND restarts to rise (9.3 x 10^{11} m^{-3}; Fig. 1a) and D_m decreases (D_m : 64 µm and σ: 34 µm; Fig. 1b-c), possibly as a result of a second nucleation event.

In both series no fragmentation evidences (i.e. glass powder or fragments in decompressed capsules) were found at this faster decompression rate.

Decompression of CO_2-rich melts (series B and C) at 1 and 0.01 MPa s^{-1}

(i) In CO_2-rich melts, bubble nucleation occurs with a $\Delta P \leq 50$ MPa in both series B and C at 0.01 MPa s^{-1}. Instead at 1 MPa s^{-1}, BND starts to rise at 100 MPa indicating a ΔP for bubble nucleation $\leq$ 100 MPa in both series. In detail:

- Results from series C suggest bubble nucleation-dominated degassing during the whole decompression at both rates (Fig.1, Table 2). In fact, BND and porosity progressively increase (from 1.4 to 3.0 to 5.0 x 10^{12} m^{-3} and from 1.30 to 3 to 5% at 1 MPa s^{-1}, Fig. 1a,d; from 0.8 to 1.4 to 2.1 to 6.7 x 10^{12} m^{-3} and from 0.51 to 1 to 2 to 5% at 0.01 MPa s^{-1}; Fig. 1e,h), whereas D_m and σ (19-20 μm and 9-11 μm at 1 MPa s^{-1}, Fig. 1b-c; 19-20 μm and 8 - 10 μm at 0.01 MPa s^{-1}; Fig. 1f-g) remain almost constant, up to 25 MPa.
- In series B data indicate that degassing evolves similarly to series C up to a P_f of 50 MPa and then it can rapidly change in function of decompression rate (Fig.1, Table 2). In fact, BND and porosity continuously increase (from 2.6 to 2.9 x 10^{12} m^{-3} and from 0.78 to 1.29% at 1 MPa s^{-1}, Fig. 1a,d; from 1.3 to 3.2 to 3.9 to 7.9 x 10^{12} m^{-3} and from 0.34 to 1.23 to 3 to 6% at 0.01 MPa s^{-1}, Fig. 1e,h), whereas D_m and σ negligibly change (16-18 μm and 5-6 μm at 1 MPa s^{-1}, Fig. 1b-c; 16-21 μm and 4-9 μm at 0.01 MPa s^{-1}, Fig. 1f-g), up to 50 MPa.
Then, a renewed bubble nucleation occurs at the slower decompression, shown by a further increase in BND and porosity (to 7.9 x 10^{12} m^{-3} and 6%, Fig. 1e,h) coupled with constant D_m and σ (21 μm and 9 μm, Fig. 1f-g). Instead, a transition to bubble growth and coalescence dominated-degassing takes place at higher rate, inferred from a reduction in BND (to 2.4 x 10^{12} m^{-3}; Fig. 1a) as well as a rise in D_m, σ and porosity (to 35 μm, 20 μm and 11%; Fig. b-d).
(ii) Decompressed glasses of these series do not show fragmentation evidences at both decompression rates.
(iii) Moreover, the resulting vesiculation in these CO_2-rich series shows peak BND similar or higher and bubble mean diameters rather lower than samples obtained from H_2O-rich melts (series A and A2) decompressed at the same rate. These evidences suggest that the presence of CO_2 can delay the growth of existing bubbles, promoting the nucleation of new ones.

Glass volatile content
(i) In H_2O-rich melts (series A and A2; Fig. 2a,b, Table 2) H_2O concentrations generally follow the solubility values predicted by Ghiorso and Gualda (2015) as P_f decreases, with residual H_2O contents at 1 MPa s^{-1} (i.e. shorter decompression time) slightly higher than equilibrium compared to values at 0.01 MPa s^{-1}, especially at high P_f (≥ 100 MPa). In detail, H_2O content at both rates and P_f = 150 MPa, in series A is closer to pre-decompression values than in series A2 (possibly in agreement with an incipient and advanced stage of bubble nucleation indicated by textural data for series A and A2 respectively) and at our faster rates dissolved H_2O greater than equilibrium were observed at P_f = 50 MPa in series A (likely consistent with the probable second nucleation event at P_f = 25 MPa inferred from textural parameters).
(ii) For CO_2-rich melts, CO_2 concentrations in series C (Fig. 2c,d, Table 2) are close to the solubility values during the whole decompression at both 1 and 0.01 MPa s^{-1},considering both the solubility model of Ghiorso and Gualda (2015) and Papale et al., (2006), with only slightly minor CO_2 values reached at our slower rate at high P_f. In detail, taking in account solubility values predicted by Papale et al. (2006), residual CO_2 at both decompression rates slightly departs from the equilibrium at low P_f, reaching a maximum deviation at 50 MPa.
(iii) Instead CO_2 content in series B follows closed-system degassing curve (i.e. equilibrium between melt and total volatile amounts exolved along all previous decompression path; see Papale, 1999; Newman and Lowenstern, 2002) at both rates (Fig. 3 a-b) and is below the detection limit at P_f of 50 MPa and 100 MPa at our faster and slower rates, respectively. However it reaches values lower than equilibrium solubility predicted by both Ghiorso and Gualda (2015) and Papale et al. (2006) at both P_f of 150 and 100 MPa (Fig. 3c-d, Table 2). Conversely H_2O concentrations show more complex trends (Fig. 3e-f, Table 2). In fact at high P_f (> 50 MPa), H_2O deviates from closed-system degassing curve starting from 100 MPa at 1 MPa s^{-1} and 150 MPa at 0.01 MPa s^{-1}. In detail, at both rates it decreases down to a minimum of ~1.5 wt.% and then increases up to values close to solubility related to X_{H2O}=1 of ~2.5 wt.% at P_f of 50 MPa. Then at the lowest P_f of 25 MPa it

remains almost constant at 1 MPa s^{-1}, whereas decrease roughly follows the isopleth with X_{H2O}=1 at 0.01 MPa s^{-1}.

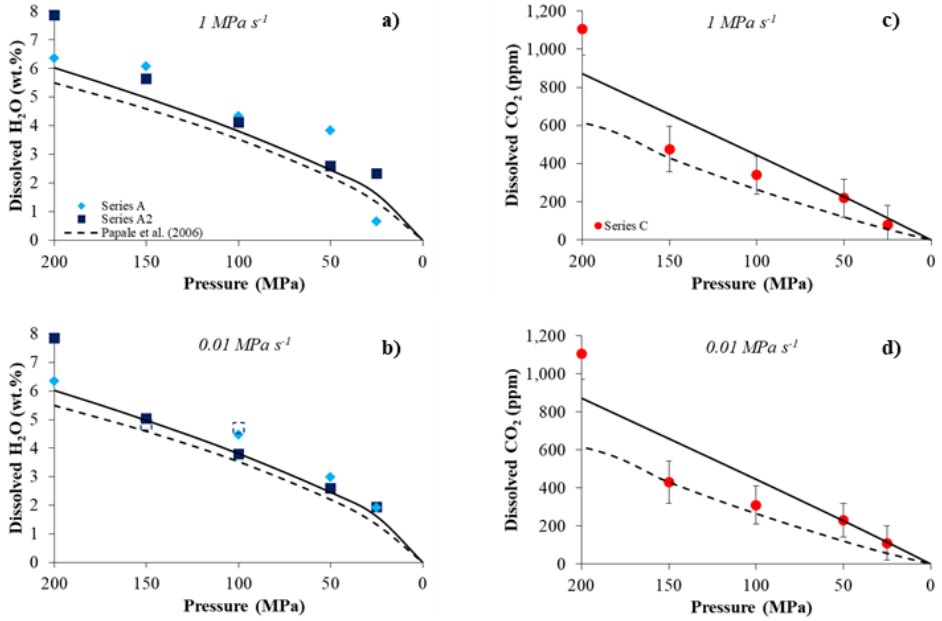

Fig. 2. Final pressures vs. residual H_2O in series A and A2 (a, b) and CO_2 in series C (c, d) of decompressed samples at 1 MPa s^{-1} (a, c; upper panels) and 0.01 MPa s^{-1} (b, d; bottom panels). Solubility data from Ghiorso and Gualda (2015). These equilibrium values aren't in good agreement with those obtained from other models (e.g. Papale et al., 2006) for series C.

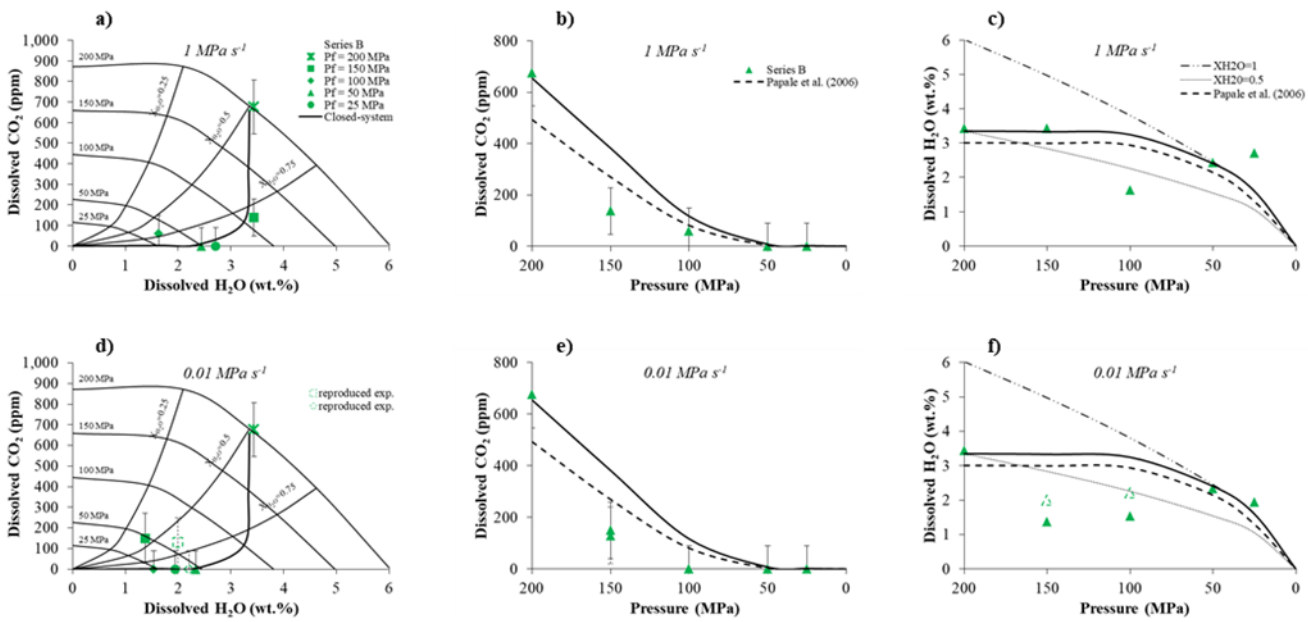

Fig. 3. Residual H_2O vs CO_2 (a, b), final pressures vs. residual CO_2 (c, d) and H_2O (e, f) of decompressed samples at 1 MPa s^{-1} (a-c; upper panels) and 0.01 MPa s^{-1} (d-f; bottom panels). Solubility data from Ghiorso and Gualda (2015). Bold curves show the closed-system degassing path for melts with initial X_{H2O}=X_{CO2}=0.5 saturated fluids which moves from values on the isopleth with X_{H2O}=X_{CO2}=0.5 towards that with X_{H2O}=1 (dashed curves).

Microlites
Fe-Ti oxide microlites were detected in all samples. Their content is very low (min: 0.0009%, max: 0.044%) and their CND (min: 2.1 x 10^9 m^{-3}, max: 1.0 x 10^{11} m^{-3}, average: 2.1 x 10^{10} m^{-3}) is always rather lower (from one to four orders of magnitude) than the BND reported above (peak BND range: 1.3 – 7.9 x 10^{12} m^{-3}). Moreover, only very rarely Fe-Ti oxides acting as nucleation sites were visually observed in the 3D images. Finally, it is noteworthy to report that CNDs and CSDs (D_m range: 17-27 μm, σ range: 4-20 μm) trends are not correlated neither with P_f nor with decompression rate or volatile content (Table 2).

2.3.3. Final remarks
(i) Reproducibility tests were performed for two samples of the series A2 and B at 0.01 MPa s^{-1} and P_f of 150 and 100 MPa (samples a2-1s_2, a2-2s_2, b-1s_2, b-2s_2; Table 2). They appear carefully reproduced excluding small variation in H_2O residual content possibly related to different initial H_2O concentrations in the starting glasses. Exception is made for sample from the series A2 decompressed to 100 MPa (i.e. a2-2s_2), which anticipates the end of the nucleation-dominated degassing phase (i.e. showing BND lower, D_m and σ higher than a2-2s) likely as a consequence of its potential higher initial water content (Figs. 1, 2 and 3, Tables 1 and 2). Furthermore, samples analysed at higher resolution from series A at P_f of 100 MPa and series A2 at P_f of 150 MPa, at both decompression rates, show a good match in BNDs and BSDs with those scanned at lower resolution (Table 2).
(ii) Bubbles contained in the glasses directly quenched at $P_f = P_i$ seems to have no influence on magma vesiculation during decompression. In fact, these small bubbles constitute a low porosity of 0.03-0.18%, (Table 2) much lower than the value estimated to prevent nucleation of new bubbles (Gardner, 2009; Preuss et al., 2016; see also Toramaru, 2014), in agreement with the low values of ΔP required to bubble nucleation observed in our experiments.
(iii) Finally, porosity measured in our samples is generally lower than the equilibrium values (obtained following Eq. 5 in Gardner et al., 1999, using ideal gas law and constitutive equations from Appendix A) at least in H_2O-rich series (Fig.1d,h). This feature was found in many experimentally decompressed samples in literature (see Marxer et al., 2015). These results can be the consequence of bubble shrinking linked to decreasing in volatile molar volume during the isobaric quench, with a strong influence of magma viscosity, as suggested by Marxer et al. (2015). Although this mechanism can partially affect bubble diameters, the homogeneous glass volatile content indicates that a total resorption of small bubbles with consequence on BND value is unlikely (e.g. McIntosh et al., 2014). However porosity corrected for the shrinking factor (i.e. ratio between volatile molecular volume calculated at the temperature of the run and of glass transition) proposed by Marxer et al. (2015) is again rather below the equilibrium values (see results for series A in Fig.1d,h). Anyway, the similar trend of porosity in function of P_f observed for both decompression rates rules out volatile diffusive transfer or bubbles floating towards the void space of the undamaged decompressed capsules as alternative mechanisms. Moreover bubbles loss through a permeable gas flow can be excluded as general process of porosity decrease because an extensive bubble interconnection was reported only in one sample.

3. Discussion

3.1. Bubble birth
Experiments were performed under super-liquidus temperature of 1200 °C to promote homogeneous bubble nucleation according to phase equilibria of Fanara et al. (2012), however Fe-Ti oxides microlites were observed in the obtained samples. They were likely formed during quench, as inferred also in similar studies (Allabar et al., 2018 and references therein), in fact (i) are present in all samples, also in glasses directly quenched at $P_f = P_i$ and have very small size (≤ 27

μm), (ii) lack of specific trends in CNDs and CSDs as P_f decrease, (iii) do not show any link between mean diameter or content and decompression rate. However our results from microlites investigation suggest a negligible role of heterogeneous nucleation. In fact, in all decompressed samples (i) CND of Fe-Ti oxide microlites is always lower than peak BNDs at least of one (up to four) orders of magnitude, (ii) very few cases of Fe-Ti oxides acting as nucleation sites were observed.

3.1.1. When?: critical pressure and volatile concentration for bubble nucleation

H_2O-rich melts

Variations in BND and residual glass H_2O content in function of P_f in series A and A2 (X_{H2O}=1, saturation pressure P_{SAT} of 225 and 300 MPa respectively; obtained using average volatile content in pre-decompression glasses and Ghiorso and Gualda, 2015 solubility model) suggest that the ΔP required for homogeneous nucleation decreases as dissolved H_2O content increases at both decompression rates of 1 and 0.01 MPa s^{-1}, in agreement with the classical nucleation theory (CNT, see Appendix A; Fig. 4). In fact, series A shows an incipient nucleation event started at a ΔP of 50 MPa and ended at a ΔP of 100 MPa, whereas in series A2 nucleation is in an advanced stage already at a ΔP of 50 MPa. The subsequent BND decrease, starting from P_f lower than 100 MPa, marks the transition from bubble nucleation- to growth-dominated degassing (Figs. 1 and 2a-b).

Moreover, textural and chemical data indicate also a possible second nucleation event at $P_f \leq 25$ MPa in series A and continuation or resumption in bubble nucleation up to 50 MPa in series A2.

Therefore a supersaturation pressure (ΔP_{HoN}, i.e. $P_B^* - P_{HoN}$, where P_B^* is the pressure inside the critical nucleus and P_{HoN} is the nucleation pressure, see Appendix A) < 66 and << 126 MPa as well as a supersaturation concentration (ΔC_{HoN}, i.e. difference between the initial and equilibrium concentration at P_{HoN}) < 1.4 and << 2.5 wt.% can be estimated for series A and A2, respectively (less-then signs are included because the first available pressure for our experiments is only at 150 MPa). Inverting equations of nucleation rate (Eq. A6) from CNT and using BND values at P_f = 150 MPa, surface tensions of < 0.062 and << 0.095 N m^{-1} were obtained for series A and A2 respectively.

A wide range of supersaturation pressures were reported in literature for hydrous, CO_2-free, evolved alkaline melts. We investigate all the available data expanding the database of Shea et al. (2017) containing results of the main decompression experiments performed so far. Evolved alkaline melts at the investigated conditions show ΔP_{HoN} between ≤ 50 and 112 MPa, that is lower compared to other differentiated alkali-poor melts, such as rhyolites (103 - 180 MPa) and dacites (72 – 112 MPa). Instead, ΔP_{HeN} (i.e. supersaturation pressure required for heterogeneous nucleation) have similar low values ≤ 25 MPa in both evolved alkaline (13 – 25 MPa) and rhyolitic melts (about 20 MPa).

Particularly, Gardner at al. (2013) by decompressing phonolitic melts at similar conditions (i.e. T: 1150 °C, P_i: 155 MPa; dP/dt: 2-2.5 MPa s^{-1}) observed a sharp increase in ΔP for nucleation (from 64 to 103 MPa) reducing the initial H_2O content of about 1 wt.% (Gardner, 2012; Gardner et al., 2013). Similar insights can be inferred by the results of several decompression experiments performed on phonolitic melts with Vesuvius AD 79 "white pumice" composition at similar settings by different authors (i.e. T: 1050 °C, P_i: 200 MPa, dP/dt: from 0.024 to 4.8 MPa s^{-1}; Iacono Marziano et al., 2007; Marxer et al., 2015; Preuss et al., 2016; Allabar et al., 2018). In detail, a marked variation in ΔP for nucleation occurs close to the saturation concentration at the adopted P_i of 200 MPa (~ 5.4 wt.%, solubility values from Iacono Marziano et al., 2007). In fact, experiments with the highest initial H_2O content produced ΔP for nucleation of 50 MPa as well as ΔC_{HoN} of 0.9 wt.% and lower BND. In contrast, lower values of initial H_2O result in ΔP of ~ 100 MPa as well as ΔC_{HoN} of 1.3 – 1.8 wt.% and higher BND. Only few data (Gardner et al., 2013; Preuss et al., 2016) were obtained for trachytic melts at the same experimental conditions described above showing a degassing behavior very comparable to phonolites (Figs. 4 and 5).

Therefore, we suggest that initial dissolved H_2O can have crucial effects on ΔP for homogeneous bubble nucleation in evolved alkaline melts. In fact, in the framework of CNT (see Eqs. A6 and A7), its increment (i) increases P_B^* (depending on P_{SAT}) and (ii) could reduce surface tension (e.g. Bagdassarov et al., 2000; Khitarov et al., 1979; Gardner et al., 2013; Colucci et al., 2016). However, it is noteworthy to mention that CNT could have some limitations mainly related to its capillary approximation (i.e. critical bubble nuclei assumed as macroscopic objects, see Appendix A). For example Gonnermann and Gardner (2013), based on non-CNT, found a dependence of surface tension on the degree of supersaturation (i.e. increasing supersaturation, nucleation work first decreases slightly and then sharply, after a certain threshold) consistently with the view that far from equilibrium the interface between bubble nuclei and the surrounding melts becomes diffuse, instead of sharp.

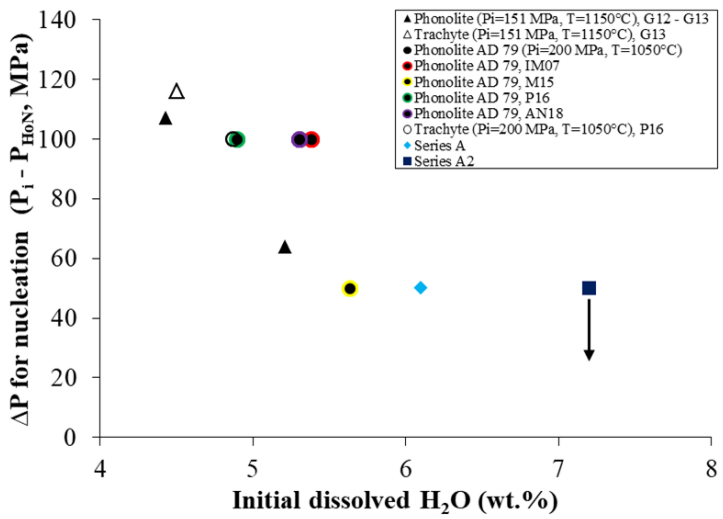

Fig. 4. Variation of pressure decrease (ΔP) required for homogeneous bubble nucleation in H_2O-rich, CO_2 free, evolved alkaline melts investigated in this study and in other experiments from literature (G12: Gardner, 2012; G13: Gardner et al., 2013; IM07: Iacono-Marziano et al., 2007; M15: Marxer et al., 2015; P16: Preuss et al., 2016; AN18: Allabar and Nowak, 2018).

CO_2-rich melts

Textural (i.e. increase in BND) and chemical (i.e. decrease in H_2O and CO_2 residual content) data at P_f = 150 MPa in series B and C (X_{H2O}=X_{CO2}=0.5 and X_{CO2}=1 respectively, saturation pressure P_{SAT} of about 200 MPa) indicate that the ΔP required for homogeneous nucleation decompressed at 0.01 MPa s^{-1} is < 50 MPa (Figs. 1, 2 and 3).

Instead when decompressed at 1 MPa s^{-1} the glasses do not show significant increase of BND at P_f = 150 MPa (Fig. 1). However, at the same P_f, CO_2 content decreases in both series (whereas H_2O in series B remains similar to pre-decompression glasses coherently with a closed-system degassing; see below and Figs. 2c-d and 3). We can exclude that this CO_2 decrease is driven by volatile diffusion toward the bubbles already contained in glasses directly quenched at P_f = P_i. In fact, during the fast decompression this process is prevented by CO_2 diffusion lengths (= $\sqrt{2Dt}$ = 68 μm in series B and 25 μm in series C; D from Zhang and Ni, 2010) lower than the average distances between these bubbles (= $[4\pi BND/3]^{-1/3}$ = 88 μm in series B and 104 μm in series C). Therefore we hypothesized that an incipient CO_2–dominated nucleation at P_{HoN} ≤ 150 MPa could occur. In fact, due to the low diffusion of CO_2 (e.g. Zhang and Ni, 2010), bubbles growth can be delayed and the nucleation can result in a high number of bubbles with very small size (and then more difficult

to quantify) during the low decompression time at high rates. Coherently, P_{HoN} (≤ 150 MPa) independence from decompression rate is predicted by CNT.
Consequently, a ΔP_{HoN} of about 44 MPa and a ΔC_{HoN} of 0.48 wt.% and 189 ppm for H_2O and CO_2 can be estimated for series B as well as a ΔP_{HoN} of about 41 MPa and a ΔC_{HoN} of 206 ppm for H_2O-free series C. From these data a surface tensions of ≤ 0.047 and ≤ 0.040 N m^{-1} results for series B and C respectively.
Our results show that, starting from similar saturation conditions (series A, B, C), CO_2 does not change significantly or slightly decreases surface tension in evolved alkaline melts, leading to similar or minor ΔP_{HoN}, even when H_2O completely lacks (i.e. series C).
Analogous findings were inferred from experimental studies made on mafic magmas (e.g. Le Gall and Pichavant, 2016a; 2016b; Mollo et al., 2017). In particular, detailed studies were made by Le Gall and Pichavant (2016a; 2016b), who inferred ΔP_{HoN} below or close to 50 MPa in basaltic melts with both pure H_2O fluids and CO_2-bearing fluids starting from the same saturation pressure. In contrast, increasing CO_2 (as well as decreasing H_2O) larger ΔP_{HoN} have been reported for rhyolitic liquids (Mourtada-Bonnefoi and Laporte, 1999; 2002; Gardner and Webster, 2016). Gardner and Webster (2016) concluded that bubble nucleation in these melts is only dictated by ΔC_{HoN} of H_2O.
In conclusion, in this section we observed that, under the reported conditions, ΔP for homogeneous nucleation: (i) increases from evolved alkaline melts and basalts to dacites to rhyolites, (ii) decreases as initial H_2O increases, (iii) only slightly changes in evolved alkaline melts and basalts whereas strongly rises in rhyolites as CO_2 increases. Therefore, we speculate that the surface tension can be strongly influenced by the complex interplay between melt polymerization degrees with dissolution and speciation mechanism of H_2O and CO_2, on which several open questions exist (e.g. Stolper, 1982; Brooker et al., 2001; Nowak et al., 2003; Guillot and Sator, 2011). In fact, it could ultimately determine the work required to form and maintain the melt-vapor interface (see also Mangan and Sisson, 2005).

3.1.2. How many, how big?: bubble number density and size

H_2O-rich melts
Peak BNDs in our experiments slightly decrease from 1 MPa s^{-1} to the slower decompression rate of 0.01 MPa s^{-1} in both series A (from 1.9 x 10^{12} m^{-3} at 1 MPa s^{-1} to 1.3 x 10^{12} m^{-3} at 0.01 MPa s^{-1}) and series A2 (from 4.9 x 10^{12} m^{-3} at 1 MPa s^{-1} to 2.8 x 10^{12} m^{-3} at 0.01 MPa s^{-1}), showing slightly higher values in series A2 (Figs. 1 and 5a, Table 2). Instead D_m assumes similar values for both series and decompression rates (at 1 MPa s^{-1}: 20 and 27 μm in series A, 16 and 24 μm in series A2 at P_f of 150 and 100 MPa; at 0.01 MPa $s^{-1:}$ about 19 μm in series A, 19 and 31 μm in series A2 at P_f of 150 and 100 MPa; Fig. 1, Table 2). A more detailed discussion on these results has been supplied in section 3.3.
The obtained behaviour differ from rhyolitic melts, which show a strong decrease in BND and an increase in D_m as the decompression rates decline, reflecting a simple competition between bubble nucleation and diffusive bubble growth (Fig. 5a). Instead, heterogeneous bubble nucleation in evolved alkaline and rhyolitic melts results in BNDs less dependent on decompression rate and only roughly overlapped with those observed for homogeneous nucleation (Fig. 5b).

CO_2-rich melts
BSD in H_2O-free series C continuously and moderately increases in function of P_f at both faster (up to 5.0 x 10^{12} m^{-3}) and slower (up to 6.7 x 10^{12} m^{-3}) decompression rates, showing an almost constant bubble mean diameter (about 20 μm) up to a P_f of 25 MPa. Instead, BND in series B rises up to P_f = 100 MPa an then more slightly increases up to P_f of 50 MPa both at 1 MPa s^{-1} (2.9 x 10^{12} m^{-3}) and 0.01 MPa s^{-1} (3.9 x 10^{12} m^{-3}), presenting only a limited increase (from about 15 to 21 μm) in D_m. Then, at 25 MPa, BND continues to rise at our lower rate (up to 7.9 x 10^{12} m^{-3}), whereas decreases at our faster rate together with a marked rise in mean diameter and porosity likely due to bubble

growth and coalescence. Peak BNDs are slightly higher than at lower decompression rates in both series. However these values are similar or higher than those of H_2O-rich melts (Figs. 1 and 5a).
Decompression experiments performed on basaltic melts carried out by Le Gall and Pichavant (2016a; 2016b) changing H_2O/CO_2 molar fraction (and starting from the same saturation pressure) also result in an almost continuous nucleation process during the whole decompression, with peak BNDs equal or higher than in CO_2-free liquids. Instead experimental data obtained by Mourtada-Bonnefoi et al. (2002; 2004) on rhyolitic melts suggest that starting from similar H_2O content (7 wt.%) and increasing CO_2 content (480 and 630 ppm), homogeneous nucleation seems to occur with a single event longer (with ΔP_{HoN} greater) and BNDs higher (of 2-3 order of magnitude) than in CO_2-free liquids by using decompression rates only slightly faster.
The observed almost continuous (or multiple events of) nucleation process (high BNDs, as well as the slight change in bubble diameters) is consistent with the lower diffusion of CO_2 which delays the growth of bubbles resulting in the consumption of residual CO_2 in the melts mainly due to bubble nucleation. This mechanism seems to be well recorded by the departure from the solubility values observed at low P_f, which allows volatile supersaturation conditions necessary for bubble nucleation.

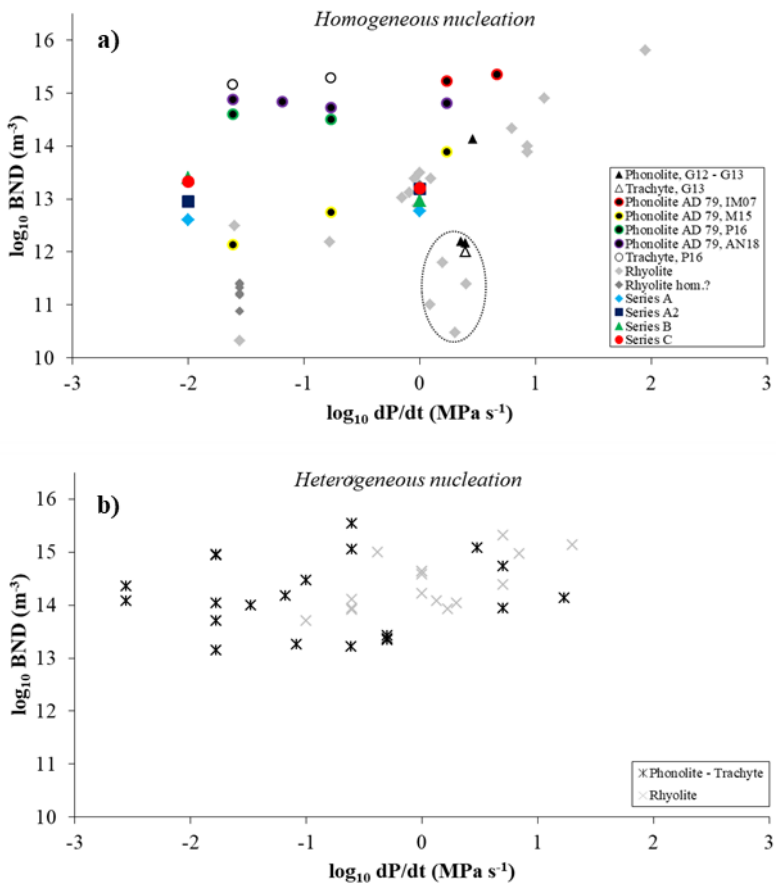

Fig. 5. Bubble number density in function of decompression rate (dP/dt) obtained from: (a) decompression-induced homogeneous nucleation in evolved alkaline (see references in Fig. 4) and rhyolitic melts (data from Mangan and Sisson, 2000; Mourtada-Bonnefoi and Laporte, 2004; Cluzel et al., 2008; Hamada et al., 2010; Gardner et al, 2013; Gonnermann and Gardner, 2013), (b) decompression-induced heterogeneous nucleation in evolved alkaline (data from: Larsen and Gardner, 2004; Mastrolorenzo and Papplardo, 2006; Larsen, 2008; Shea et al., 2010) and rhyolitic melts (data from: Gardner et al., 1999; Gardner and Denis, 2004; Cichy et al, 2011). "Rhyolite hom.?" refers to data from from Cluzel et al. (2008) who reported conditions of heterogeneous bubble nucleation, despite the estimated ΔP_{HoN} (131-137 MPa) more typical of homogeneous nucleation (see text). Dashed area possibly refers to experiments affected by incomplete nucleation (see also Hajimirza et al., 2019).

3.2. Bubble life and death

3.2.1. Degassing style: equilibrium vs. disequilibrium

Melts with pure H_2O and pure CO_2 vapor phase

Residual H_2O glass content in series A and A2 suggest an equilibrium degassing for our H_2O-rich series. However water concentrations for samples decompressed at 0.01 MPa s^{-1} closer to the solubility values than those decompressed at 1 MPa s^{-1} are in agreement with the longer time available at slower rate to diffuse volatiles from melts to bubbles. As discussed above, H_2O higher than equilibrium in glasses from the series A decompressed at 1 MPa s^{-1} and quenched at P_f = 50 MPa could be related to the onset of a second nucleation event (Fig 2a-b).

Data available from literature on Vesuvius AD 79 "white pumice" (CO_2-free) phonolites (see references above and Figs. 4) indicate that, starting from the same P_i, when nucleation begins with small ΔP (50 MPa) and ΔC_{HoN} (~0.9 wt.%), degassing evolves following equilibrium; whereas when nucleation starts with large ΔP (~ 100 MPa) and ΔC_{HoN} (~1.3 – 1.8 wt.%), degassing occurs in disequilibrium, with a stronger deviation from solubility values at higher decompression rates.

Consistently, other experimental studies performed on H_2O-rich evolved alkaline melts heterogeneously nucleated, reported low ΔP_{HoN} (13 – 25 MPa) coupled with equilibrium degassing (Mastrolorenzo et al., 2006; Larsen and Gardner, 2004; Larsen, 2008; Shea et al., 2010). The only exception was observed by Larsen (2008), who decompressed phonolitic liquids at 3 - 17 MPa s^{-1} describing porosity and residual H_2O values in equilibrium at 950 °C and in disequilibrium at 900 °C. The author linked this discrepancy to the slower water diffusion at lower temperature.

Summarizing, in H_2O-rich, CO_2-free, evolved alkaline melts, the larger the ΔP and ΔC_{HoN} required for nucleation as well as the decompression rate, the higher the deviation from equilibrium. However it is noteworthy to mention that the high H_2O diffusion (e.g. Zhang and Ni, 2010) and the low average ΔP_{HoN} in these melts guarantee minor degree of disequilibrium compared to rhyolitic magmas despite they can both feed high-energy eruptions.

HT-HP decompression experiments on CO_2-bearing, H_2O-free, magmatic melts were here performed for the first time. CO_2 content in our trachytic melts (series C) decompressed at both rates indicates that degassing occurs close to equilibrium. It reaches values lower than solubility at higher pressures, however these discrepancies are almost within the error and the equilibrium values from Ghiorso and Gualda (2015), while are not in good agreement with other solubility models (e.g. Papale et al., 2006, see Fig. 2c-d). Coherently with series A, slightly minor CO_2 values were reached at low P_f during the longer decompression at slower rate and the departure from solubility values observed at low P_f can be linked to continuous (or multiple events of) nucleation.

Melts with mixed H_2O - CO_2 vapor phase

H_2O and CO_2 glass contents in melts with mixed H_2O-CO_2 fluids (series B) show more complex trends as P_f decreases. In detail, at higher pressures, up to P_f of 50 MPa, residual CO_2 roughly follows closed-system degassing path. However it assumes values below solubility at the correspondent P_f at both decompression rates, previously discussed also for H_2O-free melts (series C). Instead, in contrast with this equilibrium path, residual H_2O starts to decrease already at 150 MPa at 0.01 MPa s^{-1} and at 100 MPa at 1 MPa s^{-1} reaching a minimum value of about 1.5 wt.% at both rates. Starting from P_f = 50 MPa, once all the dissolved CO_2 is consumed, water concentration increases up to the solubility values related to X_{H2O}=1 at both rates and at P_f = 25 MPa remains constant at the faster rate and roughly follows the isopleth with X_{H2O}=1 at the slower rate (Fig. 3). We can exclude that this rise in dissolved H_2O is linked to (i) relative enrichments induced by crystallization (e.g. Blundy et al., 2010) due to the low crystallinity of these glasses or to (ii) bubble resorptions (e.g. McIntosh et al., 2014) due to the lack also of CO_2 increments in these glasses.

Unfortunately only few other systematic studies focused on the decompression-induced degassing of melts with mixed H_2O-CO_2 fluids exist in literature. Le Gall and Pichavant (2016a, 2016b) extended the experiments carried out by Pichavant et al. (2013) by decompressing basaltic melts at about 0.04 and 0.08 MPa s^{-1} with several steps. They found on one hand that melts with low X_{H2O} (H_2O: 0.71 – 1.12 wt.%; CO_2: 840 – 1100 ppm) show a very slight decrease in H_2O and a progressive reduction in CO_2, which assumes values higher than isobars for each correspondent P_f. On the other hand, in melts with higher X_{H2O} (H_2O: 1.95 – 2.45 wt.%; CO_2: 818 – 1011 ppm; X_{H2O} ~ 0.25 – 0.56), both H_2O and CO_2 significantly decrease in function of P_f. H_2O content first decreases up to a minimum value (of about 1 wt.%) and then increases reaching the solubility values with X_{H2O} = 1 at the correspondent P_f (of 25 and ~ 50 MPa at 0.08 and 0.04 MPa s^{-1} respectively) during decompression, similarly to our results. Instead also in these melts CO_2 concentrations are well above the equilibrium values. However we want to mention that in these studies CO_2 concentration was quantified subtracting a spectrum from a volatile-free glass and not with similar water content as in this study (see section 2.2.2).
In conclusion, taking into account all the data, we can infer that volatile exolution in our melts are not completely limited by solubility related to closed-system degassing regime. It could be the consequence of a continuous melt-vapour thermodynamic re-equilibration under different conditions achieved during decompression, promoted by slower decompression rates. This process seems to mostly involve H_2O, which shows complex trends in function of P_f up to reach glass contents close to the solubility values related to X_{H2O} = 1 at Pf of 50 MPa. The possibility to achieve quick vapour-melt re-equilibration has been so far suggested by studies focused on CO_2 flushing (e.g. Blundy et al., 2010; Yoshimura and Nakamura, 2010; Dallai et al., 2011; Caricchi et al., 2018).

Final remarks
HT-HP experiments made using a wide spectrum of H_2O and CO_2 molar fractions could be very useful to discriminate the contribution of the single gas species during the degassing and then to decode the decompression history of natural melts, containing mixed H_2O-CO_2 vapor. In particular several numerical (e.g. Gonnermann and Manga, 2005) and experimental (e.g. Mollo et al., 2017; Pichavant et al., 2018 and references therein) studies justified evidences of CO_2-rich natural products (e.g. rhyolitic obsidians from 1340 A.D. Mono Craters eruption, glass inclusions and embayments in Strombolian basalts) as the consequence of disequilibrium degassing due to the diffusive fractionation resulting from the slower diffusivity of CO_2 compared to H_2O. However we found, at least for the investigated conditions, that our melts are able to degas close to equilibrium in both pure H_2O (series A) and pure CO_2 (series C) saturated series regardless of decompression rates, albeit a difference in (initial) diffusion values of about two orders of magnitude (D_{H2O} = 2.8 x 10^{-10} m^2 s^{-1}, from Fanara et al., 2013; D_{CO2} = 6.4 x 10^{-12} m^2 s^{-1}, from Zhang and Ni, 2010). Therefore, although more experimental investigations are necessary, it is possible that volatile concentration in natural products (e.g. matrix glasses and melt inclusion in volcanic rocks, volcanic gases) records the complex degassing behavior during the decompression at different conditions (e.g. decompression rate, initial H_2O/CO_2 molar fraction and its temporal change) of melts with mixed (H_2O + CO_2 $\pm$ other volatile species) fluid phases, when not affected by external process (e.g. CO_2 fluxing, magma mixing).

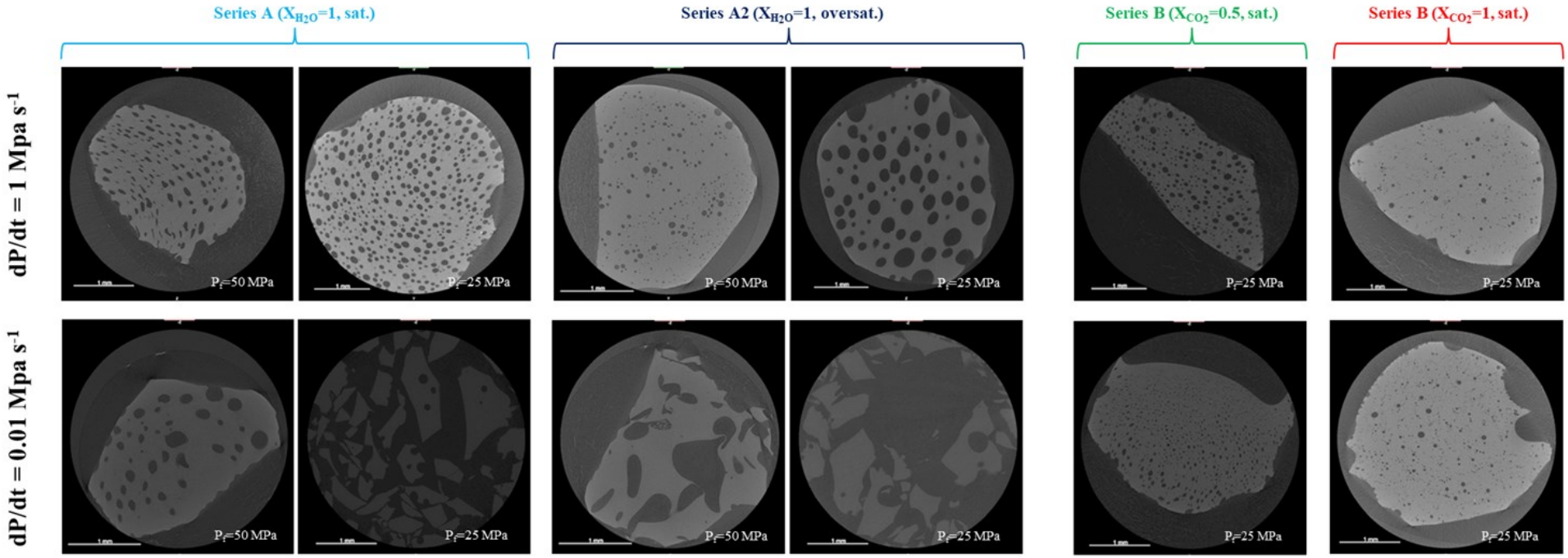

Fig. 6. Representative 2D slices selected from 3D images of samples decompressed at 1 MPa s^{-1} (upper panels) and 0.01 MPa s^{-1} (bottom panels) up to low final pressures (of 50 and 25 MPa).

3.2.2. Degassing regime: open- vs. closed-system degassing

H_2O-rich melts

H_2O-rich series show a transition from bubble nucleation- to growth and coalescence-dominated degassing at both decompression rates indicated by BND decrease coupled with D_m, σ and porosity increase starting from P_f lower than 100 MPa (Fig. 1).

Ostwald ripening is another process able to lead to this textural evidences with a timescale given by: $\tau_{Or} = P\delta(r_i^2 - r_f^2)/4RTD\gamma C_S$ with P pressure, δ average distance between bubbles (from BND, see above), r_i and r_f initial and final (i.e. minimum detectable size, 6 μm) bubble radii, R gas constant, T temperature, D water diffusion (from Fanara et al., 2013), γ surface tension (0.053 N m^{-1}, see below), C_S water solubility value (Proussevitch et al., 1993a). We chose mean bubble radius corrected for shrink factor (see above) as r_i and used data from series A at P_f of 100 MPa at 1 MPa s^{-1} to evaluate the possibility that this process occurs between P_f of 100 and 50 MPa (i.e. in 50 s). The obtained τ_{Or} of 99 (at 100 MPa) and 123 s (at 50 MPa) ruled out an important role of this process at 1 MPa s^{-1}. Moreover similar parameters obtained at 0.01 MPa s^{-1} likely indicate minor effects also in the case of lower rates.

Anyway, data obtained from glasses of both series at low P_f ($P_f \geq 50$ MPa) and slower decompression show marked evidences of bubble coalescence, the development of permeability (particularly evident in samples a2-3s from series A2 quenched at $P_f = 50$ MPa at 0.01 MPa s^{-1}, see Figs. 1e-h and 6) and evidences of fragmentation, in contrast with those observed at the faster decompression (Figs. 1 and 6, Table 2). These results suggest that while during our higher decompression rate bubbles remained in mechanical equilibrium with melts following a closed-system degassing regime, at our slower rate permeable networks of interconnected bubbles were formed and degassing occurred possibly under open-system regime (here defined only in terms of mechanical equilibrium, in fact thermodynamic equilibrium between melt and fluids escaped from the melts to the void space in closed capsules cannot be excluded).

Magma becomes permeable when coalescing bubbles reach a porosity that exceeds the percolation threshold. However, several open questions exist about percolation threshold, in fact theoretical studies and measurements on experimental or natural samples returned a range from about 30 to 78% (Burgisser et al., 2017 and references therein). In our melts porosity deviates from the equilibrium values in contrast with residual dissolved H_2O (see above for a detailed discussion), making it difficult a detailed quantitative study on the influence of bubbles parameters on percolation threshold. Taking into account the samples a2-3s we can constrain a relatively low percolation threshold between 28% (measured porosity) and 60% (i.e. equilibrium porosity). However, following Burgisser et al. (2017) we inferred that percolation threshold could not depend only on total porosity, but can be strongly influenced by the ratio σ/D_m, with more disperse bubble size distributions that strongly favour permeability. In fact, these textural features are promoted by the continuous bubble coalescence observed at our lower decompression rates. In contrast, the potential second nucleation events and continuation or resumption of nucleation observed respectively in series A and A2 at 1 MPa s^{-1} reduce standard deviation as well as decrease D_m growth, hindering the development of permeable interconnected bubble networks (Fig. 1).

Interestingly, also Mongrain et al. (2008), decompressing a more viscous phonolitic melts at 800 °C with a decompression rate ≤ 0.25 MPa s^{-1}, reported open-system degassing regime conditions starting from $P_f \leq 40 - 50$ MPa, resulting in bubbles with collapse evidences. In contrast, closed-system degassing regime was obtained from decompression experiments on alkaline melts, at different temperature (850 to 1150 °C), up to low P_f when decompression rates ≥ 0.25 MPa s^{-1} have been used (Iacono-Marziano et al. 2007; Larsen, 2008; Shea et al., 2008; Gardner, 2012; Gardner et al., 2013).

Finally, as mentioned, samples decompressed at 1 MPa s^{-1} did not show fragmentation evidences up to a the lowest reached P_f (25 MPa), likely due to the low viscosity of these magmas, which makes bubble overpressures unlikely, as also indicated by the lack in high volatile oversaturation at these low pressures. Instead, samples decompressed at 0.01 MPa s^{-1} and quenched at P_f of 25 MPa were fragmented. We suggest a criterion of inertia-driven fragmentation (Namiki and Manga, 2008) for these melts, which in fact occurs when inertial forces generated by the bubble expansion exceed viscous forces (that limit expansion) as well as surface tension forces and drive the breakup of the melt into discrete parcels.

CO_2-rich melts

Melts with pure CO_2 fluids (series C) show a nucleation-dominated degassing with a progressive increase in BND coupled with almost constant values of D_m and σ, attributed to the slower diffusivity of CO_2 as discussed above. Instead in melts with mixed H_2O-CO_2 fluids (series B) the exolution of CO_2 up to P_f = 100 - 50 MPa has strong effects on bubble populations, which show similarities with those of series C (Figs. 1 and 6). In conclusion, CO_2 seems to act delaying bubble growth and coalescence in favor of bubble nucleation and then promoting closed-system degassing regime.

However, in series B magma vesiculation can change after a stasis (between 100 and 50 MPa) marked by a possible melt re-equilibration with fluids at X_{H2O} = 1 (with an increment in H_2O melt content, Fig. 3) that leads to H_2O-dominated degassing. In fact, at P_f = 25 MPa a renewed nucleation occurs when melts are decompressed at slower rates, in contrast to faster rates where no new bubbles are formed and the pre-existing ones rapidly expand. Therefore we can suppose that this transition to H_2O-dominated degassing could be crucial for magma ascent and fragmentation of natural melts (with mixed H_2O-CO_2 fluids), especially when characterized by initial H_2O/CO_2 molar fraction ratio, containing high amount of water and promoting a deeper CO_2 exhaustion.

3.3. Deciphering decompression conditions from textural and chemical parameters

Magma vesiculation evolution under the selected experimental settings was numerically modeled in order to test our ability to predict the obtained experimental data. In fact, a correct numerical reproduction of laboratory results as well as the identifications of specific limitations in the models is a crucial step to reconstruct decompression conditions using textural and chemical parameters of natural rocks as constraints.

Magma vesiculation during isothermal decompression at constant rate has been modelled coupling the method of moments for bubble size distributions, bubble nucleation and growth rate equations, mass conservation of volatiles. This approach allows to numerical simulate, under controlled conditions, the variation in BSD parameters (such as BND, bubble mean size, porosity) as well as in residual glass volatile content, measurable also in experimental and natural samples. Detailed information are furnished in Appendix A. This section is focused on H_2O-rich series, on which a bigger dataset is available from literature and less uncertainties (e.g. degassing path in H_2O-CO_2-rich melts can deviate from closed-system degassing curves, very small CO_2-dominated bubbles with size below detection limit; see above) exist.

Our numerical simulations using series A data show the presence of a narrow single homogeneous nucleation event without reproducing second nucleation events (Fig. 7). Results obtained for decompression rates of 1 MPa s^{-1} are in very good agreement with experimental data (Fig. 7 a-c). In fact, they show a ΔP required for homogeneous nucleation (defined when nucleation rate J > 1 m^{-3} s^{-1}) of 36 MPa, an amplitude of the nucleation event (Δn) of 17 MPa (from 164 to 148 MPa), a ΔC_{HoN} of 0.88 wt.%, a peak BND of 9.7 x 10^{11} m^{-3} and a D_m (at $P_f = \Delta P_{HoN} + \Delta n$) of 39 μm. Instead, results for decompression rate of 0.01 MPa s^{-1} show the same ΔP for nucleation and ΔC_{HoN} obtained from the faster rates, in agreement to experimental results. However, in contrast with measured

data, they show an inferior Δn of 9 MPa (from 164 to 155 MPa), a very lower (of 3 order of magnitude) BND of 1.3 x 10^9 m^{-3} and higher (of 1 order of magnitude) D_m of 282 μm (Fig. 7d-f).
Therefore, a parametric study was made in order to explain the discrepancies between modeled and measured data at the slower rate. Starting from simulation performed at 0.01 MPa s^{-1}, the main parameters (i.e. viscosity, initial H_2O content, surface tension, diffusion) were changed, keeping the others fixed (i.e. initial values from constitutive equations in Appendix A). The obtained data show that (i) viscosity has negligible effects on results until it reaches values of 10^7 Pa s, at which BND starts to slightly increase and D_m to decrease without altering ΔP for nucleation, Δn and ΔC_{HoN}. However these are unrealistic high values of viscosity for evolved alkaline melts at high temperature (e.g. our anhydrous trachytic melt at 1200 °C assume values of $10^{4.4}$ Pa s). (ii) An increase or decrease of 0.5 wt.% in initial water content (H_2O_i; i.e. 6.6 and 5.6 wt.%) respectively almost nullifies or increases up to 63 MPa the ΔP for nucleation without changing Δn and results in a decrease of 22% (0.69 wt.%) or increase of the 16% (1.02 wt.%) ΔC_{HoN}. Moreover, they leave values of BND (1.5 and 1.2 x 10^9 m^{-3}) and D_m (220 and 330 μm) in the same order of magnitude, coherently with the small differences observed between series A and A2. (iii) A reduction or rise in surface tension of 0.01 N m^{-1} (correspondent to variation estimated by Bagdassarov et al., 2000 by changing H_2O_i of 0.5 wt.%; i.e. 0.0043 and 0.063 N m^{-1}) respectively almost decrease down to 23 or increase up to 49 MPa the ΔP for nucleation varying Δn to values of 7 and 11 MPa; decrease of 29% (0.63 wt.%) or increase of the 33% (1.18 wt.%) ΔC_{HoN}; only slightly change values of BND (2.6 x 10^9 and 7.5 x 10^8 m^{-3}) and D_m (202 and 380 μm). Instead, (iv) decreasing or increasing diffusion of 1 order of magnitude (i.e. 2.8 x 10^{-9} and 2.8 x 10^{-11} m^2 s^{-1}) ΔP for nucleation and ΔC_{HoN} don't change, despite Δn varies to 12 and 7 μm respectively. In contrast, BND abruptly raised (3.7 x 10^{10} m^{-3}) or reduced (4.9 x 10^7 m^{-3}) of about one order and a half of magnitude, whereas D_m sharply decreases (103 μm) or increases (773 μm).
These results indicate that the only parameter that can significantly control the BND, Dm and Δn values and then justify the difference observed between experimental and numerical data is the water diffusion.
Therefore we suggest that the adopted mean field approximation for the diffusive growth of a single bubble (in Eq. A9) could be inappropriate to simulate magma vesiculation in evolved alkaline melts as they are characterized by a high water diffusion. In detail, we can infer that during decompression at high rates (e.g. 1 MPa s^{-1}), the low decompression time does not guarantee much time for bubble diffusive growth allowing good BND prediction with our model. In contrast at lower rates it is necessary to use another approach. A more sophisticated (multi-bubble) cell model for diffusive bubble growth was proposed by Proussevitch et al. (1993b) assuming the presence for each bubble of a spherical shell of finite volume, in which mass of melt and volatile are conserved. The resulting concentration volatile profile between the bubble interface and the shell edge drives the diffusion growth of the bubbles. We hypothesize that the high water diffusion of evolved alkaline melts could be able to change rapidly this profile reducing the diffusive growth rate faster than with the mean field approximation. This could result in a greater probability to consume excess H_2O in the melt nucleating new bubbles between adjacent shells (also favoured by low surface tension of these melts) than growing the existing one, with a consequent increase in Δn and BND and decrease in D_m.
Interestingly, the widely used decompression rate meter of Toramaru (2006) is based on the same assumptions as ours and several experimental studies on evolved alkaline melts found difficulties to reproduce experimental results with this model (e.g. Preuss et al., 2016; Allabar and Nowak, 2018), in contrast to rhyolitic melts (e.g. Mourtada-Bonnefoi and Laporte, 2004; Cluzel et al., 2008; Hamada et al., 2010). Therefore, despite an accurate combination between a more sophisticated diffusive bubble growth model and (improved) CNT is not trivial, other numerical and experimental

investigations are necessary to improve our ability to predict decompression rates from textural and chemical parameters in natural rocks with evolved alkaline compositions.

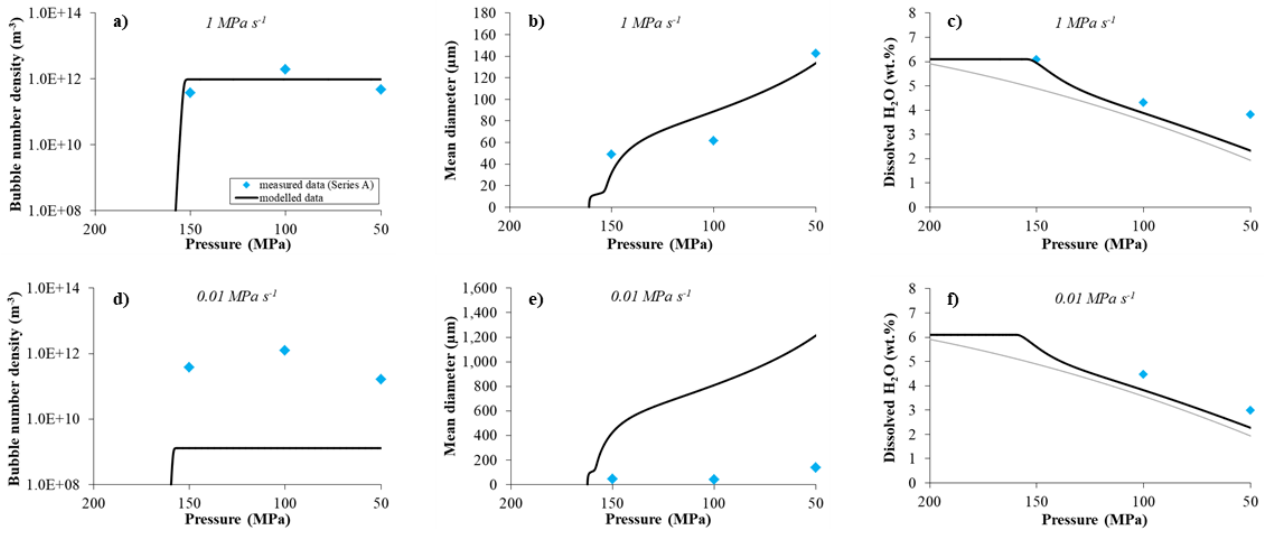

Fig. 7. Measured vs. modelled (see Appendix A) bubble number densities (a, d), bubble mean diameter corrected for shrink factor (b, e) and residual H_2O dissolved in the glasses (c, f) at 1 MPa s^{-1} (a-c; upper panels) and 0.01 MPa s^{-1} (d-f; bottom panels). Data at final pressure of 25 MPa are not included because affected by a potential second nucleation event at 1 MPa s^{-1} and by fragmentation at 0.01 MPa s^{-1}.

4. Conclusions

Our study shows that in evolved alkaline melts:

- Pressure decrease (ΔP) required for homogeneous bubble nucleation (i) is independent of decompression rate, (ii) decreases as initial dissolved H_2O content increases, (iii) does not change significantly with volatile composition (i.e. pure H_2O, pure CO_2, mixed H_2O-CO_2 fluids) starting from similar saturation conditions;
- The resulting bubble number density (i) is mainly due to a single nucleation event and slightly decreases as the decompression rate declines in H_2O-rich melts, despite potential second nucleation events can occur at low final pressures and faster decompression rates, (ii) almost continuously increases during decompression, resulting in higher values, in CO_2-rich melts;
- Homogeneous bubble nucleation can occur with lower supersaturation pressures and higher bubble number density than in rhyolitic melts, especially at slow decompression rates, possible enhancing magma buoyancy and eruption explosivity;
- The high volatile diffusion strongly controls their vesiculation evolution, however it makes difficult to numerically reproduce magma degassing, especially during slower decompressions, with simplified diffusive bubble growth models, useful to correctly decrypt information from natural rocks.

Once bubbles are nucleated:

- Degassing style can evolve close to equilibrium in melts with pure H_2O and pure CO_2 fluids almost regardless of decompression rates. In particular, in H_2O-rich melts, equilibrium degassing is promoted by lower ΔP for nucleation. Instead melts with mixed (H_2O + CO_2) fluids can have more complex degassing behaviors in function of different decompression conditions (e.g. decompression rate, initial H_2O/CO_2 molar fraction);

- In H_2O-rich melts (i) at faster decompression rates, closed-system degassing regime occurs as well as evidences of magma fragmentation, and likely of bubble overpressures, are not observable up to a final pressure of 25 MPa, (ii) at slower rates, open-system degassing regime occurs, with consequent formation of permeable network of bubbles (percolation threshold between 28 to 60%) and inertial magma fragmentation;
- In CO_2-rich melts (i) the low CO_2 diffusion delays bubble growth (promoting magma nucleation), (ii) magma vesiculation can rapidly change after the (deep) exhaustion of CO_2 at high pressures marking the transition to H_2O-dominated degassing, with possible critical effects on eruption explosivity.

Appendix A. Numerical modeling of magma vesiculation

Method of moments

Methods of moments allow to describe BSD in response of bubble nucleation and growth using a population balance equation. Although coalescence and other processes (e.g. Ostwald ripening, shrinking) can affect BSD but, because they remained not sufficiently constrained so far, were not modelled here. This methods was introduced in the study of magmatic bubbles by the pioneering work of Toramaru (1989; 1995).

Considering a BSD function $F(R,t)$ dependent on bubble radius (R) and time (t), it can be quantitatively characterized through the moments M_i, defined as:

$$M_i = \int_{R_c}^{\infty} R^i F(R,t) dR \qquad \text{(A1)}$$

where R_c is the critical radius to create bubble nuclei (see below).

The following physical interpretation results assuming a spherical shape: M_0 is the total number of bubbles per unit volume of melt, that is BND; M_1 is the sum of the bubble radius per unit volume of melt, and then the mean bubble radius $R_m = M_1/M_0$; πM_2 is the total surface area of bubbles per unit volume of melt; $V_b = 4\pi M_3/3$ is the total volume of bubbles per unit volume of melt, and then porosity is $V_b/(1+V_b)$.

The temporal variation of the BSD moments is therefore given by:

$$\frac{dM_o}{dt} = J \qquad \text{(A2)}$$

and in a more general form by:

$$\frac{dM_i}{dt} = iGM_{i-1} + \frac{dM_0}{dt} R_c^i \qquad \text{(A3)}$$

where J and G ($= dR_m/dt$) are the bubble nucleation and growth rate respectively. In order to derivate J and G we schematically review the main concepts on bubble nucleation and growth below.

Bubble nucleation

Nucleation can be examined following the classical nucleation theory (CNT; e.g. Hirth et al., 1970). It states that volatiles in a metastable state can enter in a stable state as the results of fluctuations, which form a new phase (i.e. bubble nuclei), in (unstable) thermodynamic equilibrium with the metastable supersaturated bulk liquid. Since the creation of an interface is an energetically unfavourable process the nuclei need a critical size (R_c) below which they are unstable and can disappear. It is given by the Laplace equation:

$$R_c = 2\gamma/(P_B^* - P) \qquad \text{(A4)}$$

where γ is the surface tension, P melt pressure and P_B^* pressure inside the critical nucleus:

$$P_B^* = P_{SAT}\, exp\left(\frac{V_m}{kT}(P - P_{SAT})\right) \quad \text{(A5)}$$

with V_m volume of volatile molecules in the liquid, k Boltzmann constant, T temperature, P_{SAT} volatile saturation pressure, assuming critical nuclei as macroscopic objects (i.e. capillary approximation) and ideal gas behavior.

In this framework, the probability to homogeneously produce spherical critical nuclei by fluctuation of volatile molecules can be estimated predicting the nucleation rate (J):

$$J = J_0\, exp\left(\frac{-W_n}{kT}\right) \quad \text{(A6)}$$

where

$$W_n = \left(\frac{16\pi\gamma^3}{3(P_B^* - P)^2}\right) \quad \text{(A7)}$$

and

$$J_0 = \frac{2V_m n_0^2 D}{a_0}\sqrt{\frac{\gamma}{kT}} \quad \text{(A8)}$$

comes from Hurwitz and Navon (1994), with n_0 number of volatile molecules per unit volume of melt ($n_0 = C_m \rho_m N_A / M_v$ with C_m melt volatile concentration in mass fraction, ρ_m melt density, N_A Avogadro number, M_v molar mass of volatiles), a_0 $\left(\approx n_0^{-1/3}\right)$ mean distance between neighboring volatile molecules and D is the diffusion of volatile molecules in the melt. Although other pre-exponential factors were proposed, its change results in very small variation of the nucleation rate (e.g. Navon and Lyakhovsky, 1998; Lubetkin, 2003).

Bubble growth

Nuclei with a critical radius can grow as a consequence of diffusion of volatile exolved from the melts and vapour expansion. They can be treated assuming ideal gas behaviour and spherical bubbles and critical nuclei in mechanical equilibrium with melt (for detail see Toramaru, 1989; Proussevitch et al., 1993b; Hajimirza et al., 2019).

Diffusion of volatile into bubbles is governed by mass conservation of volatiles. Using the mean field approximation for the diffusive mass flux (i.e. $F = D[(C_m - C_i)/R_m]$) the mass of volatiles into a single bubble with radius R_m per unit volume (m_b) is given by:

$$\frac{d}{dt}\left(\rho_g R_m^3\right) = \frac{dm_b}{dt} = 4\pi R_m^2 F \rho_m = 4\pi R_m D(C_m - C_i)\rho_m \quad \text{(A9)}$$

where C_m and C_i are volatile concentration in melt and at fluid-melt interface, ρ_g and ρ_m vapor and melt density. Therefore, the mass of total fluid phase (m_g) can be defined as follow:

$$m_g = \int_{R_c}^{\infty} m_b F(R,t)dR \quad \text{(A10)}$$

and its temporal change expressed in terms of moments is:

$$\frac{dm_g}{dt} = \frac{dm_b}{dt}M_0 + \frac{dM_0}{dt}m_c \quad \text{(A11)}$$

with m_c mass of critical nucleus.

It follows that residual glass volatile content during decompression is given by: $C_m = C_0 - (m_g/\rho_m)$.

The mass m_g can be used to calculate the pressure inside a bubble (P_B) and therefore determine the bubble growth rate using the Rayleigh-Plesset equation:

$$G = \frac{R_m}{4\mu_m}\left[(P_B - P) - \frac{2\gamma}{R_m}\right] \quad \text{(A12)}$$

where μ_m is melt viscosity. This equation describes the momentum balance for an expanding bubble, in which difference of pressure inside bubble and in the surrounding melt is balanced by viscous and surface tension forces whereas inertial terms are negligible.

Governing and constitutive equations

The system of ordinary differential equations defined by Eqs. (A2), (A4) and (A11) were solved using constitutive equations suitable for evolved alkaline melts. In detail, solubility laws were obtained by polynomial regressions from Ghiorso and Gualda (2015), H_2O diffusion at 1100-1400 °C from Fanara et al. (2013), melt density from Richet et al. (2000), melt viscosity from Giordano et al. (2008). Moreover the empirical Eq. 13 of Shea (2017), based on results from existing bubble nucleation experiments, was used to estimate the surface tension.

References

Allabar, A., Nowak, M. (2018). Message in a bottle: Spontaneous phase separation of hydrous Vesuvius melt even at low decompression rates. Earth Planet. Sci. Lett. 501, 192–201.

Bagdassarov, N., Dorfman, A., Dingwell, D. (2000). Effect of alkalis, phosphorus, and water on the surface tension of haplogranite melt. Am. Mineral. 85, 33–40.

Benne, D., Behrens, H. (2003). Water solubility in haplobasaltic melts. Eur. J. Mineral. 15, 803–814.

Blake, S. 1984. Volatile oversaturation during the evolution of silicic magma chambers as an eruption trigger. J. Geophys. Res. Solid Earth 89, 8237–44.

Blundy, J., Cashman, K.V., Rust, A.,Witham, F. (2010). A case for CO2-rich arcmagmas. Earth Planet. Sci. Lett. 290, 289–301.

Brooker R. A., Kohn S. C., Holloway J. R. and McMillan P. F. (2001). Structural controls on the solubility of CO_2 in silicate melts Part I: bulk solubility data. Chem. Geol. 174, 225–239.

Buono, G., Pappalardo, L., Petrosino, P. (2019). Magma storage and ascent during the largest eruption of Somma-Vesuvius volcano: Pomici di Base (22 ka) plinian event. Boll. Geofis. Teor. Appl., in press.

Burgisser, A., Chevalier, L., Gardner, J. E., Castro, J. M. (2017). The percolation threshold and permeability evolution of ascending magmas. Earth Planet. Sci. Lett. 470, 37–47.

Caricchi, L., Sheldrake, T.E., Blundy, J. (2018). Modulation of magmatic processes by CO_2 flushing. Earth Planet. Sci. Lett. 491, 160–171.

Cashman, K. V., Mangan, M. T. (1994). Physical aspects of magmatic degassing: II. Constraints on vesiculation processes from textural studies of eruptive products. Rev. Mineral. Geochem. 30, 447–478.

Cashman, K.V., Scheu, B. (2015). Magma Fragmentation. In H. Sigurdsson, B. Houghton, S. R. McNutt, H. Rymer, J. Stix (Eds.), The Encyclopedia of Volcanoes (Second Edition) (pp. 459-471). Academic Press, London.

Cassidy, M., Manga, M., Cashman, K., Bachmann, O. (2018). Controls on explosive-effusive volcanic eruption styles. Nat. Commun. 9, 2839.

Cichy, S.B., Botcharnikov, R.E., Holtz, F., Behrens, H. (2011). Vesiculation and microlite crystallization induced by decompression: a case study of the 1991-95 Mt Unzen eruption (Japan). J. Petrol. 52, 1469–1492.

Cluzel, N., Laporte, D., Provost, A., Kannewischer, I. (2008). Kinetics of heterogeneous bubble nucleation in rhyolitic melts: implications for the number density of bubbles in volcanic conduits and for pumice textures. Contrib. Mineral. Petrol. 156, 745–763.

Colucci, S., Battaglia, M., Trigila, R. (2016). A thermodynamical model for the surface tension of silicate melts in contact with H2O gas. Geochim. Cosmochim. Acta 175, 113–127.

Dallai, L., Cioni, R., Boschi, C., D'Oriano, C. (2011). Carbonate-derived CO2 purging magma at depth: Influence on the eruptive activity of Somma-Vesuvius, Italy. Earth Planet. Sci. Lett. 310, 84–95.

Fanara, S., Botcharnikov, R.E., Husen, A., Buddensieck, J., and Behrens, H. (2012). Pre-eruptive conditions of the Campanian Ignimbrite eruption: experimental constraints from phase equilibria and volatile solubility studies. Proceedings of IODP-ICDP Kolloquium, Kiel, Germany.

Fanara, S., Behrens, H., Zhang, Y. (2013). Water diffusion in potassium-rich phonolitic and trachytic melts. Chem. Geol. 346, 149–161.

Fanara, S., Botcharnikov, R.E., Palladino, D.M., Adams, F., Buddensieck, J., Mulch, A., Behrens, H. (2015). Volatiles inmagmas related to the Campanian ignimbrite eruption: experiments vs. natural findings. Am. Mineral. 100, 2284–2297.

Fanara, S. Sottili, G., Silleni, A., Palladino, D.M., Schmidt, B.C. (2017). CO_2 bubble nucleation upon pressure release in potassium-rich silicate magmas. Chem. Geol. 461, 171–181.
Gurioli, L., Andronico, D., Bachelery, P., Balcone-Boissard, H., Battaglia, J., Boudon, G.,Burgisser, A., Burton, M.R., Cashman, K., Cichy, S., Cioni, R., Di Muro, A., Dominguez,L., D'Oriano, C., Druitt, T., Harris, A.J.L., Hort, M., Kelfoun, K., Komorowski, J.C.,Kueppers, U., Le Pennec, J.L., Menand, T., Paris, R., Pioli, L., Pistolesi, M., Polacci, M.,Pompilio, M., Ripepe, M., Roche, O., Rose-Koga, E., Rust, A., Schiavi, F., Scharff, L.,Sulpizio, R., Taddeucci, J., Thordarson, T. (2015). MeMoVolc consensual document: a review of cross-disciplinary approaches to characterizing small explosive magmatic eruptions. Bull. Volcanol. 77, 49
Gardner, J.E. (2012). Surface tension and bubble nucleation in phonolite magmas. Geochim. Cosmochim. Acta 76, 93–102.
Gardner, J.E. (2009). The impact of pre-existing gas on the ascent of explosively erupted magma. Bull. Volcanol.71, 835–844.
Gardner, J.E., Denis, M.H. (2004). Heterogeneous bubble nucleation on Fe–Ti oxide crystals in high-silica rhyolitic melts. Geochim. Cosmochim. Acta 68, 3587–3597.
Gardner, J.E., Ketcham, R.A. (2011). Bubble nucleation in rhyolite and dacitemelts: temperature dependence of surface tension. Contrib. Mineral. Petrol. 162:929–943.
Gardner, J.E., Webster, J.D. (2016). The impact of dissolved CO_2 on bubble nucleation in water-poor rhyolite melts. Chem. Geol. 420, 180–185.
Gardner, J.E., Hilton, M., and Carroll, M.R. (1999). Experimental constraints on degassing of magma: isothermal bubble growth during continuous decompression from high pressure. Earth Planet. Sci. Lett. 168, 201–218.
Gardner, J.E., Ketcham, R.A., Moore, G. (2013). Surface tension of hydrous silicate melts: constraints on the impact of melt composition. J. Volcanol. Geotherm. Res. 267, 68–74.
Ghiorso, M.S., Gualda, G.A.R. (2015). An H_2O–CO_2 mixed fluid saturation model compatible with rhyolite-MELTS. Contrib. Mineral. Petrol. 169, 1245.
Giachetti, T., Gonnermann, H. M., Gardner, J. E., Burgisser, A., Hajimirza, S., Earley, T. C., Truong, N. Toledo, P. (2019). Bubble coalescence and percolation threshold in expanding rhyolitic magma. Geochem. Geophys. Geosyst. 20, 1054–1074.
Giordano, D., Russell, J.K., Dingwell, D.B. (2008). Viscosity of magmatic liquids: a model. Earth Planet. Sci. Lett. 271, 123–134.
Gonnermann, H.M., Gardner, J.E. (2013). Homogeneous bubble nucleation in rhyolitic melt: experiments and nonclassical theory. Geochem. Geophys. Geosyst. 14, 4758–4773.
Gonnermann, H., Manga, M. (2005). Nonequilibrium magma degassing: results from modeling of the ca. 1340 A.D. eruption of Mono Craters, California. Earth Planet. Sci. Lett. 238, 1–16.
Guillot, B., Sator, N. (2011) Carbon dioxide in silicate melts: a molecular dynamics simulation study. Geochim. Cosmochim. Acta 75, 1829–1857.
Hajimirza, S., Gonnermann, H. M., Gardner, J. E., Giachetti, T. (2019). Predicting homogeneous bubble nucleation in rhyolite. J. Geophys. Res. Solid Earth 124, 2395-2416.
Hamada, M., Laporte, D., Cluzel, N. (2010). Simulating bubble number density of rhyolitic pumices from Plinian eruptions: constraints from fast decompression experiments. Bull. Volcanol. 3, 735–746.
Hirth, G., Pound, G.M., St Pierre, G.R. (1970). Bubble nucleation. Metall. Trans. 1, 939–945.
Huber, C., Su, Y., Nguyen, C., Parmigiani, A., Gonnermann, H.M., Dufek, J. (2014). A new bubble dynamics model to study bubble growth, deformation, and coalescence. J.Geophys. Res. Solid Earth 119, 216–239.
Hughes, E.C., Neave, D.A., Dobson, K.J., Withers, P.J., Edmonds, M. (2017). How to fragment peralkaline rhyolites: observations on pumice using combined multi-scale 2D and 3D imaging. J. Volcanol. Geotherm. Res. 336, 179–191.
Hurwitz, S., Navon, O. (1994). Bubble nucleation in rhyolitic melts: experiments at high pressure, temperature, and water content. Earth Planet. Sci. Lett. 122, 267–280.
Iacono-Marziano, G., Schmidt, B.C., Dolfi, D. (2007). Equilibrium and disequilibrium degassing of a phonolitic melt (Vesuvius AD 79 “white pumice”) simulated by decompression experiments. J. Volcanol. Geotherm. Res. 161, 151–164.
Kashchiev, D. (2003). Thermodynamically consistent description of the work to form a nucleus of any size. J. Chem. Phys. 118, 1837–1851.
Kashchiev, D. (2004). Multicomponent nucleation: Thermodynamically consistent description of the nucleation work. J. Chem. Phys. 120, 3749–3758.
Khitarov, N.I., Lebedev, Y.B., Dorfman, A.M., Bagdasarov, N.S. (1979). Effects of temperature, pressure and volatiles on the surface tension of molten basalt. Geochem. Int. 16, 78–86.
Larsen, J.F. (2008). Heterogeneous bubble nucleation and disequilibrium H_2O exsolution in Vesuvius K-phonolite melts. J. Volcanol. Geotherm. Res. 275, 278–288.
Larsen, J.F., Gardner, J.E. (2004). Experimental study of water degassing from phonolite melts: implications for volatile oversaturation during magmatic ascent. J. Volcanol. Geotherm. Res. 134, 109–124.

Le Gall, N., Pichavant, M. (2016a). Experimental simulation of bubble nucleation and magma ascent in basaltic systems: implications for Stromboli volcano. Am. Mineral. 101, 1967–1985.
Le Gall, N., Pichavant, M. (2016b). Homogeneous bubble nucleation in H_2O- and H_2O-CO_2-bearing basaltic melts: results of high temperature decompression experiments. J. Volcanol. Geotherm. Res. 327, 604–621.
Liedl, A., Buono, G., Lanzafame, G., Dabagov, S. B., Della Ventura, G., Hampai, D. et al. (2019). A 3D imaging textural characterization of pyroclastic products from the 1538 AD Monte Nuovo eruption (Campi Flegrei, Italy). Lithos 340–341, 316–331.
Lubetkin, S.D. (2003). Why is it much easier to nucleate gas bubbles than theory predicts? Langmuir 19, 2575–2587.
Mader, H.M., Manga, M.M., Koyaguchi, T. (2004). The role of laboratory experiments in volcanology. J. Volcanol. Geotherm. Res. 129, 1 – 5.
Mangan, M.T., Sisson, T.W. (2000). Delayed, disequilibrium degassing in rhyolite magma decompression experiments and implications for explosive volcanism. Earth Planet. Sci. Lett. 183, 441–455.
Mangan, M.T., Sisson, T.W. (2005). Evolution of melt-vapor surface tension in silicic volcanic systems: experiments with hydrous melts. J. Geophys. Res. 110, B01202.
Marxer, H., Bellucci, P., Nowak, M. (2015). Degassing of H_2O in a phonolitic melt: a closer look at decompression experiments. J. Volcanol. Geotherm. Res. 297, 109–124.
Mastrolorenzo, G., Pappalardo, L. (2006). Magma degassing and crystallization processes during eruptions of high-risk Neapolitan-volcanoes: Evidence of common equilibrium rising processes in alkaline magmas. Earth Planet. Sci. Lett. 250, 164–181.
McIntosh, I.M., Llewellin, E.W., Humphreys, M.C.S., Nichols, A.R.L., Burgisser, A., Schipper, C.I., Larsen, J.F. (2014). Distribution of dissolved water in magmatic glass records growth and resorption of bubbles. Earth Planet. Sci. Lett. 401, 1–11.
Mollo, S., Vetere, F., Beherens, H., Tecchiato, V., Langone, A., Scarlato, P., Perugini, D. (2017). The effect of degassing and volatile exsolution on the composition of a trachybasaltic melt decompressed at slow and fast rates. Per. Min. 86, 185–197.
Mongrain, J., Larsen, J.F., King, P.L. (2008). Rapid water exsolution, degassing, and bubble collapse observed experimentally in K-phonolite melts. J. Volcanol. Geoth. Res. 173, 178–184.
Mourtada-Bonnefoi, C.C., Laporte, D. (1999). Experimental study of homogeneous bubble nucleation in rhyolitic magmas. Geophys. Res. Lett. 26, 3505–3508.
Mourtada-Bonnefoi, C.C., Laporte, D. (2002). Homogeneous bubble nucleation in rhyolitic magmas: an experimental study of the effect of H_2O and CO_2. J. Geophys. Res. 107, 2066.
Mourtada-Bonnefoi, C.C., Laporte, D. (2004). Kinetics of bubble nucleation in a rhyolitic melt: an experimental study of the effect of ascent rate. Earth Planet. Sci. Lett. 218, 521–537.
Namiki, A., Manga, M. (2008). Transition between fragmentation and permeable outgassing of low viscosity magmas. J. Volcanol. Geoth. Res. 169, 48–60.
Navon, O., Lyakhovsky, V. (1998). Vesiculation processes in silicic magmas. Geol. Soc. London Spec. Pub. 145, 27–50.
Newman, S., Lowenstern, J.B. (2002). VolatileCalc: a silicate melt–H_2O–CO_2 solution model written in Visual Basic for Excel. Comput. Geosci. 28, 597–604.
Nowak, M., Porbatzki, D., Spickenbom, K., Diedrich, O. (2003). Carbon dioxide speciation in silicate melts: a restart. Earth Planet. Sci. Lett. 207, 131–139.
Papale P. (1999). Modeling of the solubility of a two-component H_2O+CO_2 fluid in silicate liquid. Am. Mineral. 84, 477–492.
Papale P., Moretti R., Barbato D. (2006). The compositional dependence of the saturation surface of H_2O+CO_2 fluids in silicate melts. Chem. Geol. 229, 78–95.
Pappalardo, L., Mastrolorenzo, G. (2010). Short residence times for alkaline Vesuvius magmas in a multi-depth supply system: Evidence from geochemical and textural studies. Earth Planet. Sci. Lett. 296, 133–143.
Pappalardo, L., Mastrolorenzo, G. (2012). Rapid differentiation in a sill-like magma reservoir: A case study from the campi flegrei caldera. Sci. Rep. 2, 712.
Pappalardo, L., Buono, G., Fanara, S., Petrosino, P. (2018). Combining textural and geochemical investigations to explore the dynamics of magma ascent during Plinian eruptions: a Somma–Vesuvius volcano (Italy) case study. Contrib. Mineral. Petrol. 173, 61.
Pichavant, M., Di Carlo, I., Rotolo, S.G., Scaillet, B., Burgisser, A., Le Gall, N., Martel, C. (2013). Generation of CO_2-rich melts during basalt magma ascent and degassing. Contrib. Mineral. Petrol. 166, 545–561.
Pichavant, M., Le Gall N., Scaillet B. (2018). Gases as Precursory Signals: Experimental Simulations, New Concepts and Models of Magma Degassing. In J. Gottsmann, J. Neuberg, B. Scheu (Eds.), Volcanic Unrest (pp. 139-154). Springer, Cham.
Plank, T. A., Barth, A., Newcombe, M. E., Gonnermann, H., Hauri, E. (2018). The Minutes and Hours Before Eruption: Decompression Rate Scales to Explosivity. American Geophysical Union, Fall Meeting 2018, San Francisco, USA.

Preuss, O., Marxer, H., Ulmer, S., Wolf, J., Nowak, M. (2016). Degassing of hydrous trachytic Campi Flegrei and phonolitic Vesuvius melts: experimental limita-tions and chances to study homogeneous bubble nucleation. Am. Mineral.101, 859–875.
Proussevitch, A.A., Sahagian, D.L., Kutolin, A.T. (1993a) Stability of foams in silicate melts, J. Volcanol. Geotherm. Res. 59,161–178.
Proussevitch, A.A., Sahagian, D.L., Anderson A.T. (1993b). Dynamics of diffusive bubble growth in magmas: isothermal case, J. Geophys. Res. 98, 22283–22307.
Proussevitch, A.A., Sahagian, D.L., Tsentalovich, E.P. (2007). Statistical analysis of bubble and crystal size distributions: formulations and procedures. J. Volcanol. Geotherm. Res. 164, 95–111.
Richet, P., Whittington, A., Holtz, F., Behrens, H., Ohlhorst, S., Wilke, M. (2000). Water and the density of silicate glasses. Contrib. Mineral. Petrol. 138, 337–347.
Roux, J, Lefèvre, A. (1992). A fast-quench device for internally heated pressure vessels. Eur. J. Mineral. 4, 279–282.
Schanofski, M., Fanara S., Schmidt, B.C. (2019). CO_2–H_2O solubility in K-rich phonolitic and leucititic melts. Contrib. Mineral. Petrol. 174, 52.
Schmidt, B.C., Behrens, H. (2008). Water solubility in phonolite melts: influence of melt composition and temperature. Chem Geol. 256, 259–268.
Schmidt, B.C., Blum-Oeste, N., Flagmeier, J. (2013). Water diffusion in phonolite melts. Geochim. Cosmochim. Acta 107, 220–230.
Shea, T. (2017). Bubble nucleation in magmas: a dominantly heterogeneous process? J. Volcanol. Geotherm. Res. 343, 155–170.
Shea, T., Houghton, B.F., Gurioli, L., Cashman, K.V., Hammer, J.E., Hobden, B.J. (2010). Textural studies of vesicles in volcanic rocks: an integrated methodology. J. Volcanol. Geotherm. Res. 190, 271–289.
Sottili, G., Fanara, S., Silleni, A. Palladino, D.M., Schmidt, B.C. (2017). CO_2-crystal wettability in potassic magmas: implications for eruptive dynamics in light of experimental evidence for heterogeneous nucleation. Geophys. J. Int. 209, 688–694.
Sparks, R.S.J., Barclay, J., Jaupart, C., Mader, H.M., Phillips, J.C. (1994). Physical aspects of magmatic degassing. I. Experimental and theoretical constraints on vesiculation. Rev. Mineral. Geochem. 30, 413–445.
Stolper, E. (1982) The speciation of water in silicate melts. Geochim. Cosmochim. Acta 46, 2609–2620.
Su, Y., Huber, C. (2017). The effect of non-linear decompression history on H2O/CO2 vesiculation in rhyolitic magmas. J. Geophys. Res. Solid Earth 122, 2712–2723.
Toramaru, A. (1989). Vesiculation process and bubble size distributions in ascending magmas with constant velocities. J. Geophys. Res. 94, 17523–17542.
Toramaru, A. (1995). Numerical study of nucleation and growth of bubbles in viscous magmas. J. Geophys. Res. 100, 1913–1931.
Toramaru, A. (2006). BND (bubble number density) decompression rate meter for explosive volcanic eruptions. J. Volcanol. Geotherm. Res. 154, 303–316.
Toramaru, A. (2014). On the second nucleation of bubbles in magmas under sudden decompression. Earth Planet. Sci. Lett. 404, 190–199.
Wallace, P. J., Plank, T., Edmonds, M., Hauri, E. H. (2015). Volatiles in magmas. In H. Sigurdsson, B. Houghton, S. R. McNutt, H. Rymer, J. Stix (Eds.), The Encyclopedia of Volcanoes (Second Edition) (pp. 163-183). Academic Press, London.
Yoshimura, S., Nakamura, M. (2010). Chemically driven growth and resorption of bubbles in a multivolatile magmatic system. Chem. Geol. 276, 18–28.
Zhang, Y., Ni, H. (2010). Diffusion of H, C, and O components in silicate melts. Rev. Mineral. Geochem. 72, 311–408

5. General conclusions and perspectives

In this work degassing mechanisms and timescales during the ascent of alkaline magmas in explosive eruptions have been investigated combining physico-chemical examinations of volcanic rocks (mainly 3D imaging textural characterization) with experimental and numerical simulations. Improving the knowledge on magma degassing behaviour can be crucial to better understand the link between surface-monitored signals and processes of magma transfer in Earth's crust from reservoirs to surface and its influence on the eruptive style. In particular alkaline magmas represent a very interesting case study because, although their low viscosity, they frequently fed highly explosive eruptions, as in the case of the high-risk Neapolitan alkaline Volcanism (i.e. Campi Flegrei, Ischia, Somma-Vesuvius).
In detail, in this work:

i. A new protocol of 3D imaging textural characterization for volcanological applications was defined using automatic algorithms. It is able to quantitatively investigate materials with highly interconnected pore networks, difficult to examine with the procedures adopted so far in volcanology. The protocol allows simultaneously to (1) correctly separate vesicles from the networks, quantifying their morphological parameters (e.g. number density, size distribution, shape) and (2) measure the degree of interconnection of the networks. This kind of protocols facilitate the decryption of information on the evolution of magma degassing recorded in natural or experimental volcanic rocks, from 3D images acquired with imaging techniques rapidly expanding in several fields of the geosciences, like X-ray computed microtomography (X-μCT).
ii. Conceptual models and constraints on degassing of alkaline magmas during different eruptive scenarios and ascent conditions were furnished starting from 3D imaging textural characterization (using X-μCT) of natural rocks emitted during eruptions with different explosivity index from the Neapolitan alkaline volcanism, HT-HP isothermal decompression experiments, numerical modeling of magma vesiculation and reviewed literature data. The obtained results can provide useful tools for a better interpretation of eruptive dynamics during past eruptions as well as of surface-monitored signals arising from active volcanoes during magma ascent.
iii. The effects of external environmental factors (e.g. interactions between magma and wall-rocks or external water) on magma degassing were examined through petrological investigations (i.e. textural and chemical characterization, thermodynamic and kinetic calculations). In particular, this study allowed to shed light on the influence of the rapid release, and assimilation by the magma, of external CO_2 on the increase of eruption explosivity, constraining mechanisms and timescales with which it can occur during highly-explosive, caldera-forming eruptions. It is suggested that it can be crucial to integrate these processes in hazard assessment of volcanoes with plumbing systems located in carbonate bedrocks (e.g. Campi Flegrei, Colli Albani Volcanic District, Etna, Merapi, Nisyros, Popocatépetl, Somma-Vesuvius), albeit they have been often neglected so far.

Acknowledgments

I would like to thank first of all my tutors Lucia Pappalardo and Prof. Paola Petrosino for offering me the opportunity to work on this project and for their precious support, availability and interesting discussions. In particular Lucia Pappalardo for introducing me to numerous volcanological questions and for her extreme patience in debating them with me.
I would also like to acknowledge Giovanni Macedonio for providing me really stimulating information and basic knowledge on numerical approaches in physical volcanology. At the same time I wish to thank Sara Fanara for letting me discover the potential of experiments in volcanology with immense availability and, together with Burkhard Schmidt, Prof. Sharon Webb and Max Schanofski, for giving me the possibility to use laboratories at the Georg-August University of Göttingen as well as to discuss with them about magmatic processes from another (experimental) prospective. The support given by the DAAD (German Academic Exchange Service) during the months spent abroad has been really appreciated. I'm very grateful to have worked and debated on several issues covered in this thesis also with Prof. Danilo Palladino, Gianluca Sottili and Monica Spagnoli.
The intense collaboration especially with Gabriele Lanzafame, Andrea Liedl, Lucia Mancini and Giancarlo Della Ventura has been fundamental for my improvement in 3D image processing and 3D X-ray imaging. Moreover, I want to express all my gratitude to Prof. Chris Harris and Bejamin Edwards for the very interesting and useful collaboration.
An essential part of this work has been made thanks to the information, supports and discussions with several people of the DiSTAR and Vesuvius Observatory, in particular Ilenia Arienzo, Stefano Caliro, Giuseppe Mastrolorenzo, Fabio Mazzeo, Carlo Pelullo, Zaccaria Petrillo, Ciro Sepe as well as all the technical staff.
Finally I would gratefully acknowledge Dr. Rosa Anna Corsaro and Burkhard Schmidt for the revision and comments to this thesis.

Appendix 1.

Magma storage and ascent during the largest eruption of Somma-Vesuvius volcano: Pomici di Base (22 ka) plinian event

This work is published in a special volume of Bollettino di Geofisica Teorica ed Applicata (in press; doi: https://doi.org/ 10.4430/bgta0294) - containing studies developed starting from presentations selected at the 36th National Congress of GNGTS (National Group of Solid Earth Geophysics; Trieste, Italy; 2017) - under the same title with authors:

Buono G.[a,b], Pappalardo L.[a], Petrosino P.[b]

a - Istituto Nazionale di Geofisica e Vulcanologia, Osservatorio Vesuviano, Italy
b - University of Naples Federico II, Department of Earth, Environmental and Resources Science, Italy

It includes preliminary data improved in the section 3.1. I contributed to all phases (field activities, rock characterization, data interpretation, writing) and investigations of the work.

Abstract

The reconstruction of the pre-eruptive storage conditions as well as syn-eruptive magma ascent dynamics of past eruptions is of fundamental importance to decipher the relationship between surface-monitored signals and the sub-volcanic processes in order to learn more about the eruptive behavior of active volcanoes. The Pomici di Base plinian eruption is the first (22 ka) and largest (>4.4 km^3) event of the Somma-Vesuvius volcanic complex. Here we present the preliminary results of a geochemical, isotopic, two-dimensional (2D) and three-dimensional (3D) textural study performed on volcanic products emitted during the plinian phase of this eruptive event with the aim to reconstruct in more detail the magmatic evolution of this large caldera-forming eruption. Particularly, it was fed by chemically and thermally zoned magmas extracted from a crystal mush zone in a magma chamber with top at ~4.5 km depth. During this eruption, crustal (limestone) contamination and subsequent CO_2 liberation as well as changes in degassing mechanisms mainly controlled the eruptive dynamics.

1. Introduction

The knowledge of processes occurred in magma chamber and volcanic conduit during high-magnitude eruptions is a primary goal in volcanology, due to the influence of these sub-volcanic processes on the behavior of precursory phenomena that are detected by monitoring systems during volcanic crises. In fact, a severe difficulty in volcanic forecast is to correlate the evolution of the geochemical and geophysical signals recorded at the surface with the dynamics of magma transfer at depth. In detail, magma migration towards the surface is strongly controlled by intensive magmatic variables (e.g. magma and volatiles composition, temperature) as well as storage (e.g.

depth and volume of magma chambers) and ascent (e.g. decompression rate, open vs. closed degassing regime) conditions (e.g. Gonnermann and Manga, 2007; Blundy and Cahsman, 2008), which can be influenced by external factors (e.g. edifice load and related stress field, conduit geometry, interaction with country rocks or external water; e.g. Borgia et al., 2005; Houghton et al., 2010).

In the last decades, quantitative textural studies on volcanic rocks combined with conventional geochemical analyses, have proved to be a fundamental approach in exploring the pre-eruptive and syn-eruptive conditions allowing to improve our ability to interpret volcano-monitoring signals and perform hazard assessments. In particular, three-dimensional textural investigation in the last two decades has been successfully applied in several field of geosciences (e.g. Cnudde and Boone, 2013) and recently many studies have demonstrated the potential of this technique also to examine volcanic processes (e.g. Shea et al., 2010; Baker et al., 2012).

In more densely populated regions, as the Neapolitan high-risk volcanic area, this information would be essential for a better assessment of the volcanic hazard.

In this case study we have performed a geochemical (major-minor elements and Sr-Nd isotopic ratios) and (2D and 3D) textural investigation of volcanic products emitted during the Pomici di Base plinian eruption of Somma-Vesuvius volcano. This event represents the first (22 ka) and largest (volume >4.4 km^3) explosive eruption of Somma-Vesuvius volcano (Bertagnini et al., 1998; Landi et al., 1999). Moreover, it delineates the end of a period of open-conduit activity and the transition to the explosive character of the volcano as well as the beginning of caldera collapse events (e.g. Cioni et al., 2008; Santacroce et al., 2008; De Vivo et al., 2010). The obtained preliminary results allowed us to achieve information on the evolution of plumbing system and eruptive dynamics during this eruption.

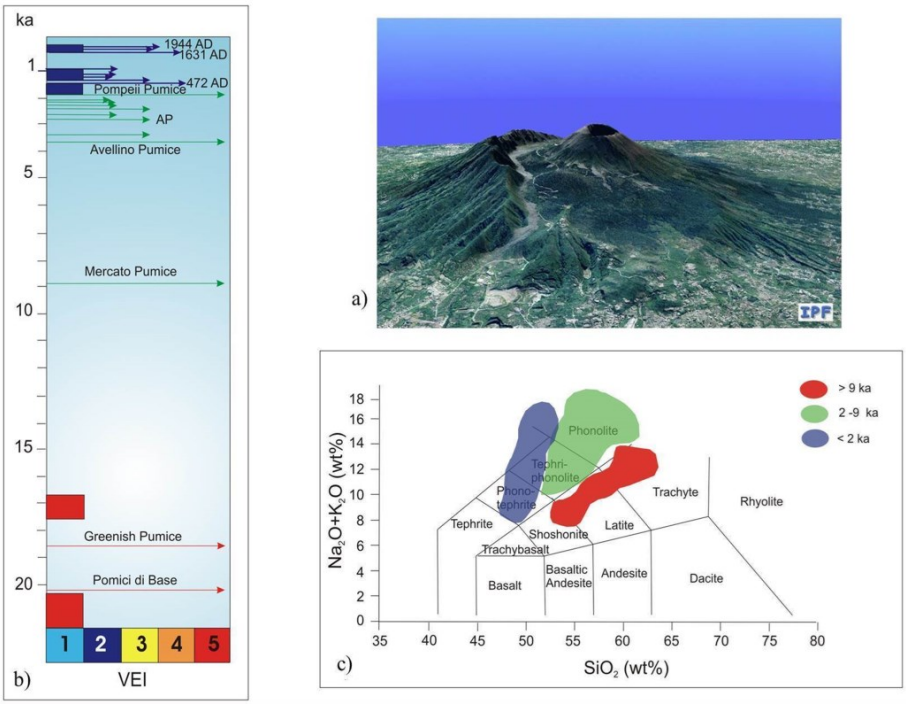

Fig. 1. (a) 3D view of current Somma-Vesuvius volcano (courtesy of G. Vilardo). (b) Schematic chronogram of Somma-Vesuivus activity as recorded by stratigraphic successions (after Cioni et al., 2008). (c) Total Alkalis vs. Silica (TAS) for Somma-Vesuvius rocks (after Santacroce et al., 2008). Colors are related to volcanism older than 9 ka (red), between 9 and 2 ka (green) and younger than 2 ka (blue).

2. Volcanological Background

The Somma-Vesuvius volcano, located at the south-east of metropolitan area of Naples is one of the most dangerous volcanoes in the world (Fig. 1a). The strato-volcano consists of the old edifice of Mt. Somma, featured by a summit caldera structure occupied in its center by the younger Vesuvius cone, whose last eruption occurred in 1944 (e.g. Cole and Scarpati, 2010; Pappalardo et al., 2014; Cubellis et al., 2016). The volcanism started with an early period of effusive and slightly explosive activity of the Mt. Somma, interrupted >22 ka and followed by a period characterized by at least four plinian eruptions (Pomici di Base, Mercato Pumice, Avellino Pumice, Pompeii Pumice; Fig. 1b) staggered with minor events covering a large range of magnitude and intensity. After 79 AD (Pompeii Pumice) eruption, the Vesuvius cone began to form during periods of open conduit activity, the last of which manifested in 1631-1944, ended with the current quiescent state (e.g. Cioni et al., 2008; Santacroce et al., 2008; De Vivo et al., 2010).The Somma-Vesuvius volcanic products can be subdivided into three potassic and high-potassic series on the basis of their chemical compositions (Fig. 1c): 1) slightly silica-undersaturated series, older than 9 ka; 2) mildly silica-undersaturated series, between 9 and 2 ka; 3) strongly silica-undersaturated series, younger than 2 ka (Joron et al., 1987). The large variability of Somma-Vesuvius magmas has been related to changes in the primary melts feeding the activity and to the effect of shallow level crystallization under different thermodynamic conditions (e.g. Santacroce, 1987; Civetta et al., 1991; Santacroce et al., 1993; Belkin and De Vivo, 1993; Trigila and De Benedetti, 1993; Marianelli et al., 1995; 1999; 2005; Ayuso et al., 1998; Cioni et al., 1998; Cioni, 2000; Lima et al., 2003; Peccerillo, 2005; Di Renzo et al., 2007; Mastrolorenzo and Pappalardo, 2006; Scandone et al., 2007; Scaillet et al., 2008; Pappalardo and Mastrolorenzo, 2010; 2012). Moreover, several geochemical studies have stressed the importance of crustal contamination in the evolution of Vesuvius magma (e.g. Savelli, 1968; Fulignati et al., 1995; 1998; Gilg et al., 1999; 2001; Del Moro et al., 2000; Pappalardo et al., 2004; Piochi et al., 2006; Iacono Marziano et al. 2008; 2009; Dallai et al., 2011; Jolis et al., 2013; 2015; Pichavant et al., 2014).Degassing during Somma-Vesuvius eruptions was investigated in several textural studies (Mastrolorenzo and Pappalardo, 2006; Cioni et al., 2011; Shea et al., 2012; Zdanowicz et al., 2018; Pappalardo and Mastrolorenzo, 2010; Pappalardo et al., 2014). Closed-system degassing regime during fast magma ascent (from hours to days) and open-system degassing regime during slow magma ascent (from days to months) have been invoked for highly explosive and moderately explosive–effusive events respectively, resulting in a general decrease in bulk vesicularity and increase in degassing-induced microlites content in juvenile products as the volcanic explosive index (VEI) decrease (e.g. Mastrolorenzo and Pappalardo, 2006; Pappalardo and Mastrolorenzo, 2010).

The plinian Pomici di Base eruption is the oldest and largest explosive event generated by the Somma-Vesuvius volcano (e.g. Delibras et al., 1979; Bertagnini et al., 1998; Landi et al., 1999).

The eruption occurred from a vent located 1-2.5 km west of the present cone, the eruptive column reached an height of 15-17 km (mass discharge rate, MDR = 2-2.5 x 10^7 kg/s) and emplaced a volcanic deposit with volume higher than 4.4 km^3 (Bertagnini et al., 1998).

Delibrias et al. (1979) were the first to recognize the plinian character of this event and obtained a ^{14}C age of 17050±140 yr B.P on the paleosol underneath the deposits, in agreement with the values of 18750±420 - 19170±420 yr B.P measured by Bertagnini et al. (1998). Other studies measured an age of about 22 ka by using K/Ar method on sanidine (22520±1000 yr B.P, Capaldi et al., 1985) and ^{14}C method on charcoal (maximum cal. age of 22030±175 yr B.P, Andronico et al., 1995; Siani et al., 2004).

Bertagnini et al. (1998) recognized three different eruptive phases: 1) an early opening phase, during which thin ash and pumice fall deposits were emplaced (U-1 in Fig. 2); 2) a plinian phase, principally consisting of a fallout deposit (U-2 in Fig. 2), although on the volcano's slopes small-volume pyroclastic density currents (PDCs; pyroclastic surge) units are recognizable. The plinian fallout is composed by three different layers: a basal white pumiceous layer (U-2a and U-2b), a transitional layer (U-2c), an upper thick black scoria bed (U-2d and U-2e), with a relative thickness of 2:1:5; 3) a final phreatomagmatic phase, during which a lithic-rich fallout and PDCs (pyroclastic surge and flow) deposits (U-3 – U-6 in Bertagnini et al., 1998) were generated, associated with caldera collapse (Bertagnini et al., 1998; Cioni et al., 1999).
Magma storage zone as well as syn-eruptive dynamics are debated. Landi et al. (1999) proposed that the eruption was fed by a low-aspect-ratio trachytic-latitic magma chamber located at pressure of about 300-400 MPa and hypothesized the replenishment of shoshonitic magma as eruption trigger. On the contrary, Balcone-Boissard et al. (2015) obtained a shallower pressure value of 100 MPa for the magmatic reservoir of the Pomici di Base eruption deduced from the Cl-buffering effect. Recently Pappalardo et al. (2018) proposed that limestone contamination could has been a significant process affecting both magma evolution as well as eruptive dynamics.

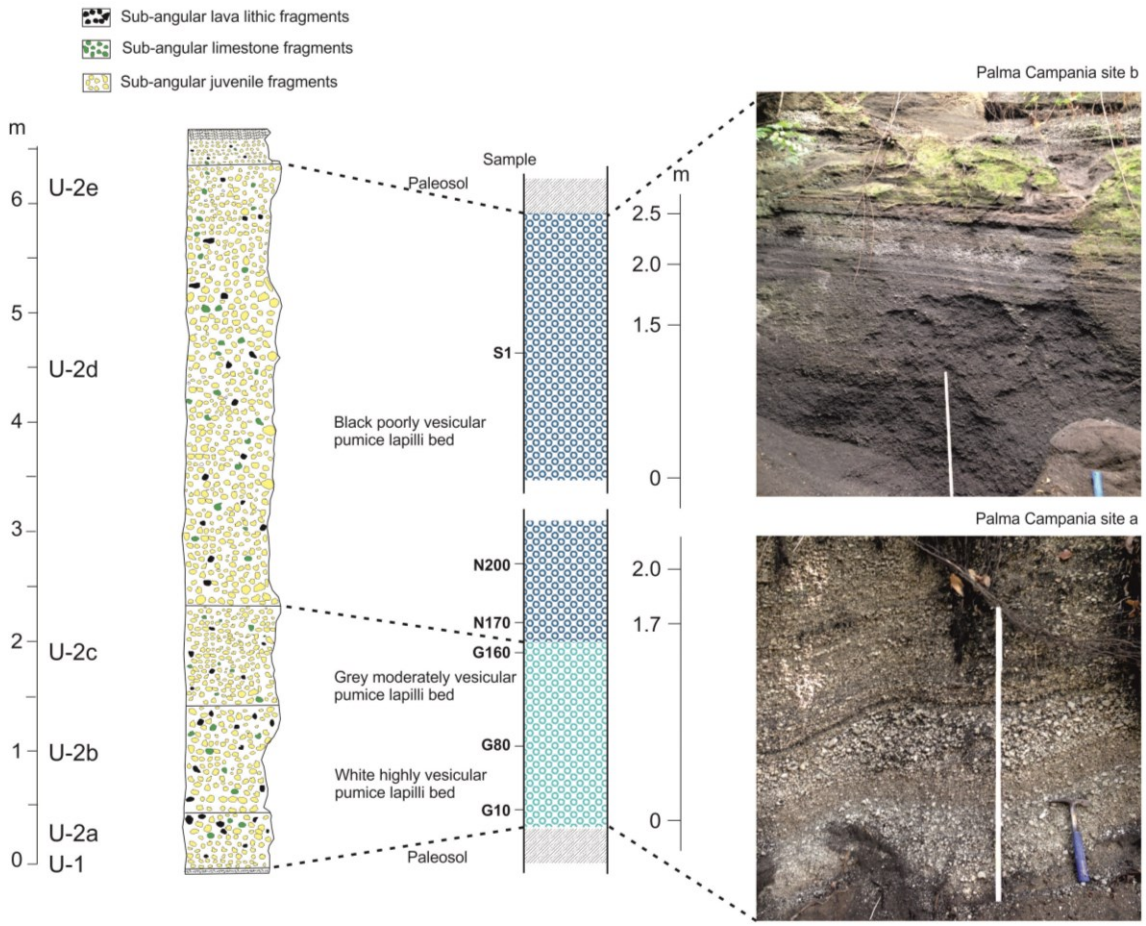

Fig. 2. Representative photos and schematic stratigraphic column for the Pomici di Base eruption and localization of samples collected for this study. The sampling interval was dictated by changes in grain size and color, according to the different stratigraphic units recognized by Bertagnini et al. (1998; on the left).

3. Methods

3.1. Density analysis

In order to account for possible density variations with size, we used clasts within a -5 to -2 phi size range for density measurements. Sets of 100 clasts for each granulometric class (where present) were weighted and coated with a thin film of paraffin wax, then their density was determined using a water pycnometer. We considered the volume of the paraffin wax film to be negligible because its density was about equal to that of water (1 g/cm^3). We obtained bulk vesicularities by comparing the densities of juvenile vesicular clasts with the dense-rock equivalent densities (2.4 and 2.6 g/cm^3 for pumices and scoriae respectively) for the composition of interest (as in Houghton and Wilson, 1989). Modal density/vesicularity clasts were selected for textural and geochemical analysis (see Balcone-Boissard et al., 2015 and references therein).

3.2. Geochemical analyses

Major-minor elements and Cl contents of matrix-glass and minerals (feldspars and pyroxenes) compositions were measured by scanning electron microscope (SEM) JEOL JSM 5310 (15 kV, ZAF Correction Routine) with energy dispersive spectrometer (EDS) at CISAG (Centro Interdipartimentale di Servizio per Analisi Geomineralogiche) at the University of Naples Federico II. Instrument calibration was based on international mineral and glass standards. Mean precision was <5% for SiO_2, Al_2O_3, K_2O, CaO, FeO and around 10% for the other elements (e.g. Morabito et al., 2014).

3.3. Radiogenic isotopes

Isotopic analyses for Sr and Nd via thermal ionization mass spectrometry (TIMS) were obtained at the Istituto Nazionale di Geofisica e Vulcanologia—Sezione di Napoli ‘‘Osservatorio Vesuviano’’ (INGV-OV), using a ThermoFinnigan Triton TI multi-collector mass spectrometer. Samples were processed through conventional HF–HNO_3–HCl dissolution before Sr and middle REE (MREE) were separated by standard cation exchange column chemistry, and Nd was further purified on an anion column. Sr and Nd were then loaded onto Ta and Re filaments, respectively. Sr and Nd blanks were negligible for the analyzed samples during the periods of measurements. Measured $^{87}Sr/^{86}Sr$ ratios were normalized for within-run isotopic fractionation to $^{87}Sr/^{86}Sr = 0.1194$, and $^{143}Nd/^{144}Nd$ ratios to $^{143}Nd/^{144}Nd = 0.7219$. The mean measured value of $^{87}Sr/^{86}Sr$ for NIST–SRM 987 was 0.710215 ± 0.000008 (2σ, n=36) and of $^{143}Nd/^{144}Nd$ for La Jolla was 0.511843 ± 0.000006 (2 σ, n = 11). The quoted error is the standard deviation of the mean (2σ) for n = 180. Sr and Nd isotope ratios have been normalized to the recommended values of NIST SRM 987 ($^{87}Sr/^{86}Sr$ = 0.71025) and La Jolla ($^{143}Nd/^{144}Nd$ = 0.51185) standards, respectively.

3.4. Textural analyses

The microstructure of the sample was investigated by X-ray microtomography (μ-CT) using a Carl Zeiss Xradia 410 Versa 3D X-ray microscope at the Istituto Nazionale di Geofisica e Vulcanologia—Sezione di Napoli ‘‘Osservatorio Vesuviano’’ (INGV-OV, Naples) selecting representative pumice and scoria clasts less than 3-4 cm in diameter, that cooled rapidly, thus reducing post-fragmentation vesicle expansion effects (e.g. Thomas and Sparks, 1992; Tait et al., 1998). In detail, μCT allowed the direct observation and 3D quantitative characterization of the number and size of vesicles, which are impossible to determine using conventional 2D techniques and constitute fundamental parameters to investigate magma degassing during its ascent toward the surface.

μ-CT images were acquired on each sample at different optical magnification (10X and 20X). Cylinders of 0.5 cm in diameter were cut from the representative samples and the scan was performed over a 360° rotation using 4001 projections, 80 KV voltage, 10 W power. The resulting nominal voxel (volumetric pixel) size ranges from 0.9 to 2 μm depending on the magnification used. Reconstruction of the attenuation data was performed using filtered back-projection, producing a stack of 967 cross-sectional, grey-scale digital images. Vesicles forming the pore network have been analyzed by segmenting and processing regions of a given range of grayscale values from the rest of the image using the Avizo software.
Finally, microlite content was measured acquiring for each sample at least 4–5 back-scattered electron (BSE) 2D images (270 × 200 μm) with SEM, then processed and analyzed using ImageJ software.

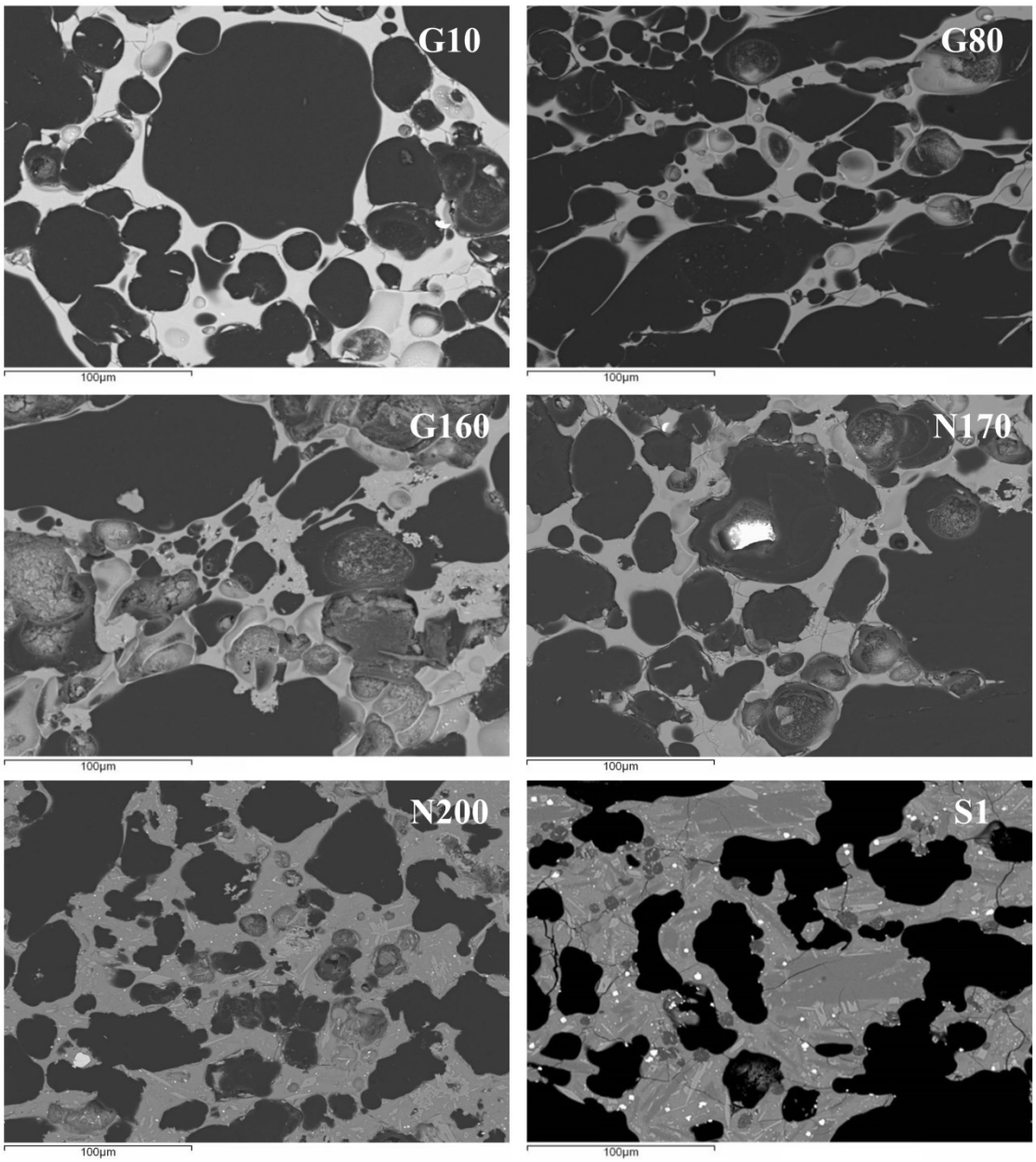

Fig. 3. Representative back-scattered electron images of juvenile rocks from Pomici di Base eruption.

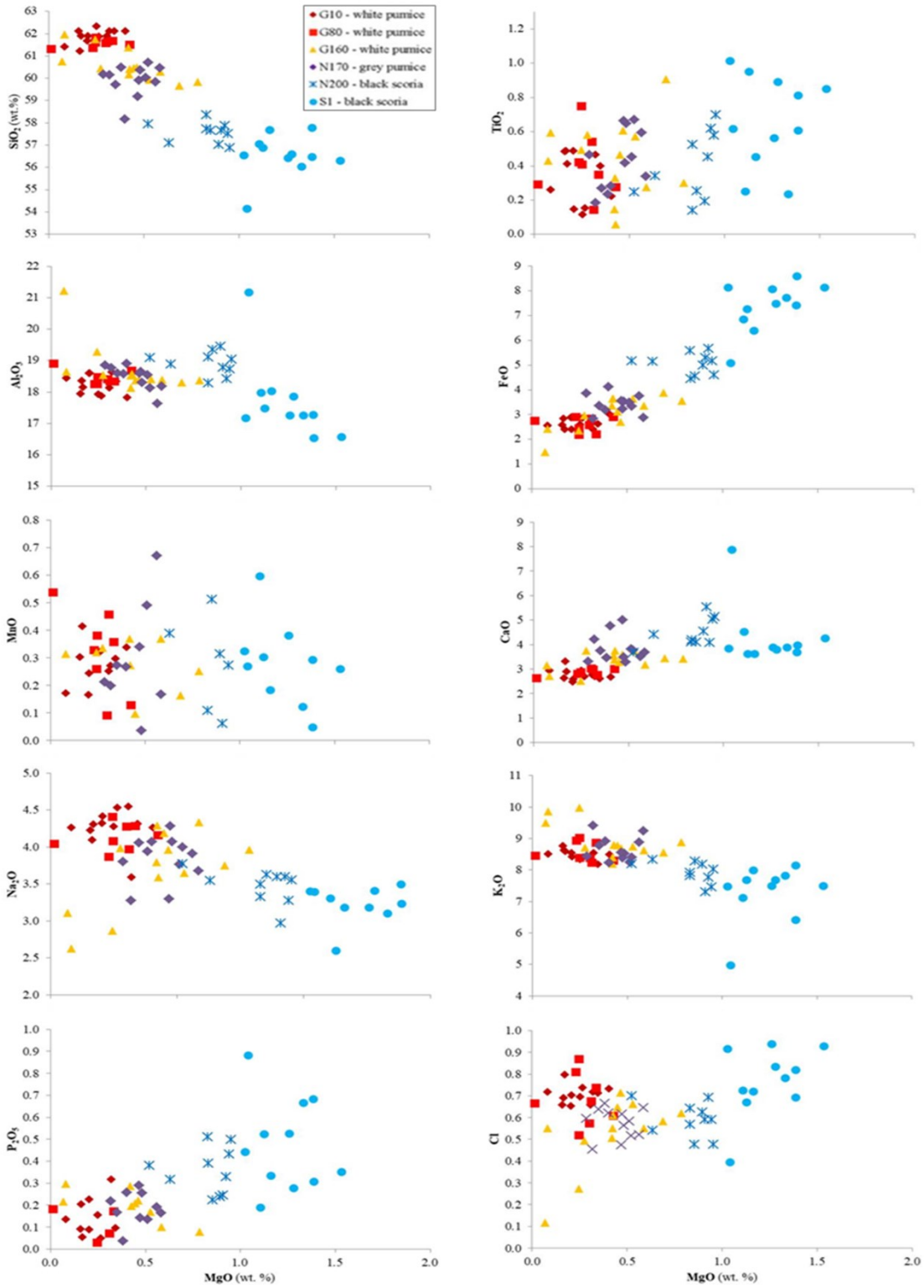

Fig. 4. Major element variation diagrams for Pomici di Base rocks.

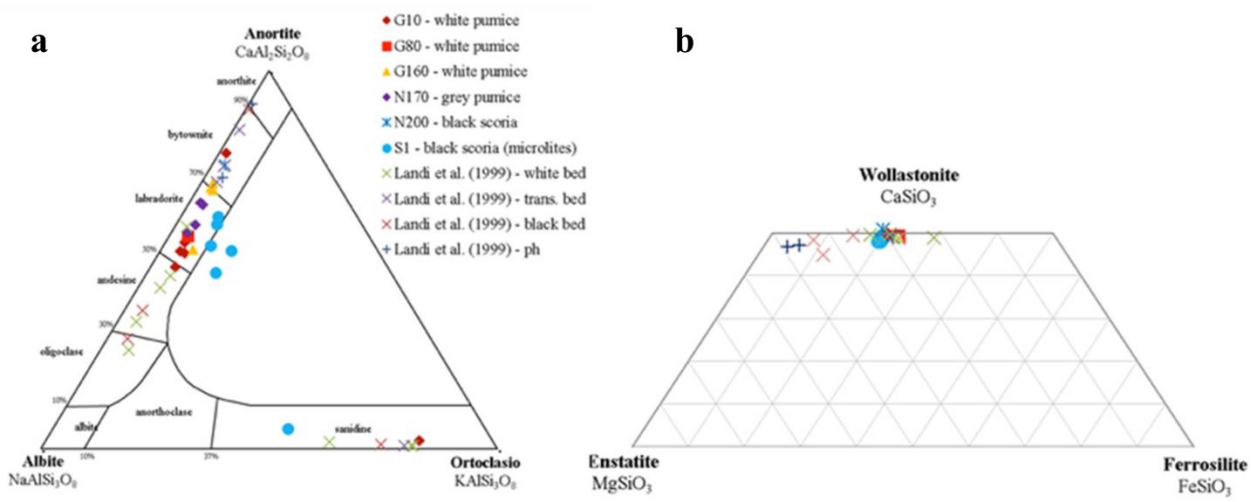

Fig. 5. Ab-An-Or ternary (a) and Di-Hd-En-Fs quadrilater (b) diagrams showing the composition of feldspars and clinopyroxene crystals for Pomici di Base rocks. Ph = Phreatomagmatic phase. The compositional trend toward the center of the ternary diagram for microlites in sample S1 can be the result of water exolution and the consequent increment of magma liquidus temperature during its ascent, able to promote an extensive crystallization.

4. Results

4.1. Petrographic features

Qualitative preliminary observations of thin sections under polarizing microscope and 2D/3D images reveal that the collected samples from the base to the top of fallout units have porphyritic texture with low content of phenocrysts (<5 vol.%) that are present as isolated crystals as well as in aggregate. Crystals have a maximum size of 3 mm and are constituted in order of decreasing abundance by sanidine>plagioclase>clinopyroxene>biotite and in minor amount by amphibole, magnetite and garnet. The content of plagioclase and mafic minerals increases in scoria samples at the top of the stratigraphic sequence, in which they appear also as discrete micro-phenocrysts (<<1 mm). Generally, phenocrysts show euhedral or sub-euhedral habit, however minor evidence of disequilibrium is observed (e.g. irregular edges, zoned clinopyroxene crystals with a marked "resorbed core").

The degree of vesicularity and crystallization (microlite) varies progressively in the matrix glass from the bottom upward in the stratigraphic sequence. In particular, the basal and intermediate (white to gray) pumice samples show high vesicularity and absence of microlites, while the upper black scoria are characterized by poorly-vesiculated, microlite-rich groundmass (Fig. 3).

4.2. Glass composition

In the classification Total Alkali versus Silica diagram (TAS, Fig. 1), the composition of the analyzed matrix-glasses ranges from trachyte (white to gray pumices) to latite (black scoriae) upwards of stratigraphic succession.

On Harker variation diagrams (Fig. 4), there is a systematic increase in SiO_2 and Na_2O as well as a regular decrease in TiO_2, FeO, CaO, P_2O_5 and Cl with the decrement of MgO content, chosen as differentiation index. The concentrations of Al_2O_3 and MnO remain roughly constant, while K_2O content weakly increases in the less evolved rocks and then remains constant in the course of differentiation (Fig. 4, Table 1).

4.3. Mineral Chemistry

The anorthite (An) content of plagioclase phenocrysts varies from An_{51} to An_{80} with an average increase from trachytic to latitic samples, instead in microlites of latitic scoriae (S1 sample) takes values of An_{51-77}. The sanidine show a decrease in Or content (from Or_{84} to Or_{54}) from trachytic to latitic composition (Fig. 5a, Table 1). Ternary end-member composition plot of clinopyroxene indicates a moderate Fe enrichment with differentiation, with ferrosilite values ranging from to Fs_{38} to Fs_{45} (Fig. 5b, Table 1).

4.4. Sr and Nd isotopic composition

Sr isotopic composition varies in the analyzed groundmasses from 0.707527 to 0.707605 towards the less differentiated terms. Crystal phases have $^{87}Sr/^{86}Sr$ values ranging from 0.707470-0.707500 in clinopyroxene and 0.707499-0.707500 in sanidine, which partially overlap with isotopic values of trachytic groundmasses. Nd isotopic compositions are much less variable and cluster around 0.512429-0.512452 both in matrix-glasses and minerals (Fig. 6, Table 1).

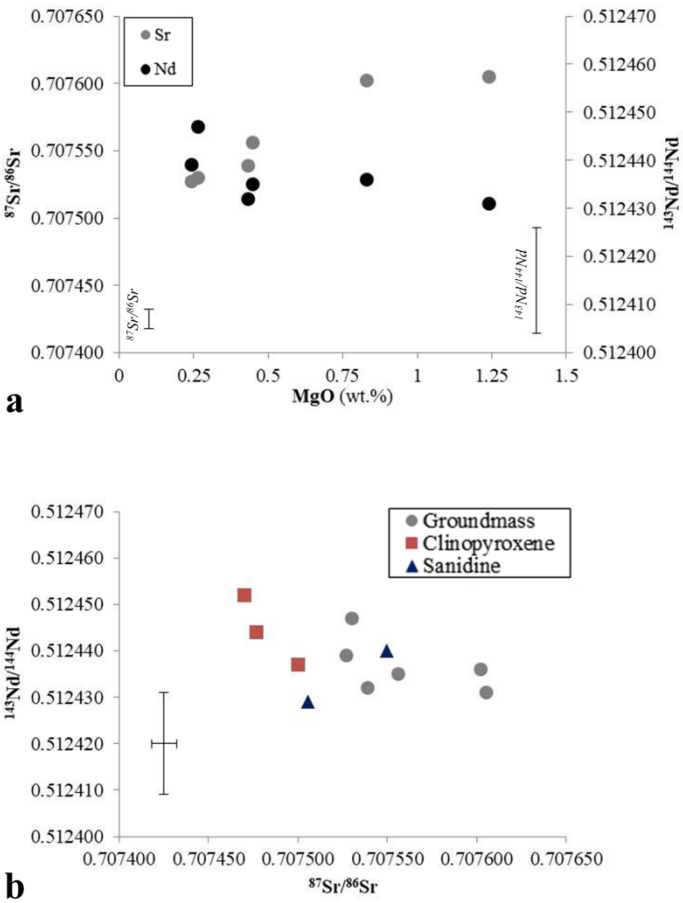

Fig. 6. a) MgO (wt.%) vs. Sr and Nd isotopic ratios for separated groundmasses. b) $^{143}Nd/^{144}Nd$ versus $^{87}Sr/^{86}Sr$ compositions for separated groundmasses and minerals.

4.5. Vesicularity and textural data

Clast vesicularity as well as density are strongly related to stratigraphic height, varying significantly during the eruption. Particularly white and intermediate pumices have a modal vesicularity of 75-76% (modal density: 0.57-0.61 g/cm^3) that increases at 48-59% (1.11-1.40 g/cm^3) in the upper black scoriae (Table 2).

Low-density pumices are characterized by at least two vesicle populations: small (<20 µm) spherical bubbles and irregularly shaped large bubbles (>20 µm), showing many stages of coalescence, separated by thin (few µm) microlite-free glass. Sometimes evidence of stretched bubbles is present particularly in gray pumices. Black and high-density scoriae have markedly different textures, which are characterized predominantly by small bubble population and subordinately by large polylobate, amoeboid bubbles separated by thick (>10 µm) microlite-bearing glass (15–31 vol.%; Fig. 3 and Fig. 7, Table 2).

Vesicle Size Distributions (VSDs, fractions for different equivalent sphere diameters) reveal polymodal trends for both white and gray pumices showing two peaks at 5-10 µm and 20-30 µm; on the contrary VSDs for black scoriae generally show a less evident bimodality with distributions skewed toward finer sizes, while larger vesicle mode is relatively poorly represented (Fig. 7).

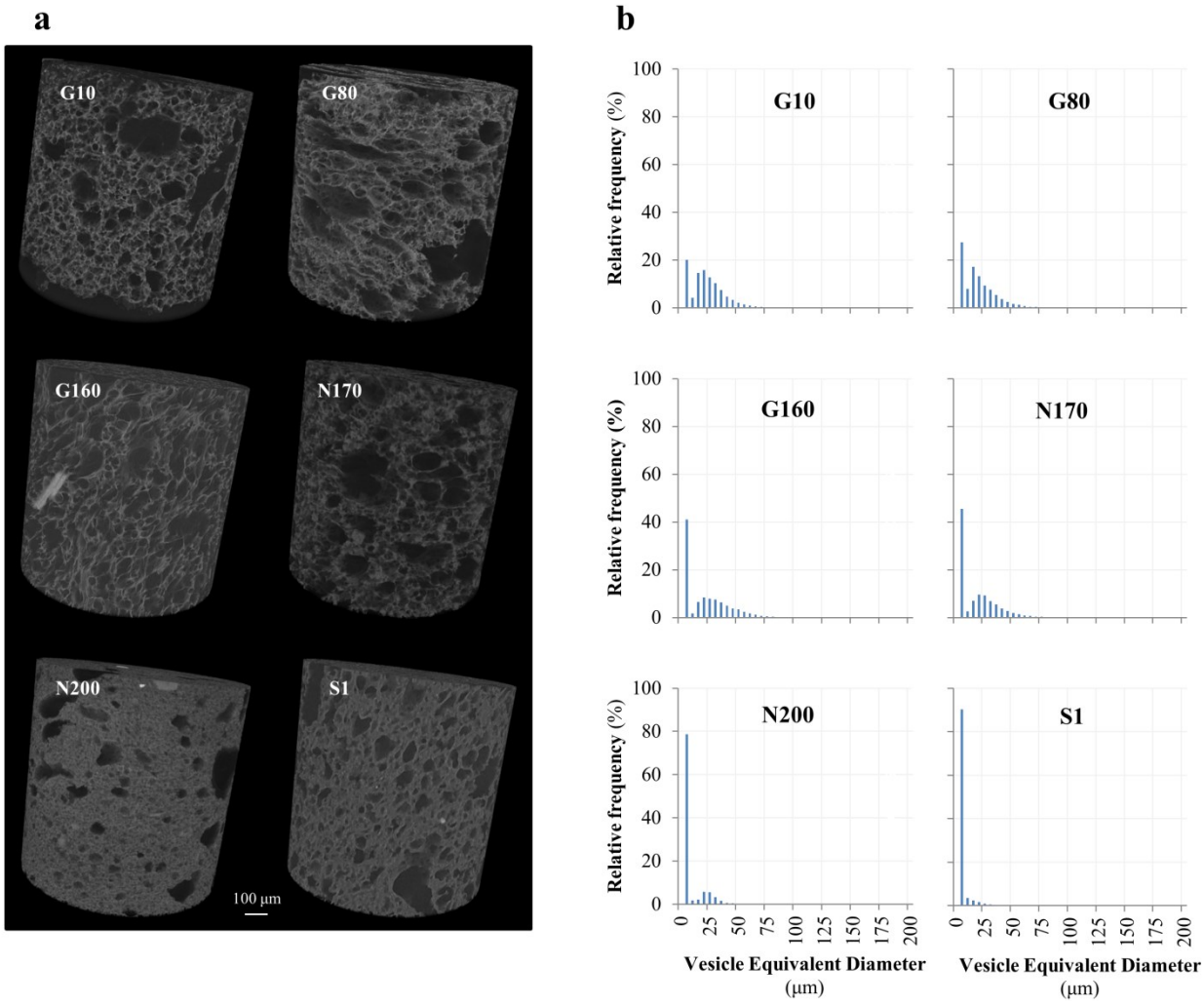

Fig. 7. a) µ-CT 3D images. Volume range: 0.36 - 0.49 mm^3. b) Vesicle size distributions. Histograms show vesicle size frequency for Pomici di Base rocks.

Sample	G10				G80				G160			
Phase	*Glass*	*Pl*	*Sn*	*cpx*	*glass*	*Pl*	*sn*	*cpx*	*Glass*	*pl*	*sn*	*cpx*
# of analyses	12	5	1	2	8	1	0	1	13	4	0	1
SiO_2	60.13 (1.91)	52.74 (4.54)	64.87	48.02 (0.50)	60.30 (1.35)	52.40		44.39	59.73 (2.14)	50.50 (3.55)		47.45
TiO_2	0.29 (0.33)	0.12 (0.38)	0.00	0.70 (0.37)	0.39 (0.36)	0.13		2.16	0.44 (0.44)	0.06 (0.14)		1.02
Al_2O_3	17.70 (0.71)	30.18 (4.23)	19.53	4.26 (2.39)	18.06 (0.62)	29.50		8.58	18.43 (1.62)	31.25 (1.58)		5.52
FeO	2.56 (0.44)	0.44 (0.25)	0.15	12.73 (1.87)	2.53 (0.58)	0.77		13.07	3.02 (1.35)	0.61 (0.61)		13.26
MnO	0.23 (0.25)	0.00 (0.00)	0.07	0.57 (0.23)	0.31 (0.30)	0.16		0.22	0.19 (0.30)	0.07 (0.26)		0.50
MgO	0.24 (0.18)	0.06 (0.13)	0.03	9.70 (0.24)	0.26 (0.23)	0.00		9.02	0.42 (0.43)	0.05 (0.15)		9.15
CaO	2.68 (0.40)	12.60 (4.60)	0.53	23.18 (0.83)	2.81 (0.24)	12.77		22.05	3.29 (0.76)	13.95 (3.02)		22.16
Na_2O	4.15 (0.57)	3.55 (2.06)	1.60	0.13 (0.09)	4.05 (0.36)	3.69		0.31	3.65 (1.09)	2.72 (1.26)		0.39
K_2O	8.23 (0.33)	0.66 (0.52)	13.95	0.02 (0.05)	8.40 (0.70)	0.66		0.08	8.78 (1.07)	0.58 (0.64)		0.00
P_2O_5	0.11 (0.18)	0.08 (0.28)	0.19	0.01 (0.04)	0.06 (0.16)	0.00		0.18	0.13 (0.22)	0.03 (0.10)		0.26
Cl	0.69 (0.08)				0.67 (0.24)				0.52 (0.33)			
Total	97.00 (2.80)	100.44 (2.80)	100.93	99.32 (4.86)	97.82 (2.35)	100.08		100.05	98.61 (3.42)	99.80 (0.68)		99.71
$^{87}Sr/^{86}Sr$	0.707527 ± 6		0.707499 ± 6	0.707500 ± 6	0.707530 ± 7				0.707539 ± 6		0.707550 ± 6	0.707477 ± 6
$^{143}Nd/^{144}Nd$	0.512439 ± 7		-	0.512437 ± 7	0.512447 ± 7				0.512432 ± 6		0.512440 ± 6	0.512444 ± 6
Sample	**N170**				**N200**				**S1**			
Phase	*Glass*	*Pl*	*Sn*	*cpx*	*glass*	*Pl*	*sn*	*cpx*	*Glass*	*pl*	*sn*	*cpx*
# of analyses	12	4	0	0	10	1	0	2	11	5	1	6
SiO_2	59.55 (3.13)	50.91 (2.49)			57.21 (1.77)	47.82		44.10 (1.42)	55.82 (1.93)	52.61 (3.56)	58.74	44.58 (2.18)
TiO2	0.43 (0.35)	0.08 (0.23)			0.40 (0.39)	0.30		1.61 (1.32)	0.65 (0.53)	0.19 (0.32)	0.88	1.68 (0.85)
Al_2O_3	18.35 (1.13)	30.31 (2.51)			18.78 (0.82)	33.13		8.82 (2.92)	17.46 (2.57)	27.94 (2.33)	21.66	9.55 (2.04)
FeO	3.39 (0.80)	0.53 (0.32)			5.01 (0.83)	1.04		11.97 (2.54)	7.27 (1.91)	1.11 (0.45)	0.78	11.29 (0.86)
MnO	0.22 (0.41)	0.01 (0.03)			0.16 (0.38)	0.25		0.23 (0.00)	0.25 (0.33)	0.10 (0.28)	0.27	0.27 (0.41)
MgO	0.44 (0.19)	0.06 (0.26)			0.83 (0.28)	0.00		9.60 (0.09)	1.23 (0.31)	0.28 (0.26)	0.00	9.98 (1.03)
CaO	3.81 (1.09)	13.14 (1.39)			4.45 (1.07)	15.97		22.68 (0.33)	4.22 (2.43)	12.02 (2.25)	1.12	21.57 (1.13)
Na_2O	3.83 (0.69)	3.08 (0.65)			3.46 (0.50)	1.93		0.12 (0.12)	3.22 (0.56)	3.05 (0.74)	3.71	0.01 (0.04)
K_2O	8.62 (0.93)	0.50 (0.25)			7.88 (0.77)	0.42		0.22 (0.21)	7.21 (1.83)	1.77 (1.09)	7.49	0.30 (0.47)
P_2O_5	0.15 (0.20)	0.05 (0.21)			0.35 (0.21)	0.00		0.31 (0.21)	0.47 (0.41)	0.16 (0.36)	0.00	0.56 (0.51)
Cl	0.57 (0.15)				0.59 (0.16)				0.76 (0.31)			
Total	99.35 (4.91)	98.69 (2.12)			99.12 (2.01)	100.86		99.67 (0.58)	98.54 (2.60)	99.24 (0.99)	94.64	99.79 (2.51)
$^{87}Sr/^{86}Sr$	0.707556 ± 8		0.707506 ± 6	0.707470 ± 6	0.707602 ± 6				0.707605 ± 7		0.707534 ± 6	-
$^{143}Nd/^{144}Nd$	0.512435 ± 6		0.512429 ± 7	0.512452 ± 6	0.512436 ± 6				0.512431 ± 6		-	0.512452 ± 7

Table 1. Geochemical composition of representative glasses and phenocrysts (data refer to microlites only for sample S1) in the analyzed samples. Value in brackets is 2σ (standard deviation). pl = plagioclase, sn = sanidine, cpx = clinopyroxene.

Sample	Melt composition	Bulk vesicularity (%)	Microlite content (vol.%)
G10	Trachyte	75	-
G80	Trachyte	76	-
G160	Trachyte	76	-
N170	Trachyte	75	-
N200	Latite	59	15
S1	Latite	48	31

Table 2. Key petrological features of the analyzed samples.

5. Discussion

5.1. Pre-eruptive processes

Our geochemical data show the existence of a chemically-zoned magma chamber, from trachyte to latite. We have estimated pre-eruptive temperature and pressure by using the clinopyroxene-liquid thermo-barometer developed for alkaline differentiated magmas by Masotta et al. (2013). Particularly, thermometric calculations indicate that crystallization temperature continuously increases from 907±46 °C in the upper trachytic layer to 1059±46 °C towards the basal latite with an estimated average pressure of 137±85 MPa. The last value is in agreement with the results obtained by using Cl-content on matrix-glasses (Balcone-Boissard et al., 2015). In fact, an average pressure of 106±11 MPa (using Cl solubility from Signorelli and Carrol, 2002 and considering an analytical uncertainty of 10% for Cl concentration) can be inferred for the upper trachytic magma. We neglected the latitic terms from this calculation due to the lack of data on Cl solubility for this melt composition and their high-microlite content that weaken the estimate. Therefore a depth of 4.33±0.45 km can be calculated for magma chamber top assuming a lithostatic system with an average crustal density of 2.5 g/cm^3. Interestingly the two different barometers used in this work estimate similar values of storage pressures and allow to achieve useful information to better reconstruct the time evolution of the Somma-Vesuvius plumbing system, for which very few data exist on its initial eruptive periods (see Scaillet et al., 2008; Balcone-Boissard et al., 2015). In particular, a broad pressure range of 300-500 MPa has been further reported by Landi et al. (1999) for Pomici di Base compositions on the basis of two feldspars (Stormer, 1975) and feldspar-liquid (Kudo and Weill, 1970) barometers calibrated on limited databases.

Moreover, our geochemical and temperature trends suggest that factional crystallization played a dominant role in the magma evolution from latitic to trachytic compositions. In fact, the general increase in SiO_2, Na_2O, K_2O and decrease in TiO_2, FeO, CaO, P_2O_5, together with the almost constant trend of Al_2O_3, are compatible with the crystallization of sanidine, plagioclase and clinopyroxene, which coherently show an average decrease in Or content, an enrichment in An content and a reduction in Fe content respectively. However the low crystal content in juvenile products is in contrast with the high crystallization indicated by mass balance calculations to obtain this differentiation. These features suggest that magma was likely extracted by a crystal mush (see also Landi et al., 1999).

The highest $^{87}Sr/^{86}Sr$ ratios observed in separated groundmasses respect to sanidine and clinopyroxene crystals imply the involvement of crustal contamination processes. Particularly, isotopic variations suggest that assimilation was a later process occurred mainly after precipitation of minerals. The potential influence of contamination in the petrogenesis of the analyzed Pomici di Base rocks was tested using the EC-AFC (Energy-Constrained Assimilation and Fractional Crystallization) model by Pappalardo et al. (2018). Best fit was obtained considering a magma contamination by limestone rocks (Triassic limestone with $^{87}Sr/^{86}Sr$ = 0.709 and $^{143}Nd/^{144}Nd$ =

0.512; e.g. Piochi et al. 2006; Di Renzo et al., 2007) at an ambient temperature of 300 °C (see De Lorenzo et al., 2006, for the constrained depth). The results show that the observed Sr and Nd isotopic variation is justified by the ingestion of 2-4% of carbonate rocks by a magma, which has crystallized for about 55% of its initial mass. The carbonatic contamination hypothesis is also supported by the abundance of carbonatic metamorphosed clasts found in the Pomici di Base deposits and juvenile rocks (Bertagnini et al., 1998 and Landi et al.,1999). Experimental data show that the contamination by carbonate country rocks (extended from about 2 to 10 km beneath Somma-Vesuvius; e.g. Berrino et al., 1998) during magma storage promotes the release of large amounts of CO_2-rich fluids and consequently can be cause of ignition and/or increase of the degree of explosiveness of the eruption (e.g. Iacono Marziano et al., 2008; Deegan et al., 2010; 2011; Mollo et al., 2010; Jolis et al., 2013; Blythe et al., 2015). Hovewer, the high values of Sr isotopic ratios in latitic groundmasses, in disequilibrium with phenocrysts and trachytic glasses, indicate more complex contamination mechanisms (see below).

5.2. Syn-eruptive processes

White and gray trachytic pumices, erupted from a stable plume during an early stage of the plinian phase, show polymodal VSDs trends suggesting different nucleation stages. Particularly, the large vesicles population represents the early-formed bubbles with varying history of interaction and coalescence, while the population of small bubbles reflects a late-stage nucleation event in the shallow conduit and then depicts the vesiculation state of the magma at the time of fragmentation (Baker et al., 2012; Gonnermann and Houghton, 2012; Liedl et al., 2019). The evidence of coalescence between larger bubbles, separated by thin films of matrix-glass (1 to 10 μm), associated to high degree of vesiculation suggest that bubble growth has occurred up to the achievement of a porosity threshold (65-75%; e.g. Sparks, 1978; Gardner et al., 1996), at which the experimental data indicate an abrupt increase in permeability with a small increment in vesicularity (Takeuchi et al., 2009; Rust and Cashman, 2011). These data suggest that fragmentation is most likely to occur under closed-system degassing conditions when the magma exceeds the critical porosity (between 70-80%). In particular, in case of rapid magma ascent in volcanic conduit, the gas fails to move away from the liquid even when it is characterized from an high permeability, thus favoring the expansion of the gas that leads to the fragmentation. Rapid ascent rate is confirmed by the absence of microlites in the pumice samples, in agreement with decompression experiments showing non-crystallization of microlites in the case of ascent rates lower than few hours (e.g. a delay of ∼1–4 hours in the nucleation of microlites after decompression has been observed by Couch et al., 2003).

Latitic black-scoriae, erupted at the end of this sustained-column phase, show lower porosity associated to the presence of polylobate thick-walled bubbles and microlite-bearing groundmass glass. These features suggest that the more mafic and less viscous melt, about the 75% of the total involved magma during this eruption (Landi et al., 1999), suffered at shallow level, during rising from a deep source, outgassing and decompression-induced microlite growth, producing abrupt rheological changes. In this scenario the dominant presence of small round bubbles represent a late stage vesiculation of the partially degassed magma, that has been in this way forced to erupt explosively. New available (Pappalardo et al., 2018) textural data suggest that this nucleation event was triggered by the ongoing decarbonation process and the related conspicuous release of CO_2-rich fluids that was more intense in these hot less-evolved liquids. This hypothesis is supported by the high Sr isotopic ratios in latitic groundmass. High temperature and pressure carbonate assimilation experiments demonstrated that decarbonation can be very fast (minutes to days; e.g. Deegan et al., 2011; Blythe et al., 2015) and may promote the migration of CO_2 bubbles from the dissolving carbonate throughout the magma so enhancing the ability of the magma itself to erupt explosively (Dallai et al., 2011, Freda et al., 2010).

6. Conclusions

Here we present our preliminary results of a geochemical, isotopic and textural study performed on pyroclasts emitted during the caldera-forming Pomici di Base (22 ka) plinian eruption from Somma-Vesuvius volcano.
Particularly geochemical and isotopic data suggest the existence, immediately before the eruption, of a magma chamber with a top located at a depth of about 4.5 km and characterized by a compositional (from trachyte to latite) and thermal (from ~900 to 1050 °C) zoning. Magmas, geochemically cogenetic, were probably extracted from a crystal-rich mush zone in the magma reservoir. However, the variation of Sr and Nd isotopic ratios indicates the occurrence of a crustal (limestone) contamination process (<5%), and a subsequent CO_2 liberation, during magma storage.
Textural data suggest a degassing process under closed-system conditions at the beginning of the plinian fallout phase, during the fast emission of trachitic magmas. In contrast, during the following emission of latitic magmas, the degassing took place under open-system conditions, at decreasing decompression rates thus producing the collapse of the eruptive column and the consequent triggering of the phreatomagmatic phase.

Acknowledgements

The results of this paper were presented at 36° national congress GNGTS, 14-16 november 2017, Trieste, Italy.
The authors wish to thank I. Arienzo (INGV-OV), R. de Gennaro (University of Naples Federico II) for essential helps during isotopic and SEM-EDS analyses, respectively. We acknowledge two anonymous reviewers for suggestions that greatly improved the manuscript.

References

Andronico D., Calderoni G., Cioni R., Sbrana A., Sulpizio R. and Santacroce R .;1995: Geological map of Somma–Vesuvius volcano. Per. Min., 64 (1–2), 77–78.
Ayuso R.A., De Vivo B., Rolandi G., Seal II R.R. and Paone A.; 1998: Geochemical and isotopic (NdPb-Sr-O) variations bearing on the genesis of volcanic rocks from Vesuvius, Italy. J. Volcanol. Geotherm. Res., 82, 53-78.
Baker D.R., Mancini L., Polacci M., Higgins M.D., Gualda G.A.R., Hill R.J. and Rivers M.L.; 2012: An introduction to the application of X-ray microtomography to the three-dimensional study of igneous rocks. Lithos, 148, 262−276.
Balcone-Boissard H., Boudon G., Cioni R., D.Webster J., Zdanowicz G., Orsi G. and Civetta L.; 2015: Chlorine as a geobarometer for alkaline magmas: Evidence from a systematic study of the eruptions of Mount Somma - Vesuvius. Sci. Rep., 6, 21726.
Belkin H. E. and De Vivo B.; 1993: Fluid inclusion studies of ejected nodules from Plinian eruptions of Mt. Somma-Vesuvius. J. Volcanol. Geotherm. Res., 58, 98-100.
Berrino G., Corrado G. and Riccardi U.; 1998: Sea gravity data in the Gulf of Naples: a contribution to delineating the structural pattern of the Vesuvian area. J. Volcanol. Geoth. Res., 82, 139–150.
Bertagnini A., Landi P., Rosi M. and Vigliargio A.; 1998: The Pomici di Base plinian eruption of Somma-Vesuvius. J. Volcanol. Geotherm. Res., 83, 219–239.
Blundy J. and Cashman K.; 2008: Petrologic reconstruction of magmatic system variables and processes. In: Putirka K. and Tepley F. (eds), Minerals, Inclusions, and Volcanic Processes, Mineralogical Society of America and Geochemical Society, Reviews in Mineralogy and Geochemistry, 69, 179–239.
Blythe L.S., Deegan F.M., Freda C., Jolis E.M., Masotta M., Misiti V., Taddeucci J. and Troll V.R.; 2015: CO_2 bubble generation and migration during magma–carbonate interaction. Contrib. Mineral. Petrol., 169 (4), 1–16.
Borgia A., Tizzani P., Solaro G., Manzo M., Casu F., Luongo G., Pepe A., Berardino P., Fornaro G., Sansosti E., Ricciardi G.P., Fusi N., Di Donna G. and Lanari R.; 2005: Volcanic spreading of Vesuvius, a new paradigm for interpreting its volcanic activity. Geophysical Research Letters, 32, L03303.
Capaldi G., Gillot P.Y., Munno R., Orsi G. and Rolandi G.; 1985: Sarno Formation: the major plinian eruption of the Somma-Vesuvius. IAVCEI 1985, Scientific Assembly, Giardini di Naxos.

Cioni R.; 2000: Volatile content and degassing processes in the AD 79 magma chamber at Vesuvius (Italy). Contributions to Mineralogy and Petrology, 140, 40-54.
Cioni R., Marianelli P. and Santacroce R.; 1998: Thermal and compositional evolution of the shallow magma chambers of Vesuvius: evidence from pyroxene phenocrysts and melt inclusions. Journal of Geophysical Research, 103, 18277-18294.
Cioni R., Santacroce R. and Sbrana A.; 1999: Pyroclastic deposits as a guide for reconstructing the multi-stage evolution of the Somma-Vesuvius Caldera. Bulletin of Volcanology, 60, 207–222.
Cioni R., Bertagnini A., Santacroce R. and Andronico D.; 2008: Explosive activity and eruption scenarios at Somma-Vesuvius (Italy): Towards a new classification scheme. Journal of Volcanology and Geothermal Research, 178, 331–346.
Cioni R., Bertagnini A., Andronico D., Cole P.D. and Mundula F.; 2011: The 512 AD eruption of Vesuvius: Complex dynamics of a small scale subplinian event. Bulletin of Volcanology, 73, 789–810.
Civetta L., Galati R. and Santacroce R.; 1991: Magma mixing and convective compositional layering within the Vesuvius magma chamber. Bulletin of Volcanology, 53, 287–300.
Cnudde V. and Boone M.N.; 2013: High-resolution X-ray computed tomography in geosciences: a review of the current technology and applications. Earth-Science Reviews, 123, 1–17.
Cole P.D. and Scarpati C.; 2010: The 1944 eruption of Vesuvius. The 1944 eruption of Vesuvius, Italy: combining contemporary accounts and field studies for a new volcanological reconstruction. Geological Magazine, 147, 391–415.
Couch S., Sparks R.S.J. and Carroll M.R.; 2003: The kinetics of degassing-induced crystallization at Soufriere Hills volcano, Montserrat. Journal of Petrology, 44, 1477-1502.
Cubellis E., Marturano A. and Pappalardo L.; 2016: The last Vesuvius eruption in March 1944: reconstruction of the eruptive dynamic and its impact on the environment and people through witness reports and volcanological evidence. Nat. Hazards, 82, 95.
Dallai L., Cioni R., Boschi C. and D'Oriano C.; 2011: Carbonate-derived CO2 purgingmagma at depth: Influence on the eruptive activity of Somma-Vesuvius, Italy. Earth Planet. Sci. Lett., 310, 84–95.
De Lorenzo S., Di Renzo V., Civetta L., D'Antonio M. and Gasparini P.; 2006: Thermal model of the Vesuvius magma chamber. Geophys. Res. Lett., 33, L17302.
De Vivo B., Petrosino P., Lima A., Rolandi G. and Belkin H.E.; 2010: Research progress in volcanology in the Neapolitan area, southern Italy: a review and some alternative views. Mineralogy and Petrology, 99, 1-28.
Deegan F.M., Troll V.R., Freda C., Misiti V., Chadwick J.P., McLeod C.L. and Davidson J.P.; 2010: Magma-carbonate interaction processes and associated CO_2 release at Merapi volcano, Indonesia: insights from experimental petrology. J. Petrol., 51, 1027-1051.
Deegan F.M., Troll V.R., Freda C., Misiti V. and Chadwick J.P.; 2011: Fast and furious: crustal CO_2 release at Merapi volcano, Indonesia. Geol. Today, 27, 57-58.
Del Moro A., Fulignati P., Marianelli P. and Sbrana A.; 2001: Magma contamination by direct wall rock interaction: constraints from xenoliths from the wall of carbonatehosted magma chamber (Vesuvius 1944 eruption). J. Volcanol. Geotherm. Res., 112, 15–24.
Delibrias G., Di Paola G.M., Rosi M. and Santacroce R.; 1979: La storia eruttiva del complesso vulcanico Somma-Vesuvio ricostruita dalle successioni piroclastiche del Monte Somma. Rendiconti della Società Italiana di Mineralogia e Petrologia, 35, 411–438.
Di Renzo V., Di Vito M.A., Arienzo I., Carandente A., Civetta L., D'Antonio M., Giordano F.,Orsi G. and Tonarini S.; 2007: Magmatic history of Somma-Vesuvius on the basis of new geochemical and isotopic data from a deep borehole (Camaldoli della Torre). J. Petrol., 48, 753-784.
Freda C., Gaeta M., Giaccio B., Marra F., Palladino D.M., Scarlato P. and Sottili G.; 2011: CO_2- driven large mafic explosive eruptions: The Pozzolane Rosse case study from the Colli Albani Volcanic District (Italy). Bull. Volcanol., 73 (3), 241–256.
Fulignati P., Gioncada A. and Sbrana A.; 1995: The magma chamber related hydrothermal system of Vesuvius, first mineralogical and fluid inclusion data on hydrothermalized subvolcanic and lavic samples from phreatomagmatic eruptions. Per. Mineral., 64, 185–187.
Fulignati P., Marianelli P. and Sbrana A.; 1998: New insights on the thermometamorphicmetasomatic magma chamber shell of the 1944 eruption of Vesuvius. Acta Vulcanol., 10 (1), 47–54.
Gardner J.E., Thomas R.M.E., Jaupart C. and Tait S.; 1996: Fragmentation of magma during Plinian volcanic eruptions. Bulletin of Volcanology, 58 (2–3), 144–162.
Gilg H.A., Lima A., Somma R., Ayuso R.A., Belkin H.E. and De Vivo B.; 1999: A fluid inclusion and isotope study of calc-silicate ejecta from Mt. Somma-Vesuvius: evidence for interaction of high-temperature hypersaline fluids with the sedimentary basement. Proceedings of ECROFI XV, Potsdam, Germany, (abstracts and program), Terra Nostra, 99 (6), 118-120.
Gilg H.A., Lima A., Somma R., Belkin H.E., De Vivo B. and Ayuso R.A.; 2001: Isotope geochemistry and fluid inclusions study of skarns from Vesuvius. Mineral. Petrol., 73, 145–176.
Gonnermann H.M. and Houghton B.F.; 2012: Magma degassing during the Plinian eruption of Novarupta, Alaska, 1912. Geochem. Geophys. Geosyst., 13, Q10009.

Gonnermann H.M. and Manga M.; 2007: The fluid mechanics inside a volcano. Ann. Rev. Fluid Mech., 39, 321–356.
Houghton B.F. and Wilson C.J.N.; 1989: A vesicularity index for pyroclastic deposits. Bull. Volcanol., 51, 451–462.
Houghton B.F., Carey R.J., Cashman K.V., Wilson C,J,N,, Hobdenm B.J. and Hammer J.E.; 2010: Diverse patterns of ascent, degassing, and eruption of rhyolite magma during the1.8 ka Taupo eruption, New Zealand: evidence from clast vesicularity. Journal of Volcanology and Geothermal Research, 195, 31-47.
Iacono Marziano G., Gaillard F. and Pichavant M.; 2008: Limestone assimilation by basaltic magmas: an experimental re-assessment and application to Italian volcanoes. Contrib. Mineral. Petrol., 155, 719-738.
Iacono Marziano G., Gaillard F., Scaillet B., Pichavant M. and Chiodini G.; 2009: Role of non-mantle CO2 in the dynamics of volcano degassing: The Mount Vesuvius example. Geology, 37, 319-322.
Jolis E.M., Freda C., Troll V.R., Deegan F.M., Blythe L.S., McLeod C.L. and Davidson J.P.; 2013: Experimental simulation of magma–carbonate interaction beneath Mt. Vesuvius, Italy. Contrib. Mineral. Petrol., 166, 1335–1353.
Jolis E.M., Troll V.R., Harris C., Freda C., Gaeta M., Orsi G. and Siebe C.; 2015: Skarn xenolith record crustal CO2 liberation during Pompeii and Pollena eruptions, Vesuvius volcanic system, central Italy. Chem. Geol., 415, 17–36.
Joron J.L., Metrich N., Rosi M., Santacroce R. and Sbrana A.; 1987: Chemistry and petrography. In: Santacroce, R. (ed.) Somma-Vesuvius. Quaderni de 'La Ricerca Scientifica, 114, 105-174.
Kudo A.M. and Weill D.F.; 1970: An igneous plagioclase thermometer. Contrib. Mineral. Petrol., 25, 62-65.
Landi P., Bertagnini A. and Rosi M.; 1999: Chemical zoning and crystallization mechanisms in the magma chamber of the Pomici di Base plinian eruption of Somma-Vesuvius (Italy). Contrib. Mineral. Petrol., 135, 179–197.
Liedl A., Buono G., Lanzafame G., Dabagov S.B., Della Ventura G., Hampai D., Mancini L., Marcelli A. and Pappalardo L.; 2019: A 3D imaging textural characterization of pyroclastic products from the 1538 CE Monte Nuovo eruption (Campi Flegrei, Italy). Lithos, 340-341, 316-331.
Lima A., Danyushevsky L.V., De Vivo B. and Fedele L.; 2003: A model for the evolution of the Mt. Somma-Vesuvius magmatic system based on fluid and melt inclusion investigations. In: De Vivo B. and Bodnar R.J. (eds),, Melt Inclusions in Volcanic Systems: Methods, Applications and Problems, Elsevier, New York, pp. 227-249.
Marianelli P., Métrich N., Santacroce R. and Sbrana A.; 1995: Mafic magma batches at Vesuvius: a glass inclusion approach to the modalities of feeding stratovolcanoes. Contrib. Mineral. Petrol., 120, 159–169.
Marianelli P., Metrich N. and Sbrana A.; 1999: Shallow and deep reservoirs involved in magma supply of the 1944 eruption of Vesuvius. Bull. Volcanol., 61, 48-63.
Marianelli P, Sbrana A, Metrich N and Cechetti A.; 2005: The deep feeding system of Vesuvius involved in recent violent strombolian eruptions. Geophysical Research Letters, 32, L2306.
Masotta M., Mollo S., Freda C., Gaeta M. and Moore G.; 2013: Clinopyroxene–liquid thermometers and barometers specific to alkaline differentiated magmas. Contrib. to Mineral. and Petrol., 166, 1545–1561.
Mastrolorenzo G and Pappalardo L.; 2006: Magma degassing and crystallization processes during eruptions of high-risk Neapolitan volcanoes: Evidence of common equilibrium rising processes in alkaline magmas. Earth Plan. Sci. Lett., 250, 164–181.
Mollo S., Gaeta M., Freda C., Di Rocco T., Misiti V. and Scarlato V.; 2010: Carbonate assimilation in magmas: A reappraisal based on experimental petrology. Lithos, 114, 503–514.
Morabito S., Petrosino P., Milia A., Sprovieri M. and Tamburrino S.; 2014: Global and Planetary Change, 123, 121–138.
Pappalardo L., and Mastrolorenzo G.; 2010: Short residence times for alkaline Vesuvius magmas in a multi-depth supply system: Evidence from geochemical and textural studies. Earth and Planetary Science Letters, 296, 133–143.
Pappalardo L. and Mastrolorenzo G.; 2012: Rapid differentiation in sill-like magma reservoir: a case study from the Campi Flegrei caldera. Sci. Rep., 2, 712.
Pappalardo L., Piochi M. and Mastrolorenzo G.; 2004: The 35500 yr BP–1944 AD magma plumbing system of Somma–Vesuvius: constraints on its behaviour and present state through a review of isotope data. Annals of Geophysics, 47, 1363–1375.
Pappalardo L., D'Auria L., Cavallo A. and Fiore S.; 2014: Petrological and seismic precursors of the paroxysmal phase of the last Vesuvius eruption on March 1944. Sci. Rep., 4, 6297.
Pappalardo L., Buono G., Fanara S. and Petrosino P.; 2018: Combining textural and geochemical investigations to explore the dynamics of magma ascent during Plinian eruptions: a Somma–Vesuvius volcano (Italy) case study. Contrib. Mineral. Petrol., 173, 61.
Peccerillo A.; 2005: Plio-Quaternary Volcanism in Italy. Springer, Berlin, 365 pp.
Pichavant M., Scaillet B., Pommier A., Iacono-Marziano G. and Cioni R.; 2014: Nature and evolution of primitive Vesuvius magmas: An experimental study. J. Petrol., 55 (11), 2281-2310.
Piochi M., Ayuso R.A., De Vivo B. and Somma, R.; 2006: Crustal contamination and crystal entrapment during polybaric magma evolution at Mt. Somma-Vesuvius volcano, Italy: Geochemical and Sr isotope evidence. Lithos, 86, 303–329.
Rust A.C., and Cashman K.V.; 2011: Permeability controls on expansion and size distributions of pyroclasts. Journal of Geophysical Research, 116, B11202.
Santacroce R.; 1987: Somma-Vesuvius. CNR Quaderni de La Ricerca Scientifica, 114 (8), Roma.
Santacroce R., Bertagnini A., Civetta L., Landi P. and Sbrana A.; 1993: Eruptive dynamics and petrogenetic processes in a very shallow magma reservoir: the 1906 eruption of Vesuvius. Journal of Petrology , 34, 383-425.

Santacroce R., Cioni R., Marianelli P., Sbrana A., Sulpizio R., Zanchetta G., Donahue D.J. and Joron J.L.; 2008: Age and whole rock–glass compositions of proximal pyroclastics from the major explosive eruptions of Somma-Vesuvius: A review as a tool for distal tephrostratigraphy. Journal of Volcanology and Geothermal Research, 177, 1–18.
Savelli C.; 1968: The problem of rock assimilation by Somma-Vesuvius magmas, II. Compositions of sedimentary rocks and carbonate ejecta from Vesuvius area. Contrib. Mineral. Petrol., 18, 43–64.
Scaillet B., Pichavant M. and Cioni R.; 2008: Upward migration of Vesuvius magma chamber over the past 20.000 years. Nature, 455, 216–219.
Scandone R., Cashman K. and Malone S.D.; 2007: Magma Supply, Magma Ascent and the Style of Volcanic Eruptions. Earth. Planet. Sci. Lett., 253, 513-529.
Shea T., Houghton B.F., Gurioli L., Cashman K.V., Hammer J.E. and Hobden B.J.; 2010: Textural studies of vesicles in volcanic rocks: an integrated methodology. Journal of Volcanology and Geothermal Research., 190, 271–289.
Shea T., Gurioli L., and Houghton B.F.; 2012: Transitions between fall phases and pyroclastic density currents during the AD 79 eruption at Vesuvius: Building a transient conduit model from the textural and volatile record. Bulletin of Volcanology, 74, 2363–2381.
Siani G., Sulpizio R., Paterne M. and Sbrana A.; 2004: Tephrostratigraphy study for the last 18,000 14C years in a deep-sea sediment sequence for the South Adriatic. Quat Sci Rev, 23, 2485–2500.
Signorelli S. and Carroll M.R.; 2002: Experimental study of Cl solubility in hydrous alkaline melts: constraints on the theoretical maximum amount of Cl in trachytic and phonolitic melts. Contrib. Mineral. Petrol., 143, 209–218.
Sparks R.J.S.; 1978: The dynamics of bubble formation and growth in magmas: A review and analysis. Journal of Volcanology and Geothermal Research, 3 (1–2), 1–37.
Stormer J.C.; 1975: A practical two-feldspar geothermometer. Am Mineral, 60, 667-674.
Tait, S., Thomas, R., Gardner, J. and Jaupart, C.; 1998: Constraints on cooling rates and permeabilities of pumice in an explosive eruption jet from colour and magnetic mineralogy. J. Volcanol. Geotherm. Res., 86, 79–91.
Takeuchi S., Tomiya A. and Shinohara H.; 2009: Degassing conditions for permeable silicic magmas: Implications from decompression experiments with constant rates. Earth and Planetary Science Letters, 283 (1–4), 101–110.
Thomas R.M.E. and Sparks, R.S.J.; 1992: Cooling of tephra during fallout from eruption columns. Bull. Volcanol., 54, 542–553.
Trigila R. and De Benedetti A.; 1993: Petrogenesis of Vesuvius historical lavas constrained by Pearce element ratios analysis and experimental phase equilibria. Journal of Volcanology and Geothermal Research , 58, 315-343.
Zdanowicz G., Boudon G., Balcone-Boissard H., Cioni R., Mundula F., Orsi G., Civetta L. and Agrinier P.; 2018: Geochemical and textural constraints on degassing processes in sub-Plinian eruptions: case-study of the Greenish Pumice eruption of Mount Somma-Vesuvius. Bulletin of Volcanology, 80, 38.